Université Grenoble Alpes

THÈSE

pour obtenir le grade de

DOCTEUR DE LA COMMUNAUTE UNIVERSITE GRENOBLE ALPES

Spécialité : **Automatique-Productique**

Arrêté ministériel : 7 août 2006

Présentée par
Thanh Phong PHAM

Thèse dirigée par **Olivier SENAME** et
codirigée par **Luc DUGARD**

préparée au sein du **GIPSA-Lab**
dans **Electronique, Electrotechnique, Automatique, Traitement du Signal (EEATS)**

LPV observer and Fault-tolerant control of vehicle dynamics: application to an automotive semi-active suspension system

Thèse soutenue publiquement le **19 Mai 2020**,
devant le jury composé de:

M. Didier THEILLIOL
Professeur, Université de Lorraine, Président
M. Thierry Marie GUERRA
Professeur, Université Polytechnique Hauts-de-France, Rapporteur
M. Peter GÁSPÁR
Directeur de Recherche, Académie des Sciences, Hongrie, Rapporteur
M. Olivier SENAME
Professeur, Grenoble INP, Directeur de thèse
M. Luc DUGARD
Directeur de recherche, CNRS Grenoble, Co-Directeur de thèse

Dedicated to my parents
and my wife Dan Khue

Acknowledgements

First of all, I would like to express my gratitude and my enormous thanks to my supervisors Professor Olivier Sename and Luc Dugard who gave me this opportunity to do this research. Olivier and Luc, I thank you for everything you have done for me, your support, your advice, and your enthusiasm. You have given me better conditions as well as good opportunities in my research. It was really my luck and my pleasure to work with you and I hope that we can have collaborations in the future.

I would like to thank all the members of the jury, Professor Didier Theillol who is the president of my jury and my examiner, Professor Peter Gaspar and Professor Thierry Marie Guerra for their time to review my thesis and give me constructive reviews and comments. All these comments are very useful in order to improve the quality of the thesis.

Besides, I would like to thank Dr. Mazen Alamir and Prof. Damien Koenig who are members of my CSI jury and Prof. Christian Commault. Thank you so much for your time and your advice to me during three years of the thesis. I would also like to thank Professor Peter Gaspar, Professor Szabó Zoltán, Dr. Balázs Németh, Mr. András Mihály, Mr. Dániel Fényes, Ms. Zsófia Farkas for welcoming me at the Hungarian Academy of Sciences.

Also, a few words for my dear friends in GIPSA-Lab: Tan, Canh, Vuong, Linh, Tien, Hung, Duc, Huy, Bao, Karthik, Constantinos, Sebin, Mukhtar, Makia, Marcelo, Dimitrios, Chhayarith, ... I am grateful to all of you. I am also grateful to Marielle, Sylvie, Patricia, Gabriel... and all members of the staff of GIPSA-Lab. Without you, my work might have not run smoothly.

Finally, I want to thank my parents, my parents in law, and all my family for their confidence in me. They are always behind me and encourage me during my difficulties. Last but not least, my wife Dan Khue, it is not easy to express all my words to you. You are always next to me, support me and with me, we go there together until the end of this great adventure.

Sincerely
Thanh-Phong PHAM

Contents

Résumé des contributions (in French)

Ce texte synthétise les résultats d'un travail de thèse d'une durée de trois années (de Avril 2017 à Mai 2020) effectué dans l'équipe SLR (Systèmes Linéaires et Robustesse) du Département Contrôle des Systèmes au GIPSA-Lab. Cette thèse a été effectuée sous la direction de M. Olivier SENAME (Professeur à Grenoble INP) et de M. Luc DUGARD (Directeur de Recherche au CNRS). Ce travail a été soutenu par le projet 911 du Ministère de l'Éducation et de la Formation du Vietnam.

Introduction

De nos jours, la dynamique des véhicules est d'une importance capitale dans l'industrie automobile. En effet, au cours de la dernière décennie, l'ingénierie automobile a connu une croissance rapide des systèmes semi-actifs et actifs. Il y a eu beaucoup de recherche, de développement et de mise en œuvre de tels sous-systèmes semi-actifs et actifs tels que les actionneurs de freinage, de direction ou de suspension. En particulier, les systèmes de suspension automobile ont également reçu beaucoup d'attention de la part de l'industrie et du monde universitaire en raison de leur rôle essentiel dans la réduction des effets des perturbations routières sur les passagers à bord (confort) et dans le maintien du contact pneu-route (sécurité).

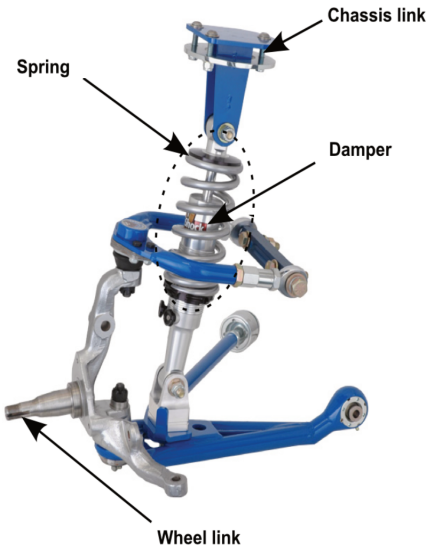

Figure 1: Représentation schématique d'un véhicule commun Système de suspension [Savaresi et al. 2010].

La configuration du système de suspension comprend trois composants principaux (voir Figure 1): 1) un ressort hélicoïdal; 2) un amortisseur; 3) les éléments mécaniques pour relier

la masse suspendue (châssis) et la masse non suspendue (roue). Selon les caractéristiques de l'amortisseur habituellement décrites par le diagramme Force / Vitesse du piston (voir Figure 2 pour les amortisseurs idéaux), l'amortisseur est largement classé en a) passif b) semi-actif c) actif. Parmi ces catégories, l'amortisseur semi-actif est un candidat potentiel sur le marché automobile en raison des avantages de l'amortisseur semi-actif par rapport aux amortisseurs actifs et passifs tels que la demande de puissance négligeable, les caractéristiques de sécurité, l'amélioration des performances du véhicule et le faible coût. Et poids. A titre d'exemple qui sera examiné en détail ultérieurement, la figure 3 présente le diagramme Force-Vitesse d'un amortisseur ER du banc d'essai INOVE, dans les configurations passive (gauche) et semi-active (droite). De nombreux travaux de recherche ont donc été consacrés à la modélisation, l'estimation et les plans de contrôle du système de suspension semi-active

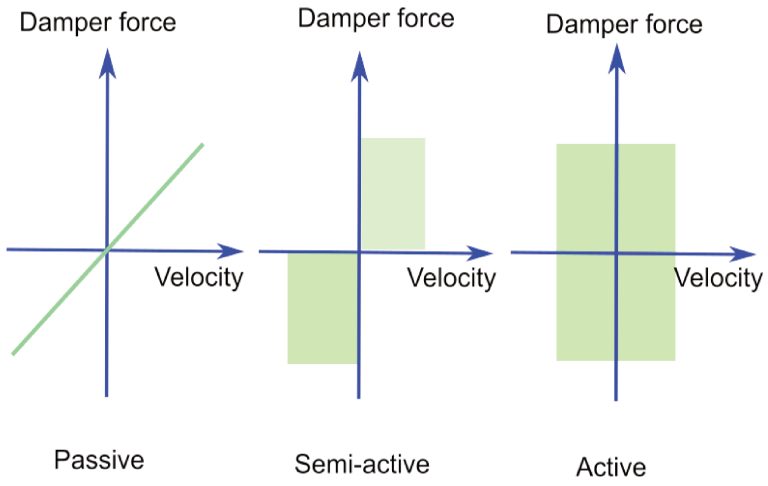

Figure 2: Force vs vitesse du piston: diagramme des amortisseurs passifs idéaux (à gauche), semi-actifs (au milieu) et actifs (à droite).

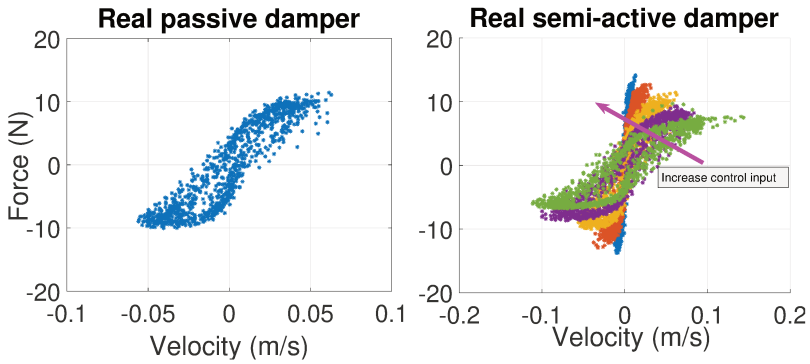

Figure 3: Diagramme force / vitesse du piston de vrais amortisseurs passifs (à gauche), semi-actifs (à droite).

Motivation et objectifs

L'industrie automobile exige continuellement des véhicules plus sûrs et plus confortables.

Par conséquent, les véhicules automobiles sont équipés de nombreuses technologies modernes, de sous-systèmes intelligents en différents domaines d'ingénierie tels que la mécanique, l'électronique, les communications, la commande automatique. Avec ces technologies, la dynamique du véhicule est d'une importance capitale car elle a un très fort impact sur la performance globale du véhicule. Les progrès technologiques dans le contrôle de la dynamique du véhicule sont considérés comme l'une des solutions pour améliorer la performance des véhicules. Cela concerne de nombreux actionneurs (ESC- contrôle électronique de la stabilité, ABS- système de freinage antiblocage de roue, contrôle des suspensions), qui peuvent être utilisés pour améliorer le confort de conduite, la stabilité et la sécurité. Parmi ces actionneurs, les systèmes de suspension sont cruciaux pour la dynamique du véhicule. En effet, le rôle des suspensions dans la dynamique du véhicule est très important: elles établissent le lien entre la route et la carrosserie du véhicule, gérant non seulement la dynamique verticale, mais aussi les dynamiques de roulis et de tangage, causées par leurs mouvements non synchronisés. Le corps principal de travail de cette thèse se concentre sur le thème des systèmes de suspension de véhicule, en particulier sur ceux utilisant les amortisseurs semi-actifs. Les contributions sont principalement orientées dans trois directions : Modélisation et identification de deux modèles non linéaires orientés contrôle pour les amortisseurs ER qui équipent le banc d'essai INOVE de GIPSA-lab. La connaissance en temps réel de l'amortisseur est d'une grande importance pour le diagnostic dynamique et le contrôle du véhicule. Par conséquent, trois observateurs robustes (dans le contexte Hinf pour les systèmes non linéaires de type Lipschitz et les systèmes non linéaires à paramètres variant) sont proposés pour estimer la force d'amortissement de l'amortisseur ER. La commande tolérante aux fautes du système de suspension semi-active est effectuée à l'aide de l'approche LPV avec un modèle de défaut de l'amortisseur.

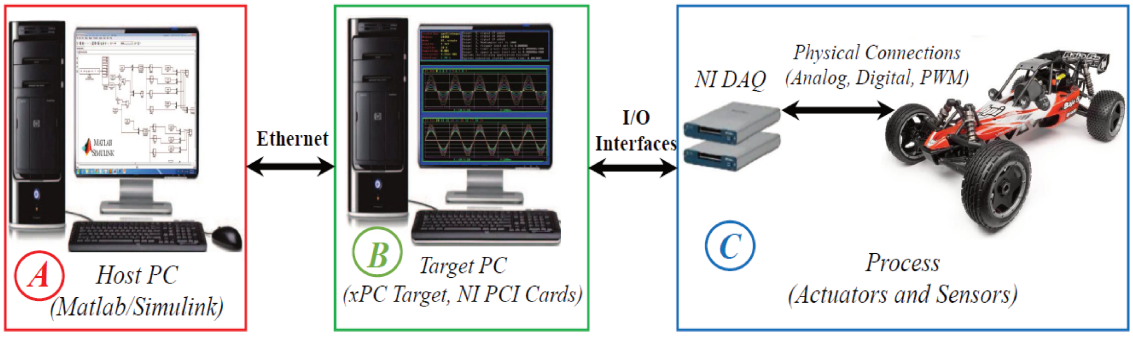

Figure 4: Schéma de la plateforme expérimentale INOVE [Tudón-Martínez et al. 2015]

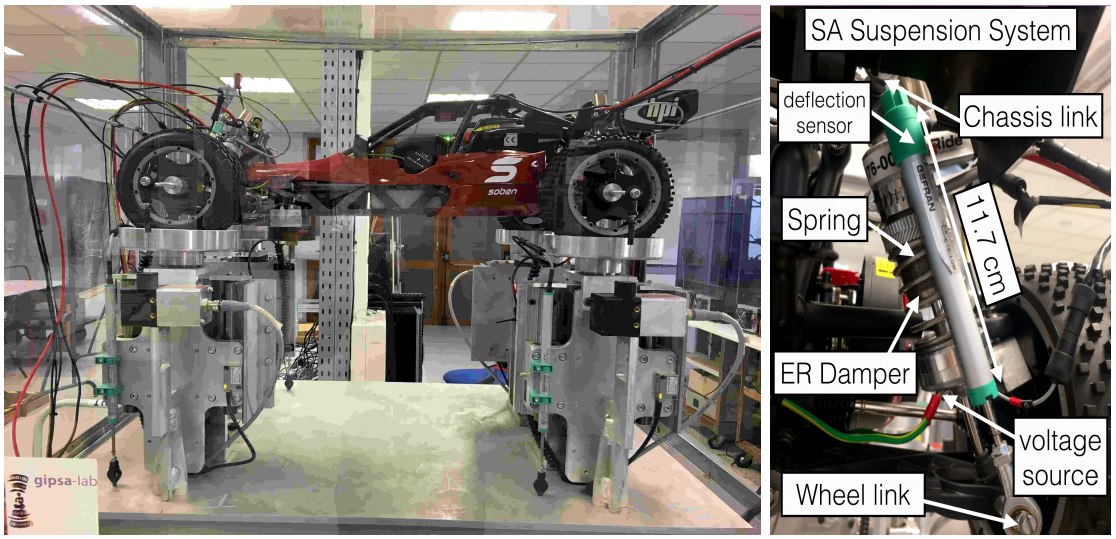

Figure 5: Le banc d'essai expérimental INOVE au GIPSA-lab.

Contributions

Le chapitre 1 présente l'étude de modélisation et l'identification de deux modèles simplifiés pour les amortisseurs électrorhéologiques utilisés dans les systèmes de suspension de véhicules. Les modèles exhibent les comportements principaux de l'amortisseur ER (non linéarité et dynamique). Les deux modèles sont validés par différents tests sur la plate-forme expérimentale INOVE de GIPSA-lab.

- Un modèle Bingham étendu

$$\begin{cases} F_d = k_0 x_p + c_0 \dot{x}_p + F_{er} \\ \tau(u)\dot{F}_{er} + F_{er} = \sigma u^{\beta} \text{sign}(\dot{x}_p) \end{cases}$$

- Un modèle Guo étendu

$$\begin{cases} F_d = k_0 x_p + c_0 \dot{x}_p + F_{er} \\ \tau(u)\dot{F}_{er} + F_{er} = f_c.u.tanh(k_1 x_p + c_1 \dot{x}_p) \end{cases}$$

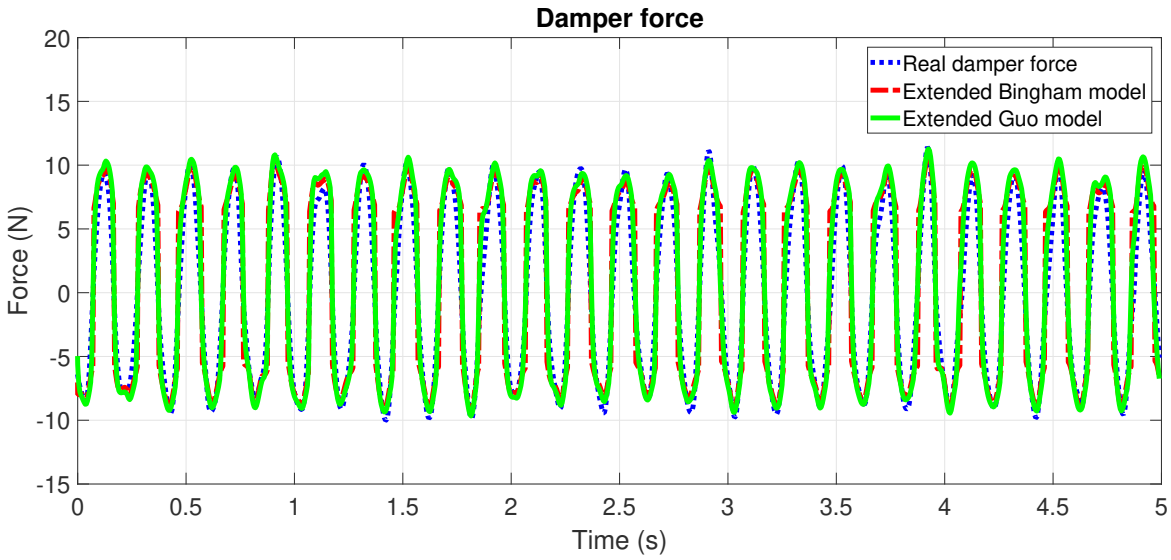

Figure 6: Résultats de la validation: basé sur un modèle et profil de route sinusoïdal à force réelle

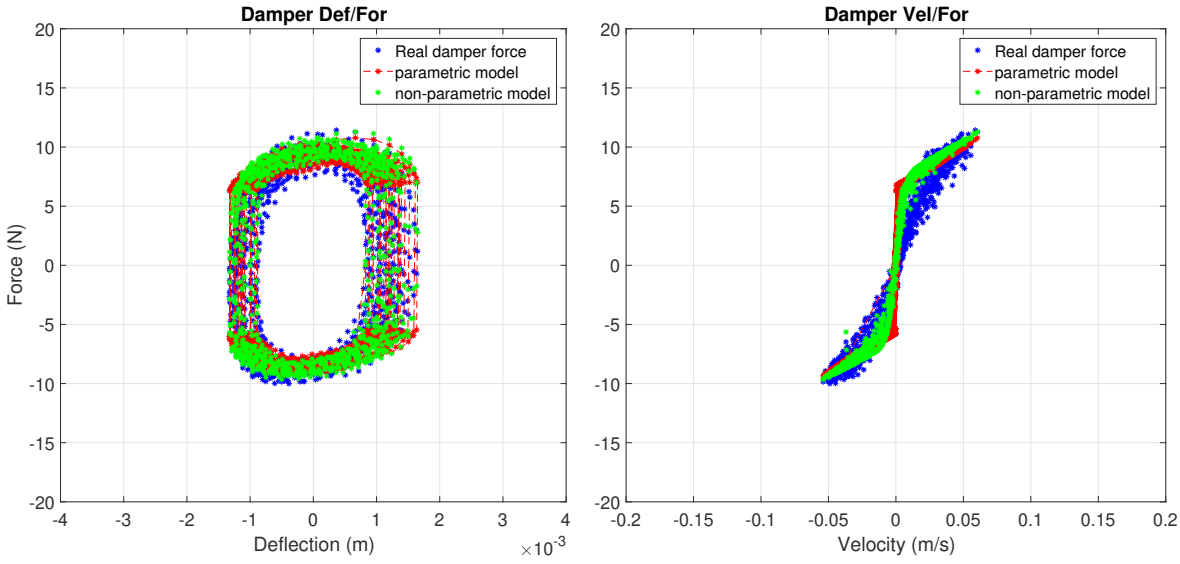

Figure 7: Résultats de la validation: Diagrammes des amortisseurs - Profil routier sinusoïdal

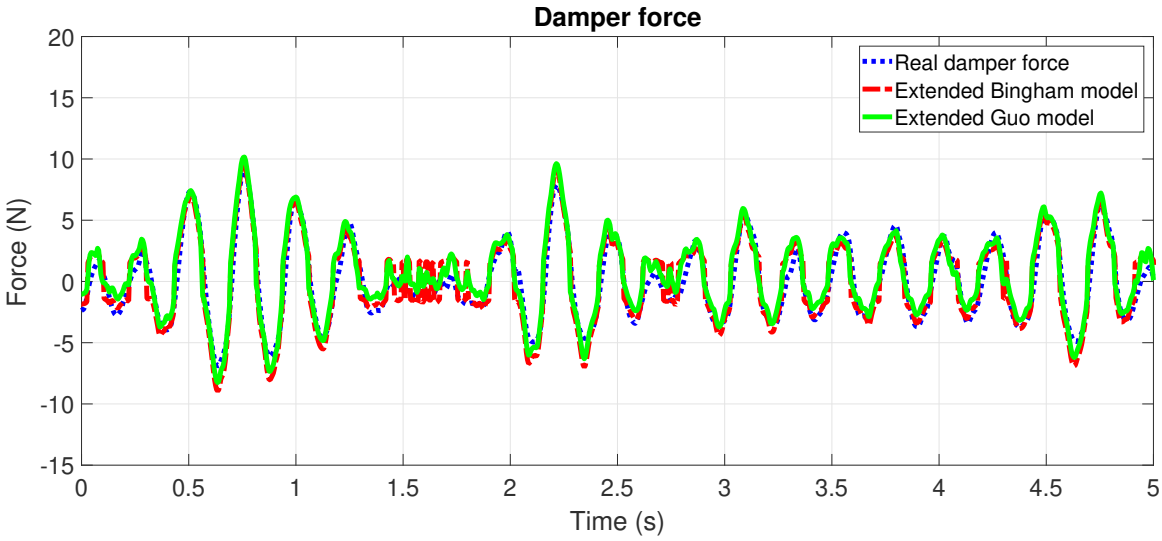

Figure 8: Résultats de la validation: basés sur un modèle et force réelle - Profil routier ISO

Le chapitre 2 présente les modèles de quart de véhicule étendus, qui seront utilisés pour la conception des observateurs et des contrôleurs — les modèles de quart de véhicule étendu d'un modèle d'amortisseur dynamique non linéaire du premier ordre. L'équation dynamique du système de quart de véhicule est écrite dans le cadre des systèmes LTI pour la conception du contrôle et sous forme de deux systèmes non linéaires (Lipschitz non linéaire et formulation non linéaire à paramètres variant) pour la conception des observateurs.

La deuxième partie de la thèse est consacrée à l'une des principales contributions avec la proposition de trois observateurs pour estimer la force d'amortissement de l'amortisseur ER dans le système de suspension, ce qui est d'une grande importance pour le diagnostic et le contrôle dynamique du véhicule. La structure de cette partie est la suivante:

Le chapitre 3 présente une extension de la synthèse d'un observateur Hinf unifié pour les Systèmes non linéaires Lipschitz soumis à des bruits d'entrée et de mesure inconnus. Les objectifs sont de découpler les effets des perturbations d'entrée inconnues bornées et de minimiser les effets des bruits de mesure sur les erreurs d'estimation des variables d'état en utilisant un Critère Hinf, alors que la non linéarité satisfait à la condition de Lipschitz. Cette nouvelle approche est développée pour estimer la force d'un amortisseur électrorhéologique (ER) dans un système de suspension automobile et elle est mise en œuvre sur le banc d'essai INOVE de GIPSA-lab (véhicule réel 1/5 échelle) pour l'évaluation des performances en temps réel. L'observateur unifié d'ordre complet considéré H_∞ est donné par

$$\begin{cases} \dot{z} = Nz + Jy + H\Phi(\hat{x})u + Mv \\ \dot{v} = Pz + Qy + Gv \\ \hat{x} = Rz + Sy \end{cases}$$

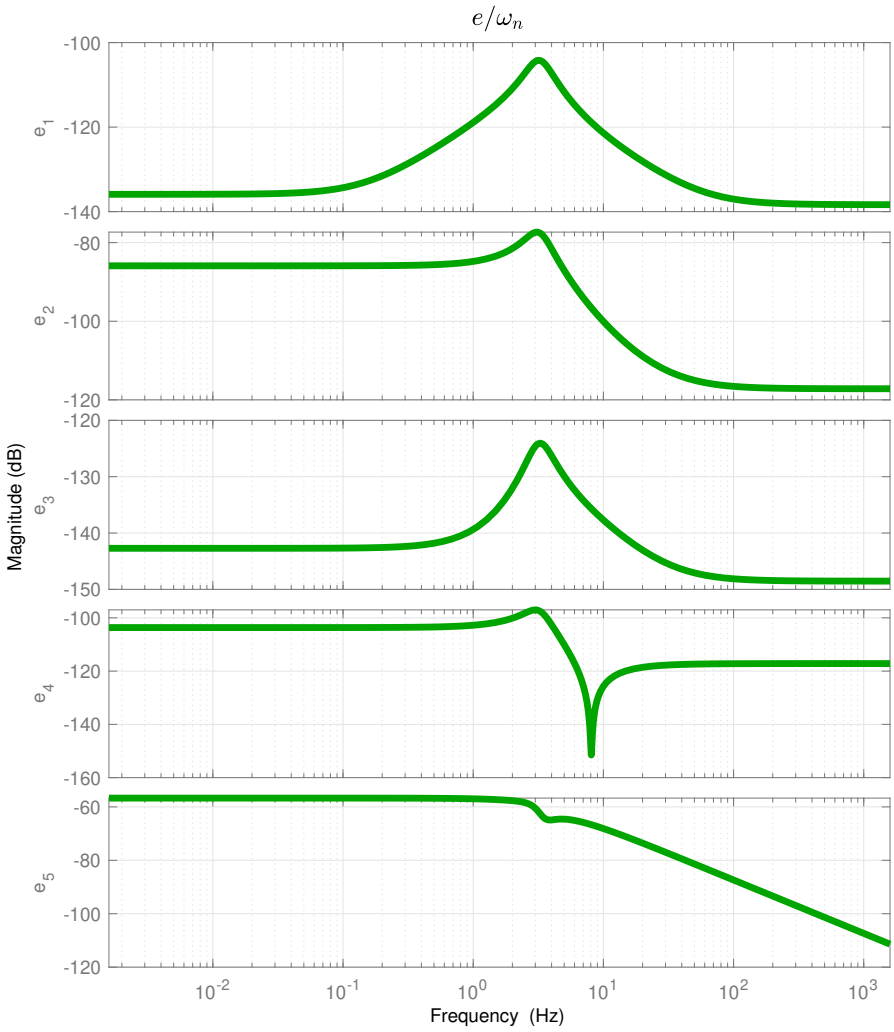

Figure 9: $\|e/\omega_n\|$- Diagrammes de Bode de l'observateur unifié $\mathcal{H}_\infty$

Le chapitre 4 propose un observateur non linéaire à paramètre variant (NLPV) pour estimer, en temps réel, la force d'un amortisseur électrorhéologique (ER) dans un système de suspension automobile. L'effet des perturbations du profil de la route et des bruits de mesure sur les erreurs d'estimation est traité via le cadre Hinf. En outre, la non linéarité prise en compte dans le modèle d'amortisseur (et utilisée dans la formulation de l'observateur) est bornée par une condition de Lipschitz. Ce chapitre aborde le problème de conception de l'observateur NLPV via une de Lyapunov fonction constante (méthode polytopique) et une Lyapunov fonction de à paramètre-dépendant (méthode de quadrillage). Pour l'évaluation de leurs performances, les observateurs sont mis en œuvre sur le banc d'essai INOVE de

GIPSA-lab (véhicule réel à l'échelle 1/5). L'observateur $NLPV$ est choisi comme suit

$$\begin{cases} \dot{\hat{x}} = A\hat{x} + L(\rho)(y - C\hat{x}) + B(\rho)\Phi(\hat{x}) \\ \hat{z}_e = C_z\hat{x} \end{cases}$$

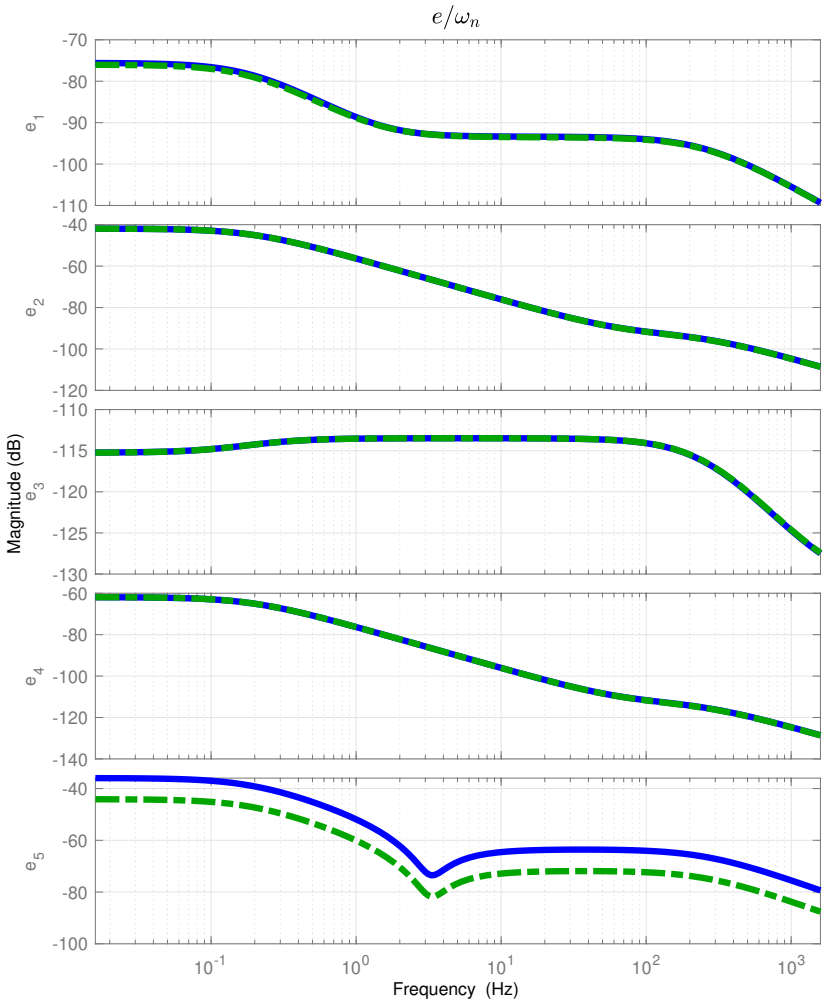

Figure 10: $\|e/\omega_n\|$-Diagrammes de Bode de l'observateur NLPV w.r.t. bruits de mesure - méthode polytopique.

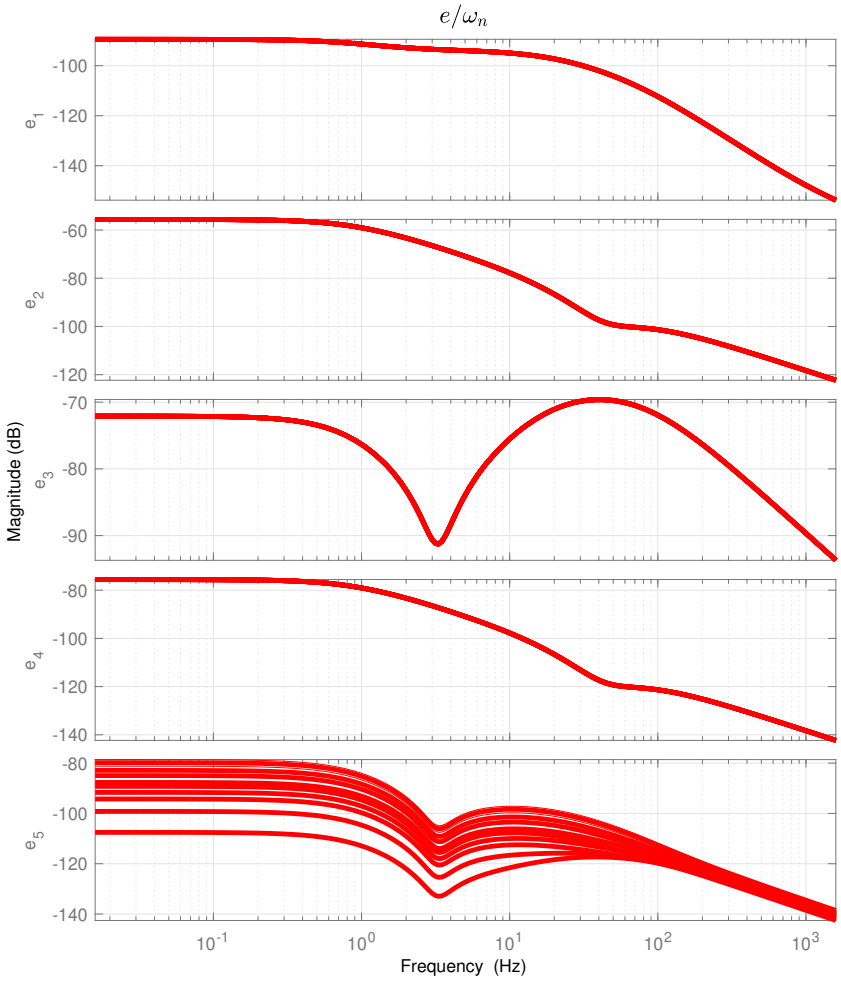

Figure 11: $\|e/\omega_n\|$-Diagrammes de Bode de l'observateur NLPV w.r.t. bruits de mesure - méthode de quadrillage.

Le chapitre 5 présente quelques résultats de comparaison de trois méthodes d'estimation de la force d'amortissement (Observateur Hinf et deux observateurs NLPV). Trois points de comparaison différents sont étudiés : le comportement vis-à-vis du profil de route inconnu, b) la minimisation de l'effet de bruit de capteur sur les erreurs d'estimation, c) le temps de convergence des observateurs.

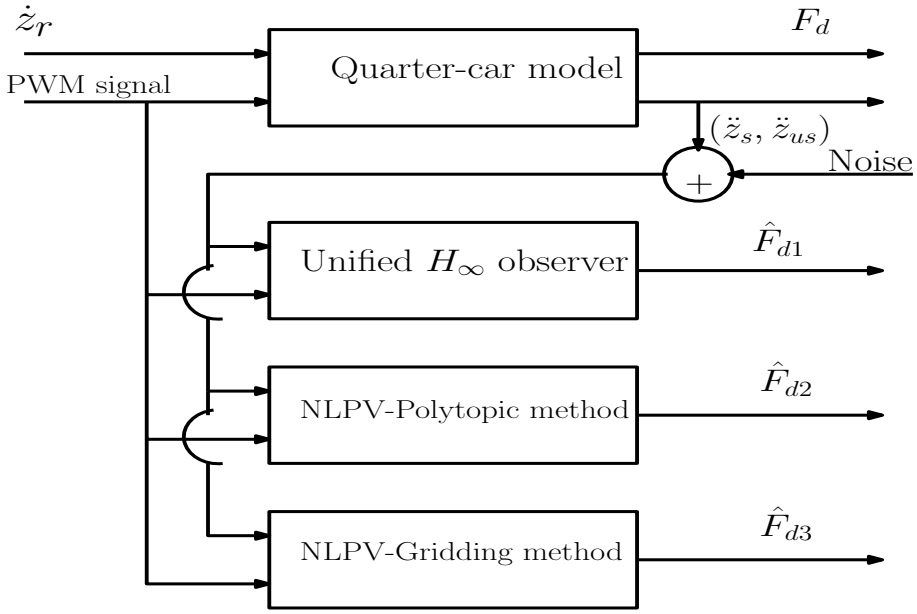

Figure 12: Schéma de principe pour la simulation des trois observateurs proposés dans le scénario de comparaison.

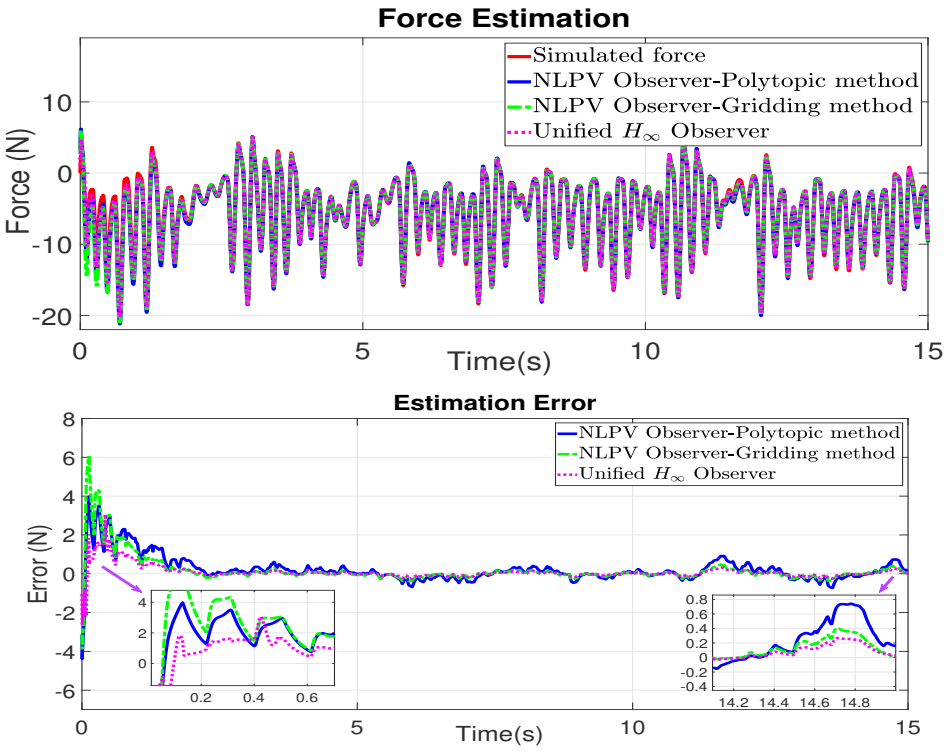

Figure 13: Simulation senario: (haut) Force de l'amortisseur, (bas) Erreur d'estimation

Le chapitre 6 présente la méthode de la commande LPV tolérante aux défauts pour la suspension semi-active système, en particulier, lorsque certaines défaillances se produisent sur l'amortisseur. Synthétiquement, les contributions de ce chapitre sont doubles : i) la première partie analyse les défauts possibles sur ces amortisseurs et incorpore leur effet sur le modèle développé, qui joue un rôle important dans le diagnostic et la fiabilité des systèmes de suspension; ii) la seconde partie développe les techniques de commande tolérante aux défauts basées sur la méthode LPV et sur les modèles de défaillance.

Perspectives

Au cours de la thèse, plusieurs développements ont été initiés et certains résultats ont été obtenus. Selon nous, les perspectives suivantes semblent également être d'un grand intérêt et pourraient être poursuivi et développées:

Perspectives à court terme

La mise en œuvre en temps réel de l'approche de contrôle tolérant aux fautes doit être effectuée sur le banc d'essai INOVE pour valider expérimentalement la performance de la méthode proposée. Dans la thèse, la non-linéarité dans l'amortisseur semi-actif modèle est bornée par une condition de Lipschitz. Alternativement, cette fonction non linéaire peut être également maintenue à l'intérieur d'un bloc à paramètres variant en utilisant une transformation fractionnelle linéaire (LFT). La comparaison entre les deux approches donnerait une analyse plus approfondie et mettrait en avant l'intérêt de chaque méthode. Comme vu au chapitre 3, l'observateur Hinf unifié d'ordre complet entraine des coûts de mise en œuvre importants. Par conséquent, il faut concevoir des observateurs d'ordre réduit et étudier leur comportement, par rapport a l' observateur d'ordre complet. Comme nous l'avons vu au chapitre 6, de l'efficacité la perte de l'amortisseur devrait être étudiées pour continuer à garantes les performances du véhicule. Par conséquent, l'observateur des défaillances utilisé pour estimer la perte du facteur d'efficacité joue un rôle important dans le diagnostic et la commande tolérant aux défauts. Concernant le problème de conception de l'observateur, la dynamique du système peut être décrite sous forme d'un système descripteur non linéaire Lipschitz. Ce modèle sera utilisé pour concevoir l'observateur des défaillances dans le cadre de travaux futurs.

Perspectives à long terme

Tous les travaux de cette thèse ont porté sur le quart de véhicule modèle. Pour le futur, les méthodes seront étendues au système de suspension de véhicule complet.

Au chapitre 4, la stabilité robuste de l'observateur NLPV est développée en utilisant les valeurs maximales et minimales de. Par conséquent l'approche par scénario peut être appliquée pour assouplir les contrainte avec l'ensemble de valeurs.

Comme mentionné au chapitre 6, trois raisons (problèmes électriques, fuite d'huile et déformation physique) concernent la perte d'efficacité de l'amortisseur. Chaque raison a un effet différent sur les performances du système. Par conséquent, les stratégies FTC doivent s'adapter à la différence de chaque défaut.

List of Figures

List of Tables

Table of Acronyms

ER	Electro-Rheological
LTI	Linear Time Invariant
LPV	Linear Parameter Varying
NLPV	NonLinear Parameter Varying
MPC	Model Predictive Control
LMI	Linear Matrix Inequality
BMI	Bilinear Matrix Inequality
SDP	Semi-Definite Programming
DOF	degree of freedom
COG	center of gravity
FD	Fault Diagnosis
FTC	Fault Tolerant Control
PDLF	Parameter Dependent Lyapunov Function

$\mathbb{R}$	Real values set
$\mathbb{C}$	Complex values set
A^*	Conjugate of $A \in \mathbb{C}$
A^T	Transpose of $A \in \mathbb{R}$
$A \prec (\preceq) 0$	Matrix A is symmetric and negative (semi)definite
$A \succ (\succeq) 0$	Matrix A is symmetric and positive (semi)definite
$Co(X)$	Convex hull of set X
$A = A^T$	Matrix A is real symmetric
$He(A) = A^T + A$	

Thesis framework and contribution

Contents

0.1 Thesis framework

This dissertation presents the results of the three years PhD work (from April 2017 to April 2020), performed in the SLR (Systèmes Linéaires et Robustesse) team from the Control Systems department of GIPSA-Lab, on the **LPV observer and Fault-tolerant control of vehicle dynamics: application to an automotive semi-active suspension system** under the direction of **Olivier SENAME** (Professor Grenoble INP) and **Luc DUGARD** (Reseacher Director CNRS). This work has been partially supported by the 911 scholarship from the Vietnamese government and the ITEA3 European Project through EMPHYSIS (Embedded Systems With Physical Models in the Production Code Software) under Grant 15016.

This thesis presents a continuation and further developments from the studies of former PhD students in the same SLR team:

- Ricardo Ramirez-Mendoza (see [Ramirez Mendoza 1997]), "Sur la modélisation et la commande de véhicules automobiles", which was the first study in the automotive framework. The work was focused on the description and modeling of vehicles, as well as first attempts on control methodologies for active cruise control.
- Damien Sammier (see [Sammier 2001]), "Sur la modélisation et la commande de suspension de véhicules automobiles" presented the modeling and control design of an active suspension (using H_∞ control for LTI system). The semi-active suspension modeling and control were also studied for a PSA Peugeot-Citroën semi-active damper.
- Alessandro Zin (see [Zin 2005]), "Sur la commande robuste de suspensions automobiles en vue du contrôle global de châssis", which extended the previous works with a strong attention on H_∞/LPV control of an active suspension in order to improve robustness properties. A sketch of global chassis control through the use of the four suspensions was also derived using an anti-roll distribution.

- Charles Poussot-Vassal (see [Poussot-Vassal 2008a]) "Commande robuste LPV multivariable de chassis automobile" provided tools and control design methodologies in order to improve comfort and safety in automotive vehicles. The two main contributions were the semi-active suspension control (using an LPV approach to handle the dissipativity constraint of the damper and to improve the passenger comfort and road holding) and the Global Chassis Control (involving the control of the braking and steering actuators for vehicle active safety improvement).

- Sébastien Aubouet (see [Aubouet 2010])"Semi-active SOBEN suspensions modeling and control" presented an observer design methodology allowing the suspension designer to build and adjust an appropriate observer, estimating the non-measured variables. Then, the previous results of Charles Poussot-Vassal, for semi-active suspension control, were extended to the full vertical car, and completed with both a pole placement method, a scheduling strategy based on a damper model and a local damper control for a semi-active hydraulic suspension designed by SOBEN.

- Anh-Lam DO (see [Do 2011]) "Approche LPV pour la commande robuste de la dynamique des véhicules: amélioration conjointe du confort et de la sécurité", which concentrated on controller design for semi-active suspension system aiming at providing a good compromise between comfort and road holding while taking into account the important physical characteristics and constraints. The main contributions were a LPV modeling and control for nonlinear semi-active suspension systems, a constrained control (passitivity constraint and mechanical limits), and the controller design was performed, based on multi-objective optimization problems using genetic algorithm.

- Soheib Fergani (see [Fergani 2014]) "Robust Multivariable Control for vehicle dynamics" presented Global Chassis MIMO controllers that enhance the overall dynamics of the vehicle while preserving the vehicle stability in critical driving situations. The controllers were developped based on the $LPV/\mathcal{H}_\infty$ approach and took into account simultaneously the braking, steering and suspension actuators. Then, some stratetegies have been developed to estimate the road profile characteristics and to adapt the vehicle control, depending on the road roughness. Finally, fault tolerant control strategies have been also considered to handle the actuators failures while keeping the vehicle stability and safety.

- Manh Quan Nguyen (see [Nguyen 2016]) "LPV approaches for modeling and control of vehicle dynamics: application to a small car pilot plant with ER dampers" presented suspension control methods in the framework of Linear Parameter Varying (LPV) approach with input constrained and Model Predictive Control (MPC) approach. Moreover, several observers have been designed to estimate the fault in the damper. Then, an LPV/FTC fault scheduling control is designed to prevent vehicle performance deterioration by using the fault information from the estimation step.

0.2 General introduction and problem statement of the thesis

The automotive industry continually demands safer and more comfortable vehicles. Therefore, automotive vehicles are equipped with many modern technologies, intelligent subsystems in different engineering fields such as mechanics, electronics, communications, automatic control. Along with these technologies, the vehicle dynamic is of paramount importance that decides the overall vehicle performance. Technological advances in vehicle dynamics control are considered one of the solutions to enhance the performance of the vehicles. It concerns many actuators (ESC- electronic stability control, ABS- anti-lock braking system, controlled suspensions), which can be used to enhance the driving comfort, stability, and safety. Among these actuators, the suspension systems are crucial for vehicle dynamics. Indeed, the role of suspensions in vehicle dynamics is intuitive: they establish the link between the road and the vehicle body, managing not only the vertical dynamics, but also the rotational dynamics (roll, pitch) caused by their unsynchronized motions.

The main body of the work of this thesis concentrates on the topic of the vehicle suspension systems, especially with these using the semi-active dampers. The contributions are mainly focussed in three directions:

- The modeling and identification of two nonlinear control-oriented models for ER dampers equipped in the INOVE testbed of GIPSA-lab are studied.
- The real-time knowledge of the damper is of great importance for vehicle dynamic diagnosis and control. Therefore, three robust observers (in the H_∞ context for Nonlinear Lipschitz and Nonlinear Parameter Varying systems) are proposed to estimate the damping force of ER damper.
- The fault-tolerant control of the semi-active suspension system is addressed by using the LPV approach and damper fault model.

0.3 Structure of the thesis

In this thesis, the main contributions will be presented following the organization:

0.3.1 Part I: System description identification and modelling

The first part gives the modeling and identification results of the quarter-car model equipped with an Electro-Rheological damper. This part is composed of the following chapters:

- Chapter 1 presents the modeling study and identification of two control-oriented models for Electro-Rheological dampers used in vehicle suspension systems,. The models capture the main behaviors of the ER damper (nonlinearity and dynamic). Both models are validated with various tests on the INOVE experimental plat-form of GIPSA-lab.

- Chapter 2 provides the extended quarter car models, which will be used for the design of observers and controllers—the quarter car models augmented with a first-order dynamical nonlinear damper model. The dynamical equation of the quarter car system is written in an LTI system for control design and two nonlinear systems (Nonlinear Lipschitz and nonlinear Parameter Varying formulation) are considered later for observer design.

0.3.2 Part II: Some approaches for damper force estimation

The second part is devoted to one of the main contributions of the thesis. Three observers are proposed to estimate the damping force of ER damper in the suspension system, which is of great importance for vehicle dynamic diagnosis and control. The structure of this part is as the followings:

- Chapter 3 presents an extension of the synthesis of a unified $\mathcal{H}_\infty$ for the nonlinear Lipschitz systems subject to unknown input and measurement noises. The objectives are to decouple the effects of bounded unknown input disturbances and to minimize the effects of measurement noises on the estimation errors of the state variables by using an $\mathcal{H}_\infty$ criterion, while the nonlinearity satisfies the Lipschitz condition. This new approach is developed to estimate the damping force of an Electro-Rheological (ER) damper in an automotive suspension system and is implemented on the INOVE testbench from GIPSA-lab (1/5-scaled real vehicle) for real-time performance assessment.

- Chapter 4 proposes a nonlinear parameter varying (NLPV) observer to estimate, in real-time, the damper force of an electrorheological (ER) damper in the road vehicle suspension system. The effect of road profile disturbances and measurement noises on the estimation errors is handled via the $\mathcal{H}_\infty$ framework. Moreover, the nonlinearity coming from the damper model (and considered in the observer formulation) is bouned by a Lipschitz condition. This chapter addresses the design problem of NLPV observer via a constant Lyapunov function (polytopic method) and a parameter-dependent Lyapunov function (gridding method). For performance assessment, the observers are implemented on the INOVE testbench of GIPSA-lab (1/5-scaled real vehicle).

- Chapter 5 presents some comparison results of three damper force estimation methods ($\mathcal{H}_\infty$ observer and two NLPV observers). Three different comparison points are studied: behavior against unknown road profile, b) minimization of the sensor noise effect on the estimation errors, c) convergence time improvement.

0.3.3 Part III: Application to fault-tolerant control

The final part presents the results on Fault-Tolerant Control, to be applied on the semi-active suspension system:

- Chapter 6 presents the LPV Fault-Tolerant Control method for the semi-active suspension system, in particular, when some faults occur upon the damper. Synthetically, the contributions of this chapter are two-fold: i) the first part analyses the possible faults on these dampers and incorporates their effect on the developed model, which plays an important role in the diagnosis and reliability of suspension systems; ii) the second develops the Fault-Tolerant Control techniques based on the LPV method and the fault model.

0.4 Contributions

International journal paper

J1 Pham, T.P., Sename, O., and Dugard, L. (2019). *Unified H_∞ observer for a class of nonlinear Lipschitz systems: application to a real ER automotive suspension.* **IEEE Control Systems Letters**, 3(4), 817-822. The contents of this paper have been presented at 58th IEEE Conference on Decision and Control.

J2 Morato, M.M, Pham, T.P., Sename, O. and Dugard, L. *Development of a Simple ER Damper Model for Fault-Tolerant Control Design*, Submitted to **Journal of the Brazilian Society of Mechanical Sciences and Engineering** (accepted).

International conference papers with proceedings

C1 Pham, T.P., Sename, O., and Dugard, L. (2019). *Unified H_∞ observer for a class of nonlinear Lipschitz systems: application to a real ER automotive suspension*, In Proceedings of the 58^{th} **IEEE Conference on Decision and Control**, Nice, France, December 2019.

C2 Pham, T.P., Sename, O., and Dugard, L. (2019). *Real-time Damper Force Estimation of Vehicle Electrorheological Suspension: A NonLinear Parameter Varying Approach*, In Proceedings of the 3^{rd} **IFAC Workshop on Linear Parameter-Varying Systems**, Eindhoven, Netherlands, November 2019.

C3 Pham, T.P., Sename, O., Dugard, L. and Vu, V.T.(2019). *LPV force observer design and experimental validation from a dynamical semi-active ER damper model*, In Proceedings of the 7^{th} **IFAC Symposium on Systems Structure and Control**, Sinaia, Romania, September 2019.

C4 Pham, T.P., Sename, O. and Dugard, L. (2019). *Comparative study of three robust observers for automotive damper force estimation*, In Proceedings of the 8^{th} **International Conference on Mechatronics and Control Engineering**, Paris, France , July 2019.

C5 Pham, T.P., Sename, O. and Dugard, L. (2019). *Real-time Estimation of Damping Force of Vehicle Electrorheological Suspension System: a new H_∞ approach and experimental validation*, In Proceedings of the 9^{th} **IFAC International Symposium on Advances in Automotive Control**, Orléans, France , June 2019.

C6 Pham, T.P., Sename, O., Dugard, L. and Vu, V.T.(2018). *Real-time Estimation of the Damping Force of Vehicle Electrorheological Suspension*, In Proceedings of the 16^{th} **International Conference on Vehicle System Dynamics, Identification and Anomalies**, Budapest, Hungary , November 2018.

C7 Vu, V.T., Sename, O., Dugard, L., Pham, T.P., Pham, T.T. and Dinh, V.P. (2018). *H_∞/LPV Active Braking Control System to Prevent Rollover of Heavy Vehicles*, In Proceedings of the 16^{th} **International Conference on Vehicle System Dynamics, Identification and Anomalies**, Budapest, Hungary , November 2018.

National conference papers with proceedings

C8 Vu, V.T., Sename, O., Dugard, L., Dinh, V.P., Pham, T.P. (2018). *H_∞/LPV control for an active anti-roll bar system to improve the roll stability of heavy vehicles*, In Proceedings of the 10^{th} **National conference on mechanics**, Hanoi, Vietnam , December, 2017.

Submitted journal

J3 Pham, T.P., Sename, O. and Dugard, L. *A NonLinear Parameter Varying observer for real-time damper force estimation of an automotive Electro-Rheological suspension system*, Submitted to **International Journal of Robust and Nonlinear Control** (Revision).

Part I

System description identification and modelling

Chapter 1

Electro-Rheological (ER) damper model identification

Contents

This chapter presents the modeling study and identification of two control-oriented models for Electro-Rheological dampers used in vehicle suspension systems. The primary purpose is to consider the overall behaviors of these ER dampers, which basically, present a resistance against shearing that varies according to a controlled electric field. Two different model structures are used to represent the behaviors of these dampers. The first one uses a parametric approach to model the damper (section 1.4.1). The other makes use of a hysteresis based method to characterize the damper (section 1.4.2). In these models, the damper is characterized by the combination of linear and nonlinear terms. Therefore, an identification procedure using square and nonlinear least square methods is proposed to identify the model parameters (section 1.5). Finally, the models are validated with various tests on the INOVE experimental plat-form (section 1.6). The part of this work has been done with 2 Master students (Manuel A Molina Villa and Marcelo Menezes Morato).

1.1 Introduction

Nowadays, vehicle dynamics are of paramount importance in the automotive industry. Indeed, over the last decade, automotive engineering has witnessed rapid growth in semi-active and active systems. There has been a lot of research, development, and implementation of such semi-active and active subsystems such as braking, steering or suspension actuators (see [Savaresi et al. 2010]), [Tanelli, Corno, and Saveresi 2014], [Do, Sename, and Dugard 2012], [Yamamoto 2017], [Priyandoko, Mailah, and Jamaluddin 2009], [Yoshimura et al. 2001]), [Bremner 2005]). In particular, the automotive suspension systems have also received a lot of consideration from industry and academia due to their vital role in reducing the effects of the road disturbances on the on-board passengers (comfort) and in maintaining tire-road contact (safety) (see [Gillespie 1992], [Savaresi et al. 2010]).

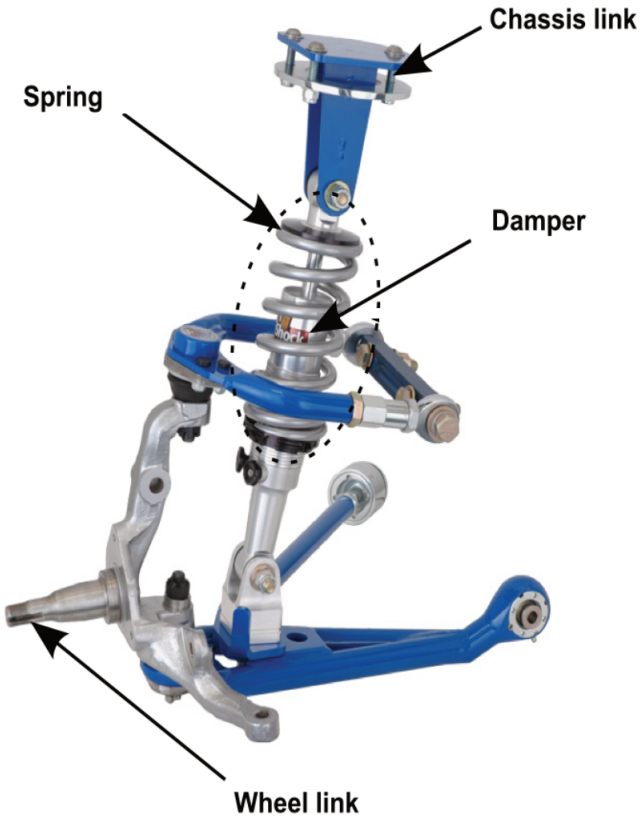

Figure 1.1: Schematic Representation of a Common Vehicle Suspension System [Savaresi et al. 2010].

The configuration of the suspension system includes three main components (see Figure 1.1): 1) a coil spring; 2) a damper; 3) the mechanical elements to link the sprung mass (chassis) and unsprung mass (wheel). According to the damper characteristics usually described by the Force vs. Piston Velocity diagram (see Figure 1.2 for the ideal dampers), the damper is

broadly classified into a) passive b) semi-active c) active. Amongst these categories, the semi-active damper is a potential candidate in the automotive market due to the advantages of the semi-active damper compared to active and passive ones such as negligible power demand, safety characteristics, improvement of the vehicle performance and low cost and weight (see in [Savaresi et al. 2010]). As an example that will be considered in details later, Figure 1.3 presents the Force-Velocity diagram of an ER damper of the INOVE testbed, in the passive (left) and semi-active (right) configurations. Many research works have therefore been devoted to the modeling, estimation, and control designs of the semi-active suspension system (see [Choi, Lee, and Park 2001], [Poussot-Vassal et al. 2012], [Dugard et al. 2012] and references therein).

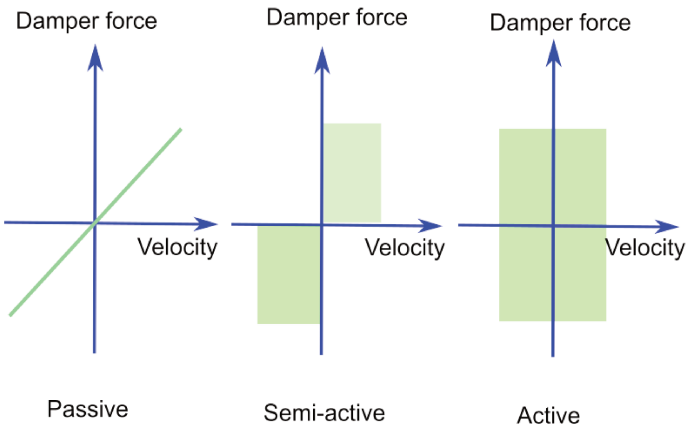

Figure 1.2: Force vs. Piston Velocity: diagram of ideal Passive (left), Semi-active (middle) and Active (right) dampers.

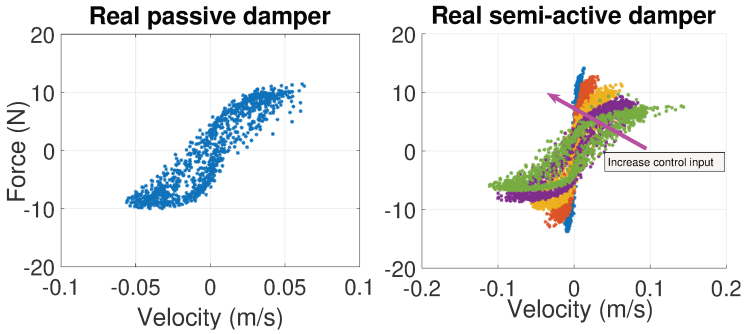

Figure 1.3: Force vs. Piston Velocity diagram of real Passive (left), Semi-active (right) dampers.

The semi-active dampers concern those with controlled fluids since they have a fast time response and are less costly. There are, nowadays, three main semi-active damper technologies: 1) Electro-Hydraulic (EH) dampers, i.e. hydraulic devices usually equipped with solenoid valves [Aubouet 2010]; 2) Magneto-Rheological (MR) [Metered, Bonello, and Oyadiji 2010; J Lozoya-Santos et al. 2012; Witters and Swevers 2010; Ashfak, Rasheed, and Jaleel 2013]

and 3) Electro-Rheological (ER) shock absorbers, both damper types being filled with a Rheological fluid that varies its apparent viscosity under the action of a magnetic (see [Carlson, Catanzarite, and St. Clair 1996]) or an electric field (see [Acerbi and Mingione 2002]), respectively. Since the INOVE platform is equipped with ER dampers, this chapter mostly deals with such systems. For more information concerning the other types of dampers, the reader is referred to the works give above and references therein.

As explained in [Choi, Lee, and Chang 2001; Kamelreiter, Kemmetmüller, and Kugi 2012], ER dampers used in semi-active suspension systems, are able to achieve very good results in terms of enhancing a car's drive. Nevertheless for control design purpose, reduced-order models (that describe the behavior of the force delivered by Electro-Rheological dampers) must be available in order to run in real-time in the embedded Electronic Control Unit (ECU) of these modern automotive applications (that usually run within 1 to 10 ms).

1.2 Related works on ER damper modelling

In order to capture the main characteristics of the ER damper, many models have been derived using several methodologies with different complexity and accuracy. In terms of ER damper modelling studies, these either use parametric or non-parametric approaches:

- Non-parametric models characterize the delivered force by special, well-suited functions (polynomial, trigonometric, delayed functions, *etc* [Choi, Lee, and Park 2001]) or by artificial intelligence methods (fuzzy logics, neural networks, *etc* [Kim, Langari, and Hurlebaus 2009], [Savaresi, Bittanti, and Montiglio 2005], [Witters and Swevers 2010]). As the non-parametric models usually stand for quite complex functions, they are out of the scope of this chapter.
- Parametric models characterize the delivered force by the combination of the behaviors of the spring, dashpots and other mechanical parts (considering each of their mechanisms and operating area) [Dyke et al. 1996]. Some interesting works are: [Gamota and Filisko 1991], that describes the *ER* fluid behaviour in moderate frequency excitations; [Kamath and Wereley 1997] and [Makris, Burton, and Taylor 1996] present models derived from simple, basic mechanical laws. More recently, [Hernández-Alcántara et al. 2016] presented very interesting experimental results, even including faulty situations of the damper, and proposed a parametric model adapted from the *MR* damper model given in [Guo, Yang, and Pan 2006].

On the other hand, the damper models may be classified in terms of static and dynamic characteristics:

- Static models include Bingham model with Coulomb friction (see [Stanway, Sproston, and Stevens 1987]), hysteresis based model (see [Guo, Yang, and Pan 2006], [J Lozoya-Santos et al. 2012]).

- Dynamic models considers the Bouc-Wen model in ([Wen 1976], [Ahmadian, Song, and Southward 2004] and [Spencer Jr et al. 1997]).
- Based on several approximators such as neural network ([Chang and Roschke 1998], [Chang and Zhou 2002]), fuzzy ([Schurter and Roschke 2000]), polynomial ([Du, Sze, and Lam 2005]) and among others ([Savaresi, Bittanti, and Montiglio 2005]), proposed black box model can be also divided into static or dynamic groups, depending on the typical model.

It must be remarked that the parametric modelling approach is of interest as it can lead to reasonably simplified (reduced-order) functions that describe the delivered ER damper force quite well. The Bingham and Guo models are representative, however, they only characterize the static nonlinear behavior of semi-active suspensions. Therefore, how to extend the models by taking into account both nonlinear and dynamic behaviors of the ER damper while facilitating control-design goals including Fault Detection and Diagnosis/Fault Tolerant Control (FDD/FTC) schemes is one of our objectives.

1.3 INOVE testbench

For validation and identification purposes, as well as for many experimental tests to assess the proposed algorithms, a real $\frac{1}{5}$-sized vehicle test-rig is used in this work. This testbed is the INOVE Soben-Car experimental platform available in GIPSA-lab [1] and it allows dealing with several configurations and use cases.

This platform, which involves a scaled car, is controlled in real-time using Matlab Real-Time Workshop and a host computer. The target PC is connected to the host computer via the Ethernet communication standard (see Figure 1.4). The control policies and estimation approaches are implemented with a sampling frequency of 200Hz (i.e. sampling time 5ms)

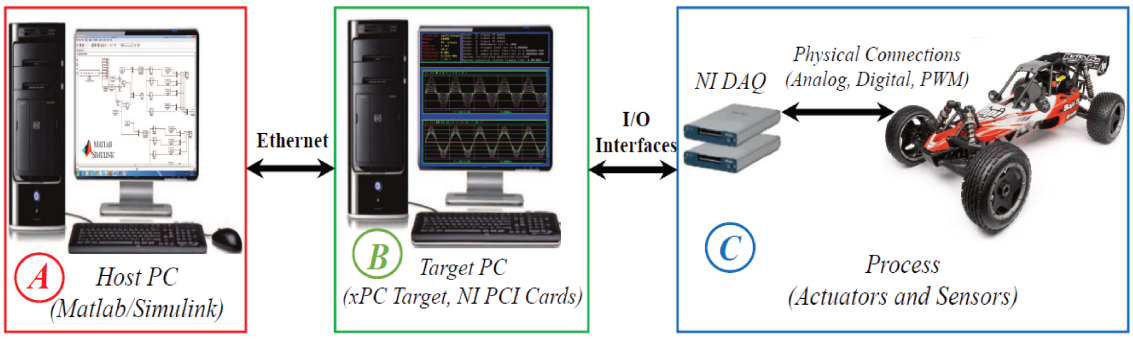

Figure 1.4: Schematic of INOVE experimental platform [Tudón-Martínez et al. 2015]

The scaled car is equipped with a semi-active suspension system involving four ER dampers

[1] http://www.gipsa-lab.fr/projet/inove/index.html

which have a force range of $\pm 50\,\mathrm{N}$ and have been designed by *Fludicon* ©. These ER dampers are adjusted using a controlled voltage inside the range of $[0\,,\,5000]\,\mathrm{V}$, generated by amplifier modules. The control input for each module is a PWM signal at $25\,\mathrm{kHz}$. In terms of capturing the vehicle's behavior, this testbed is equipped with a wide variety of sensors as follows:

- 8 accelerometers to measure the sprung and unsprung mass accelerations.
- An Attitude and Heading Reference System (AHRS) to measure the movement of sprung mass in three axels such as the longitudinal, lateral and vertical accelerations and pitch, roll, and yaw rates.
- 12 displacement sensors to measure the deflection of each ER damper.
- 4 force sensors to measure the dampers' forces

In order to generate road profiles, four linear servomotors placed under the four wheels of the vehicle mimic the desired road profiles. A photo of the scaled car INOVE and of the front-left ER damper of the experimental platform is given in Figure 1.5.

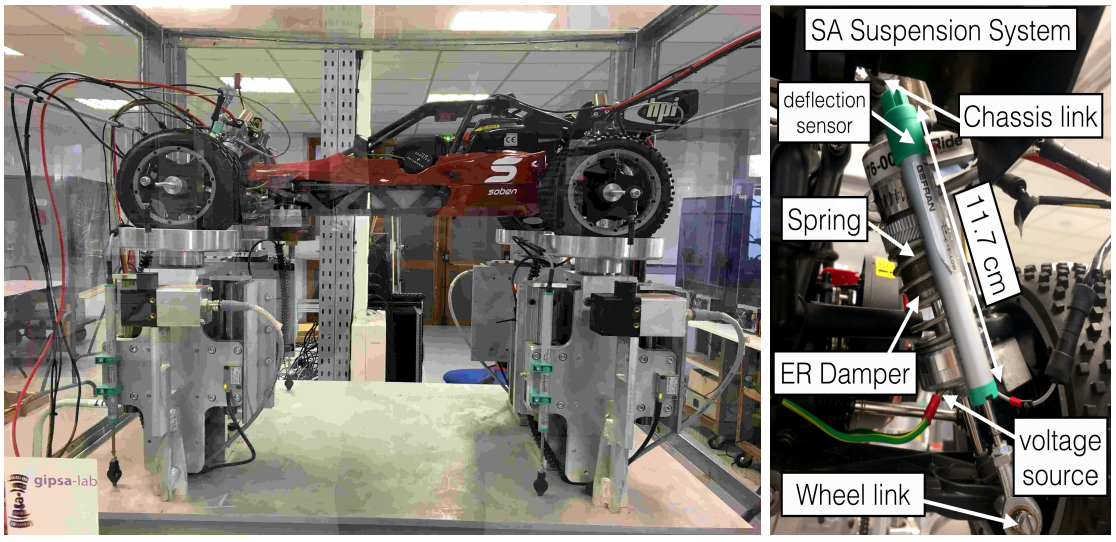

Figure 1.5: The experimental testbed INOVE at GIPSA-lab.

For safety, the working region of the ER dampers in INOVE testbed is limited to the range of $[0, 0.3]$ applied PWM signal (that corresponds to voltages from 0V to 1500V) and constrained in $[-0.15\,,\,0.15]\,\frac{\mathrm{m}}{\mathrm{s}}$ for velocities. The reasons for these limitations are:

- In our application, the corresponding damper forces with low applied voltages are enough to control the real 1/5-scaled car (in terms of improvements for passenger comfort and road holding);

- In the INOVE test bench, we do not control the velocity of damper. This value directly depends on the type of road profile acting on the car. These profiles, on the other hand, are limited, to be realistic but also due to the excitation bounds of the servomotors that generate them.

Finally, this unique 1/5 scale automotive system has been developed to study the vertical behavior of the ground car, therefore, neither the steering nor breaking systems are mounted in the car.

1.4 ER damper modelling and identification

In this section, we aim at presenting two models sufficiently simple for design and implementation (reduced-order) while maintaining an overall good representation of the dynamical damper behaviour, so that they can be used for control design and run in real-time with embedded semi-active suspension controllers (usually with sampling periods within 1ms to 10 ms). Therefore, a parametrical approach and a hysteresis based methodology for the control-oriented modelling are proposed here; the identification procedure and the results on the model accuracy results are also herein discussed.

1.4.1 An extended Bingham model with dynamic characteristics

A schematic diagram of ER shock absorbers is given in Figure 1.6: basically, it has two chambers (upper and lower), divided by a piston that provides the force, and electrodes that induce an electric field over an ER fluid. These chambers are fully filled with the Rheological fluid. As the piston moves, the ER fluid flows from one chamber to the other through the annular duct between inner and outer cylinders. Starting from this schematic configuration and knowing its operating principle, a quasi-static model can be derived on the basis of the Bingham Rheological laws of ER fluid [Bird, Dai, and Yarusso 1983]. From this point, a complete control-oriented dynamic model for the ER damper is then proposed.

The fluid used in the ER shock absorbers is a colloidal suspension whose apparent viscosity varies according to an applied external electric field. Reader must notice that these dampers usually have a gas chamber located outside the lower chamber (see Fig. 1.6), that acts as an accumulator of the ER fluid induced by the motion of the piston. In the absence of electric field, the ER damper produces a damping force caused solely by the viscous fluid resistance. However, if some electric field is applied to the ER damper, it produces an additional damping force owing to the yield stress of the ER fluid. Note that control strategies are mainly concerned with these variable damping rate: by varying the applied electric field, one controls the delivered damping force. The force generated by ER dampers, namely F_d, directly depends on the difference of pressures between the chambers, once the base and lateral surfaces are constant. The pressure inside the two chambers of the damper can be expressed in terms of the gas chamber pression (P_a), of a pressure drop ΔP_a between chambers (which are rather

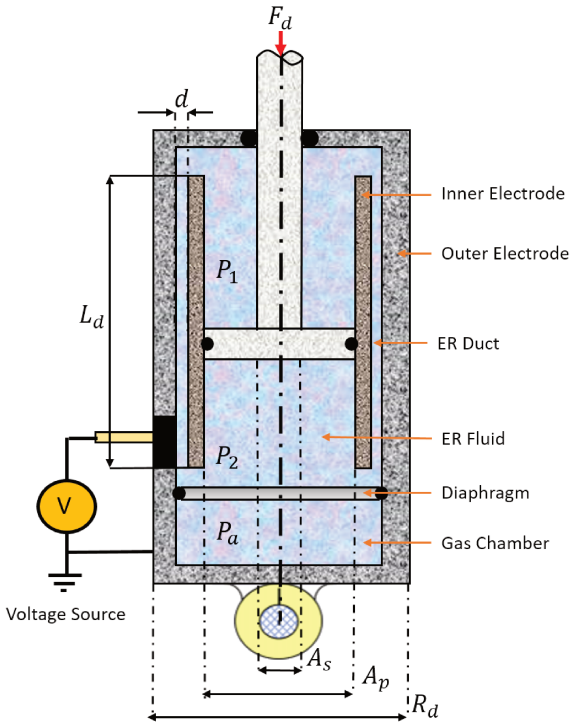

Figure 1.6: Schematic Representation of an ER Damper, adapted from [Choi and Han 2003]

small and can be neglected for control purposes). Yet, the pressure in the higher chamber (P_1) is given by the gas chamber pressure minus a pressure drop ΔP_d term, due to the ER fluid that flows through the annular duct.

Considering these relationships, it is possible to obtain a (first) analytical force model that takes into account the physical parameters of the damper, given in terms of P_a, the contact areas and the pressure drop due to the ER fluid flow:

$$F_d = P_a A_s + \Delta P_d (A_p - A_s) \tag{1.1}$$

where A_p and A_s are the piston and piston rod areas, respectively. Also, the term $P_a A_s$ and $\Delta P_d (A_p - A_s)$ represent for gas compliance and the force due to apparent viscosity, respectively. The first term $P_a A_s$ related to the piston displacement x_p will be discussed later.

Bear in mind that the behavior of such ER fluids is quite peculiar, thanks to the possibility of change of its apparent viscosity factor due to an applied electric field. But, how does the above force model vary according to the changes upon the controllable electric field? To answer this issue precisely, one must imperiously visit the Bingham flow laws [Bingham 1929], which contemplate the description of two behaviours: a nominal behaviour of the fluid (without any external electric flied) and a controlled behaviour (with an external electric field). The total shear resistance is, therefore, expressed as the addition of these two cases.

The nominal situation of the fluid flow (no electric field) can be given as a regular fluid friction between pipes (see [Yakoh and Aoyama 2000]), depending on the flow rate ($\dot{x}_p$), the

nominal viscosity of the fluid (μ) and the geometry of the pipe (length L_d, radius R_d and gap d).

As state in [Choi et al. 1998], the Rheological properties of ER fluids are reversibly changed with the application of an external electric field E. Roughly, from Newtonian flow behaviour, the ER fluid particles change to a Bingham plastic behaviour, in which particles become aligned in chain forms, according to the applied E; as discusses [Jordan and Shaw 1989], this behaviour can be sufficiently represented by an exponentiation of the applied electric field (with α and β being intrinsic parameters of the ER fluid) and c, a coefficient that stands for the fluid's flow velocity profile.

Thereby, with the above considerations, the second term in Eq. (1.1) can be re-written, answering the above question and incorporating the effect of the applied electric field, which leads to a final parametric static model. This model is given by Equation (1.2), where the first term represents the elastic force from the gas compliance, the second term represents the damping force due to the ER fluid apparent viscosity (when no electric field is applied) and the third one stands for the force due to the yield stress of the rheological fluid, which can be continuously controlled by the intensity of the electric field applied to the damper. Statical validation of a similar model has been seen in [Reineh and Pelosi 2013].

$$F_d = P_a A_s + \frac{6\mu L_d}{\pi d^3 R_d}\dot{x}_p + (A_p - A_s)\frac{cL_d}{d}\alpha E^{\beta}\text{sign}(\dot{x}_p) \tag{1.2}$$

where L_d is the electrode length, d is the electrode gap and E is the applied electric field.

Notice that the term "sign($\dot{x}_p$)" appears in the yield stress term of the damper force F_d, given that the force's direction depends on the direction of the piston's velocity, depending on whether the damper is in compression or in release (thus if it is postive or negative).

The goal of this chapter is to propose a reduced-order control-oriented model, which can be run in real-time in embedded ECUs of semi-active suspension systems. Hence, the simplifications of the equation (1.2) are mentioned as follows:

- The first factor involved in the proposed model (1.2) is the elastic characteristic of the ER damper, generated by the presence of the gas chamber inside the system. This factor is related to the force generated by the compression of the gas, and its behavior can be accurately approximated by the behaviour of a spring, as described in Equation (1.3). This assumption is quite reasonable and coherent with the existent damper models: as stated in [Choi and Han 2003], k_0 represents the effective stiffness of the damper due to the gas pressure.

$$P_a A_s \quad \approx \quad k_0 x_p \tag{1.3}$$

- On the other hand, the second term in Equation (1.2) represents the damping force due to the natural fluid viscosity of the ER damper, in the absence of electric field. Therefore, c_0 encompasses the constants $\left(\frac{6\mu L_d}{\pi d^3 R_d}\right)$

- Considering that the applied electric field is uniform, one has:

$$E = -\frac{U}{d} = -\frac{U_m}{d}u \tag{1.4}$$

where $U(t)$ is the applied voltage; U_m is maximum voltage; u is the duty cycle of PWM channel. In the considered vehicle test-bed, u may only vary from 0 to 0.3. From this point onwards, the magnitude of the electrical field is saturated, i.e. the biggest field is achieved with $u = 0.3$. Substituting (**??**) into the last term in Equation (1.2), one obtains:

$$\begin{aligned}(A_p - A_s)\frac{cL_d}{d}\alpha E^{\beta}\text{sign}(\dot{x}_p) &= (A_p - A_s)\frac{cL_d}{d}\alpha(-\frac{U_m}{d})^{\beta}u^{\beta}\text{sign}(\dot{x}_p) \\ &= \sigma u^{\beta}\text{sign}(\dot{x}_p)\end{aligned} \tag{1.5}$$

where $\sigma = (A_p - A_s)\frac{cL_d}{d}\alpha(-\frac{U_m}{d})^{\beta}$

Substituting (1.3)-(1.5) into (1.2), the following model is obtained

$$F_d = k_0 x_p + c_0 \dot{x}_p + \sigma u^{\beta}\text{sign}(\dot{x}_p) \tag{1.6}$$

It is worth noting that the above model (1.6) ignores the dynamic characteristic of the ER damper. To incorporate the dynamical behaviour of the delivered force by such ER dampers, Eq. (1.6) must be extended. The dynamic behaviour of a system can be studied in time and frequency domains. Herein, a time-wise procedure is followed: after several empirical tests, it was noted that the dynamics of the ER fluid can be approximated accurately enough by a first order system, with a varying time constant $\tau(\cdot)$ depending on the control input u, which is coherent with existing studies on Magneto-Rehological dampers (see [Koo, Goncalves, and Ahmadian 2006]),then one has $\tau(u)$. Therefore, equation (1.6), related to the force due to the yield stress of the Rheological fluid, will be no longer considered as static, but dynamic, as represented below:

$$\tau(u)\dot{F}_{er} + F_{er} = \sigma u^{\beta}\text{sign}(\dot{x}_p) \tag{1.7}$$

As a result, coupling the static equation (1.6) with the dynamic law (1.7) leads to the following model of the *ER* damper force:

$$\begin{cases} F_d = k_0 x_p + c_0 \dot{x}_p + F_{er} \\ \tau(u)\dot{F}_{er} + F_{er} = \sigma u^{\beta}\text{sign}(\dot{x}_p) \end{cases} \tag{1.8}$$

1.4.2 An extended Guo model with dynamic characteristics

In order to improve the Bingham model accounting for the hysteresis phenomenon, authors in [Guo, Yang, and Pan 2006] proposed the following model

$$F_d = a_2(\dot{x}_p + \frac{V_0}{X_0}x_p) + a_1 tanh(a_3(\dot{x}_p + \frac{V_0}{X_0}x_p)) \tag{1.9}$$

where F_d is the damper force, x_p and $\dot{x}_p$ are displacement and velocity of the piston respectively, a_1 is the dynamic yield force of the ER fluid, a_2 and a_3 are regarded as the post-yield and pre-yield viscous damping coefficients, respectively. $V_0 = |\dot{x}_0|$ and $X_0 = |x_0|$ where $\dot{x}_0$ and x_0 represent the piston velocity and displacement respectively, when F_d is zero. Note that using the original Guo model (1.9), it is not control-oriented due to the absence of the input signal in the model. Therefore, [J Lozoya-Santos et al. 2012] presented the following control-oriented model based on Guo model as follows:

$$F_d = k_0 x_p + c_0 \dot{x}_p + f_c \cdot u \cdot tanh(k_1 x_p + c_1 \dot{x}_p) \tag{1.10}$$

where c_0, c_1, k_0, k_1, f_c are constant parameters and u is control input.

As mentioned in section 1.4.1, in order to take into account the dynamical behavior of the ER fluid, it is important to complete the above model (1.10) by including a first-order dynamical equation in the controlled term $f_c \cdot u \cdot tanh(k_1 x_p + c_1 \dot{x}_p)$

$$\tau(u)\dot{F}_{er} + F_{er} = f_c \cdot u \cdot tanh(k_1 x_p + c_1 \dot{x}_p) \tag{1.11}$$

Therefore, the complete nonlinear damper dynamical model is given as

$$\begin{cases} F_d = k_0 x_p + c_0 \dot{x}_p + F_{er} \\ \tau(u)\dot{F}_{er} + F_{er} = f_c.u.tanh(k_1 x_p + c_1 \dot{x}_p) \end{cases} \tag{1.12}$$

A unified identification procedure is presented in the next section to get the parameter values of both proposed models.

1.5 Identification procedure of the model parameters

In the models presented in sections 1.4.1 and 1.4.2, the ER damper is characterized by the combination of linear and nonlinear terms. Therefore, an identification procedure using linear least square and nonlinear least square methods is proposed to identify the model parameters. Then validation results are shown to assess the fidelity and accuracy of the proposed model. This has been carried out considering the front-left ER damper of the INOVE Soben-Car vehicle platform, as explained in Section 1.3.

To cope with the hysteresis effect, one may consider different approaches, such as Bouc-Wen models [Ismail, Ikhouane, and Rodellar 2009] or nonlinear auto-regressive terms [Martins and Aguirre 2016]. But, both strategies would add unwanted complexity to the proposed model, which is not this thesis's aim. Therefore, each parameter of the proposed models will be identified separately for the release and the compression movements. This leads to a model whose parameter values depend on the piston behavior. Doing so, the effect of the incipient friction is naturally incorporated.

Different experimental configurations were carried out to estimate the parameters characterizing the final global models (1.8) and (1.12) . These tests consist in changing the magnitude

and the frequency of the external inputs of the *ER* shock absorber (Velocity, Electric Field) in order to identify the response of the system. To identify the values, it is necessary to check the damper output (Force) with respect to the inputs (Velocity, Electric Field, *etc*).

All the conducted identification procedures are explained in the sequel.

1.5.1 Linear terms

To identify the parameters (k_0, c_0) in both models, the experimental tests consist in submitting the damper to a null control signal ($u = 0$), in this case, the damper force is generated from a passive uncontrolled damper. Therefore, k_0 and c_0 are equal for the 2 proposed models. The following block-scheme (see Figure 1.7) illustrates the experimental scenario of the data collection to identify the parameters in the linear term

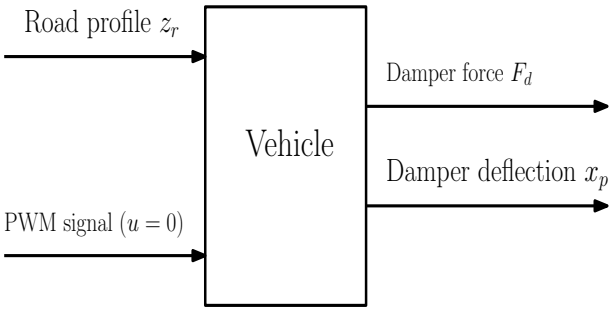

Figure 1.7: Block diagram for the data collection in the linear term identification.

In order to collect the experimental data for this identification step, the experimental scenarios are designed as follows:

- The control input $u = 0$
- The road profile is the sine waves with different frequency, shown in the top of Figures 1.8, 1.9 and 1.10.

Notice that we only show the experimental data of three tests in this part.

The displacements and damper force of the damper are shown in the middle and bottom of Figures 1.8, 1.9 and 1.10.

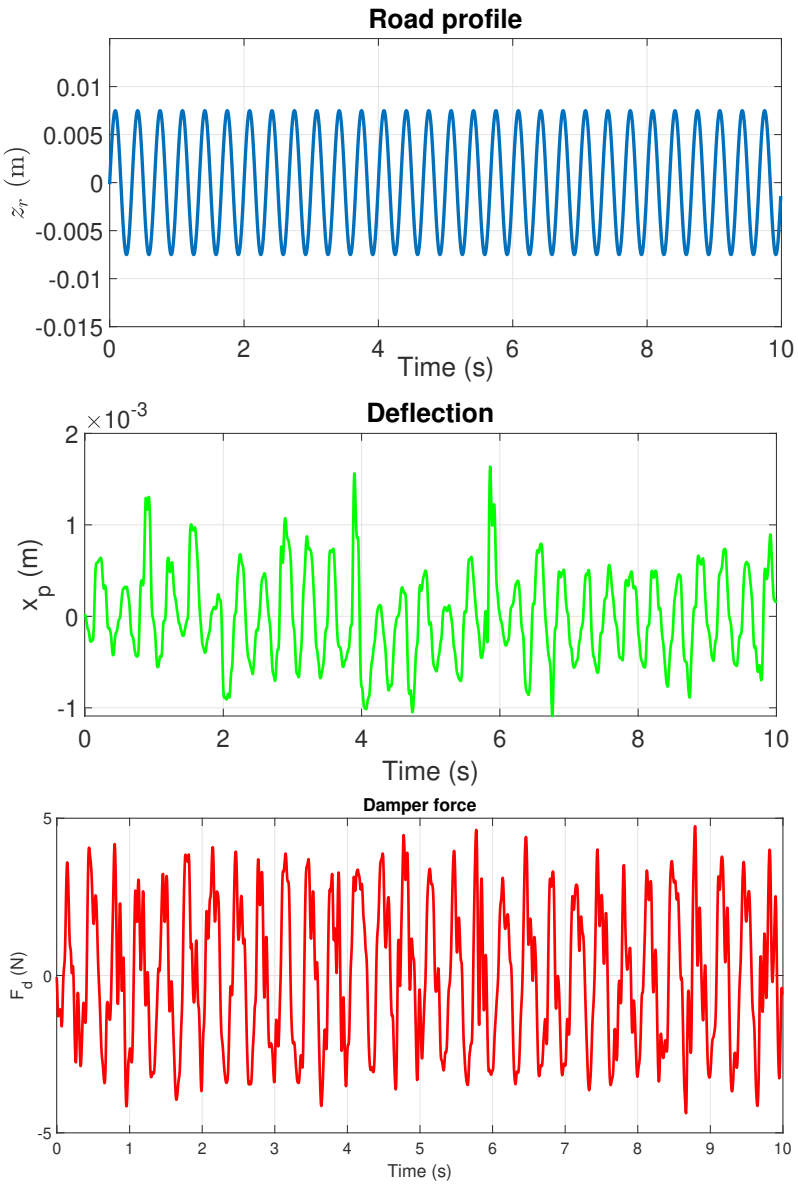

Figure 1.8: Linear identification (Test 1): (top) Road profile, (middle) displacement, (bottom) damper force.

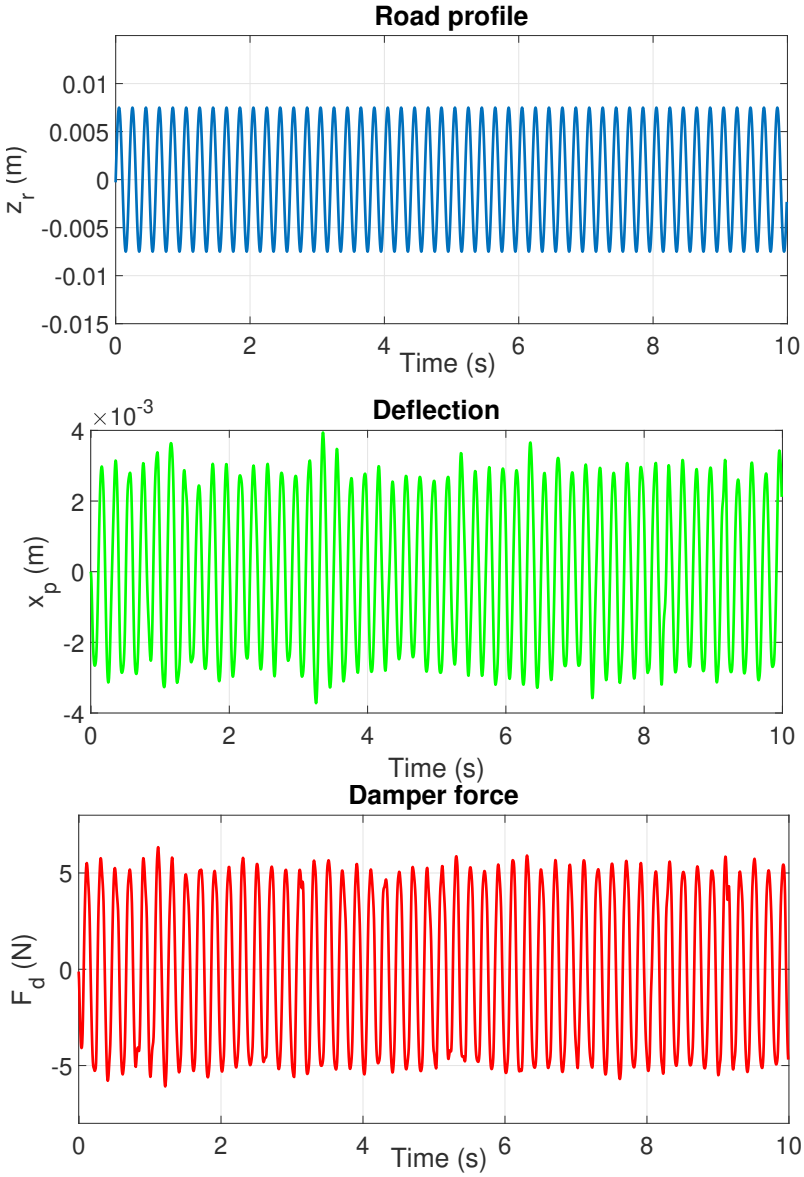

Figure 1.9: Linear identification (Test 2): (top) Road profile, (middle) displacement, (bottom) damper force.

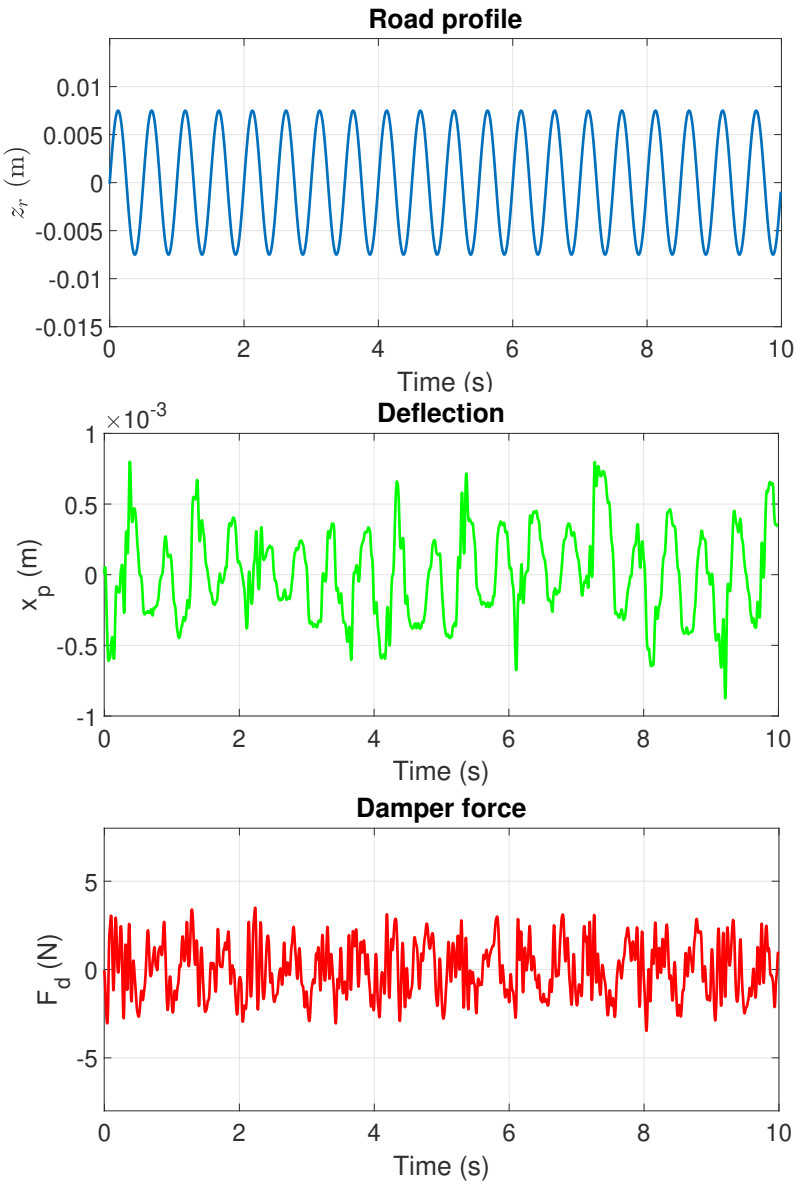

Figure 1.10: Linear identification (Test 3): (top) Road profile, (middle) displacement, (bottom) damper force.

During these tests, the damper force , displacement and velocity are measured for identification as shown in Figure 1.11. In this case, the damper force, when no electric field is applied to the damper, results from the gas compliance and ER fluid viscosity. Thereforce, the damper force is obtained as follows:

$$\begin{aligned} F_d(t) &= k_0 x_p(t) + c_0 \dot{x}_p(t) \\ &= [x_p(t), \dot{x}_p(t)] \begin{bmatrix} k_0 \\ c_0 \end{bmatrix} \end{aligned} \tag{1.13}$$

The parameters k_0 and c_0 in (1.13) are identified by the Least Squares Method, see [Ljung

1999], which resides in solving the following optimization problem:

$$\underset{\theta_1}{min} \quad \frac{1}{N}\sum_{i=1}^{N}(y_i - x_i\theta_1)^2 \tag{1.14}$$

where N is the number of samples, $\theta_1 = \begin{bmatrix} k_0 \\ c_0 \end{bmatrix}$, y_i is the measured damper force, x_i are the sensors measurements $(x_p(t), \dot{x}_p(t))$.

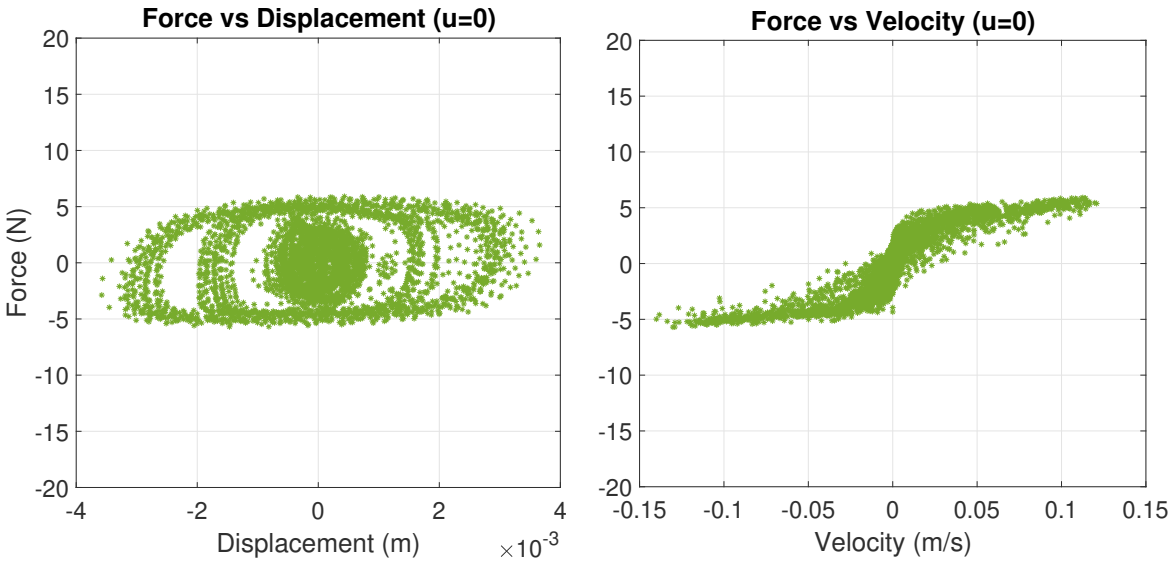

Figure 1.11: Damper Force vs Displacement and Damper force vs. Velocity diagrams of the real data for identifying k_0 and c_0.

1.5.2 Nonlinear term

The second part to be identified contains the parameters related to the force due to the yield stress of the ER fluid, which can be continuously controlled by the intensity of the electric field applied to the damper. During this experiment, the damper undergoes a sinusoidal deflection with different electric fields values. Indeed the force provided by the damper at a given deflection velocity can be controlled by changing the input voltage ($U(t)$, controlled by a PWM signal) of the ER damper. Therefore, once the parameters k_0 and c_0 are determined, the last parameters to be identified of the achieved damper force laws are α and β in the extended Bingham model (1.8) and f_c, k_1 and c_1 in the extended Guo model (1.12). They are related with the effect of the control signal (electric field, $E(t)$) upon the damper's behavior. Considering the used testbed, the relationship between a controlled PWM signal and the voltage applied to the damper is shown in the Table 1.1; see Equation (1.4) for the relationship between applied tension and electric field. Then, the parameters in nonlinear terms can be identified by analyzing the damper force, at the same piston velocity profile, with different

Table 1.1: Relationship: PWM and Applied Tension

PWM Signal $v(t)$	$U(t)$
0 %	0 kV
20 %	1 kV
40 %	2 kV
60 %	3 kV
80 %	4 kV
100 %	5 kV

applied Electric fields. The block-scheme (see Figure 1.12) presents the experimental scenario of the data collection to identify the parameters in the nonlinear term.

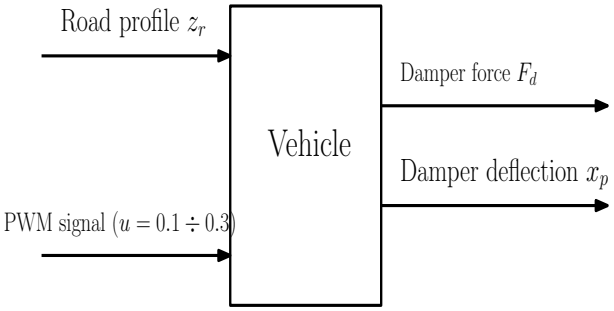

Figure 1.12: Block diagram for the data collection in the nonlinear term identification.

The experimental tests are used to collect the data as follows:

- The PWM signals vary inside the set $[10\,,\,30]\,\%$.

- The road profile is the sine waves with different frequency, shown at top of Figures 1.13, 1.14 and 1.15.

The data of the experimental tests are shown in Figures 1.13, 1.14 and 1.15. Notice that we do many experimental test with different value of duty cycle of PWM signal varying in the set $[10\,,\,30]\,\%$. Here we show the data of three tests with $u = 0.1$, $u = 0.2$ and $u = 0.3$, respectively.

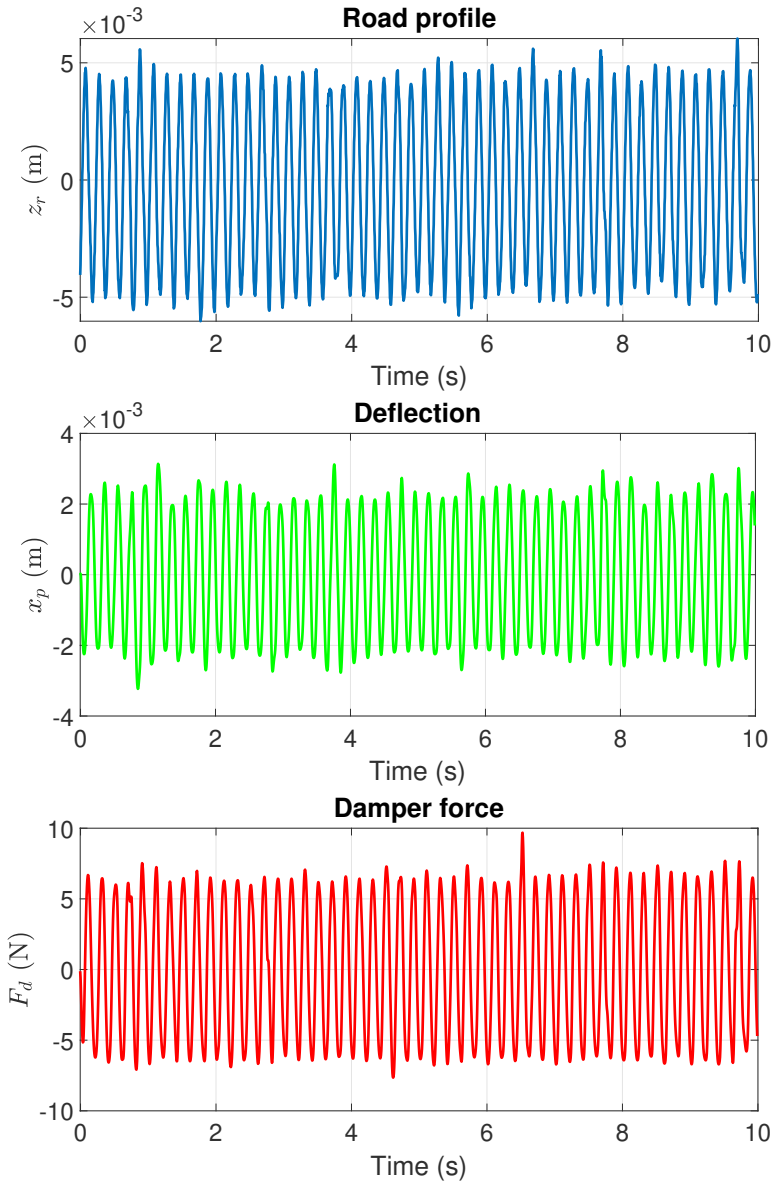

Figure 1.13: Test 2 (Nonlinear identification) $u = 0.1$: (top) Road profile, (middle) displacement, (bottom) damper force.

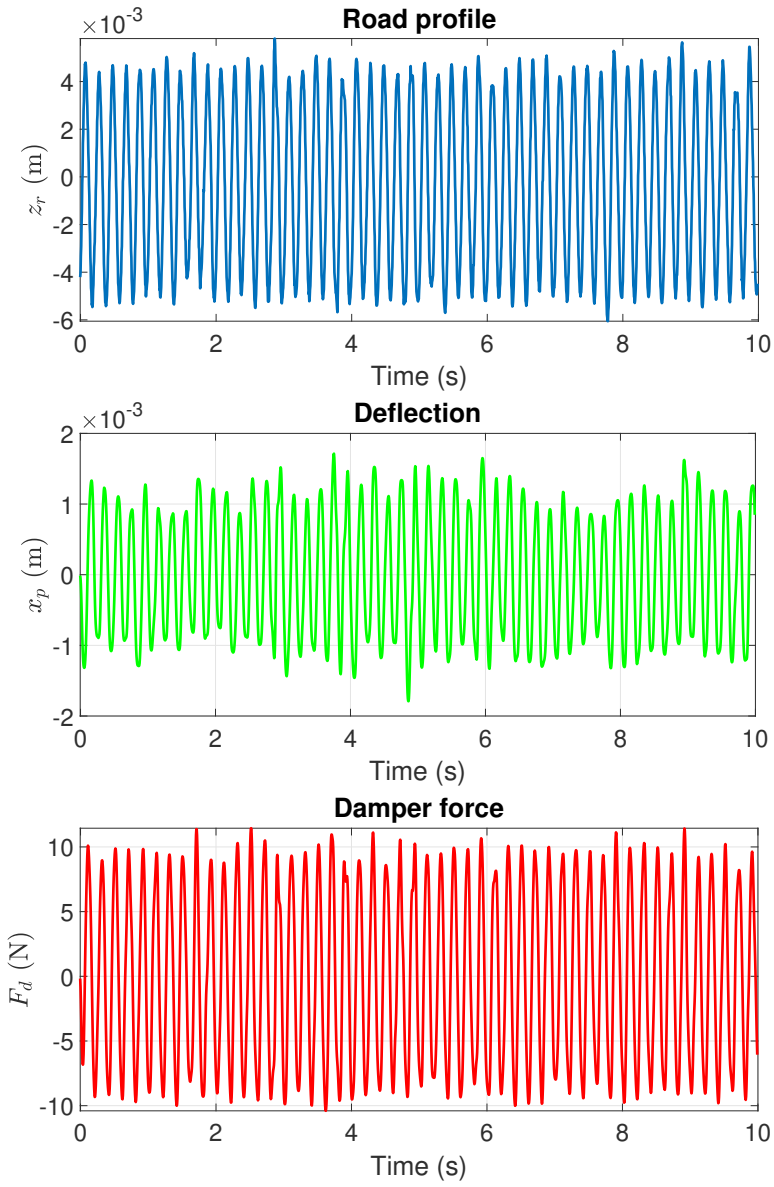

Figure 1.14: Test 2 (Nonlinear identification) $u = 0.2$: (top) Road profile, (middle) displacement, (bottom) damper force.

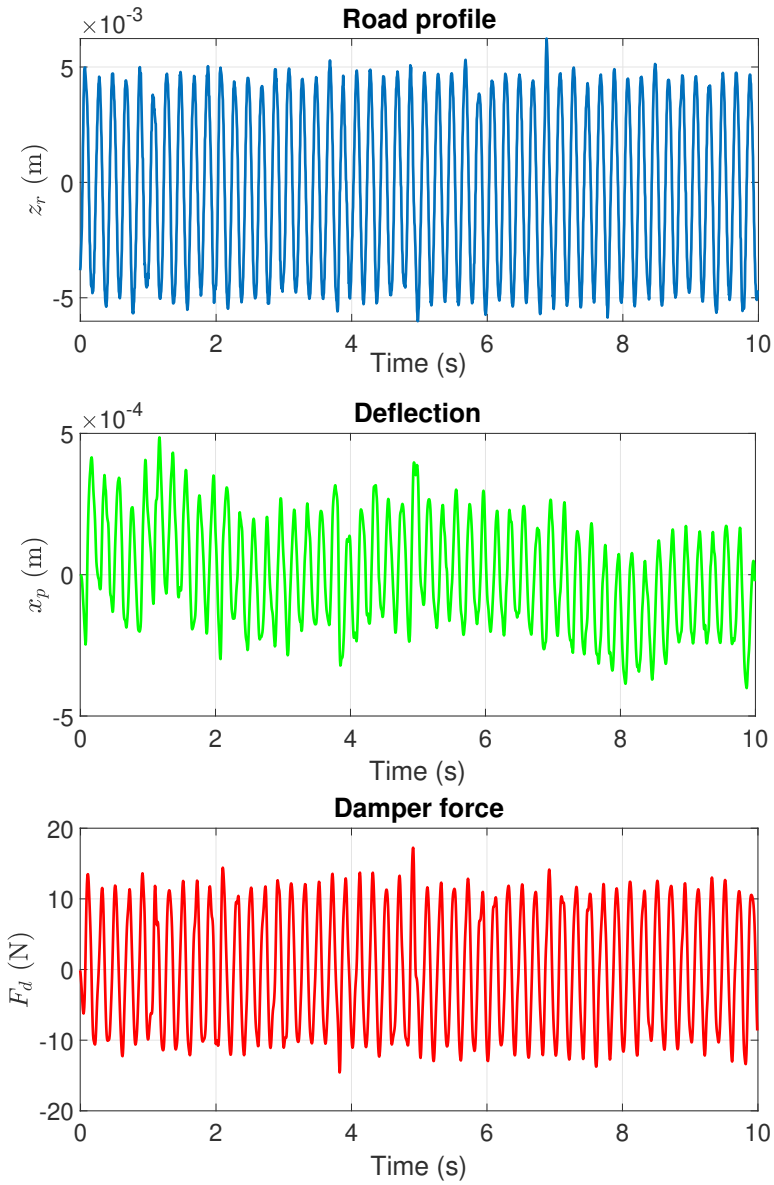

Figure 1.15: Test 3 (Nonlinear identification) $u = 0.3$: (top) Road profile, (middle) displacement, (bottom) damper force.

The collected data of damper force, displacement and velocity are shown in Figure 1.16

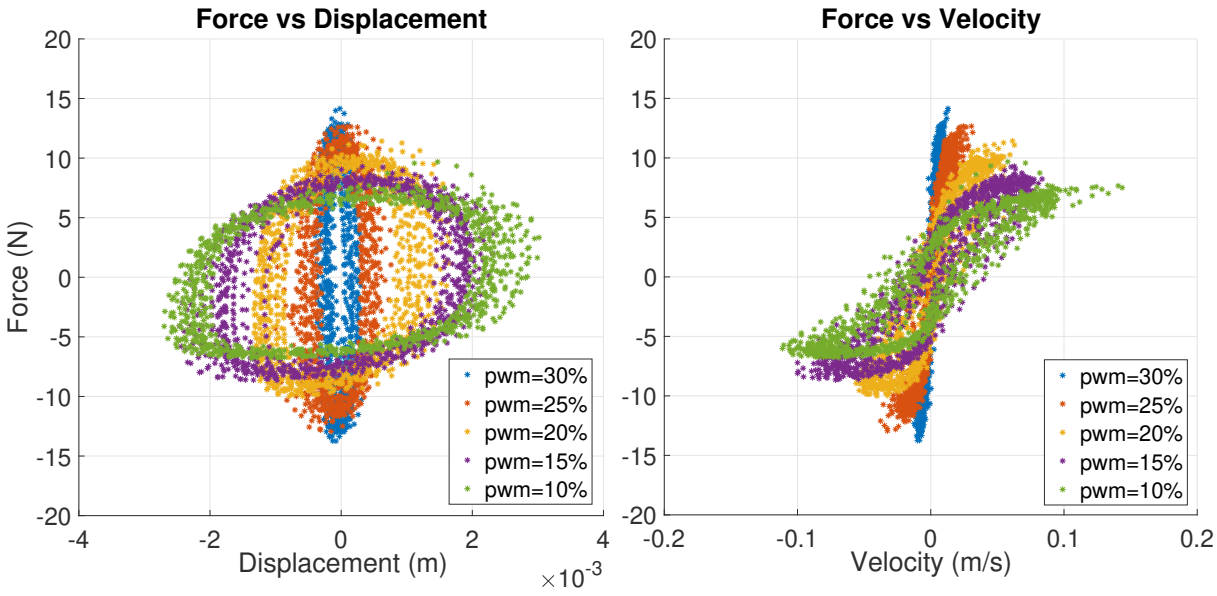

Figure 1.16: Damper Force vs. Displacement and Damper force vs Velocity diagrams of the real data for identifying the parameters in nonlinear terms.

The parameters σ, β f_c, k_1 and c_1 are estimated using a Nonlinear Least Squares Method [Marquardt 1963], considering the force values for different PWM signals ($u = 0.1 \div 0.3$). Based on the identified parameters k_0 and c_0 from the previous procedure, the force due to yield stress is calculated as follows:

$$F_{YS}(t) = F_d(t) - k_0 x_p(t) - c_0 \dot{x}_p(t) \tag{1.15}$$

where $F_{YS}(t)$ represents only the portion of the damper force due to yield stress of the ER fluid.

Case 1: Identify σ and β in the extended Bingham model (1.8)

Based on the extended Bingham model (1.8), $F_{YS}(t)$ can be straightforward rewritten as:

$$\begin{aligned} F_{YS} &= \sigma u^{\beta} sign(\dot{x}_p) \\ &= \begin{cases} \sigma u^{\beta} & \dot{x}_p > 0 \\ 0 & \dot{x}_p = 0 \\ -\sigma u^{\beta} & \dot{x}_p < 0 \end{cases} \end{aligned} \tag{1.16}$$

The parameters δ and β are estimated using a Nonlinear Least Squares Method with the cost function given by:

$$J_1 = \min_{\theta_2} \quad \sum_{i=1}^{N} (y_{2i} - f_{2i}(x_{2i}, \theta_2))^2 \tag{1.17}$$

where the vector θ_2 contains the parameters (σ, β), y_{2i} is the measurement data of $F_{YS}(t)$, considering Equation (1.15), $f_{2i}(x_{2i}, \theta_2)$ represents the force from yield stress in Equation

(1.16), x_{2i} contains the duty cycle of PWM channel (u) and piston's velocity ($\dot{x}_p$), the available measurements from the testbed.

Case 2: Identify f_c, k_1, c_1 in the extended Guo model (1.12)

Similarly, for the extended Guo model (1.12), $F_{YS}(t)$ is derived as

$$F_{YS}(t) = f_c \cdot u \cdot tanh(k_1 x_p + c_1 \dot{x}_p) \tag{1.18}$$

Similarly, the parameters f_c, k_1 and c_1 are estimated through a Nonlinear Least Squares Method with the following cost function:

$$J_2 = \underset{\theta_3}{min} \quad \sum_{i=1}^{N} (y_{2i} - f_{3i}(x_{3i}, \theta_3))^2 \tag{1.19}$$

where the vector θ_3 includes the parameters (f_c, k_1, c_1), y_{2i} is the measurement data of $F_{YS}(t)$ in eq. (1.15), $f_{3i}(x_{3i}, \theta_3)$ is the nonlinear function (1.18), x_{3i} contains the control input ($u(t)$), the displacement ($x_p(t)$) and piston's velocity ($\dot{x}_p(t)$). All identified parameters of the two models are given in Tables 1.2 and 1.3

Table 1.2: Identified ER damper parameters of the extended Bingham model

Parameters	Value		Unit
	Compression	Release	
k_0	263.1168	170.4045	N/m
c_0	64.6433	68.8289	N.s/m
σ	12.8157	17.0442	N
β	0.2373	0.3948	–

Table 1.3: Identified ER damper parameters of the extended Guo model

Parameters	Value		Unit
	Compression	Release	
k_0	263.1168	170.4045	N/m
c_0	64.6433	68.8289	N.s/m
f_c	29.2780	28.0699	N
k_1	204.0283	218.1615	1/m
c_1	492.6448	512.6200	s/m

1.5.3 The varying time constant

In order to identify $\tau(u)$, the same experimental data in subsection 1.5.2 is used to identify $\tau(u)$, considered 5 fixed PWM (i.e. u_{eq}) signals $\{0.1, 0.15, 0.2, 0.25, 0.3\}$. The identification

process is then divided into the two following steps:
Step 1: During each experimental test with a constant value u_{eq}, the corresponding force F_{er} is obtained from the test bed force sensor (see section 1.3) while F_{nl} is calculated, based on the static model of the ER damper as follows:

$$F_{nl} = \sigma u_{eq}^{\beta} \tag{1.20}$$

Then, the fixed time constant $\tau(u_{eq})$ can be identified by estimating the transfer fucntion between F_{er} and F_{nl}. Finally, the set of time constants τ for all u_{eq} is shown in Table 1.4.

Table 1.4: Values of time constant τ with different PWM signals

PWM	τ	Unit
0.1	0.0137	s
0.15	0.0221	s
0.2	0.0365	s
0.25	0.055	s
0.3	0.0631	s

Step 2: Based on the values given in Table 1.4, the relationship between τ and u can be approximated by the following polynomial function (Figure 1.17)

$$\tau(u) = 0.3643u^2 + 0.1124u + 0.002 \tag{1.21}$$

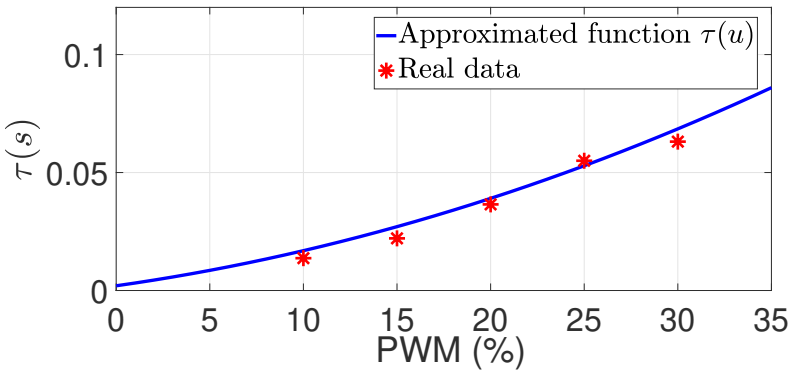

Figure 1.17: Relation between τ and u

1.6 Validation results

Now, the final validation results of the proposed Electro-Rheological damper models are presented, considering the adjusted identified parameters for the *INOVE Soben-Car* mechatronic test-rig.

1.6.1 Case 1

In case 1, two models are validated with the data collected for the identification in subsection 1.5.2. The new adjusted Force *vs.* Deflection and Force *vs.* Deflection Velocity diagrams are given, respectively, in Figures 1.18 and 1.19, which compare the proposed damper models and the real data measured from available sensors on the platform. In these Figures, it is clear that there exists an overall good agreement between model and data.

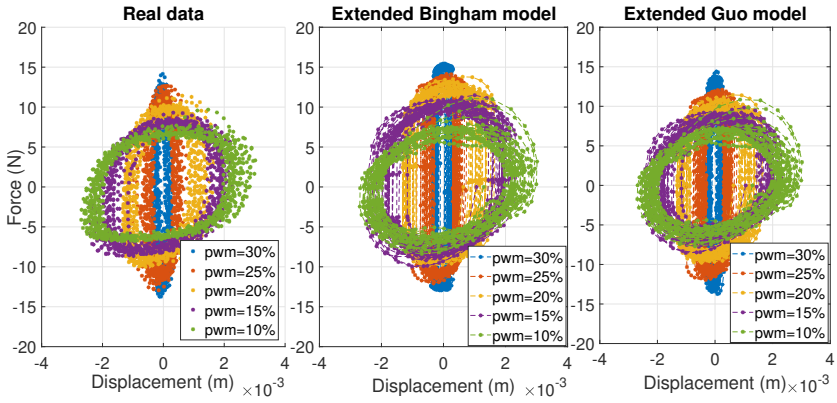

Figure 1.18: Final Model Validation Results: Force vs. Displacement (Case 1)

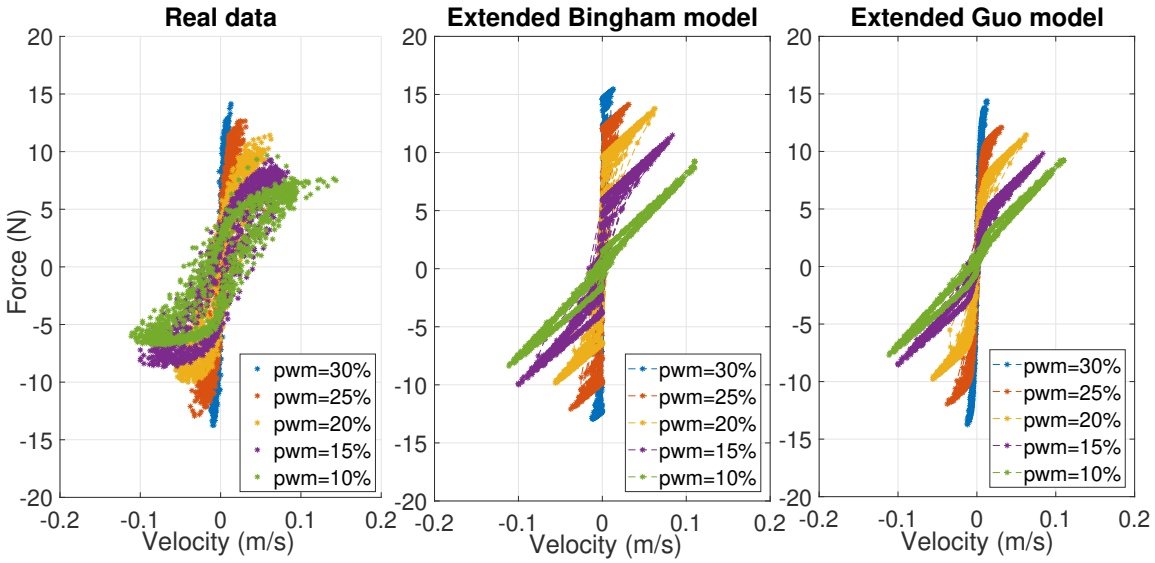

Figure 1.19: Final Model Validation Results: Force vs. Velocity

1.6.2 Case 2

It was discussed that the static models, as in equations (1.8) and (1.10) are not able to graps the whole delivered force by an ER damper (over time), this would only be achieved with the dynamical models, as in equations (6.1) and (1.12). Hence, considering the same data in Case 1, results comparing the real (measured) force and model-based results (from both statical and dynamical models) are given in Figures 1.20 and 1.21. According to these Figures, the dynamic model represents a better modeling result than using the static one when velocity is zero.

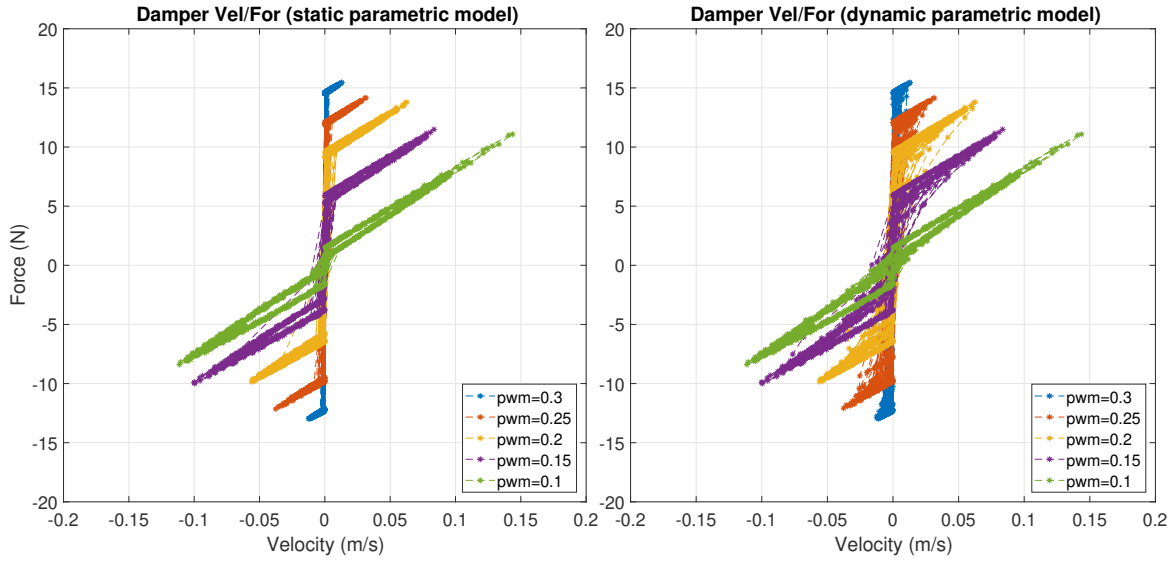

Figure 1.20: Validation Results: Static vs. Dynamical Bingham model

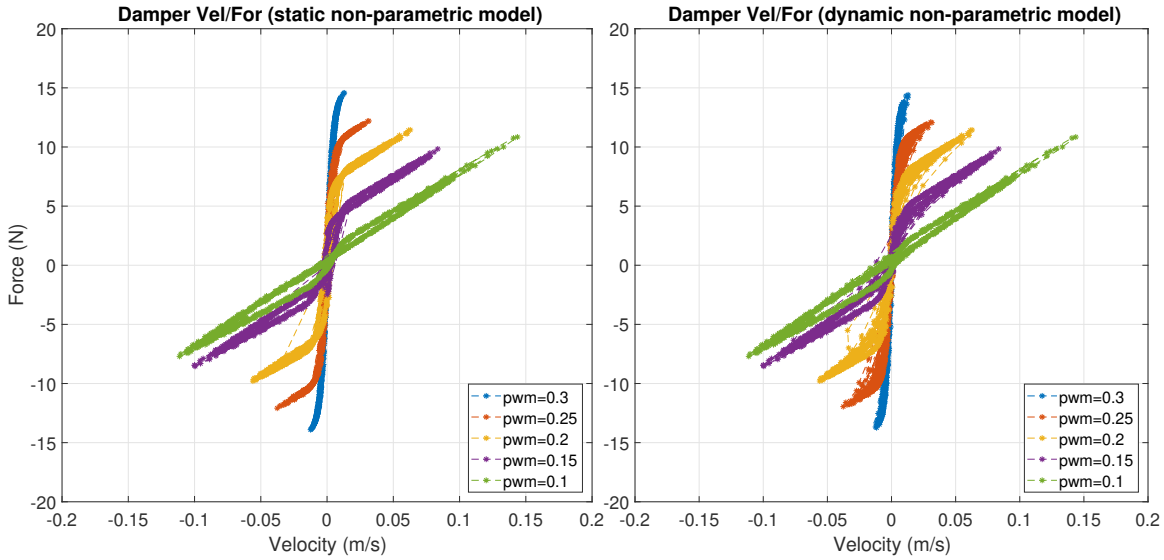

Figure 1.21: Validation Results: Static vs. Dynamical Guo model

1.6.3 Case 3

One considers the road profile of a vehicle running at 120 km/h in a straight line on a dry road with a sequence of 10 mm sinusoidal bumps (shown in top of Figure 1.22) and PWM signal $u = 0.2$. The results comparing the model-based computed force and the real (measured) force are given by Figures 1.24 and 1.22. The modelling error is shown in Figure 1.23. Clearly, the model is well adjusted.

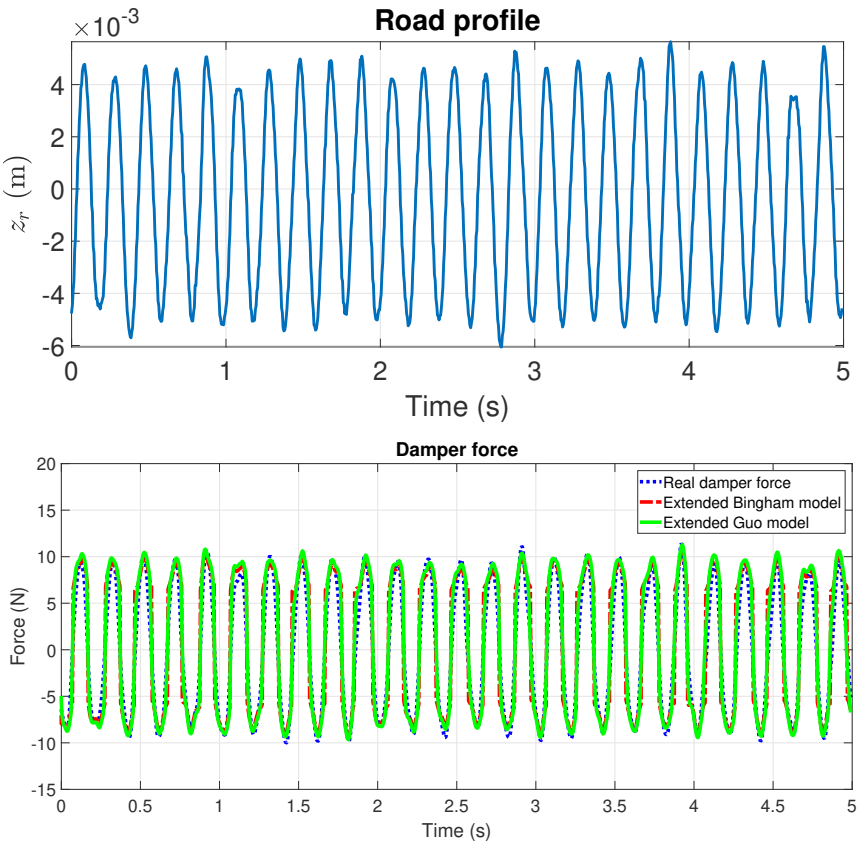

Figure 1.22: Validation Results: (top) Road profile, (bottom) Model-based and Real Force - Sinusoidal Road Profile (Case 3)

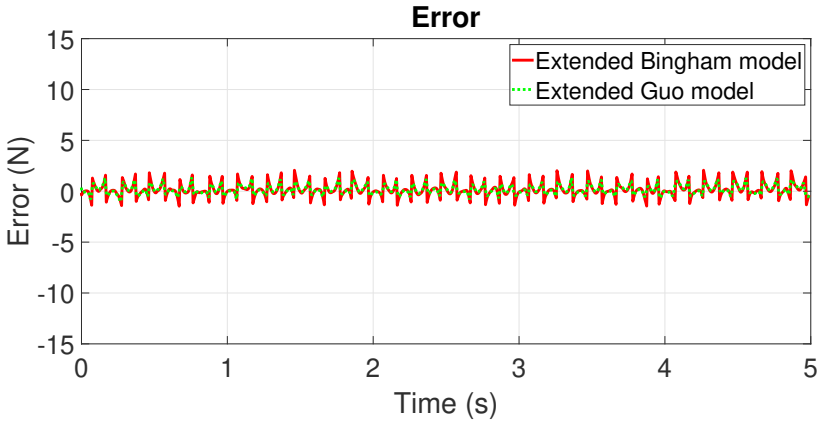

Figure 1.23: Validation Results: Error-Sinusoidal Road Profile (Case 3)

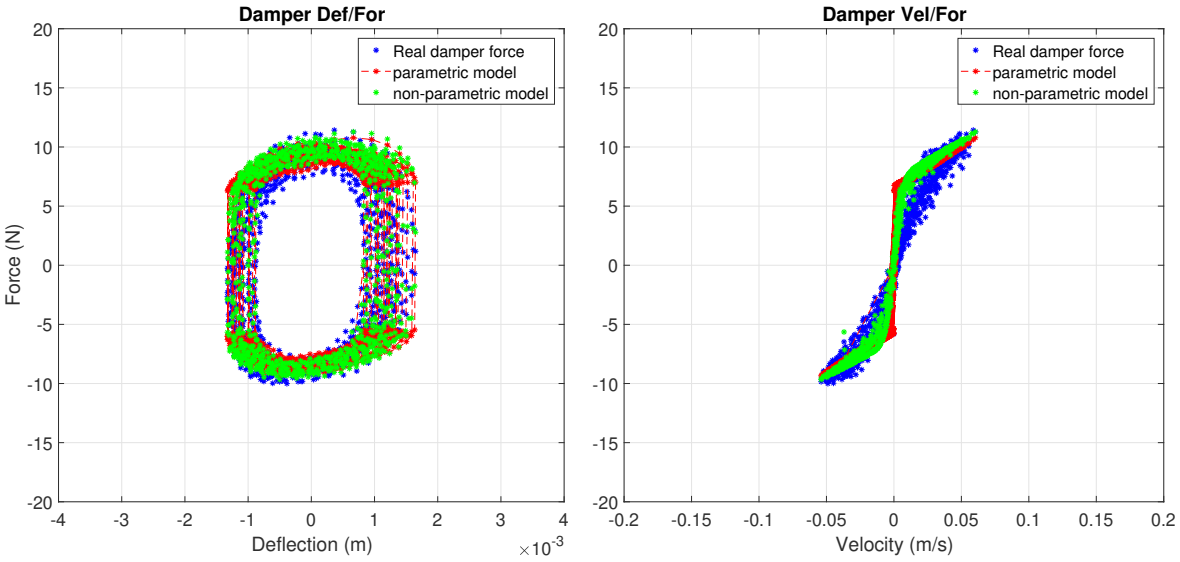

Figure 1.24: Validation Results: Damper Diagrams - Sinusoidal Road Profile (Case 3)

1.6.4 Case 4

In this validation case, an ISO 8608 road profile signal (shown in Figure 1.25) is used and the PWM signal is $u = 0.225$. The damper forces computed from the two models are compared with the real damper force, as shown in the Figure 1.26.

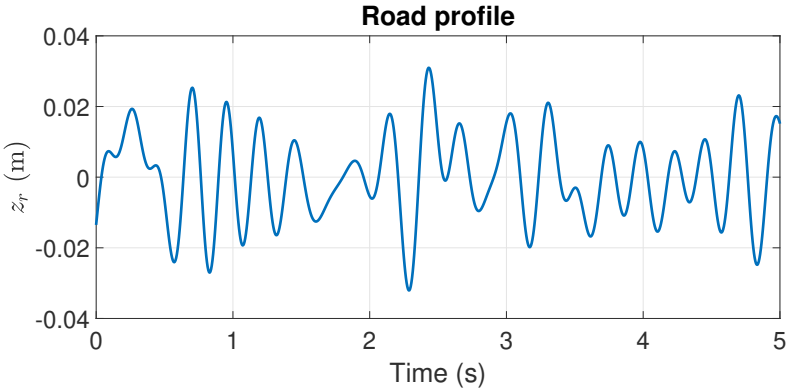

Figure 1.25: Validation Results: ISO Road Profile (Case 4)

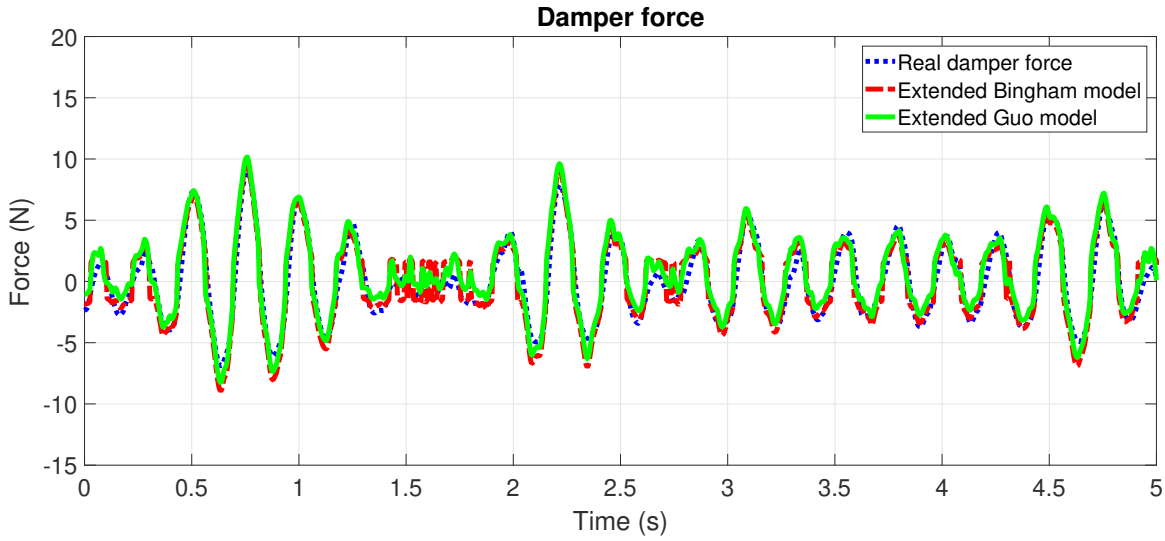

Figure 1.26: Validation Results: Model-based and Real Force - ISO Road Profile (Case 4)

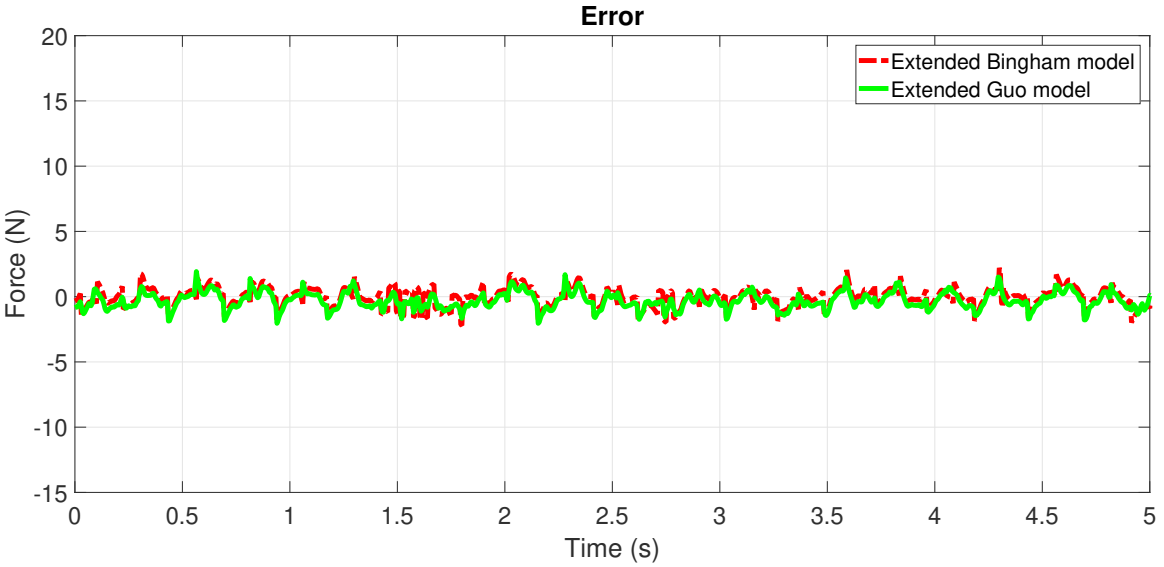

Figure 1.27: Validation Results: Error -ISO Road Profile (Case 4)

The proposed models are now accurate and describe very well the dynamics of an Electro-Rheological damper, which is one of the main goals of this chapter. To further illustrate this accuracy, Table 1.5 presents the normalized root-mean-square errors, considering the difference between the adjusted model force and the real measured force for cases 3 and 4.

Table 1.5: Final Validation: Normalized Root-Mean-Square Errors

Road profile	Extended Bingham model *NRMSE*	Extended Guo model *NRMSE*
sine wave	0.1036	0.0851
ISO road	0.0780	0.0734

1.7 Conclusions

This chapter presented two control-oriented models for an Electro-Rheological damper, in the case of (semi-active) automotive applications. The first model is derived from Bingham law, while the other is extended from Guo model. Then, an identification procedure using linear least square and nonlinear least square methods proposed to identify the model parameters. The proposed models were validated with various tests on the INOVE experimental platform (small scaled car). The overall results assess the ability and the accuracy of the proposed models to represent the real damping force of the ER semi-active damper.

Moreover, in terms of implementation cost, let it be stressed that:

- The proposed models , fairly simple and reduced-order, can be to run in real-time in embedded vehicle suspension control applications.

- One can easily design estimation approach and control policies based on these models

In the rest of this thesis, the extended Guo and static Bingham models are used to synthesize the controllers and observers for the automotive suspension system. To simplify the design observer and controller procedure, the parameters of the damper model in the compression and the varying time constant $\tau(u)$ is chosen as a constant ($\tau = 0.0365$), considered as a nominal value of $\tau(u)$. Now the extended Guo model is as the follows

$$\begin{cases} F_d = k_0 x_p + c_0 \dot{x}_p + F_{er} \\ \tau \dot{F}_{er} + F_{er} = f_c.u.tanh(k_1 x_p + c_1 \dot{x}_p) \end{cases} \tag{1.22}$$

and the static Bingham model is the following ones

$$F_d = k_0 x_p + c_0 \dot{x}_p + \sigma u^{\beta} \text{sign}(\dot{x}_p) \tag{1.23}$$

and the prameters are shown in the following table

Table 1.6: Identified *ER* damper parameters of the extended Guo and static Bingham model

Parameters	Value	Unit
k_0	263.1168	N/m
c_0	64.6433	N.s/m
f_c	29.2780	N
k_1	204.0283	1/m
c_1	492.6448	s/m
τ	0.0365	s
σ	12.8157	N
β	0.2373	–

The extended Guo model (1.22) captures the nonlinear and dynamic behaviors of the ER damper; therefore, it is used to design the observer and controller. The static Bingham model (1.23) developed using the physical laws, extends to analyze the fault conditions in the ER damper. It must be noticed that small model-life mismatches (as the ones we have with our model) are overlapped by robustness qualities of the usual state-of-the-art control approaches used in embedded semi-active control systems.

Chapter 2

Extended Quarter Car Modeling

Contents

This chapter provides four extended quarter car models that will be used for the design of observers and controllers. The quarter car models are augmented with a first-order dynamical nonlinear damper model (extended Guo model in section 1.4.2), which captures the main behavior of the ER suspension system. For control design purposes, the system dynamics are separated into two subsystems as presented in section 2.2.1. Besides, the dynamical equations of the quarter car system are written within a nonlinear Lipschitz formulation in section 2.2.2 and a NonLinear Parameter Varying formulation in section 2.2.3. Finally, a Nonlinear Lipschitz Descriptor representation considering an actuator fault in section 2.2.4.

The models have been presented in the following publications:

- *Unified H_∞ observer for a class of nonlinear Lipschitz systems: application to a real ER automotive suspension. IEEE Control Systems Letters*, 3(4), 817-822.

- *Real-time Damper Force Estimation of Vehicle Electrorheological Suspension: A Non-Linear Parameter Varying Approach*, 3^{rd} *IFAC Workshop on Linear Parameter-Varying Systems, Netherlands, 2019.*

- *Real-time Estimation of Damping Force of Vehicle Electrorheological Suspension System: a new H_∞ approach and experimental validation*, 9^{th} *IFAC International Symposium on Advances in Automotive Control, France, 2019.*

2.1 Introduction

As previously mentioned in Chapter 1, vehicle systems are composed of many subsystems such as suspension, steering and braking systems, and others (see Fig 2.1). Hence, many vehicle models are presented in the literature considering the characteristic of the subsystems (see [Gillespie 1992], [Milliken and Milliken 1995], [Kiencke and Nielsen 2005]), [Tanelli, Corno, and Saveresi 2014]. The related studies focus on the vertical dynamic of the vehicle equipped with a suspension system to improve the comfort and safety of on-board passengers as presented in [Fleps-Dezasse, Svaricek, and Brembeck 2018], [Poussot-Vassal 2008b], [Kloiber, Koch, and Lohmann 2010], [Unger et al. 2013], [Choi, Lee, and Park 2002]. It is worth noting that the vehicle's behavior depends on the type of suspension system; therefore, understanding the behavior of the automotive suspension system is a crucial task. As mention in the introduction section of Chapter 1, the passive and active suspensions have drawbacks. In order to overcome such disadvantages, several models including a semi-active suspension system have been investigated [Fleps-Dezasse, Svaricek, and Brembeck 2018], [Poussot-Vassal 2008b], [Nguyen 2016], [Fergani 2015], [Do 2011]. To better understand the vehicle vertical dynamics, the main characteristics of semi-active suspension such as the nonlinear and dynamic behaviors should be considered in the vehicle model.

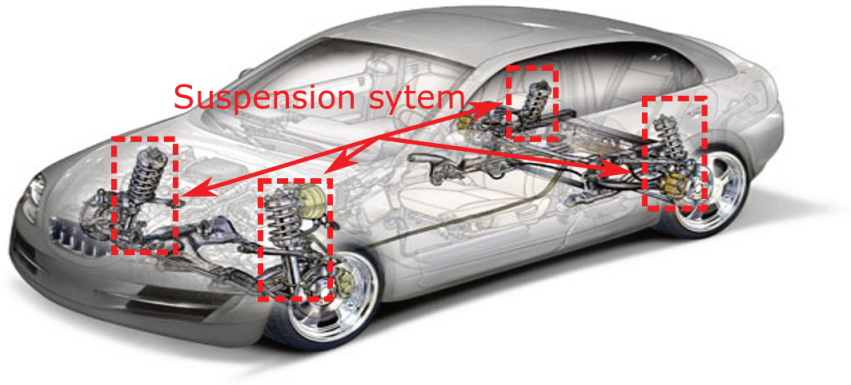

Figure 2.1: Suspension system on vehicle

Along the line of research for the vertical dynamic models of the automotive systems, there have been several contributions to the literature. Some models were developed by former PhD students in the SLR team. The models can be classified into three categories:

- The works by [Poussot-Vassal 2008a; Nguyen 2016] proposed a quarter car model based on the linearized model of the semi-active damper. To overcome this limitation, the quarter vehicle model augmented with a nonlinear semi-active suspension model presented in [Do 2011; Kloiber, Koch, and Lohmann 2010]; however, the dynamic characteristic of the semi-active damper was ignored.
- Based on the static nonlinear model of the semi-active damper, half car models were

proposed in [Zin 2005], [Rathai, Sename, and Alamir 2019], [Canale, Milanese, and Novara 2006]

- Full vertical vehicle model based on the linearized semi-active suspension model was introduced in [Nguyen 2016]. [Fleps-Dezasse, Svaricek, and Brembeck 2018] presented a full car model using a static nonlinear model of the semi-active damper.

On the other hand, the dynamic response of the vehicle system could be influenced by faults in the semi-active damper such as oil leakages, physical deformation, electrical issues; therefore, their detection plays a vital role in safety and FTC strategies of real cars. For this purpose, few recent studies have been concerned with the modelling of loss effectiveness of the damper, as seen in [Hernández-Alcántara et al. 2016]. Furthermore, some works have been dedicated to the study of faults estimation in the semi-active damper (see [Morato et al. 2019], [Nguyen, Sename, and Dugard 2016]), [Nguyen, Sename, and Dugard 2015a], [Do, Koenig, and Theilliol 2018]. In these works, the loss effectiveness of the damper is represented in the multiplicative or additive fault representations to develop a fault observer; however, the derivative of fault is assumed to be zero, which simplified the theoretical problem but is not realistic. Thanks to the descriptor system representation, the dynamical system incorporating actuator fault is proposed without any assumption on the fault dynamics.

Based on the control-oriented Guo model presented in Chapter 1, this chapter proposes four extended quarter car models that will be used to design observers and controllers in chapters 3-6. Hence, the major contributions of this chapter are summarized as follows:

- The quarter car model is separated into two subsystems: LTI and qLPV systems (section 2.2.1). The aim is to reduce the complexity in designing the controller via LTI form for the quarter car system, while the qLPV representation allows to deal with the nonlinearity in the local force subsystem. Based on these models, the LPV controller is synthesized in chapter 6.

- The dynamics system is written in a nonlinear Lipschitz system form (section 2.2.2) where the road profile disturbance is considered as the unknown input. It is used to design an unknown input observer in chapter 3.

- The variations of the damper force amplification function of the voltage input in the quarter vehicle model are solved via a NLPV formulation. This model is used to develop an NLPV observer in chapter 4.

- The mathematical model of the quarter vehicle model considering the loss of efficiency of the damper is written in the nonlinear Lipschitz descriptor system representation in order to develop an observer to estimate system states and fault simultaneously in chapter 5.

2.2 Extended quarter car modeling

This section introduces the quarter-car model with the semi-active ER suspension system presented in Fig.2.2. The well-known model, considering only a single corner of a car, consists

Figure 2.2: Quarter vehicle model

of the following components:

- The sprung mass m_s represents a quarter vehicle body.
- The unsprung mass m_{us} represents the wheel and the tire of the single corner of the car.
- The suspension components located between (m_s) and (m_{us}) consists of a spring with the stiffness coefficient k_s and an ER semi-active damper composed by an uncontrolled force $F_{passive}$ plus a controlled one F_{er}.
- The tire which is modelled as a spring with the stiffness coefficient k_t.

It can be seen in Figure 2.2 that z_s and z_{us} are the vertical displacements around the equilibrium points of the sprung and unsprung masses, respectively. z_r is the road displacement input.

Besides, let us denote $z_{def} = z_s - z_{us}$ the suspension deflection, $\dot{z}_{def} = \dot{z}_s - \dot{z}_{us}$ the suspension deflection velocity and $z_{us} - z_r$ the tire deflection.

From Newton's second law of motion, the system dynamics around the equilibrium are given as:

$$\begin{cases} m_s \ddot{z}_s & = -F_s - F_d \\ m_{us} \ddot{z}_{us} & = F_s + F_d - F_t \end{cases} \tag{2.1}$$

where F_s is the spring force, F_t is the tire force and F_d stands for the damper force

The spring force and the tire force are given as:

$$F_s = k_s(z_s - z_{us}) \tag{2.2}$$

$$F_t = k_t(z_{us} - z_r) \tag{2.3}$$

The suspension equipped with the ER damper, therefore, the damper force F_d is given as in (1.22) (Chapter 1) with deflection $z_{def} = z_s - z_{us}$ (referred to as x_p in Chapter 1) and deflection velocity $\dot{x}_p = \dot{z}_{def} = \dot{z}_s - \dot{z}_{us}$.

$$\begin{cases} F_d = k_0(z_s - z_{us}) + c_0(\dot{z}_s - \dot{z}_{us}) + F_{er} \\ \tau\dot{F}_{er} + F_{er} = f_c \cdot u \cdot tanh(k_1(z_s - z_{us}) + c_1(\dot{z}_s - \dot{z}_{us})) \end{cases} \tag{2.4}$$

The parameters of the above model are shown in table 2.1.

Table 2.1: Parameter values of the quarter-car model equipped with an ER damper

Parameter	Description	value	Unit
m_s	Sprung mass	2.27	kg
m_{us}	unsprung mass	0.25	kg
k_s	Spring stiffness	1396	N/m
k_t	Tire stiffness	12270	N/m
k_0	Passive damper stiffness coefficient	263.1168	N/m
c_0	Viscous damping coefficient	64.6433	N.s/m
k_1	Hysteresis coefficient due to displacement	204.0283	N/m
c_1	Hysteresis coefficient due to velocity	492.6448	N.s/m
f_c	Dynamic yield force of ER fluid	29.2780	N
τ	Time constant	0.0365	s

Subtituting (2.2), (2.3) and (2.4) into (2.1) leads to:

$$\begin{cases} \ddot{z}_s &= -\frac{1}{m_s}\left[(k_s + k_0)(z_s - z_{us}) + c_0(\dot{z}_s - \dot{z}_{us}) + F_{er}\right] \\ \ddot{z}_{us} &= \frac{1}{m_{us}}[(k_s + k_0)(z_s - z_{us}) + c_0(\dot{z}_s - \dot{z}_{us}) + F_{er} - k_t(z_{us} - z_r)] \\ \dot{F}_{er} &= -\frac{1}{\tau}F_{er} + \frac{f_c}{\tau} \cdot u \cdot tanh(k_1(z_s - z_{us}) + c_1(\dot{z}_s - \dot{z}_{us})) \end{cases} \tag{2.5}$$

Remark 2.2.1. *In the studies where the dynamical property of the damper is not considered, F_{er} is replaced by*

$$F_{er} = f_c \cdot u \cdot tanh(k_1(z_s - z_{us}) + c_1(\dot{z}_s - \dot{z}_{us})) \tag{2.6}$$

The system dynamics are presented in Fig 2.3, where the quarter vehicle system dynamics include two subsystems, namely subsystem 1 and subsystem 2. The subsystem 1 represents for quarter car system with the inputs F_{er} and road profile while the subsystem 2 is the controlled part of the ER damper with the input u.

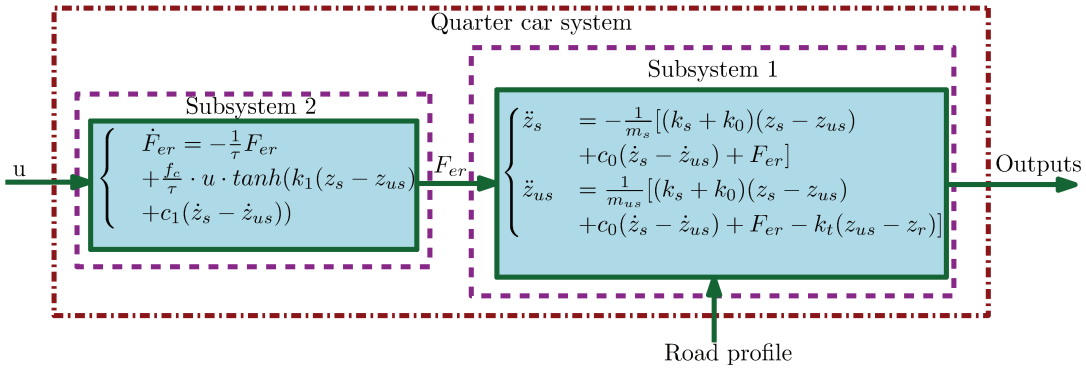

Figure 2.3: System dynamics of quarter vehicle

In the next sections, the system dynamics is rewritten into the state space representations.

2.2.1 The Linear and quasi Linear Parameter Varying subsystems

In this section, the system dynamics (2.5) is divided into two subsystems (as shown in Fig 2.3) which can be written in the linear system representation and quasi Linear Parameter Varying (qLPV) form, respectively. These models are used to synthesize the controllers for the quarter vehicle system in chapter 6.

In the subsystem 1, by choosing the control input $u_{er} = F_{er}$, the dynamical equation of the first subsystem is rewritten as:

$$\Sigma_1 : \begin{cases} \ddot{z}_s & = -\frac{1}{m_s}\left[(k_s + k_0)(z_s - z_{us}) + c_0(\dot{z}_s - \dot{z}_{us}) + u_{er}\right] \\ \ddot{z}_{us} & = \frac{1}{m_{us}}[(k_s + k_0)(z_s - z_{us}) + c_0(\dot{z}_s - \dot{z}_{us}) + u_{er} \\ & \quad -k_t(z_{us} - z_r)] \end{cases} \tag{2.7}$$

By choosing the first subsystem states as $x_s = [x_{s1}, x_{s2}, x_{s3}, x_{s4}]^T = [z_s, \dot{z}_s, z_{us}, \dot{z}_{us}]^T \in \mathbb{R}^4$, the first subsystem dynamics (2.7) can be represented in the following state space form:

$$\Sigma_1 : \left\{ \dot{x}_s \quad = A_s x_s + B_s u_{er} + D_{s\omega}\omega_s \right. \tag{2.8}$$

$\omega_s = z_r$ is the road profile.

$$A_s = \begin{bmatrix} 0 & 1 & 0 & 0 \\ -\frac{(k_s+k_0)}{m_s} & -\frac{c_0}{m_s} & \frac{(k_s+k_0)}{m_s} & \frac{c_0}{m_s} \\ 0 & 0 & 0 & 1 \\ \frac{(k_s+k_0)}{m_{us}} & \frac{c_0}{m_{us}} & -\frac{(k_s+k_0+k_t)}{m_{us}} & -\frac{c_0}{m_{us}} \end{bmatrix}, B_s = \begin{bmatrix} 0 \\ -\frac{1}{m_s} \\ 0 \\ \frac{1}{m_{us}} \end{bmatrix}, D_{s\omega} = \begin{bmatrix} 0 \\ 0 \\ 0 \\ \frac{k_t}{m_{us}} \end{bmatrix}$$

From (2.5), the dynamical equation of the second subsystem is given as follows:

$$\Sigma_2 : \left\{ \dot{F}_{er} = -\frac{1}{\tau} F_{er} + \frac{f_c}{\tau} \cdot u \cdot tanh(k_1(z_s - z_{us}) + c_1(\dot{z}_s - \dot{z}_{us})) \right. \tag{2.9}$$

In order to design an inner force tracking controller for the second subsystem, the dynamical equation can be rewritten in the following qLPV representation:

$$\Sigma_2 : \left\{ \dot{x}_{lc} \quad = A_{lc} x_{lc} + B_{lc}(\rho_{lc}) \cdot u \right. \tag{2.10}$$

where $x_{lc} = F_{er}$, $\rho_{lc} = tanh(k_1(z_s - z_{us}) + c_1(\dot{z}_s - \dot{z}_{us}))$, $A_{lc} = -\frac{1}{\tau}$, $B_{lc}(\rho_{lc}) = \frac{f_c}{\tau}\rho_{lc}$

2.2.2 A Nonlinear Lipschitz system representation

In this section, the system dynamics (2.5) can be written as a nonlinear Lipschitz system in the state-space representation in order to design the unified H_∞ observer in chapter 3.

By selecting the system states as $x = [x_1, x_2, x_3, x_4, x_5]^T = [z_s - z_{us}, \dot{z}_s, z_{us} - z_r, \dot{z}_{us}, F_{er}]^T \in \mathbb{R}^5$, the system dynamics (2.5) can be written in the state-space representation as follows

$$\left\{ \dot{x} \quad = Ax + B\Phi(x)u + D_1\omega_r \right. \tag{2.11}$$

where $\omega_r = \dot{z}_r$ is the road profile derivative,

$$\begin{aligned} \Phi(x) &= tanh\left(\begin{bmatrix} k_1 & c_1 & 0 & -c_1 & 0 \end{bmatrix} \begin{bmatrix} x_1 \\ x_2 \\ x_3 \\ x_4 \\ x_5 \end{bmatrix} \right) \\ &= tanh(\Gamma x) \end{aligned} \tag{2.12}$$

with $\Gamma = \begin{bmatrix} k_1 & c_1 & 0 & -c_1 & 0 \end{bmatrix}$.

The system matrices A, B, D_1 are as follows:

$$A = \begin{bmatrix} 0 & 1 & 0 & -1 & 0 \\ -\frac{(k_s+k_0)}{m_s} & -\frac{c_0}{m_s} & 0 & \frac{c_0}{m_s} & -\frac{1}{m_s} \\ 0 & 0 & 0 & 1 & 0 \\ \frac{(k_s+k_0)}{m_{us}} & \frac{c_0}{m_{us}} & -\frac{k_t}{m_{us}} & -\frac{c_0}{m_{us}} & \frac{1}{m_{us}} \\ 0 & 0 & 0 & 0 & -\frac{1}{\tau} \end{bmatrix}, B = \begin{bmatrix} 0 \\ 0 \\ 0 \\ 0 \\ \frac{f_c}{\tau} \end{bmatrix}, D_1 = \begin{bmatrix} 0 \\ 0 \\ -1 \\ 0 \\ 0 \end{bmatrix},$$

In the above nonlinear Lipschitz system, the nonlinear function $\Phi(x)$ satisfies a Lipschitz condition, and ω_r is considered as an unknown input. Therefore, it is useful to design the unknown input observer for the nonlinear Lipschitz system (Chapter 3).

2.2.3 NonLinear Parameter Varying system

In this section, the system dynamics can be written in a NonLinear Parameter Varying (NLPV) form to design a NLPV observer in chapter 4.

By selecting the system states as $x = [x_1, x_2, x_3, x_4, x_5]^T = [z_s - z_{us}, \dot{z}_s, z_{us} - z_r, \dot{z}_{us}, F_{er}]^T \in \mathbb{R}^5$ and the scheduling variable $\rho = u \in \mathbb{R}$ (Table 2.2), the system dynamics (2.5) can be written in the following NLPV form:

$$\begin{cases} \dot{x} & = A(x,\rho) + D_1\omega_r \\ A(x,\rho) & = Ax + B(\rho)\Phi(x) \end{cases} \tag{2.13}$$

where ω_r, $\Phi(x)$ and system matrices (A, D_1) are given as subsection 2.2.2.

$$B(\rho) = \begin{bmatrix} 0 \\ 0 \\ 0 \\ 0 \\ \frac{f_c}{\tau}\rho \end{bmatrix}, \tag{2.14}$$

Table 2.2: Range of the control input value u

Control input	Description	value
u	Duty cycle of PWM channel	[0, 1]

The nonlinear parameter varying system (2.13) is useful to design a NLPV observer since the nonlinearity $\Phi(x)$ is kept inside the parameter-varying block and the scheduling parameter is real-time accessible.

2.2.4 Nonlinear Lipschitz Descriptor system considering actuator fault

In this section, the loss efficiency of the damper is taken into account. In order to design the fault observer, the system dynamics can be written in the Nonlinear Lipschitz Descriptor system. This model is used to design the fault observer in chapter 5.

First, the damper force F_d in the healthy case (1.22) is recalled as follows:

$$\begin{cases} F_d & = k_0(z_s - z_{us}) + c_0(\dot{z}_s - \dot{z}_{us}) + F_{er} \\ \dot{F}_{er} & = -\frac{1}{\tau}F_{er} + \frac{f_c}{\tau} \cdot u \cdot tanh(k_1(z_s - z_{us}) + c_1(\dot{z}_s - \dot{z}_{us})) \end{cases} \tag{2.15}$$

Considering the loss efficiency of the damper, the damper force F_d^f in the fault case is given as:

$$F_d^f = F_d - \alpha F_d = F_d - f \tag{2.16}$$

where α is the loss effectiveness factor $\alpha \in [0,1]$ and $f = \alpha F_d$ is the loss force of the damper.

Substituting (2.15) into (2.16), the faulty damper force F_d^f is as follows:

$$\begin{cases} F_d^f & = k_0(z_s - z_{us}) + c_0(\dot{z}_s - \dot{z}_{us}) + F_{er} - f \\ \dot{F}_{er} & = -\frac{1}{\tau}F_{er} + \frac{f_c}{\tau} \cdot u \cdot tanh(k_1(z_s - z_{us}) + c_1(\dot{z}_s - \dot{z}_{us})) \end{cases} \tag{2.17}$$

The system dynamics considering the actuator fault is then rewritten as follows:

$$\begin{cases} \ddot{z}_s & = -\frac{1}{m_s}\left[(k_s + k_0)(z_s - z_{us}) + c_0(\dot{z}_s - \dot{z}_{us}) + F_{er} - f\right] \\ \ddot{z}_{us} & = \frac{1}{m_{us}}[(k_s + k_0)(z_s - z_{us}) + c_0(\dot{z}_s - \dot{z}_{us}) + F_{er} - f - k_t(z_{us} - z_r)] \\ \dot{F}_{er} & = -\frac{1}{\tau}F_{er} + \frac{f_c}{\tau} \cdot u \cdot tanh(k_1(z_s - z_{us}) + c_1(\dot{z}_s - \dot{z}_{us})) \end{cases} \tag{2.18}$$

By selecting the system states as $x_e = [x_1, x_2, x_3, x_4, x_5, x_6]^T = [z_s - z_{us}, \dot{z}_s, z_{us} - z_r, \dot{z}_{us}, F_{er}, f]^T \in \mathbb{R}^6$ and the scheduling variable $\rho = u \in \mathbb{R}$ (Table 2.2), the system dynamics can be written in the following Nonlinear Lipschitz Descriptor system:

$$\begin{cases} E\dot{x_e} & = A_f x_e + B(\rho)\Phi(x_e) + D_1\omega_r \end{cases} \tag{2.19}$$

where $\Phi(x_e) = tanh(\Gamma_e x_e)$ with $\Gamma_e = \begin{bmatrix}\Gamma & 0\end{bmatrix}$.

$$E = \begin{bmatrix} 1 & 0 & 0 & 0 & 0 & 0 \\ 0 & 1 & 0 & 0 & 0 & 0 \\ 0 & 0 & 1 & 0 & 0 & 0 \\ 0 & 0 & 0 & 1 & 0 & 0 \\ 0 & 0 & 0 & 0 & 1 & 0 \end{bmatrix}, A_f = \begin{bmatrix} 0 & 1 & 0 & -1 & 0 & 0 \\ -\frac{(k_s+k_0)}{m_s} & -\frac{c_0}{m_s} & 0 & \frac{c_0}{m_s} & -\frac{1}{m_s} & \frac{1}{m_s} \\ 0 & 0 & 0 & 1 & 0 & 0 \\ \frac{(k_s+k_0)}{m_{us}} & \frac{c_0}{m_{us}} & -\frac{k_t}{m_{us}} & -\frac{c_0}{m_{us}} & \frac{1}{m_{us}} & -\frac{1}{m_{us}} \\ 0 & 0 & 0 & 0 & -\frac{1}{\tau} & 0 \end{bmatrix},$$

$$B(\rho) = \begin{bmatrix} 0 \\ 0 \\ 0 \\ 0 \\ \frac{f_c}{\tau}\rho \end{bmatrix}$$

2.3 Conclusions

This chapter introduced several representations of the system dynamics of the quarter car system equipped with the semi-active suspension system. A dynamic nonlinear suspension model made of a quarter-car vehicle model and augmented with a first-order dynamical nonlinear damper model captures the main behaviors of the ER dampers in an automotive application. For control design, the system dynamics is separated into LTI and qLPV subsystems. Besides, the dynamical equations are then written in the nonlinear Lipschitz system representation and NLPV forms, which are used to design the damper force estimation in part II of this thesis. Finally, the quarter vehicle model considering the actuator fault was presented in the nonlinear descriptor system to develop the fault observer in this thesis.

These models will be completed by output equations depending on the measurements. For instance, if we measure the 2 accelerations $y = [\ddot{z}_s, \ddot{z}_{us}]^T$, the nonlinear Lipschitz system (2.20) becomes

$$\begin{cases} \dot{x} &= Ax + B\Phi(x)u + D_1\omega_r \\ y &= Cx + D_2\omega_n \end{cases} \tag{2.20}$$

and the nonlinear parameter varying system (2.2.3) becomes

$$\begin{cases} \dot{x} &= Ax + B(\rho)\Phi(x) + \bar{D}_1\omega \\ y &= Cx + \bar{D}_2\omega \end{cases} \tag{2.21}$$

where ω_n is the sensor noise $\omega = \begin{pmatrix} \omega_r \\ \omega_n \end{pmatrix}$ and the system matrices $C = \begin{bmatrix} -\frac{(k_s+k_0)}{m_s} & -\frac{c_0}{m_s} & 0 & \frac{c_0}{m_s} & -\frac{1}{m_s} \\ \frac{(k_s+k_0)}{m_{us}} & \frac{c_0}{m_{us}} & -\frac{k_t}{m_{us}} & -\frac{c_0}{m_{us}} & \frac{1}{m_{us}} \end{bmatrix}$, D_2 is the weighting matrix associated to ω_n, in the form $D_2 = \beta I$, with $\beta \in \mathcal{R}^+$. In our application, β is turned through the experimental test $D_2 = \begin{bmatrix} 0.01 \\ 0.01 \end{bmatrix}$, $\bar{D}_1 = \begin{bmatrix} D_1 & 0 \end{bmatrix}$, $\bar{D}_2 = \begin{bmatrix} 0 & D_2 \end{bmatrix}$.

Part II

Some approaches for damper force estimation

Introduction

As previously mentioned in Chapter 1, the semi-active damper for automotive suspension systems is one of the critical components which improves safety and comfort for on-board passengers. One of the main issues in the studies of the controlled suspension system is the control design based on a reduced number of sensors. Therefore, there have been several control methods developed in the literature (see [Savaresi and Spelta 2008], [Tudon-Martinez et al. 2017], [Poussot-Vassal et al. 2008] and references therein). A review of suspension control approaches is presented in [Poussot-Vassal et al. 2012]. Some of them consider the damper force as the control input of the suspension system and then use an inverse model or look-up tables for implementation (see for instance [Poussot-Vassal et al. 2008], [Nguyen et al. 2015], [Fleps-Dezasse, Svaricek, and Brembeck 2018]). Others use an inner force tracking control scheme in order to attain control objectives ([Priyandoko, Mailah, and Jamaluddin 2009], [Aubouet 2010]). Therefore, the damper force signal is crucial for control (and also diagnosis) of suspension systems. However, as damper force sensors are expensive and difficult to install in practice, the real-time estimation of the damper force is of paramount importance for suspension control.

The key requirements for designing damper force observers are summarized as follows:

- The embedded algorithms should use classical low-cost on-board sensors (such as accelerometers).
- The estimation methods must take the dynamic behavior of damper into account.
- The scheme should be able to deal with the bi viscous nonlinearity in the semi-active damper model.
- The observer should handle sensor noises and unknown road profile disturbances effectively.

To tackle the above requirements, LMI-based observers for Lipschitz nonlinear systems are attractive since the nonlinearity in the ER model satisfies the Lipschitz condition. Therefore, in this part, we propose three observers for nonlinear Lipschitz systems, and these new methods are developed and applied to estimate the damping force of an Electro-Rheological (ER) damper in an automotive suspension system.

Related works

Concerning the damper force estimation, some contributions have been proposed in the literature as follows:

- The work by [Koch, Kloiber, and Lohmann 2010] uses the Kalman filters to estimate the damper force but ignores the dynamic characteristic of the semi-active damper. Based

on the linear model, [Savaresi et al. 2019] proposed a damping estimation procedure using the inertial measurements. In order to consider the dynamical characteristics of the damper, [Estrada-Vela et al. 2018] proposed an H_∞ damping force observer based on a dynamic nonlinear model of the ER damper, while three sensors are required as inputs of the observer. To handle the nonlinearity while considering the dynamic characteristic of MR damper, an LPV-H_∞ based approach is introduced in [Tudon-Martinez et al. 2018] using deflection and deflection velocity data (which are costly and not common sensors) to compute the scheduling parameter.

The author has proposed several works in that context:

1. Based on the dynamic nonlinear model of the damper, [Pham et al. 2018] and [Pham, Sename, and Dugard 2019b] proposed H_2 and H_∞ damping force observers based on a dynamic nonlinear model of the ER damper. The first method is designed considering the nonlinearity as an unknown input and minimizing the effect of the unknown input disturbances (including a nonlinearity term, the measurement noise and the unknown road profile) on the estimation errors by using an H_2 criterion. The latter method aims at minimizing only the effects of measurement noises and road profiles on the state variable estimation errors by using a H_∞ criterion, while the nonlinearity is bounded through a Lipschitz condition. Besides, the comparative study of the robust observers for automotive damper force estimation is also presented by the author in [Pham, Sename, and Dugard 2019a]. These observers will not be presented in this thesis.

2. [Pham, Sename, and Dugard 2019d] proposed a unified H_∞ observer using two accelerometers to estimate the damper force in the semi-active suspension system. The objectives are to decouple the effects of unknown road profile disturbances and to minimize the effects of measurement noises on the estimation errors of the state variables by using $\mathcal{H}_\infty$ criterion while the nonlinearity is bounded through a Lipschitz condition. This observer will be presented in this chapter 3.

3. To handle the variations of the damper force amplification function of the voltage input, an NLPV observer in [Pham, Sename, and Dugard 2019c] is proposed here where the observer gain depends on the voltage control input u. The method considers two accelerometers (sprung mass and unsprung mass accelerations) as the observer inputs. The design of the observer is based on a nonlinear suspension model made of a quarter-car vehicle model, augmented with a first-order dynamical nonlinear damper model, which captures the main behavior of the ER dampers in an automotive application. It is worth noting that the damper nonlinearity is multiplied by the control input u; therefore, the latter will be considered as a scheduling parameter. Then two NLPV observers are developed, bounding the nonlinearity by a Lipschitz condition and minimizing the effect of unknown input disturbances (road profile derivative and measurement noises) on the estimation errors via the $\mathcal{H}_\infty$ framework. The NLPV observers will be proposed in the chapter 4.

The considered problem is to estimate the damper force F_d. Following the modelling step

presented in chapter 2, the estimated force $\hat{F}_d$ is then defined as

$$\hat{F}_d = k_0\hat{x}_1 + c_0(\hat{x}_2 - \hat{x}_4) + \hat{x}_5 \tag{2.22}$$

where $\hat{x}$ is the estimated states of the states x, with $x = [z_s - z_{us}, \dot{z}_s, z_{us} - z_r, \dot{z}_{us}, F_{er}]^T \in \mathbb{R}^5$.

Chapter 3

Unified $\mathcal{H}_\infty$ Observer for a Class of Nonlinear Lipschitz Systems

Contents

This chapter presents an extension of the synthesis of a unified $\mathcal{H}_\infty$ observer proposed in [Gao et al. 2016] for a specific class of nonlinear systems. The objectives are to decouple the effects of bounded unknown input disturbances and to minimize the effects of measurement noises on the estimation errors of the state variables by using an $\mathcal{H}_\infty$ criterion, while the nonlinearity satisfies Lipschitz condition. This new method is developed to estimate the damping force of an Electro-Rheological (ER) damper in an automotive suspension system; it has been implemented on the INOVE testbench from GIPSA-lab (1/5-scaled real vehicle) for real-time performance assessment. Both simulation and experimental results demonstrate

the effectiveness of the proposed observer to estimate the damper force in real-time, face to measurement noises and road disturbances.

The application of the unified $\mathcal{H}_\infty$ to estimate the damper force in the semi-active suspension system has been presented in the following journal publications [Pham, Sename, and Dugard 2019d] :

- *Pham, T.P., Sename, O., and Dugard, L. (2019). Unified H_∞ observer for a class of nonlinear Lipschitz systems: application to a real ER automotive suspension. IEEE Control Systems Letters, 3(4), 817-822. The contents of this paper have been presented at 58th IEEE Conference on Decision and Control (IEEE CDC 2019).*

3.1 Introduction

As mentioned in the introduction section of Part II, the observer for the nonlinear Lipschitz system is a potential candidate for the damper force estimation. Concerning the observer design for the nonlinear Lipschitz system, there have been several theoretical research contributions for observer design of Lipschitz nonlinear systems (see [Rajamani 1998; Zemouche and Boutayeb 2013; Pertew, Marquez, and Zhao 2006; Darouach, Boutat-Baddas, and Zerrougui 2011; Koenig 2006]) over the last decade. The above-mentioned methodologies are broadly classified into a) Proportional Observers (PO) and b) Proportional-Integral Observers (PIO). More recently, this has been extended to propose a unified form of the dynamic observer for linear systems in [Gao et al. 2016], for LPV systems in [Pérez-Estrada et al. 2018b], for Lipschitz systems in the absence of unknown inputs in [Gao, Darouach, and Alma 2018] and for nonlinear descriptor system in [Osorio-Gordillo et al. 2019].

In this chapter, we aim first to extend the unified observer given in [Gao et al. 2016] to Lipschitz systems in the presence of sensor noises and unknown input disturbances. Then this observer is developed in order to estimate the damper force of an ER damper in automotive suspension, using two accelerometers only. The two major contributions of this chapter are then the following:

- A unified $\mathcal{H}_\infty$ observer for Lipchitz nonlinear systems in the presence of unknown disturbances and measurement noises is developed minimizing, in an $\mathcal{L}_2$-induced gain objective, the effect of sensor noises and decoupling unknown disturbances.

- The proposed observer has been implemented on a real scaled-vehicle test bench, through Matlab/Simulink Real-Time Workshop. The observer performances are then assessed with experimental tests.

3.2 Unified $\mathcal{H}_\infty$ observer definition

3.2.1 Unified $\mathcal{H}_\infty$ observer definition

Let us first recall the considered nonlinear Lipschitz system of a quarter car model, as seen in Chapter 2:

$$\begin{cases} \dot{x} &= Ax + B\Phi(x)u + D_1\omega_r \\ y &= Cx + D_2\omega_n \end{cases} \tag{3.1}$$

where the nonlinearity $\Phi(x)$ is globally Lipschitz in x, i.e.: $\forall x, \hat{x} \in \mathbb{R}^n$

$$\|\Phi(x) - \Phi(\hat{x})\| \leqslant \gamma_l \|(x - \hat{x})\|, \forall x, \hat{x}, \tag{3.2}$$

where γ_l is called the Lipschitz constant, which, according to [Zemouche and Boutayeb 2013; Phanomchoeng and Rajamani 2010], is rewritten here as (with Γ a constant matrix)

$$\|\Phi(x) - \Phi(\hat{x})\| \leqslant \|\Gamma(x - \hat{x})\|, \forall x, \hat{x}. \tag{3.3}$$

Assumptions A1: the control input is bounded $|u| \leqslant U$. Notice that the value of U is 1 ($U = 1$) in this work since the control input signal u is the duty cycle of PWM signal.

The considered full-order unified H_∞ observer is given by

$$\begin{cases} \dot{z} = Nz + Jy + H\Phi(\hat{x})u + Mv \\ \dot{v} = Pz + Qy + Gv \\ \hat{x} = Rz + Sy \end{cases} \tag{3.4}$$

where $z \in \mathbb{R}^n$ is the state vector of the observer, $v \in \mathbb{R}^n$ is an auxiliary vector, $\hat{x} \in \mathbb{R}^n$ represents the estimated state vector. The observer matrices $N, J, H, M, P, Q, G, R, S$ (of appropriate dimensions) have to be designed.

Remark 3.2.1.

- *For $M = 0$ (or $P = 0$, $Q = 0$ and $G = 0$), the unified observer of the form (3.4) becomes the following PO*

$$\begin{cases} \dot{z} = Nz + Jy + H\Phi(\hat{x})u \\ \hat{x} = Rz + Sy \end{cases} \tag{3.5}$$

- *For $M = -CR$, $Q = I - CS$ and $G = 0$, from the unified observer(3.4), we obtain the following PIO*

$$\begin{cases} \dot{z} = Nz + Jy + H\Phi(\hat{x})u + Mv \\ \dot{v} = y - C\hat{x} \\ \hat{x} = Rz + Sy \end{cases} \tag{3.6}$$

3.2.2 Dynamic estimation error

First, let define the dynamic error ϵ as

$$\epsilon = z - Tx, \tag{3.7}$$

where the matrix $T \in \mathbb{R}^{n\times n}$ is an arbitrary matrix.

The following lemma gives the existence conditions of the unified observer (3.4) for system (3.1) under the assumptions $\omega_n = 0$ and A1.

Lemma 3.2.1. *For $\omega_n = 0$ and assumption A1, there exists the observer of the form (3.4) for the system (3.1) if the following two statements hold*

1. *There exists a matrix T such that the following conditions are satisfied*

$$NT - TA + JC = 0 \tag{3.8}$$
$$TD_1 = 0 \tag{3.9}$$
$$H - TB = 0 \tag{3.10}$$
$$PT + QC = 0 \tag{3.11}$$
$$RT + SC = I \tag{3.12}$$

2. *The system $\dot{\zeta} = \begin{pmatrix} N & M \\ P & G \end{pmatrix}\zeta - \begin{pmatrix} TB \\ 0 \end{pmatrix}\Delta\Phi \cdot u$ is asymptotically stable, where $\zeta \in \mathbb{R}^{2n}$ and $\Delta\Phi = \Phi(x) - \Phi(\hat{x})$.*

Proof. Differentiating (3.7) with respect to time and using (3.1) and (3.4), leads to:

$$\begin{cases} \dot{\epsilon} &= N\epsilon + (NT - TA + JC)x - TD_1\omega_r + JD_2\omega_n \\ &\quad +(H - TB)\Phi(\hat{x})u - TB(\Phi(x) - \Phi(\hat{x}))u + Mv \\ \dot{v} &= P\epsilon + (PT + QC)x + QD_2\omega_n + Gv \\ \hat{x} &= R\epsilon + (RT + SC)x + SD_2\omega_n. \end{cases} \tag{3.13}$$

Denoting $\zeta = \begin{pmatrix} \epsilon \\ v \end{pmatrix}$, the equations (3.13) can be rewritten as

$$\begin{cases} \dot{\zeta} &= \begin{pmatrix} N & M \\ P & G \end{pmatrix}\zeta + \begin{pmatrix} NT - TA + JC \\ PT + QC \end{pmatrix}x + \begin{pmatrix} TD_1 \\ 0 \end{pmatrix}\omega_r \\ &\quad + \begin{pmatrix} H - TB \\ 0 \end{pmatrix}\Phi(\hat{x})u - \begin{pmatrix} TB \\ 0 \end{pmatrix}\Delta\Phi \cdot u + \begin{pmatrix} JD_2 \\ QD_2 \end{pmatrix}\omega_n \\ \hat{x} &= \begin{pmatrix} R & 0 \end{pmatrix}\zeta + (RT + SC)x + SD_2\omega_n \end{cases} \tag{3.14}$$

where $\Delta\Phi = \Phi(x) - \Phi(\hat{x})$.

Let consider that the following decoupling conditions are satisfied:

$$NT - TA + JC = 0 \tag{3.15}$$
$$TD_1 = 0 \tag{3.16}$$
$$H - TB = 0 \tag{3.17}$$
$$PT + QC = 0 \tag{3.18}$$
$$RT + SC = I \tag{3.19}$$

then the system (3.14) becomes

$$\begin{cases} \dot{\zeta} &= \begin{pmatrix} N & M \\ P & G \end{pmatrix} \zeta - \begin{pmatrix} TB \\ 0 \end{pmatrix} \Delta\Phi \cdot u + \begin{pmatrix} JD_2 \\ QD_2 \end{pmatrix} \omega_n \\ e &= \begin{pmatrix} R & 0 \end{pmatrix} \zeta + SD_2\omega_n \end{cases} \tag{3.20}$$

where $e = \hat{x} - x$ is the state estimation error.

In the case if $\omega_n = 0$, the system (3.20) becomes

$$\dot{\zeta} = \begin{pmatrix} N & M \\ P & G \end{pmatrix} \zeta - \begin{pmatrix} TB \\ 0 \end{pmatrix} \Delta\Phi \cdot u \tag{3.21}$$

$$e = \begin{pmatrix} R & 0 \end{pmatrix} \zeta \tag{3.22}$$

in this case if the system (3.21) stable, then $\lim_{t\to\infty} \zeta(t) = 0$ and $\lim_{t\to\infty} e(t) = 0$, the lemma is proven. □

The problem of the unified $\mathcal{H}_\infty$ observer design reduces to determine the observer matrices N, J, H, M, P, Q, G, R, S such that all conditions (3.8)-(3.12) are satisfied and such that the system (3.20) is stable for $\omega_n = 0$, and for $\omega_n \neq 0$ the effect of measurement noise ω_n on the state estimation error e is minimized while $\Delta\Phi \cdot u$ is bounded.

In the next sections, the parameterisation follows the same steps as [Gao et al. 2016], presented in Subsection 3.2.3. Then we propose a theorem to solve the unified observer design problem presented in Section 3.3. Notice that the proof of the theorem uses the $S-$procedure and differs from the methods presented in [Gao et al. 2016] and [Darouach, Boutat-Baddas, and Zerrougui 2011].

3.2.3 Parameterization of the observer matrices

In order to determine the observer matrices N, J, H, M, P, Q, G, R, S of the proposed observer satisfying all the conditions equalities (3.8)-(3.12), a parameterisation is made by using the general solution of (3.8)-(3.12) as explained in [Gao et al. 2016].

Firstly, from equations (3.11) and (3.12), one obtains

$$\begin{pmatrix} P & Q \\ R & S \end{pmatrix} \begin{pmatrix} T \\ C \end{pmatrix} = \begin{pmatrix} 0 \\ I \end{pmatrix}. \tag{3.23}$$

The equation (3.23) is solvable if and only if

$$rank \begin{pmatrix} T \\ C \\ 0 \\ I \end{pmatrix} = rank \begin{pmatrix} T \\ C \end{pmatrix} = n. \tag{3.24}$$

Next, let matrix $E \in \mathbb{R}^{n\times n}$ be an arbitrary matrix of full row rank such that:

$$rank \begin{pmatrix} E \\ C \end{pmatrix} = rank \begin{pmatrix} T \\ C \end{pmatrix} = n. \tag{3.25}$$

Then there always exists a parameter matrix K such that:

$$\begin{pmatrix} T \\ C \end{pmatrix} = \begin{pmatrix} I & -K \\ 0 & I \end{pmatrix} \begin{pmatrix} E \\ C \end{pmatrix} \Leftrightarrow T = E - KC. \tag{3.26}$$

Consequently, equation (3.23) becomes:

$$\begin{pmatrix} P & Q \\ R & S \end{pmatrix} \begin{pmatrix} I & -K \\ 0 & I \end{pmatrix} \begin{pmatrix} E \\ C \end{pmatrix} = \begin{pmatrix} 0 \\ I \end{pmatrix}. \tag{3.27}$$

and there exists an exact solution set fulfilling (3.27), in the form of

$$\begin{pmatrix} P & Q \\ R & S \end{pmatrix} = \left[\begin{pmatrix} 0 \\ I \end{pmatrix} \Sigma^+ - Y_m \left(I - \Sigma\Sigma^+ \right) \right] \begin{pmatrix} I & K \\ 0 & I \end{pmatrix}, \tag{3.28}$$

where $\Sigma = \begin{pmatrix} E \\ C \end{pmatrix}$, Σ^+ is any general inverse of matrix Σ satisfying $\Sigma\Sigma^+\Sigma = \Sigma$, Y_m is a free matrix of appropriate dimension. This is equivalent to:

$$P = -Y_{m1}\beta_1,\ Q = -Y_{m1}\beta_2, \tag{3.29}$$

$$R = \alpha_1 - Y_{m2}\beta_1,\ S = \alpha_2 - Y_{m2}\beta_2, \tag{3.30}$$

with

$$\begin{aligned} &Y_{m1} = \begin{pmatrix} I & 0 \end{pmatrix} Y_m, \quad Y_{m2} = \begin{pmatrix} 0 & I \end{pmatrix} Y_m, \quad \alpha_1 = \Sigma^+ \begin{pmatrix} I \\ 0 \end{pmatrix}, \\ &\alpha_2 = \Sigma^+ \begin{pmatrix} K \\ I \end{pmatrix}, \quad \beta_1 = \left(I - \Sigma\Sigma^+ \right) \begin{pmatrix} I \\ 0 \end{pmatrix}, \quad \beta_2 = \left(I - \Sigma\Sigma^+ \right) \begin{pmatrix} K \\ I \end{pmatrix}. \end{aligned} \tag{3.31}$$

Besides, from the equations (3.9) and (3.26), one obtains

$$KCD_1 = ED_1, \tag{3.32}$$

which can be solved if and only if

$$rank \begin{pmatrix} ED_1 \\ CD_1 \end{pmatrix} = rank \left[\begin{pmatrix} E \\ C \end{pmatrix} D_1 \right] = rankD_1 = rankCD_1. \tag{3.33}$$

There exists one solution of (3.32), given as follows:

$$K = ED_1(CD_1)^+. \tag{3.34}$$

From the condition (3.10), one obtains

$$H = TB = (E - KC)B = (E - ED_1(CD_1)^+C)B. \tag{3.35}$$

On the other hand, substituting (3.26) into the decoupling condition (3.8), one obtains

$$\begin{aligned} &N(E - KC) - (E - KC)A + JC = 0 \\ \Leftrightarrow &\begin{pmatrix} N & J - NK \end{pmatrix} \Sigma = (E - ED_1(CD_1)^+C)A, \end{aligned} \tag{3.36}$$

which can also be parameterized as

$$\begin{pmatrix} N & K_1 \end{pmatrix} \Sigma = \Theta, \tag{3.37}$$

where

$$K_1 = J - NK, \tag{3.38}$$

$$\Theta = (E - ED_1(CD_1)^+C)A. \tag{3.39}$$

and the solution set of (3.37) is given by

$$\begin{pmatrix} N & K_1 \end{pmatrix} = \Theta\Sigma^+ - Y_{m3}(I - \Sigma\Sigma^+), \tag{3.40}$$

which is equivalent to

$$N = \alpha_3 - Y_{m3}\beta_1, \tag{3.41}$$

$$K_1 = \alpha_4 - Y_{m3}\beta_3, \tag{3.42}$$

where Y_{m3} is a free matrix of appropriate dimension and

$$\alpha_3 = \Theta\Sigma^+ \begin{pmatrix} I \\ 0 \end{pmatrix}, \alpha_4 = \Theta\Sigma^+ \begin{pmatrix} 0 \\ I \end{pmatrix}, \beta_3 = (I - \Sigma\Sigma^+) \begin{pmatrix} 0 \\ I \end{pmatrix}. \tag{3.43}$$

Remark 3.2.2. *If the matrices P, Q, R, S, H, N, J can be chosen according to (3.29), (3.35), (3.41), and (3.38), respectively, then, all the conditions (3.8)-(3.12) are fulfilled.*

As already mentioned above, since the conditions (3.8)-(3.12) are satisfied, the system (3.14) is rewritten as follows:

$$\begin{cases} \dot{\zeta} &= \begin{pmatrix} N & M \\ P & G \end{pmatrix} \zeta - \begin{pmatrix} TB \\ 0 \end{pmatrix} \Delta\Phi \cdot u + \begin{pmatrix} JD_2 \\ QD_2 \end{pmatrix} \omega_n \\ e &= \begin{pmatrix} R & 0 \end{pmatrix} \zeta + SD_2\omega_n. \end{cases} \tag{3.44}$$

From the results of above parameterization, the matrices of system (3.44) can be rewritten as follows:

$$\mathbb{A}_1 = \begin{pmatrix} N & M \\ P & G \end{pmatrix} = A_{11} - ZA_{12}, \tag{3.45}$$

$$\mathbb{B}_1 = \begin{pmatrix} JD_2 \\ QD_2 \end{pmatrix} = B_{11} - ZB_{12}, \tag{3.46}$$

where

$$A_{11} = \begin{pmatrix} \alpha_3 & 0 \\ 0 & 0 \end{pmatrix}, Z = \begin{pmatrix} Y_{m3} & M \\ Y_{m1} & G \end{pmatrix}, A_{12} = \begin{pmatrix} \beta_1 & 0 \\ 0 & -I \end{pmatrix},$$
$$B_{11} = \begin{pmatrix} \Theta\Sigma^+ \begin{pmatrix} K \\ I_p \end{pmatrix} D_2 \\ 0 \end{pmatrix}, B_{12} = \begin{pmatrix} \beta_2 D_2 \\ 0 \end{pmatrix}. \tag{3.47}$$

Note that the state estimation error $e \to 0$ when $\zeta \to 0$. Since Y_{m2} is a free matrix, it is fixed to $Y_{m2} = 0$ and we obtain $R = \alpha_1$ and $S = \alpha_2$. Then the following matrices are obtained

$$\mathbb{C}_1 = \begin{pmatrix} R & 0 \end{pmatrix} = \begin{pmatrix} \alpha_1 & 0 \end{pmatrix}, \tag{3.48}$$
$$\mathbb{D}_1 = SD_2 = \alpha_2 D_2. \tag{3.49}$$

Besides, let denote

$$\mathbb{W}_1 = \begin{pmatrix} -TB \\ 0 \end{pmatrix}. \tag{3.50}$$

Notice that all the matrices A_{11}, A_{12}, B_{11}, B_{12}, $\mathbb{W}_1$, $\mathbb{C}_1$, $\mathbb{D}_1$ are known.

3.3 Unified $\mathcal{H}_\infty$ Observer design

3.3.1 Problem formulation

Using the set of definitions (3.45)-(3.50), the estimation error dynamic system (3.44) is rewritten as:

$$\begin{cases} \dot{\zeta} &= \mathbb{A}_1\zeta + \mathbb{W}_1\Delta\Phi \cdot u + \mathbb{B}_1\omega_n \\ e &= \mathbb{C}_1\zeta + \mathbb{D}_1\omega_n. \end{cases} \tag{3.51}$$

Assuming that $\Phi(x)$ satisfies the Lipschitz condition (3.3), the unified $\mathcal{H}_\infty$ observer design problem is to determine the matrix Z such that:

- The system (3.51) is asymptotically stable for $\omega_n(t) = 0$.
- $\|e(t)\|_{\mathcal{L}_2} < \gamma\|\omega_n(t)\|_{\mathcal{L}_2}$ for $\omega_n(t) \neq 0$.

3.3.2 Observer design

The following theorem gives a sufficient condition to solve the above problem presented in subsection 3.3.1 into an LMI framework.

Theorem 3.3.1. *Consider the system model (3.1) and the observer (3.4). Given positive scalars γ and ϵ_l, the above design problem is solved if there exist a symmetric positive definite matrix X and a matrix Y satisfying*

$$\begin{bmatrix} \Omega_{11} & \Omega_{12} & \Omega_{13} \\ \Omega_{12}^T & -\epsilon_l I & 0 \\ \Omega_{13}^T & 0 & \epsilon_l U^T \mathbb{D}_1^T \Gamma^T \Gamma \mathbb{D}_1 U + \mathbb{D}_1^T \mathbb{D}_1 - \gamma^2 I \end{bmatrix} < 0 \tag{3.52}$$

where

$$\begin{aligned} \Omega_{11} &= A_{11}^T X - A_{12}^T Y^T + X A_{11} - Y A_{12} \\ &\quad + \epsilon_l U^T \mathbb{C}_1^T \Gamma^T \Gamma \mathbb{C}_1 U + \mathbb{C}_1^T \mathbb{C}_1, \\ \Omega_{12} &= X \mathbb{W}_1, \\ \Omega_{13} &= X B_{11} - Y B_{12} + \epsilon_l U^T \mathbb{C}_1^T \Gamma^T \Gamma \mathbb{D}_1 U + \mathbb{C}_1^T \mathbb{D}_1, \end{aligned}$$

the matrix Z is then deduced as $Z = X^{-1}Y$.

Proof. Consider the following Lyapunov function candidate

$$V(\cdot) = \zeta(\cdot)^T X \zeta(\cdot). \tag{3.53}$$

Differentiating $V(\cdot)$ along the solution of (3.51) yields

$$\begin{aligned} \dot{V}(\cdot) &= \dot{\zeta}(\cdot)^T X \zeta(\cdot) + \zeta(\cdot)^T X \dot{\zeta}(\cdot) && (3.54) \\ &= [\mathbb{A}_1 \zeta + \mathbb{W}_1 \Delta\Phi \cdot u + \mathbb{B}_1 \omega_n]^T X \zeta + \zeta^T X [\mathbb{A}_1 \zeta + \mathbb{W}_1 \Delta\Phi \cdot u + \mathbb{B}_1 \omega_n] \\ &= \begin{bmatrix} \zeta \\ (\Delta\Phi \cdot u) \\ \omega_n \end{bmatrix}^T \begin{bmatrix} \mathbb{A}_1^T X + X \mathbb{A}_1 & X \mathbb{W}_1 & P \mathbb{B}_1 \\ \mathbb{W}_1^T X & 0 & 0 \\ \mathbb{B}_1^T X & 0 & 0 \end{bmatrix} \begin{bmatrix} \zeta \\ \Delta\Phi \cdot u \\ \omega_n \end{bmatrix}. && (3.55) \end{aligned}$$

Define $\eta = \begin{bmatrix} \zeta \\ \Delta\Phi \cdot u \\ \omega_n \end{bmatrix}$, then one obtains

$$\dot{V} = \eta^T \mathbb{Q}_1 \eta, \tag{3.56}$$

where $\mathbb{Q}_1 = \begin{bmatrix} \mathbb{A}_1^T X + X \mathbb{A}_1 & X \mathbb{W}_1 & X \mathbb{B}_1 \\ \mathbb{W}_1^T X & 0 & 0 \\ \mathbb{B}_1^T X & 0 & 0 \end{bmatrix}$.

From the Lipschitz condition (3.3), the following condition is obtained

$$\Delta\Phi^T \Delta\Phi \leqslant e^T \Gamma^T \Gamma e. \tag{3.57}$$

From assumption A1, the inequality (3.57) implies

$$\begin{aligned}
&(\Delta\Phi\cdot u)^T\Delta\Phi\cdot u \leqslant U^T(\mathbb{C}_1\zeta+\mathbb{D}_1\omega_n)^T\Gamma^T\Gamma(\mathbb{C}_1\zeta+\mathbb{D}_1\omega_n)U\\
\Leftrightarrow&\begin{bmatrix}\zeta\\(\Delta\Phi\cdot u)\\\omega_n\end{bmatrix}^T\begin{bmatrix}-U^T\mathbb{C}_1^T\Gamma^T\Gamma\mathbb{C}_1U & 0 & -U^T\mathbb{C}_1^T\Gamma^T\Gamma\mathbb{D}_1U\\ 0 & I & 0\\ -U^T\mathbb{D}_1^T\Gamma^T\Gamma\mathbb{C}_1U & 0 & -U^T\mathbb{D}_1^T\Gamma^T\Gamma\mathbb{D}_1U\end{bmatrix}\begin{bmatrix}\zeta\\\Delta\Phi\cdot u\\\omega_n\end{bmatrix}\leqslant 0\\
\Leftrightarrow&\eta^T\mathbb{Q}_2\eta\leqslant 0,
\end{aligned}\tag{3.58}$$

where $\mathbb{Q}_2=\begin{bmatrix}-U^T\mathbb{C}_1^T\Gamma^T\Gamma\mathbb{C}_1U & 0 & -U^T\mathbb{C}_1^T\Gamma^T\Gamma\mathbb{D}_1U\\ 0 & I & 0\\ -U^T\mathbb{D}_1^T\Gamma^T\Gamma\mathbb{C}_1U & 0 & -U^T\mathbb{D}_1^T\Gamma^T\Gamma\mathbb{D}_1U\end{bmatrix}$.

In order to satisfy the performance objective w.r.t. the $\mathcal{L}_2$ gain disturbance attenuation, the $\mathcal{H}_\infty$ performance index is defined as:

$$\begin{aligned}
\mathcal{J}&=e^Te-\gamma^2\omega_n^T\omega_n\\
&=(\mathbb{C}_1\zeta+\mathbb{D}_1\omega_n)^T(\mathbb{C}_1\zeta+\mathbb{D}_1\omega_n)-\gamma^2\omega_n^T\omega_n\\
&=\begin{bmatrix}\zeta\\(\Delta\Phi\cdot u)\\\omega_n\end{bmatrix}^T\begin{bmatrix}\mathbb{C}_1^T\mathbb{C}_1 & 0 & \mathbb{C}_1^T\mathbb{D}_1\\ 0 & 0 & 0\\ \mathbb{D}_1^T\mathbb{C}_1 & 0 & \mathbb{D}_1^T\mathbb{D}_1-\gamma^2I\end{bmatrix}\begin{bmatrix}\zeta\\\Delta\Phi\cdot u\\\omega_n\end{bmatrix}\\
&=\eta^T\mathbb{Q}_3\eta,
\end{aligned}\tag{3.59}$$

where $\mathbb{Q}_3=\begin{bmatrix}\mathbb{C}_1^T\mathbb{C}_1 & 0 & \mathbb{C}_1^T\mathbb{D}_1\\ 0 & 0 & 0\\ \mathbb{D}_1^T\mathbb{C}_1 & 0 & \mathbb{D}_1^T\mathbb{D}_1-\gamma^2I\end{bmatrix}$.

Now, by applying the $\mathcal{S}$-procedure [Boyd et al. 1994] to both contraints (3.57) and $\mathcal{J}\geqslant 0$, then $\dot{V}<0$ if there exist scalars $\epsilon_l>0$ and $\epsilon_n>0$ such that

$$\dot{V}-\epsilon_l(\eta^T\mathbb{Q}_2\eta)+\epsilon_n\mathcal{J}<0.\tag{3.60}$$

In order to solve the design problem, we need to consider the inequality $\dot{V}+\underbrace{e^Te-\gamma^2\omega_n^T\omega_n}_{\mathcal{J}}<0$.

Therefore, we will choose $\epsilon_n=1$. Now, (3.60) becomes

$$\begin{aligned}
&\eta^T(\mathbb{Q}_1-\epsilon_l\mathbb{Q}_2+\mathbb{Q}_3)\eta<0\\
\Leftrightarrow&\begin{bmatrix}M_{11} & M_{12} & M_{13}\\ M_{12}^T & -\epsilon_lI & 0\\ M_{13}^T & 0 & \epsilon_lU^T\mathbb{D}_1^T\Gamma^T\Gamma\mathbb{D}_1U+\mathbb{D}_1^T\mathbb{D}_1-\gamma^2I\end{bmatrix}<0
\end{aligned}\tag{3.61}$$

where $M_{11}=(A_{11}-ZA_{12})^TX+X(A_{11}-ZA_{12})+\epsilon_lU^T\mathbb{C}_1^T\Gamma^T\Gamma\mathbb{C}_1U+\mathbb{C}_1^T\mathbb{C}_1$, $M_{12}=X\mathbb{W}_1$, $M_{13}=X(B_{11}-ZB_{12})+\epsilon_lU^T\mathbb{C}_1^T\Gamma^T\Gamma\mathbb{D}_1U+\mathbb{C}_1^T\mathbb{D}_1$.

Let define $Y=XZ$ and substitute into (4.23), the LMI (3.52) is obtained.

If (3.52) is satisfied, from (3.58), (3.60) implies that

$$\begin{aligned} &\dot{V} + \mathcal{J} < 0 \\ \Leftrightarrow &\dot{V} < \gamma^2 \omega_n^T \omega_n - e^T e \end{aligned} \tag{3.62}$$

By integrating the both sides of (3.62), one obtains

$$\begin{aligned} &\int_0^\infty \dot{V}(\tau) d\tau < \int_0^\infty \gamma^2 \omega_n(\tau)^T \omega_n(\tau) d\tau - \int_0^\infty e(\tau)^T e(\tau) d\tau \\ \Leftrightarrow &V(\infty) - V(0) < \gamma^2 \|\omega_n(t)\|_{\mathcal{L}_2}^2 - \|e(t)\|_{\mathcal{L}_2}^2. \end{aligned} \tag{3.63}$$

Under zero initial conditions, (3.63) becomes

$$V(\infty) < \gamma^2 \|\omega_n(t)\|_{\mathcal{L}_2}^2 - \|e(t)\|_{\mathcal{L}_2}^2 \tag{3.64}$$

which leads to

$$\|e(t)\|_{\mathcal{L}_2}^2 < \gamma^2 \|\omega_n(t)\|_{\mathcal{L}_2}^2. \tag{3.65}$$

The proof of Theorem 3.3.1 is completed. □

Remark 3.3.1. *If the matrices M, P, and Q are chosen null in the observer equations (3.4), the observer reduces, in that case, to a P observer. Therefore, LMI (3.52) can be rewritten in the following inequality:*

$$\mathfrak{Q} + \mathfrak{B} Y \mathfrak{C} + (\mathfrak{B} Y \mathfrak{C})^T < 0 \tag{3.66}$$

where

$$\mathfrak{Q} = \begin{bmatrix} \mathfrak{Q}_{11} & \mathfrak{Q}_{12} & \mathfrak{Q}_{13} \\ \mathfrak{Q}_{12}^T & -\epsilon_l I & 0 \\ \mathfrak{Q}_{13}^T & 0 & \epsilon_l U^T \mathbb{D}_1^T \Gamma^T \Gamma \mathbb{D}_1 U + \mathbb{D}_1^T \mathbb{D}_1 - \gamma^2 I \end{bmatrix}$$

$$\mathfrak{Q}_{11} = A_{11}^T X + X A_{11} + \epsilon_l U^T \mathbb{C}_1^T \Gamma^T \Gamma \mathbb{C}_1 U + \mathbb{C}_1^T \mathbb{C}_1$$

$$\mathfrak{Q}_{12} = X \mathbb{W}_1,\ \mathfrak{Q}_{13} = X B_{11} + \epsilon_l U^T \mathbb{C}_1^T \Gamma^T \Gamma \mathbb{D}_1 U + \mathbb{C}_1^T \mathbb{D}_1,\ \mathfrak{B} = \begin{bmatrix} -I \\ 0 \\ 0 \end{bmatrix}, \mathfrak{C} = \begin{bmatrix} A_{12} & 0 & B_{12} \end{bmatrix}.$$

Then, the Theorem 2.3.12 (consider as a projection lemma) in [Skelton, Iwasaki, and Grigoriadis 1997] can be applied to find a general solution for the inequality (3.66). Refer to [Gao et al. 2016] for more details.

3.3.3 Design procedure

The procedure to design the unified $\mathcal{H}_\infty$ observer can be summarized as follows:

Algorithm 1: the unified $\mathcal{H}_\infty$ observer design

Input: The system matrices A, B, C, D_1, D_2

Output: The observer matrices N, J, H, M, P, Q, G, R, S

1 Check the rank condition (3.33),
- If $rank(D_1) = rank(CD_1)$, continue step 2.
- If $rank(D_1) \neq rank(CD_1)$, stop.

2 Choose the full rank matrix $E \in \mathbb{R}^{n\times n}$ according to the condition (3.25), i.e.

$$rank \begin{pmatrix} E \\ C \end{pmatrix} = n$$

.

3 Compute matrices K, T, Θ according to the equations (3.34), (3.26). (3.39)

4 Compute the matrices α_1, α_2, α_3, α_4, β_1, β_2, β_3 as explained in equations (3.31) and (3.43).

5 Calculate the matrices A_{11}, A_{12}, B_{11}, B_{12}, $\mathbb{W}_1$, $\mathbb{C}_1$, $\mathbb{D}_1$ according to the equations (3.47)-(3.50).

6 Solve the LMI (3.52) to find the solution X, Y, γ, ϵ_l.

7 Use X and Y in step 6 to get the matrix Z following Theorem 3.3.1.

8 Determine the observer matrices (N, J, H, M, P, Q, G, R, S) by using the matrix Z obtained in step 7.

Remark 3.3.2. *In this chapter, the control input is assuming that $|u| \leqslant U$. The unified H_∞ observer design steps based on the value of U. Note that this assumption may be relaxed as briefly explained below.*

Let us first recall the considered nonlinear Lipschitz system in this chapter (3.1) as follows:

$$\begin{cases} \dot{x} &= Ax + B\Phi(x)u + D_1\omega_r \\ y &= Cx + D_2\omega_n \end{cases} \tag{3.67}$$

By choosing the scheduling parameter $\rho = u$, the nonlinear Lipschitz system is rewritten as follows:

$$\begin{cases} \dot{x} &= Ax + B(\rho)\Phi(x) + D_1\omega_r \\ y &= Cx + D_2\omega_n \end{cases} \tag{3.68}$$

In that case the unified H_∞ observer given by:

$$\begin{cases} \dot{z} = Nz + Jy + H(\rho)\Phi(\hat{x}) + Mv \\ \dot{v} = Pz + Qy + Gv \\ \hat{x} = Rz + Sy \end{cases} \tag{3.69}$$

Following the same step, as presented in Section 3.2.2, the decoupling conditions are obtained

$$NT - TA + JC = 0 \tag{3.70}$$
$$TD_1 = 0 \tag{3.71}$$
$$H(\rho) - TB(\rho) = 0 \tag{3.72}$$
$$PT + QC = 0 \tag{3.73}$$
$$RT + SC = I \tag{3.74}$$

Following the parameterisation steps in Section 3.2.3, the estimation error dynamic system is obtained:

$$\begin{cases} \dot{\zeta} &= \mathbb{A}_1\zeta + \mathbb{W}_1(\rho)\Delta\Phi + \mathbb{B}_1\omega_n \\ e &= \mathbb{C}_1\zeta + \mathbb{D}_1\omega_n, \end{cases} \tag{3.75}$$

where $\mathbb{W}_1(\rho) = \begin{pmatrix} -TB(\rho) \\ 0 \end{pmatrix}$. *Then the LMI in Theorem 3.3.1 becomes*

$$\begin{bmatrix} \bar{\Omega}_{11} & \bar{\Omega}_{12} & \bar{\Omega}_{13} \\ \bar{\Omega}_{12}^T & -\epsilon_l I & 0 \\ \bar{\Omega}_{13}^T & 0 & \epsilon_l \mathbb{D}_1^T \Gamma^T \Gamma \mathbb{D}_1 + \mathbb{D}_1^T \mathbb{D}_1 - \gamma^2 I \end{bmatrix} < 0 \tag{3.76}$$

where

$$\begin{aligned} \bar{\Omega}_{11} &= A_{11}^T X - A_{12}^T Y^T + X A_{11} - Y A_{12} \\ &\quad + \epsilon_l \mathbb{C}_1^T \Gamma^T \Gamma \mathbb{C}_1 + \mathbb{C}_1^T \mathbb{C}_1, \\ \bar{\Omega}_{12} &= X \mathbb{W}_1(\rho), \\ \bar{\Omega}_{13} &= X B_{11} - Y B_{12} + \epsilon_l \mathbb{C}_1^T \Gamma^T \Gamma \mathbb{D}_1 + \mathbb{C}_1^T \mathbb{D}_1, \end{aligned}$$

The polytopic and gridding approaches can be applied to solve LMI (3.76).

3.4 Synthesis results and frequency domain analysis

In this section, the unified $\mathcal{H}_\infty$ observer is applied to estimate the damping force in the semi-active suspension system.

First let us recall the nonlinear Lipschitz system presented in Chapter 2. The quarter car model is described by :

$$\begin{cases} \dot{x} &= Ax + B\Phi(x)u + D_1\omega_r \\ y &= Cx + D_2\omega_n \end{cases} \tag{3.77}$$

where $x = [z_s - z_{us}, \dot{z}_s, z_{us} - z_r, \dot{z}_{us}, F_{er}]^T \in \mathbb{R}^5$ represents the system states, $y = [\ddot{z}_s, \ddot{z}_{us}]^T \in \mathbb{R}^2$ represents the measured outputs, $\omega_r = \dot{z}_r$ is the road profile derivative (the unknown input) and ω_n is the sensor noises, the control signal u (duty cycle of PWM signal) is limited in the

range of $[0, 1]$, the nonlinearity $\Phi(x) = tanh(\Gamma x)$ with $\Gamma = \begin{bmatrix} k_1 & c_1 & 0 & -c_1 & 0 \end{bmatrix}$, the system matrices are as the following

$$A = \begin{bmatrix} 0 & 1 & 0 & -1 & 0 \\ -\frac{(k_s+k_0)}{m_s} & -\frac{c_0}{m_s} & 0 & \frac{c_0}{m_s} & -\frac{1}{m_s} \\ 0 & 0 & 0 & 1 & 0 \\ \frac{(k_s+k_0)}{m_{us}} & \frac{c_0}{m_{us}} & -\frac{k_t}{m_{us}} & -\frac{c_0}{m_{us}} & \frac{1}{m_{us}} \\ 0 & 0 & 0 & 0 & -\frac{1}{\tau} \end{bmatrix}, B = \begin{bmatrix} 0 \\ 0 \\ 0 \\ 0 \\ \frac{f_c}{\tau} \end{bmatrix}, D_1 = \begin{bmatrix} 0 \\ 0 \\ -1 \\ 0 \\ 0 \end{bmatrix},$$

$$C = \begin{bmatrix} -\frac{(k_s+k_0)}{m_s} & -\frac{c_0}{m_s} & 0 & \frac{c_0}{m_s} & -\frac{1}{m_s} \\ \frac{(k_s+k_0)}{m_{us}} & \frac{c_0}{m_{us}} & -\frac{k_t}{m_{us}} & -\frac{c_0}{m_{us}} & \frac{1}{m_{us}} \end{bmatrix}, D_2 = \begin{bmatrix} 0.01 \\ 0.01 \end{bmatrix}.$$

3.4.1 Synthesis results

Here we design the unified $\mathcal{H}_\infty$ observer (3.4) for the above system (3.77) by applying the design methodology mentioned in subsection 3.3.3, which allows attenuation the effect of the sensor noises on the state estimation error $e = x - \hat{x}$ while decoupling the road profile disturbance.

- Step 1: The condition (3.33) is fullfilled

$$rank(D_1) = rank(CD_1) = 1$$

- Step 2: in our application, the matrix E are chosen as follows

$$E = p \begin{bmatrix} C_\perp^T \\ R \end{bmatrix} \tag{3.78}$$

where $C_\perp$ is an orthonormal basis for the null space of C i.e. $CC_\perp = 0$, R is derived from the QR decomposition of matrix C, i.e. $C = Q \cdot R$, and $p > 0$ is a turning parameter. The matrix E is as the following

$$E = \begin{bmatrix} 0.2078 & -11.0380 & 0 & -0.0020 & 8.5889e-05 \\ 0.2078 & 0.0020 & 3.1966e-18 & 11.0380 & 8.5889e-05 \\ -0.0091 & -8.5889e-05 & 0 & 8.5889e-05 & 11.0400 \\ 5.3669e+04 & 1.0107e+03 & -5.3932e+05 & -1.0107e+03 & 44.3668 \\ -10.0219 & -1.5689e-13 & -5.2259e+04 & 1.5689e-13 & -1.9611e-14 \end{bmatrix}$$

and $rank(E) = rank\left(\begin{bmatrix} E \\ C \end{bmatrix}\right) = 5$.

- Step 3: The matrices K, T and Θ are obtained as the following

$$K = \begin{bmatrix} 0 & 0 \\ 0 & 0 \\ 0 & 0 \\ 0 & 10.9885 \\ 0 & 1.0648 \end{bmatrix},$$

$$T = \begin{bmatrix} 0.2078 & -11.0380 & 0 & -0.002 & 8.5889e-5 \\ 0.2078 & 0.002 & 0 & 11.038 & 8.5889e-5 \\ -0.0091 & -8.5889e-05 & 0 & 8.5889e-05 & 11.0400 \\ 499.2354 & 9.4016 & 0 & -9.4016 & 0.4127 \\ -5.1621e+03 & -97.0246 & 7.2760e-12 & 0 & -4.2591 \end{bmatrix},$$

$$\Theta = \begin{bmatrix} 0.0052e6 & 0.0001e6 & 0.0001e6 & -0.0001e6 & 4.2693 \\ 0.0534e6 & 0.0010e6 & -0.5417e6 & -0.0010e6 & 44.1502 \\ 0.4559 & -5.3850e-04 & -4.2155 & 5.3850e-04 & -157.7139 \\ -0.0499e6 & 0.0045e6 & -4.7620e6 & -0.0045e6 & -47.1463 \\ 0.5150e6 & 0.0045e6 & -4.7620e6 & -0.0045e6 & 0.0005e6 \end{bmatrix}.$$

- Steps 6-8: Solving the LMI (3.52), we obtain the $\mathcal{L}_2$-induced gain $\gamma = 0.1270$, $\epsilon_l = 80$, and the observer matrices N, J, H, M, P, Q, G, R and S.

$$N = \begin{bmatrix} 351.2952 & 351.2968 & -15.4219 & 2.1258e+05 & 2.0558e+04 \\ -22.8322 & -22.8332 & 1.0014 & -1.3805e+04 & -1.3350e+03 \\ -1.5984e+04 & -1.5984e+04 & 687.3905 & -9.6715e+06 & -9.3534e+05 \\ 297.1736 & 297.1687 & -15.5640 & 2.0715e+05 & 2.0034e+04 \\ -3.5038e+03 & -3.5037e+03 & 179.8412 & -2.4027e+06 & -2.3238e+05 \end{bmatrix}$$

$$J = \begin{bmatrix} 0.2519 & -0.0020 \\ -1.1418 & 11.0380 \\ -9.3096 & 4.9084e-05 \\ -2.4625 & -9.4016 \\ 24.6414 & 97.0246 \end{bmatrix}, Q = \begin{bmatrix} 0.1385 & 1.5769e-07 \\ 0.1248 & 4.4160e-08 \\ 0.1467 & -7.6048e-08 \\ 0.0574 & -1.2023e-07 \\ -0.1821 & -1.1265e-07 \end{bmatrix}$$

$$M = \begin{bmatrix} 2.4529e+06 & 4.7061e+05 & -0.1179 & -0.1172 & -0.0812 \\ -7.2526e+05 & -6.9237e+05 & 1.5819e+05 & 5.7920e+05 & 7.2210e+05 \\ -4.8875e+06 & 7.6475e+07 & 7.9674e+07 & 2.8641e+07 & -1.2562e+07 \\ -2.1106e+06 & -3.3044e+06 & -1.4177e+06 & 1.1828e+06 & 2.5429e+06 \\ 9.6594e+06 & 2.9720e+07 & 1.9238e+07 & -1.7527e+06 & -1.4433e+07 \end{bmatrix}$$

$$P = \begin{bmatrix} 1.1349e+03 & 1.1349e+03 & -49.8201 & 6.8670e+05 & 6.6411e+04 \\ 758.7158 & 758.7159 & -33.3056 & 4.5907e+05 & 4.4397e+04 \\ 153.3809 & 153.3811 & -6.7330 & 9.2805e+04 & 8.9752e+03 \\ -635.2470 & -635.2470 & 27.8857 & -3.8436e+05 & -3.7172e+04 \\ -1.0551e+03 & -1.0551e+03 & 46.3157 & -6.3839e+05 & -6.1740e+04 \end{bmatrix}$$

$$H = \begin{bmatrix} 0.0012 \\ 0.0012 \\ 157.7142 \\ 5.8958 \\ -60.8446 \end{bmatrix}, S = \begin{bmatrix} -1.2081e-05 & -3.6733e-18 \\ -1.3844e-04 & 1.8243e-16 \\ -1.7056e-06 & -2.0375e-05 \\ 1.3844e-04 & -6.8118e-18 \\ -6.0770e-06 & -1.7777e-17 \end{bmatrix}$$

$$G = \begin{bmatrix} 8.1850e+05 & -4.9005e+06 & -4.7546e+06 & -2.5593e+06 & 3.7595e+05 \\ 5.9513e+06 & -2.6474e+04 & -5.7130e+06 & -6.0137e+06 & -4.4158e+06 \\ 4.3932e+06 & 3.9719e+06 & -1.0112e+06 & -4.2251e+06 & -5.0540e+06 \\ 6.1833e+05 & 4.0555e+06 & 3.8110e+06 & 8.5602e+05 & -7.6813e+05 \\ -5.3702e+05 & 4.3647e+06 & 5.0924e+06 & 1.4737e+06 & -6.1263e+05 \end{bmatrix}$$

$$R = \begin{bmatrix} 0.0017 & 0.0017 & -7.4710e-05 & 1.8433e-05 & -1.9070e-04 \\ -0.0906 & 1.6206e-05 & -7.1142e-07 & 3.4945e-07 & 8.9622e-06 \\ -3.2373e-07 & -3.2373e-07 & -3.2373e-07 & -3.5062e-09 & -1.8944e-05 \\ -1.6206e-05 & 0.0906 & 7.1142e-07 & -3.4945e-07 & -8.9622e-06 \\ 7.1142e-07 & 7.1142e-07 & 0.0906 & 1.5340e-08 & 3.9342e-07 \end{bmatrix}$$

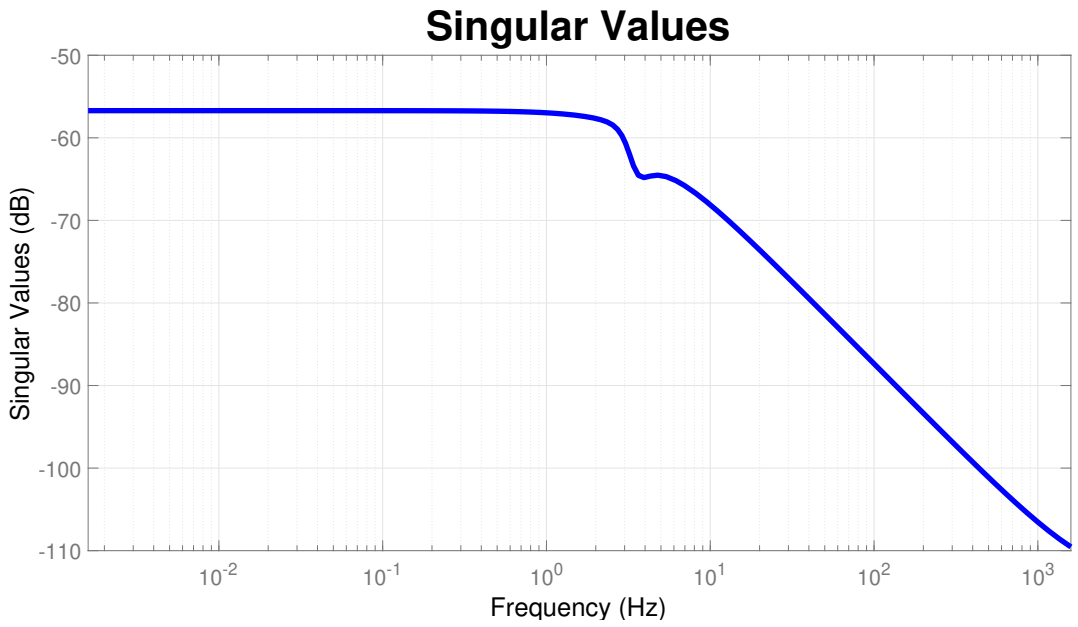

Figure 3.1: $\bar{\sigma}(e/\omega_n)$- Upper bound on the singular value

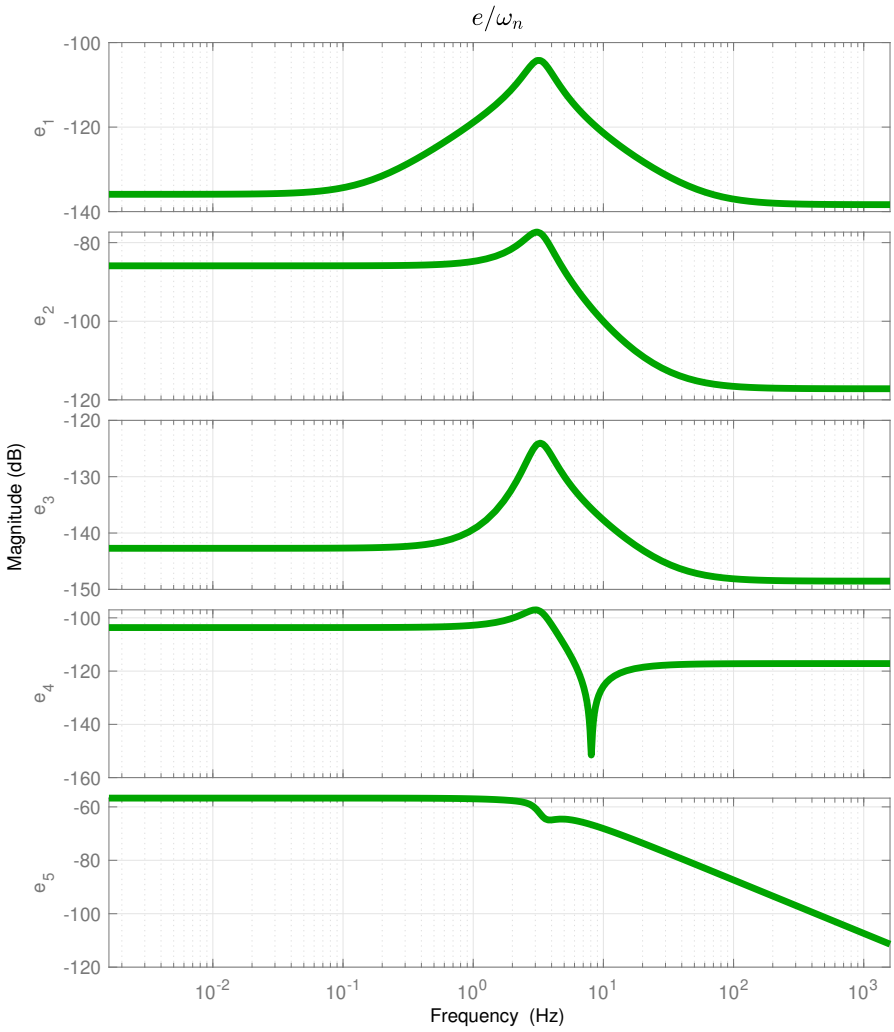

Figure 3.2: Transfer $\|e/\omega_n\|$- Bode diagrams of the unified $\mathcal{H}_\infty$ observer

3.4.2 Frequency domain analysis

The resulting attenuation of the sensor noises ω_n on the estimation error is shown in Figures 3.2 and 3.1. In Figure 3.2 the Bode diagrams of the estimation error systems with input ω_n (sensor noise) and output (the state estimation errors) are shown, which emphasize the satisfactory attenuation level of the measurement noises effect on the 5 estimation errors $e_i, i = 1 \div 5$. Moreover, according to Figure 3.1, these results emphasize the effectiveness of the proposed observer in terms of noise rejection, since the upper bound on the singular values decreases rapidly in the region of high frequency noises [3Hz-1000Hz]

3.5 Simulation Results

In this section, three time-domain simulations are performed with the nonlinear quarter-car model (3.1). The block diagram for the simulation of the observer is shown in Figure 3.3.

The initial conditions are chosen as follows:

$$x_0 = \begin{bmatrix}0, & 0, & 0, & 0, & 0\end{bmatrix}^T,$$
$$z_0 = \begin{bmatrix}0.01, & -0.4, & 0.001, & -0.15, & 2\end{bmatrix}^T,$$
$$v_0 = \begin{bmatrix}0, & 0, & 0, & 0, & 0\end{bmatrix}^T.$$

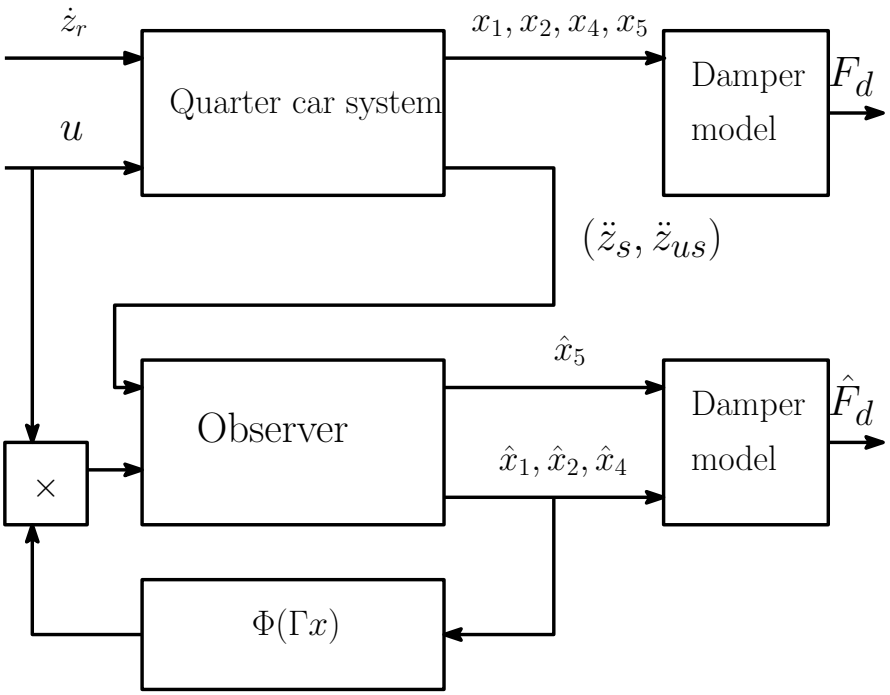

Figure 3.3: Block diagram for simulation of the observer

From the simulations, the normalized root-mean-square errors (NRMSE) are used to to quantitatively analyze the estimation error.

$$RMSE = \sqrt{\frac{\sum_{i=1}^{n}(F_{d_i} - \hat{F}_{d_i})}{n}} \tag{3.79}$$

$$NRMSE = \frac{RMSE}{F_{dmax} - F_{dmin}} \tag{3.80}$$

Three simulation scenarios are used to evaluate the performance of the proposed observer, detailed in the sequel.

3.5.1 Simulation scenario 1

In the first scenario, a chirp signal is used as the road profile to evaluate the robustness of the observer for various road frequencies (from 0 Hz to 10 Hz). This simulation scenario is given as follows:

- The road profile is a chirp signal with frequency from 0 Hz to 10 Hz and the magnitude at $4 \cdot 10^{-3}$ (m), shown in Figure 3.4 (top).
- The control input u is constant ($u = 0.35$) as seen in Figure 3.4 (bottom).

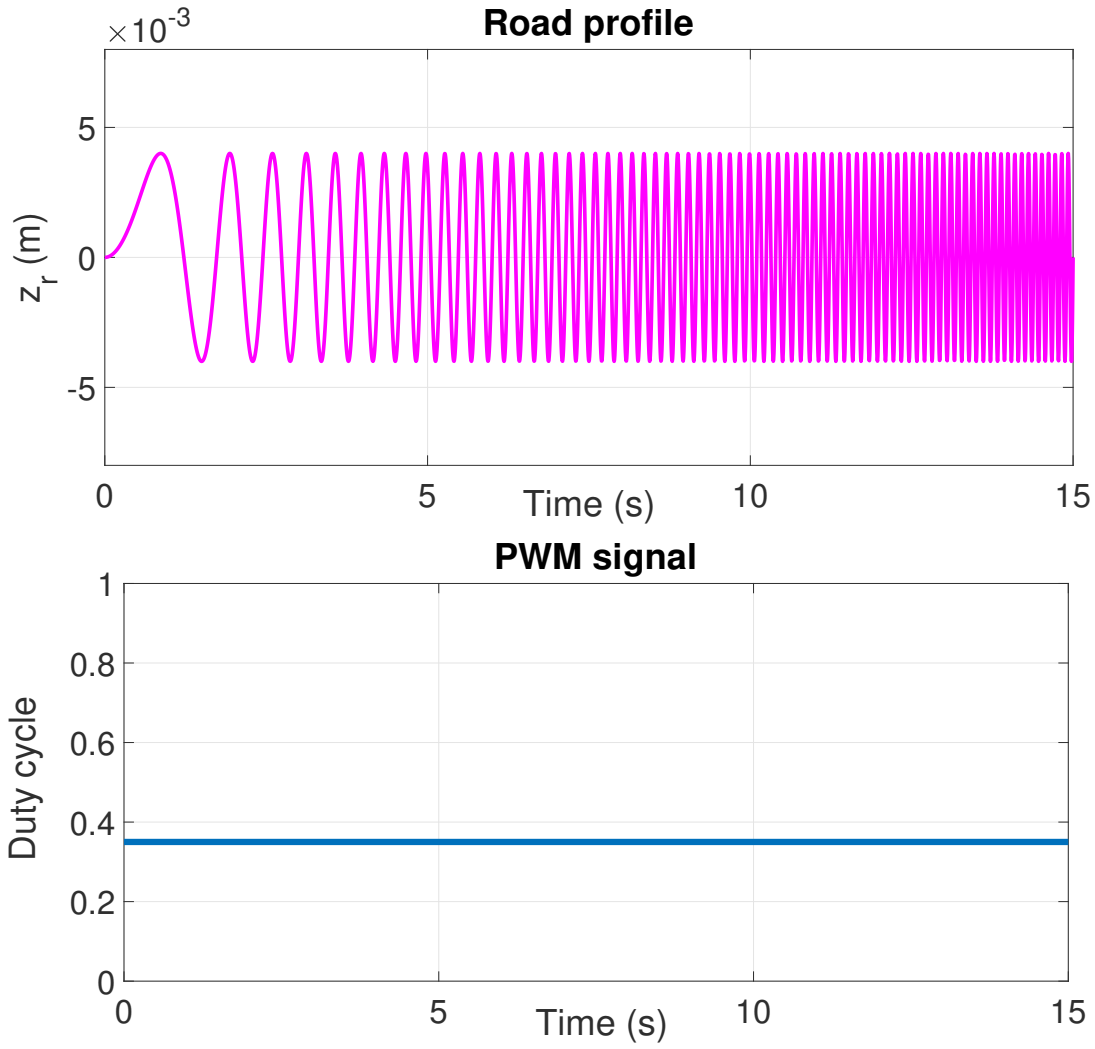

Figure 3.4: Simulation senario 1: (top) Road profile, (bottom) PWM signal

In Figure 3.5, the simulated force is shown in the solid red line, the estimated force in the

blue dash line, and the estimation error in the solid green line. We can see that the estimated force converges to the simulated one after 1 second. To further describe this accuracy, Table **??** gives the normalized root-mean-square errors ($NRMSE = 1.2\%$) in this simulation. Therefore, the robustness of the unified observer to the frequency content of the road profile disturbance is guaranteed. It can be clearly observed that the damping force is estimated with a satisfactory accuracy at all frequencies of the road profile.

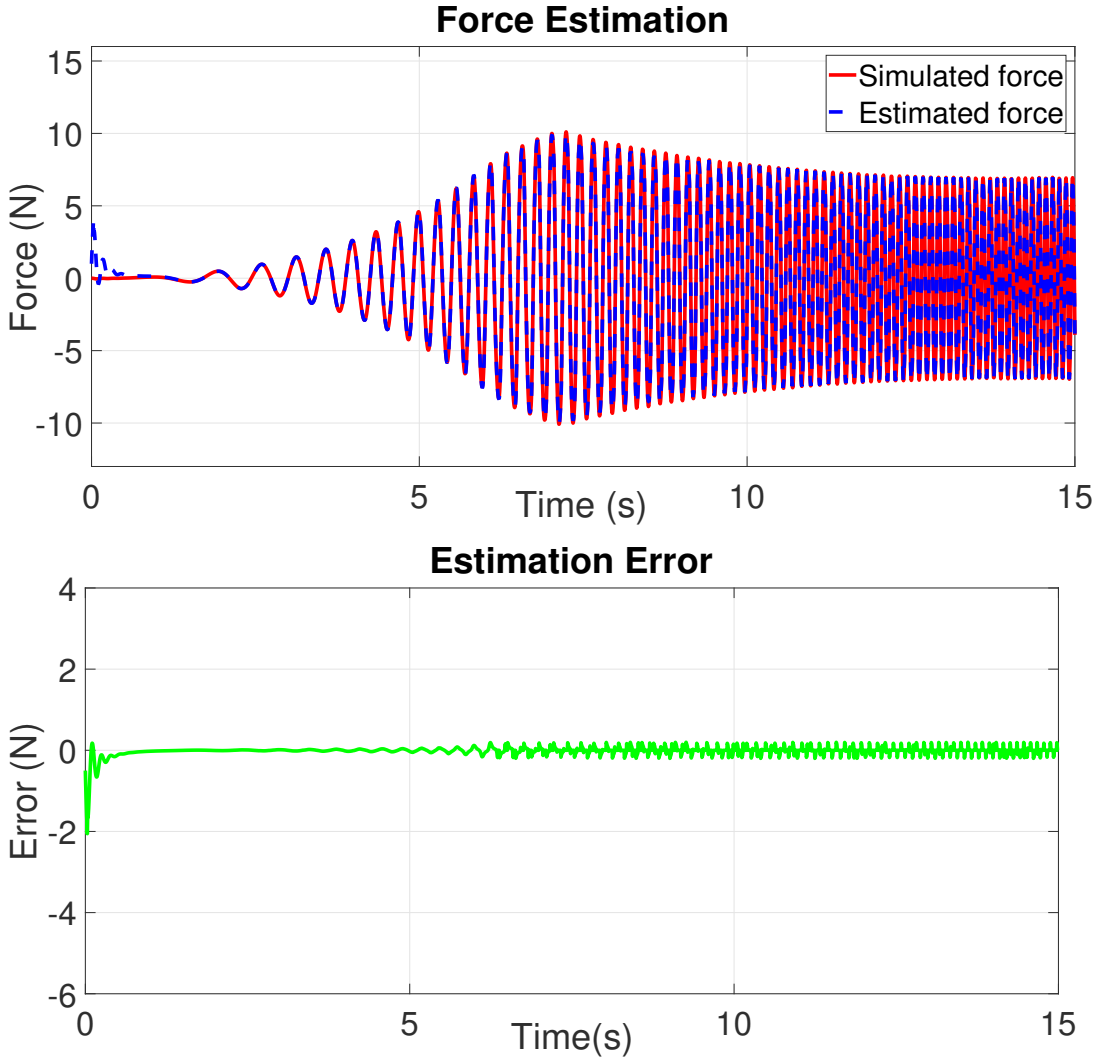

Figure 3.5: Simulation senario 1: (top) Damper force, (bottom) Estimation error

3.5.2 Simulation scenario 2

In the second simulation, the performance of the unified $\mathcal{H}_\infty$ is assessed via the simulation scenario with a typical road disturbance. The content of this scenario is detailed as follows:

- An ISO 8608 road profile signal (Type C) is used as seen in the top of Figure 3.6.

- The control input u is constant ($u = 0.35$), presented in Figure 3.6 (bottom).

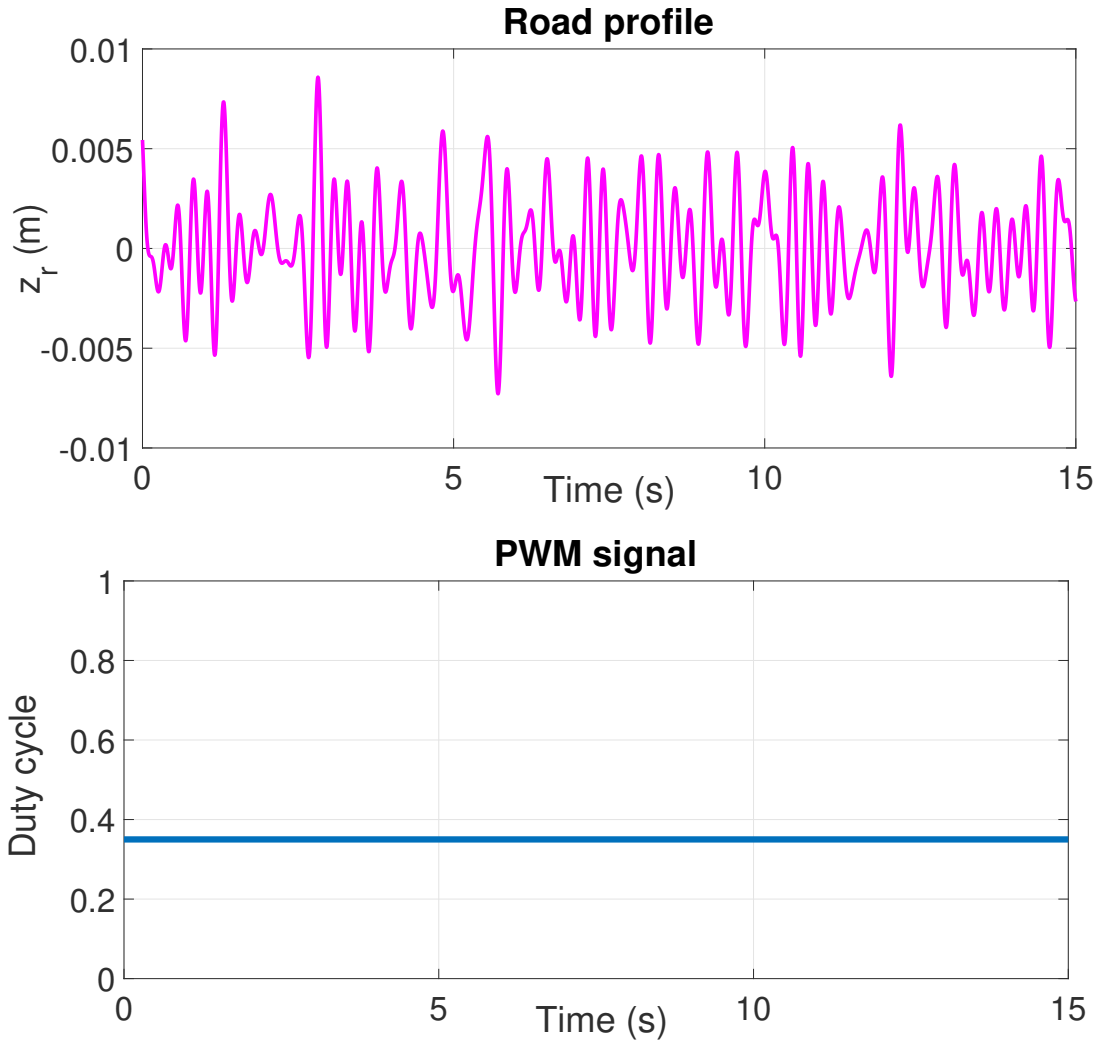

Figure 3.6: Simulation senario 2: (top) Road profile, (bottom) PWM signal

Figure 3.7 shows the damping force estimation on the left side and the estimation error on the right side. The simulation results in Figure 3.7 and the normalized root-mean-square error (0.9%) in Table **??** indicate that the proposed observer performs well in the open-loop system, considering the realistic road profile.

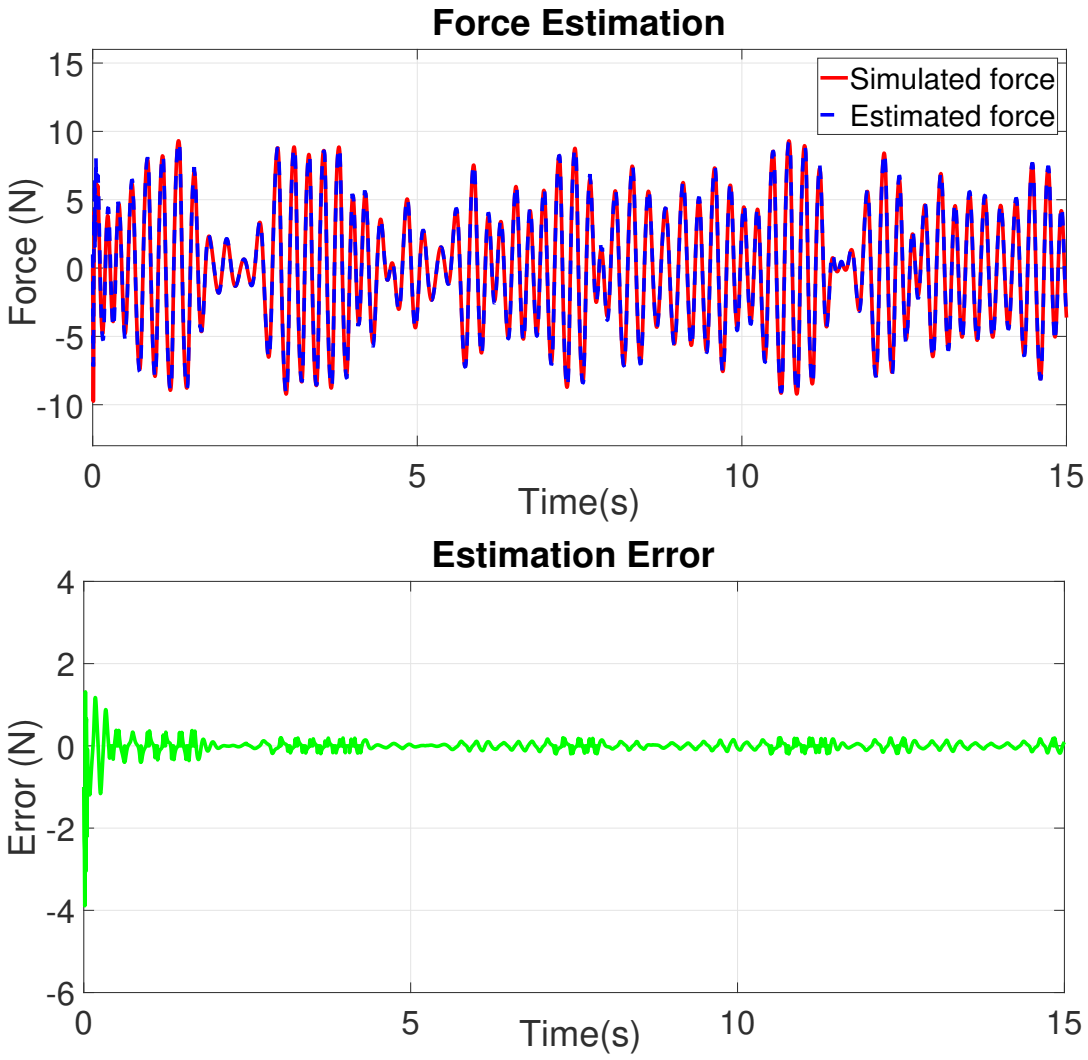

Figure 3.7: Simulation senario 2: (top) Damper force, (bottom) Estimation error

It is worth noting that the observer must work for the closed-loop system in the real application. Therefore, to assess the effectiveness of the observer in the closed-loop system, a more realistic scenario is presented in the next subsection.

3.5.3 Simulation scenario 3

The final simulation scenario is designed to evaluate the performance of the unified $\mathcal{H}_\infty$ observer in the closed-loop system, where the control input comes from a Skyhook controller.

Mathematically, the Skyhook controller output is expressed with

$$u = \begin{cases} u_{max} & if \;\; \dot{z}_s \dot{z}_{def} \geq 0 \\ u_{min} & if \;\; \dot{z}_s \dot{z}_{def} < 0 \end{cases} \tag{3.81}$$

This scenario is detailed as follows:

- An ISO 8608 road profile signal (Type C) is used.
- The control input u is obtained from a Skyhook controller

The ISO road profile and the control input in this test are shown in Figure 3.8.

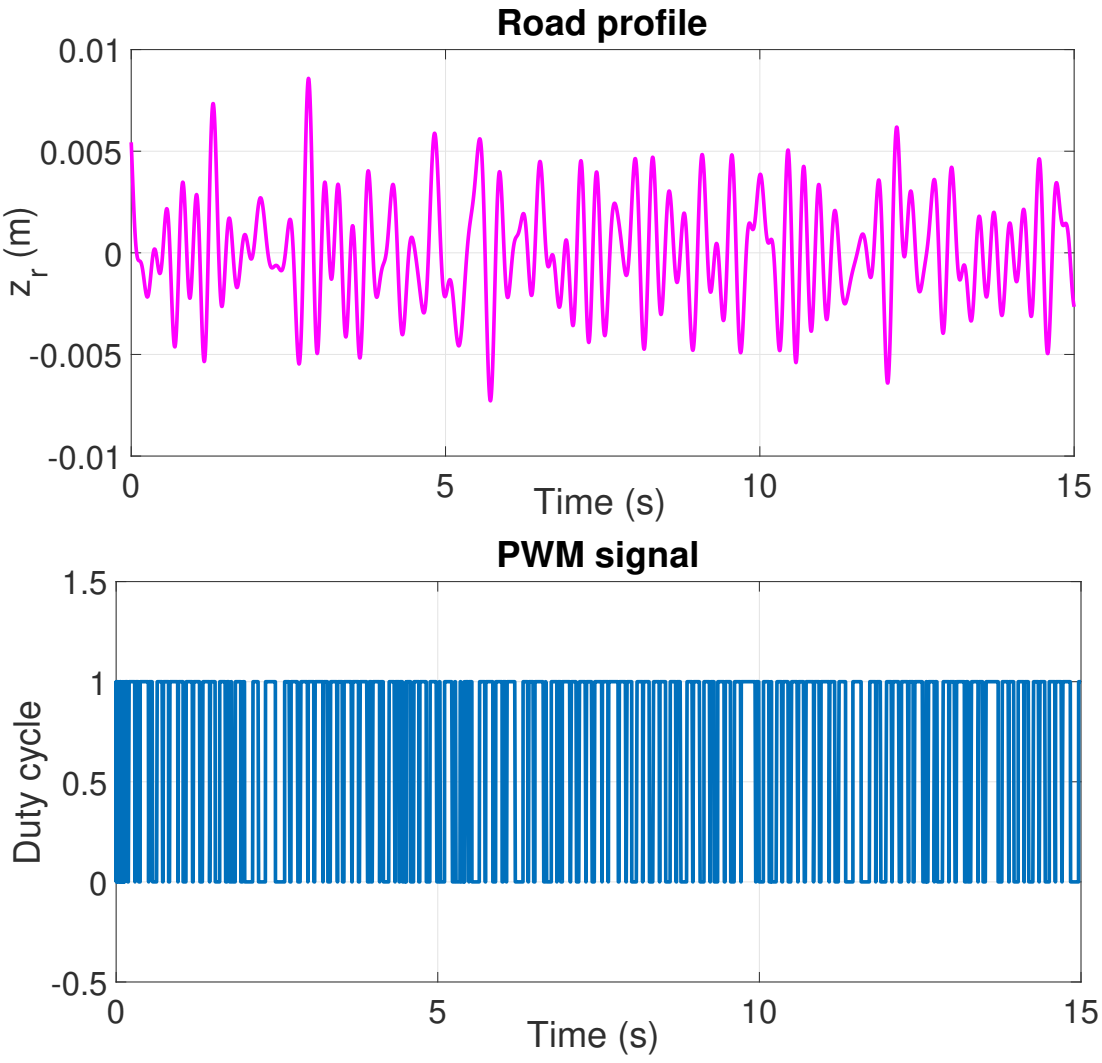

Figure 3.8: Simulation senario 3: (top) Road profile, (bottom) PWM signal

The simulation results of this test are shown in the Figure 3.9. The performance of the unified observer applied to the closed-loop system is guaranteed. We can see that the damping force is estimated with a satisfactory accuracy when the control input varies very quickly. Moreover, the normalized root-mean-square error for this simulation is 2.58%, shown in Table ??. Hence, the efficiency of the proposed observer is proved in a realistic case.

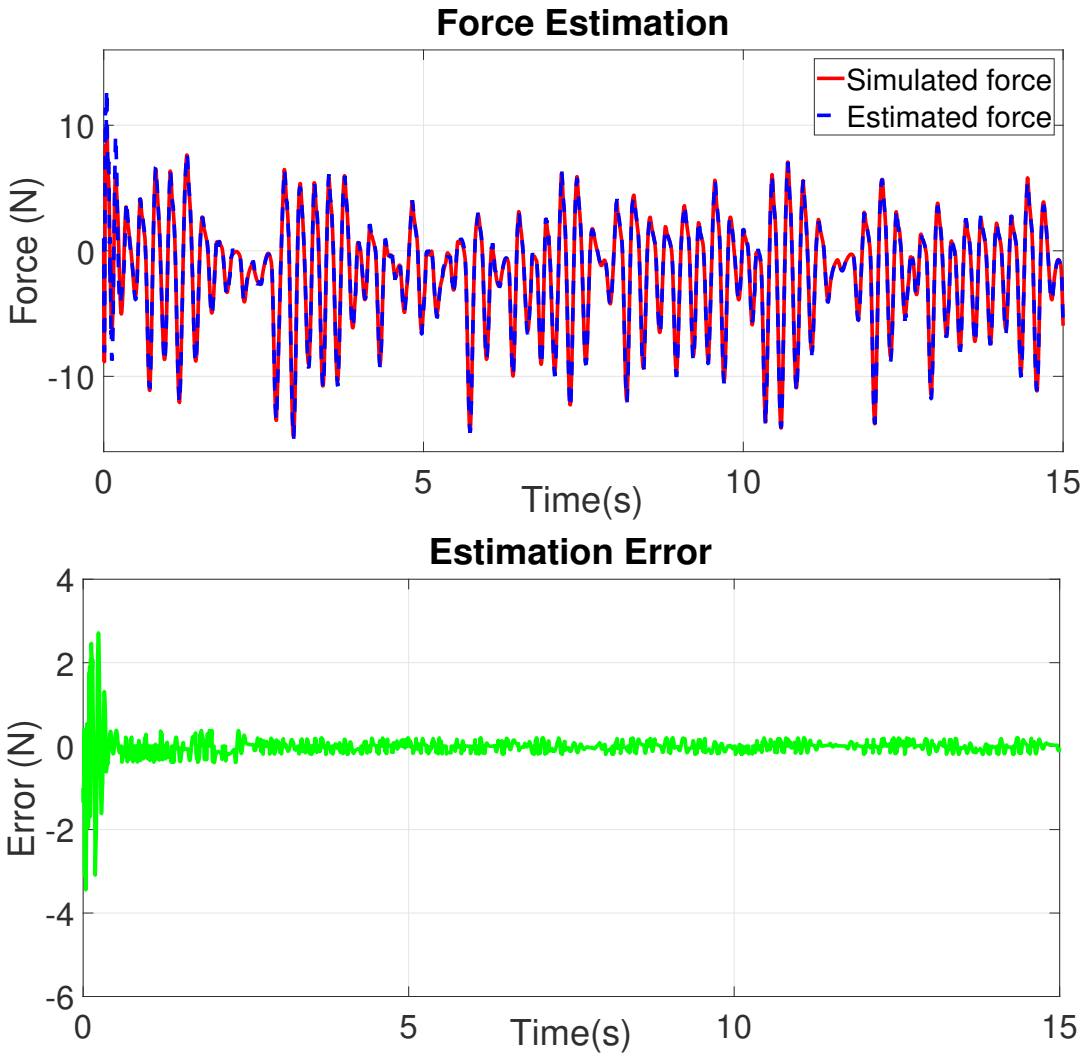

Figure 3.9: Simulation senario 3: (top) Damper force, (bottom) Estimation error

For real-time experimental performance assessment, the observer is implemented on the INOVE testbench of GIPSA-lab. More details are presented in the next section.

3.6 Experimental validation

To validate the effectiveness of the proposed algorithm, real-time experiments have been performed on the 1/5 car scaled car INOVE available at GIPSA-lab, detailed in chapter 1.

The damping force estimation algorithm is applied for the rear-left corner of the testbench using two sensors: the unsprung mass $\ddot{z}_{us}$ and the sprung mass $\ddot{z}_s$ accelerometers. For validation purpose only, a damper force sensor is used to compare the estimated force with the measured one.

The following block-scheme given in Figure 3.10 illustrates the experiment procedure of the estimation.

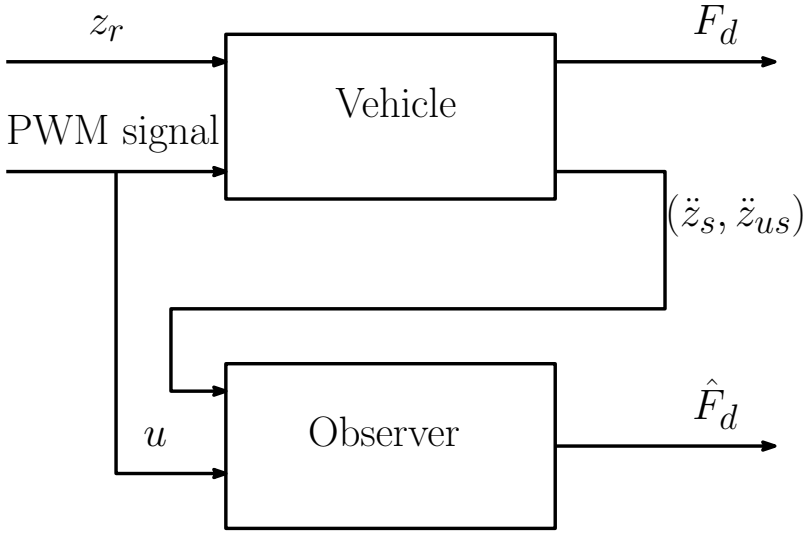

Figure 3.10: Block diagram for implementation of the observer

The experimental procedure is summarized as follows:

- The observer inputs are the measured sprung mass and unsprung mass accelerations $\ddot{z}_s$ and $\ddot{z}_{us}$, and the control input signal u.
- The observer output is the estimated force $\hat{F}_d$.
- The sensor force F_d is used for comparison only.
- Different road profiles z_r are chosen to evaluate the effectiveness of the proposed observer.
- The control input u is obtained from the Skyhook controller.

In the experimental test, the real road profile is the real displacement of the platform under the wheel, not the set-point and the control input u, in practice, is limited within $[0; 0.3]$.

Two experimental senarios are designed to validate the effectiveness of the proposed observer as presented in following subsections:

3.6.1 Experiment 1

In the first experimental scenario, the proposed observer is validated for the closed-loop system with the skyhook controller. The road disturbance in this test is a sinewave function. The scenario is the following:

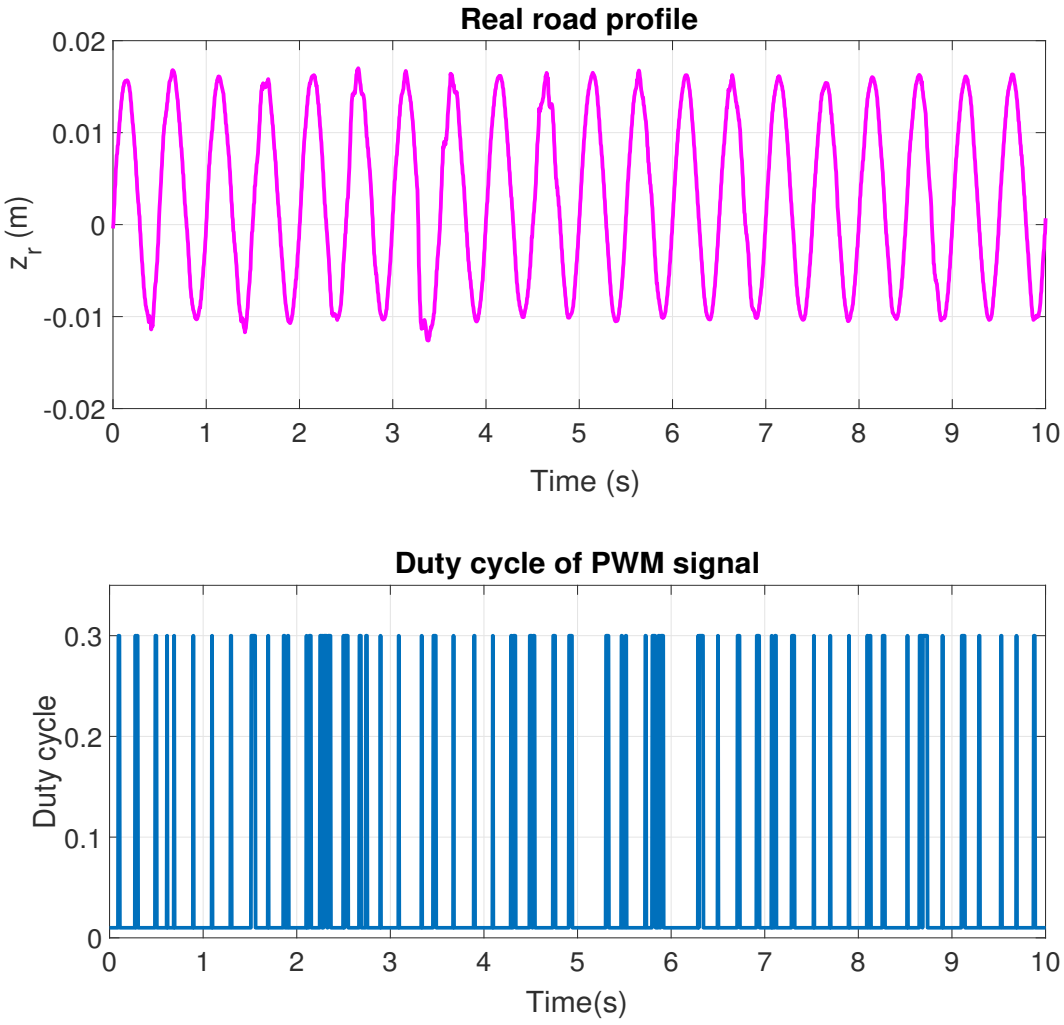

Figure 3.11: Experiment 1: (top) Road profile, (bottom) PWM signal

- The road profile is a sequence of sinusoidal bumps (see on the top of Figure 3.11).
- The control input u is obtained from a Skyhook controller (shown on the bottom of

Figure 3.11).

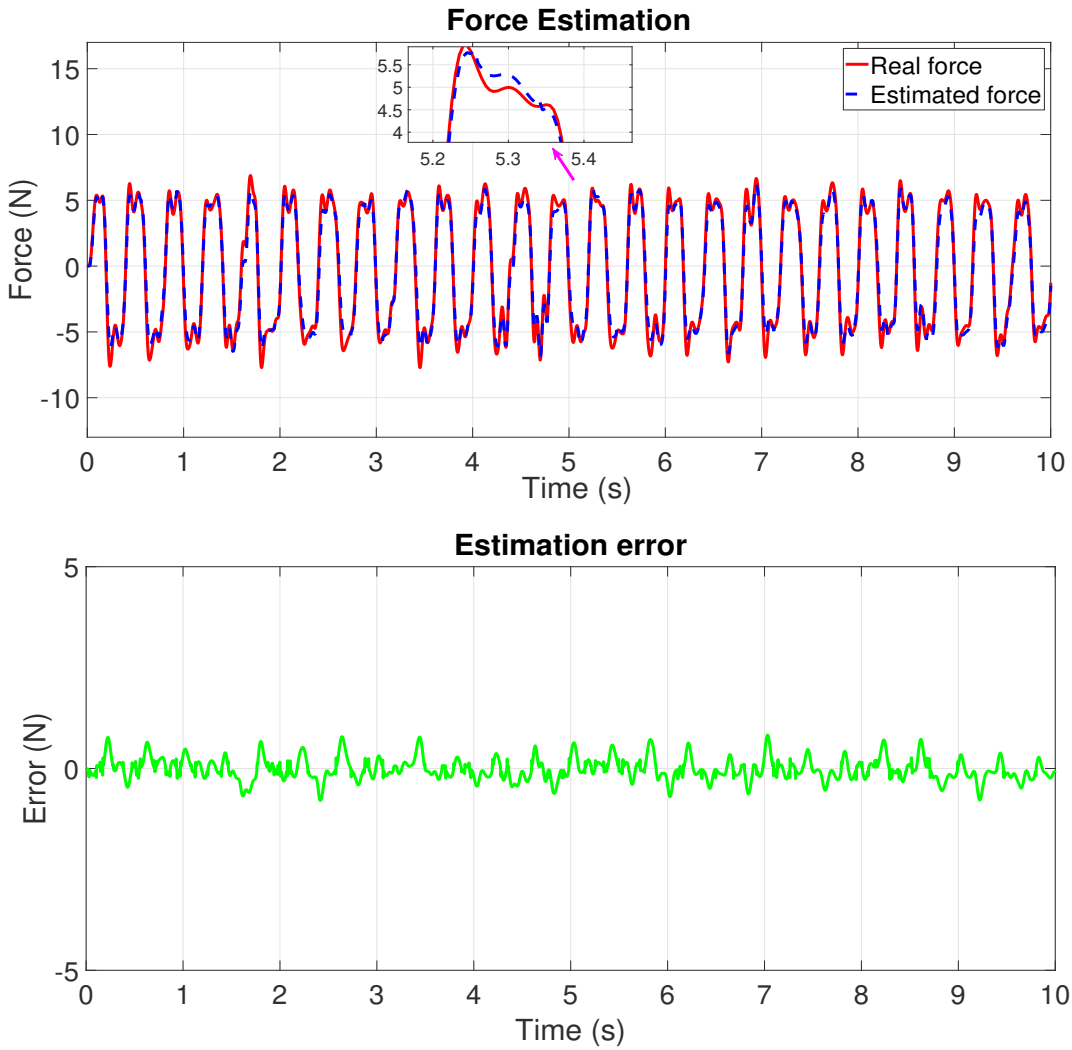

Figure 3.12: Experiment 1: (top) Damper force, (bottom) Estimation error

The experimental results of the force estimation in the first test are shown in Figure 3.12. The unified $\mathcal{H}_\infty$ presents an accuracy estimation in the case of the sinewave road profile. The normalized root-mean-square error for this test (shown in Table 3.1) is 4.4%, which confirms the efficiency of the proposed method.

3.6.2 Experiment 2

In the second experimental scenario, the performance of the unified $\mathcal{H}_\infty$ is assessed in the case of the realistic road profile (ISO standard road profile) and the control signal is obtained from

Skyhook controller. The scenario detailed as follows:

- An ISO 8608 road profile signal (Type C) is used (see on the top Figure 3.13).

- The control input u is obtained from a Skyhook controller (the bottom of Figure 3.13).

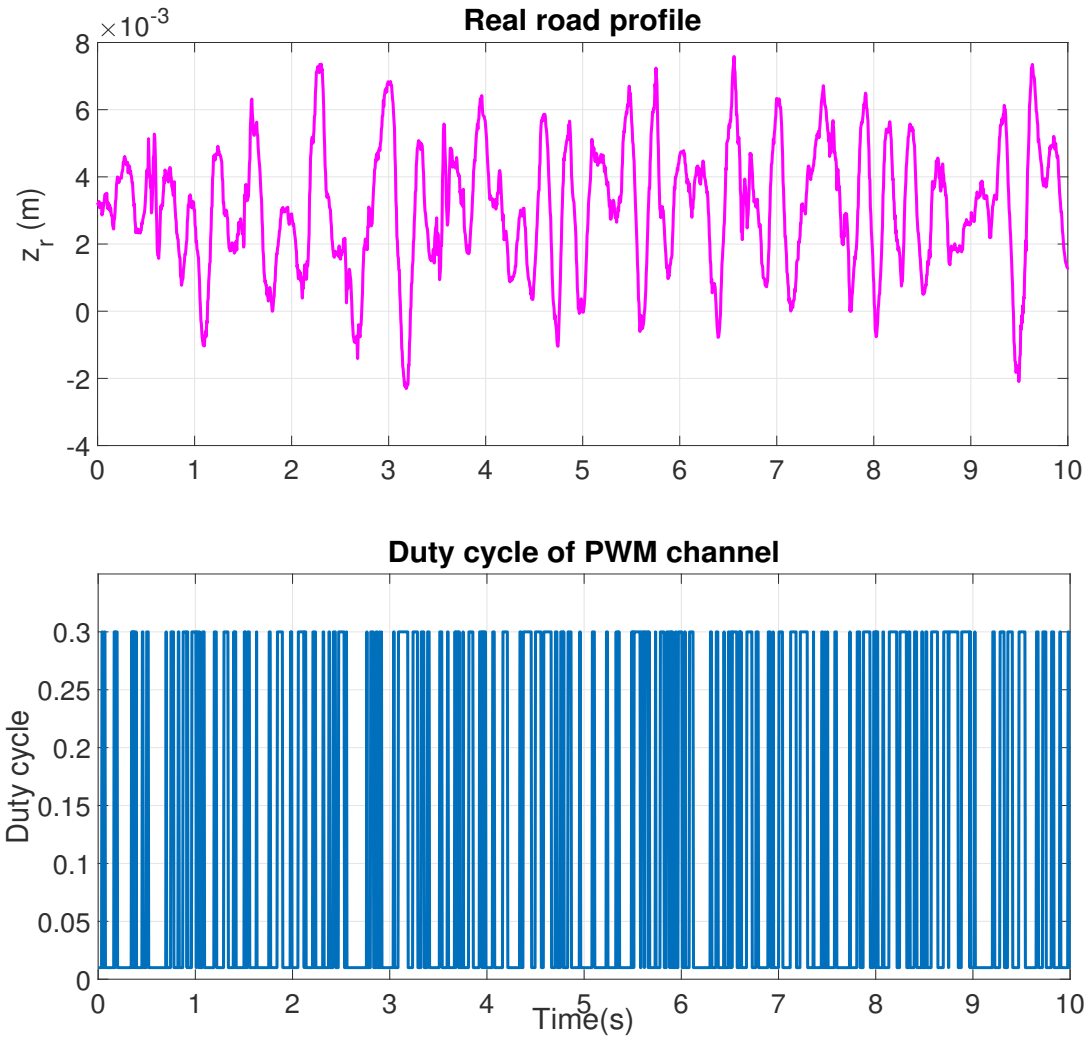

Figure 3.13: Experiment 2: (top) Road profile, (bottom) PWM signal

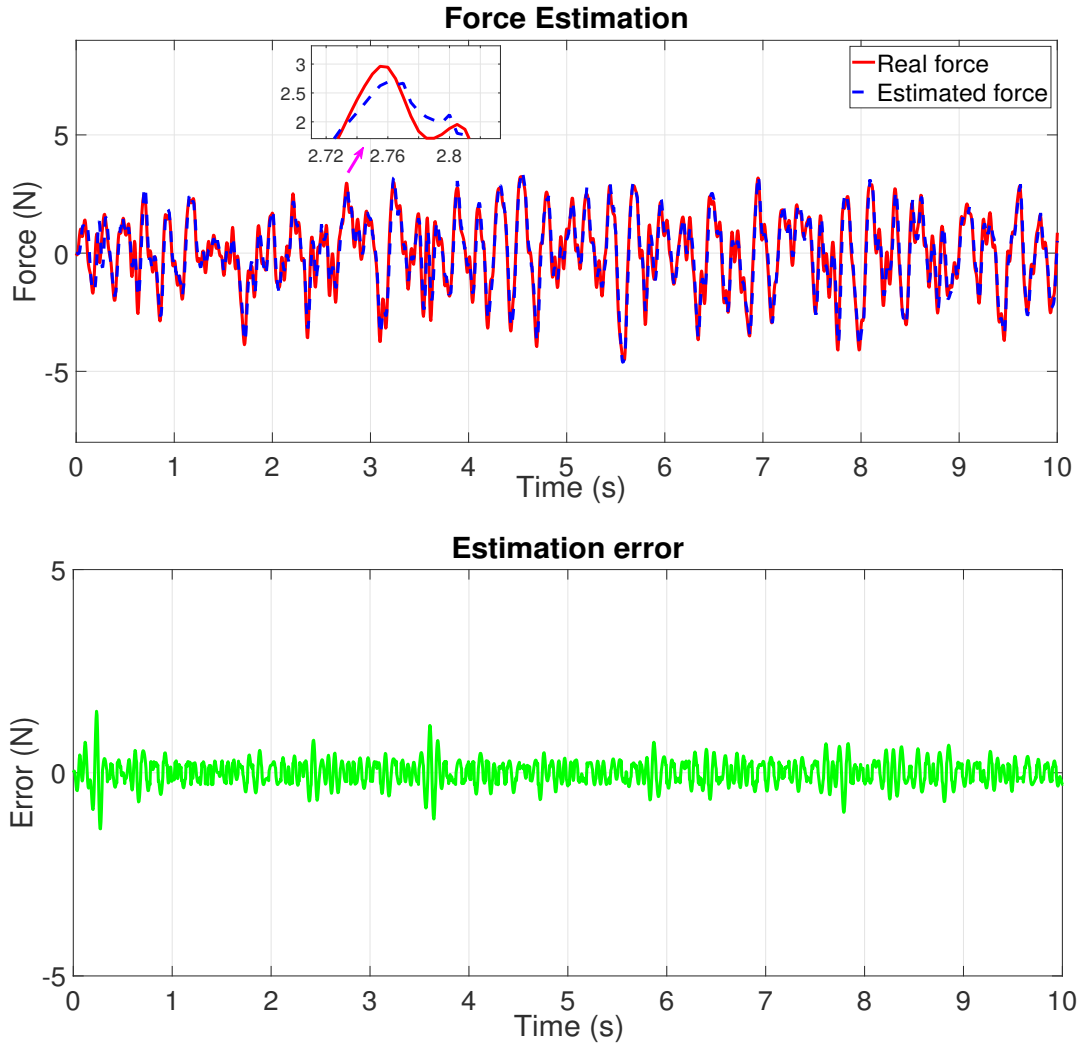

Figure 3.14: Experiment 2: (top) Damper force, (bottom) Estimation error

The experimental results of the force estimation are presented in Figure 3.14. They show the accuracy and efficiency of the proposed observer. To further describe this accuracy, the Table 3.1 gives the normalized root-mean-square errors ($NRMSE = 5.47\%$), considering the difference between the estimated and measured forces for the experimental results presented in the right side of Figure 3.14.

Table 3.1: Normalized Root-Mean-Square Errors for experiments(NRMSE)

Road Profile	NRMSE
Sinusoidal bumps	0.0440
ISO 8608 road	0.0547

3.7 Conclusion

In this chapter, we developed a unified $\mathcal{H}_\infty$ observer to estimate the damper force of an automotive suspension, using a dynamic nonlinear model of the ER damper. The model is represented in a nonlinear Lipschitz form by considering a phenomenological damper model. The unified $\mathcal{H}_\infty$ observer which is designed, gives a good estimation of the damping force while using two accelerometers only. The estimation error is decoupled from the effect of unknown road profile and is minimized w.r.t. the measurement noises, while the nonlinearity term is bounded by a Lipchitz condition. Both simulation and experiment results assess the ability and the accuracy of the proposed model to estimate the damping force of the ER semi-active damper.

As mentioned above, the variations of the damper force amplification function of the applied voltage are not considered in the design procedure of the unified $\mathcal{H}_\infty$ observer. Therefore, an NLPV observer is proposed in the next chapter to deal with this problem.

Chapter 4

Real-time Damper Force Estimation of Vehicle Electrorheological Suspension: A NonLinear Parameter Varying Approach

Contents

This chapter proposes a nonlinear parameter varying (NLPV) observer to estimate, in real-time, the damper force of an electrorheological (ER) damper in the road vehicle suspension system. The objectives are to minimize the effects of bounded unknown road profile disturbances and measurement noises on the estimation errors in the $\mathcal{H}_\infty$ framework. Furthermore, the nonlinearity coming from the damper model (and considered in the observer formulation)

is handled through a Lipschitz condition. The observer inputs are data given by two low-cost sensors (two accelerometers data from the sprung mass and the unsprung mass). For performance assessment, the observer is implemented on the INOVE testbench of GIPSA-lab (1/5-scaled real vehicle). Both simulation and experimental results demonstrate the effectiveness of the proposed observer in terms of the ability to estimate the damper force in real-time and to minimize the effects of measurement noises and road disturbances. The NLPV observer has been published in the conference paper [Pham, Sename, and Dugard 2019c].

4.1 Introduction

As mentioned in the introduction section of Part II, one of the key requirements of the damper force estimation approach is the ability to deal with the nonlinearity in the damper model. Let us recall the nonlinear Lipschitz system model (2.2.2) presented in Chapter 2:

$$\begin{cases} \dot{x} &= Ax + B\Phi(x) \cdot u + D_1\omega_r \\ y &= Cx + D_2\omega_n. \end{cases} \tag{4.1}$$

Notice that the damper nonlinearity is multiplied by the control input signal u. This is the main issue to be tackled in the observer design. To solve this issue, the dynamic system can be represented in the quasi-LPV form where the nonlinearity coupled with the control signal is considered as the varying parameter. Several LPV observers can be then applied for such a quasi-LPV system (see in [Tudon-Martinez et al. 2018], [Sato 2012], [Pérez-Estrada et al. 2018a]). It is worth noting that the real-time knowledge of the scheduling variable is paramount important to design the LPV observer. Therefore, in [Tudon-Martinez et al. 2018], it is obtained online via several measured state variables leading to an increase in the number of required sensors. The two latter methods in [Sato 2012] and [Pérez-Estrada et al. 2018a] are dedicated to the unmeasurable scheduling parameter, where it is computed from the estimated states. Then the difference between the estimated scheduling parameter and the real one is described as an uncertainty, which is solved by a robust method in the observer design procedure. This may lead to conservatism.

To maintain the nonlinearity in the structure of the observer, the NLPV estimation scheme is presented here where the observer gain depends on the voltage control input u. This chapter addresses the design problem of NLPV observer to estimate the damper force via a constant Lyapunov function (polytopic method) and a parameter-dependent Lyapunov function (gridding method). Both methods consider two accelerometers (sprung mass and unsprung mass accelerations) as inputs of observers. The major contributions of this chapter are the following:

- Two NLPV approaches (polytopic and gridding methods) for Lipchitz nonlinear systems are developed to design a damper force observer minimizing, in an $\mathcal{L}_2$-induced gain objective, the effect of unknown inputs (road profile and measurement noises).
- The proposed observers have been implemented on a real scaled-vehicle test bench. The observer performances are then assessed with experimental tests.

4.2 NLPV observer definition

Let us first recall the nonlinear parameter varying system model (2.2.3), as presented in Chapter 2, described by :

$$\begin{cases} \dot{x} &= Ax + B(\rho)\Phi(x) + \bar{D}_1\omega \\ y &= Cx + \bar{D}_2\omega \end{cases} \tag{4.2}$$

where $x = [z_s - z_{us}, \dot{z}_s, z_{us} - z_r, \dot{z}_{us}, F_{er}]^T \in \mathbb{R}^5$ represents the system states, $y = [\ddot{z}_s, \ddot{z}_{us}]^T \in \mathbb{R}^2$ represents the measured outputs, the scheduling variable $\rho = u \in \Delta_\rho \subset \mathbb{R}$ and $\omega = \begin{pmatrix} \omega_r \\ \omega_n \end{pmatrix}$, in which, ω_r is the road profile derivative and ω_n is the sensor noises.

Let define the output estimation variable

$$z_e = [x_1, x_2, x_4, x_5]^T = C_z x \tag{4.3}$$

where $C_z = \begin{bmatrix} 1 & 0 & 0 & 0 & 0 \\ 0 & 1 & 0 & 0 & 0 \\ 0 & 0 & 0 & 1 & 0 \\ 0 & 0 & 0 & 0 & 1 \end{bmatrix}$.

As previously presented in Chapters 2 and 3, let us recall the global Lipschitz condition for the nonlinearity $\Phi(x)$ in x, i.e.: $\forall x, \hat{x} \in \mathbb{R}^5$

$$\|\Phi(x) - \Phi(\hat{x})\| \leqslant \|\Gamma(x - \hat{x})\|, \forall x, \hat{x}. \tag{4.4}$$

The $NLPV$ observer for the quarter-car system (4.2) is chosen as:

$$\begin{cases} \dot{\hat{x}} = A\hat{x} + L(\rho)(y - C\hat{x}) + B(\rho)\Phi(\hat{x}) \\ \hat{z}_e = C_z\hat{x} \end{cases} \tag{4.5}$$

where $\hat{x}$ is the estimated states vector of x, $\hat{z}_e$ represents the estimated variables of z_e. The observer gain $L(\rho)$ will be determined in the next steps.

4.3 NLPV observer design

4.3.1 Problem formulation

The state estimation error is given as

$$e(t) = x(t) - \hat{x}(t) \tag{4.6}$$

Differentiating $e(t)$ with respect to time and using (4.2) and (4.5), one obtains

$$\begin{cases} \dot{e} & = \dot{x} - \dot{\hat{x}} \\ & = Ax + B(\rho)\Phi(x) + \bar{D}_1\omega \\ & -A\hat{x} - L(\rho)(y - C\hat{x}) - B(\rho)\Phi(\hat{x}) \\ & = (A - L(\rho)C)e + B(\rho)(\Phi(x) - \Phi(\hat{x})) \\ & +(\bar{D}_1 - L(\rho)\bar{D}_2)\omega \\ e_z & = C_z e \end{cases} \tag{4.7}$$

where $e_z = z_e - \hat{z}_e$.

The problem to be solved is then stated as:

- The system (4.7) is asymptotically stable for $\omega(t) = 0$
- Minimize γ such that $\|e_z(t)\|_{\mathcal{L}_2} < \gamma\|\omega(t)\|_{\mathcal{L}_2}$ for $\omega(t) \neq 0$

To solve the above problem into the LMI framework, the two susbsections will present solutions based on quadratic and robust statbilities, respectively.

Definition 4.3.1. *(Quadratic Stability) The system (4.7) is said to be quadratically stable if there exist a Lyapunov function $V_p(e) = e^T Pe > 0$, $P > 0$ for every $e \neq 0$ and $V_p(0) = 0$ such that*

$$\frac{dV_p}{dt}(e) < 0 \tag{4.8}$$

for every $e \neq 0$ and $\dot{V}_p(0, \rho) = 0$ for all $\rho \in \Delta_\rho$. Such a Lyapunov function is often referred to as a constant Lyapunov function or a parameter-independent Lyapunov function.

Definition 4.3.2. *(Robust Stability) The system (4.7) is said to be robustly stable if there exist a Lyapunov function $V_g(e, \rho) = e^T P(\rho)e > 0$, $P(\rho) > 0$ for every $e \neq 0$ and $V_g(0) = 0$ such that*

$$\frac{dV_g}{dt}(e, \rho) < 0 \tag{4.9}$$

for every $e \neq 0$ and $\dot{V}_g(0, \rho) = 0$ for all $\rho \in \Delta_\rho$. Such a Lyapunov function is often referred to as a parameter-dependent Lyapunov function.

Remark 4.3.1. *In order to distinguish between the two methodologies, the observer gain $L(\rho)\rho$ and the measurement noises attenuation level γ are denoted as $L_p(\rho)$ and γ_p for the polytopic approach and $L_g(\rho)$ and γ_g for the gridding approach.*

4.3.2 NLPV observer design using constant Lyapunov function

In this subsection, the problem of the NLPV observer design is reduced to the analysis of the stability of the system 4.7 by using a constant Lyapunov function.

According to [Apkarian, Gahinet, and Becker 1995], since the matrix $B(\rho)$ is affine in ρ and since the scheduling parameter ρ varies in a polytope $\mathcal{Y}$ of 2 vertices $\rho \in [\underline{\rho}, \overline{\rho}]$, it can be transformed into a convex interpolation as follows:

$$B(\rho) = \sum_{i=1}^{2} \alpha_i(\rho) B_i, \qquad \alpha_i(\rho) \geqslant 0, \qquad \sum_{i=1}^{2} \alpha_i(\rho) = 1 \tag{4.10}$$

where $B_1 = B(\underline{\rho})$, $B_2 = B(\overline{\rho})$ and the gain $L_p(\rho)$ is defined as follows:

$$L_p(\rho) = \sum_{i=1}^{2} \alpha_i(\rho) L_{pi} \tag{4.11}$$

with $L_{pi} \in \mathbb{R}^{5\times 2}$.

The observer vertex matrices L_{pi} are obtained by using the following theorem.

Theorem 4.3.1. *Consider the system model (4.2) and the observer (4.5). The observer design problem is solved if there exist a symmetric positive definite matrix P, a matrix Y_i with $i = 1, 2$ and a positive scalar ϵ_{lp} minimizing γ_p such that:*

$$\begin{bmatrix} \Omega_i & PB_i & P\bar{D}_1 + Y_i\bar{D}_2 \\ B_i^T P & -\epsilon_{lp} I & 0 \\ \bar{D}_1^T P - \bar{D}_2^T Y_i^T & 0 & -\gamma_p^2 I \end{bmatrix} < 0 \tag{4.12}$$

where $\Omega_i = A^T P + PA + Y_i C + C^T Y_i^T + \epsilon_{lp}\Gamma^T\Gamma + C_z^T C_z$

then the observer vertex matrices are $L_{pi} = -P^{-1}Y_i$, $i = 1, 2$.

Proof. Consider the following constant Lyapunov function candidate

$$V_p(e) = e^T P e. \tag{4.13}$$

Differentiating $V_p(e)$ and using (4.7), one gets

$$\begin{aligned} \frac{dV_p}{dt}(e) &= \dot{e}(t)^T P e(t) + e(t)^T P \dot{e}(t) \\ &= \begin{bmatrix} e \\ \Phi(x) - \Phi(\hat{x}) \\ \omega \end{bmatrix}^T \begin{bmatrix} \Omega_{1p}(\rho) & PB(\rho) & P(\bar{D}_1 - L_p(\rho)\bar{D}_2) \\ B(\rho)^T P & 0 & 0 \\ (\bar{D}_1 - L_p(\rho)\bar{D}_2)^T P & 0 & 0 \end{bmatrix} \begin{bmatrix} e \\ \Phi(x) - \Phi(\hat{x}) \\ \omega \end{bmatrix} \end{aligned} \tag{4.14}$$

where $\Omega_{1p}(\rho) = (A - L_p(\rho)C)^T P + P(A - L_p(\rho)C)$.

Defining $\eta = \begin{bmatrix} e \\ \Phi(x) - \Phi(\hat{x}) \\ \omega \end{bmatrix}$, one obtains

$$\dot{V}_p(t) = \eta^T M_p \eta \tag{4.15}$$

where

$$M_p = \begin{bmatrix} \Omega_{1p}(\rho) & PB(\rho) & P(\bar{D}_1 - L_p(\rho)\bar{D}_2) \\ B(\rho)^T P & 0 & 0 \\ (\bar{D}_1 - L_p(\rho)\bar{D}_2)^T P & 0 & 0 \end{bmatrix}$$

From (4.4), the following condition is obtained

$$\begin{aligned} &(\Phi(x) - \Phi(\hat{x}))^T (\Phi(x) - \Phi(\hat{x})) \leqslant e^T \Gamma^T \Gamma e \\ \Leftrightarrow &\eta^T Q_p \eta \leqslant 0 \end{aligned} \tag{4.16}$$

where $Q_p = \begin{bmatrix} -\Gamma^T\Gamma & 0 & 0 \\ 0 & I & 0 \\ 0 & 0 & 0 \end{bmatrix}$

Remark 4.3.2. *In the case if $\omega = 0$, the constant Lyapunov function (4.15) become*

$$\dot{V}_{p0} = \begin{bmatrix} e \\ \Phi(x) - \Phi(\hat{x}) \end{bmatrix}^T M_{p0} \begin{bmatrix} e \\ \Phi(x) - \Phi(\hat{x}) \end{bmatrix} \tag{4.17}$$

where $M_{p0} = \begin{bmatrix} \Omega_{1p}(\rho) & PB(\rho) \\ B(\rho)^T P & 0 \end{bmatrix}$ and the Lipschitz condition is

$$\begin{bmatrix} e \\ \Phi(x) - \Phi(\hat{x}) \end{bmatrix}^T Q_{p0} \begin{bmatrix} e \\ \Phi(x) - \Phi(\hat{x}) \end{bmatrix} \leqslant 0 \tag{4.18}$$

where $Q_p = \begin{bmatrix} -\Gamma^T\Gamma & 0 \\ 0 & I \end{bmatrix}$.

By applying the $\mathcal{S}$-procedure ([Boyd et al. 1994]) to constraint (4.18), the system is stable if there exists a positive scalar ϵ_{lp0} such that

$$\begin{aligned} &\begin{bmatrix} e \\ \Phi(x) - \Phi(\hat{x}) \end{bmatrix}^T M_{p0} \begin{bmatrix} e \\ \Phi(x) - \Phi(\hat{x}) \end{bmatrix} - \epsilon_{lp0} \begin{bmatrix} e \\ \Phi(x) - \Phi(\hat{x}) \end{bmatrix}^T Q_{p0} \begin{bmatrix} e \\ \Phi(x) - \Phi(\hat{x}) \end{bmatrix} < 0 \\ \Leftrightarrow &M_{p0} - \epsilon_{lp0} Q_{p0} < 0 \end{aligned} \tag{4.19}$$

Therefore, a sufficient condition for the stability of the system ((4.7)) when $\omega = 0$ is that

$$\begin{bmatrix} \Omega_{1p}(\rho) + \epsilon_{lp0}\Gamma^T\Gamma & PB(\rho) \\ B(\rho)^T P & -\epsilon_{lp0} I \end{bmatrix} < 0 \tag{4.20}$$

Now, in order to satisfy the objective design w.r.t. the $\mathcal{L}_2$ gain disturbance attenuation, the $\mathcal{H}_\infty$ performance index is defined as:

$$\begin{aligned} J_p &= e_z^T e_z - \gamma_p^2 \omega^T \omega \\ &= \eta^T R_p \eta \end{aligned} \tag{4.21}$$

where $R_p = \begin{bmatrix} C_z^T C_z & 0 & 0 \\ 0 & 0 & 0 \\ 0 & 0 & -\gamma_p^2 I \end{bmatrix}$

By applying the $\mathcal{S}$-procedure ([Boyd et al. 1994]) to both contraints (4.16) and $J_p \geq 0$, $\dot{V}_p < 0$ if there exists a scalar $\epsilon_{lp} > 0$ such that

$$\begin{aligned} &\dot{V}_p - \epsilon_{lp}(\eta^T Q_p \eta) + J_p < 0 \\ \Leftrightarrow &\eta^T (M_p - \epsilon_{lp} Q_p + R_p)\eta < 0 \end{aligned} \tag{4.22}$$

The condition (4.22) is equivalent to

$$\begin{aligned} &M_p - \epsilon_{lp} Q_p + R_p < 0 \\ \Leftrightarrow &\begin{bmatrix} \Omega_{1p}(\rho) + \epsilon_{lp}\Gamma^T\Gamma + C_z^T C_z & PB(\rho) & P(\bar{D}_1 - L_p(\rho)\bar{D}_2) \\ B(\rho)^T P & -\epsilon_{lp} I & 0 \\ (\bar{D}_1 - L_p(\rho)\bar{D}_2)^T P & 0 & -\gamma_p^2 I \end{bmatrix} < 0 \end{aligned} \tag{4.23}$$

Let define $Y_i = -PL_{pi}$ and substitute (4.10), (4.11) into (4.23), then the LMI (4.12) is obtained.

If (4.12) is satisfied, from (4.16), (4.22) implies that:

$$\dot{V}_p + J_p < 0 \tag{4.24}$$

Following the same steps, as presented in Chapter 3 (see Section 3.3.2), one obtains

$$\|e_z(t)\|_{\mathcal{L}_2}^2 < \gamma_p^2 \|\omega(t)\|_{\mathcal{L}_2}^2 \tag{4.25}$$

The proof of Theorem 4.3.1 is completed. □

The system (4.7) is quadratically stable if the Theorem (4.3.1) is satisfied. Notice that the quadratic stability is a stronger condition than the robust stability. Therefore, the NLPV observer design methodology based on robust stability is proposed in the next section.

4.3.3 NLPV observer design using parameter dependent Lyapunov function

In this section, the proposed approach is considering a parameter dependent Lyapunov function (PDLF).

In such a case, the derivative of the scheduling parameter $\dot{\rho}$ will appear and should be bounded.

The problem of the design of NLPV observer with PDLF is solved bellow.

Theorem 4.3.2. *Consider the system model (4.2) and the observer (4.5). Let assume that the parameter variation is bounded, i.e.* $|\dot{\rho}| \leq \nu$. *The observer design problem is solved if there exist a symmetric positive definite matrix* $P(\rho)$, *a matrix* $Y(\rho)$ *and a positive scalar* ϵ_{lg} *minimizing* γ_g *such that:*

$$\begin{bmatrix} \Omega_{1g}(\rho) & P(\rho)B(\rho) & P(\rho)\bar{D}_1 + Y(\rho)\bar{D}_2 \\ B(\rho)^T P(\rho) & -\epsilon_{lg} I & 0 \\ (\bar{D}_1 P(\rho) + \bar{D}_2)^T Y(\rho)^T & 0 & -\gamma_g^2 I \end{bmatrix} < 0 \tag{4.26}$$

where $\Omega_{1g}(\rho) = A^T P(\rho) + P(\rho)A + Y(\rho)C + C^T Y(\rho)^T \pm \nu \frac{\partial P}{\partial \rho} + \epsilon_{lg}\Gamma^T\Gamma + C_z^T C_z$

Then the parameter dependent observer gain is $L_g(\rho) = -P(\rho)^{-1}Y(\rho)$

Proof. Consider the following parameter dependent Lyapunov function candidate

$$V_g(e, \rho) = e^T P(\rho) e. \tag{4.27}$$

Differentiating $V_g(e, \rho)$ along the solution of (4.7) yields

$$\begin{aligned} \frac{dV_g}{dt}(e, \rho) &= \dot{e}(t)^T P(\rho) e(t) + e(t)^T P(\rho)\dot{e}(t) + e(t)^T \dot{P}(\rho) e(t) \\ &= \dot{e}(t)^T P(\rho) e(t) + e(t)^T P(\rho)\dot{e}(t) + e(t)^T \dot{\rho}\frac{\partial P}{\partial \rho} e(t) \\ &= \eta^T M_g \eta \end{aligned} \tag{4.28}$$

where

$$M_g = \begin{bmatrix} (A - L_g(\rho)C)^T P(\rho) + P(\rho)(A - L_g(\rho)C) + \dot{\rho}\frac{\partial P}{\partial \rho} & P(\rho)B(\rho) & P(\rho)(\bar{D}_1 - L_g(\rho)\bar{D}_2) \\ B(\rho)^T P(\rho) & 0 & 0 \\ (\bar{D}_1 - L_g(\rho)\bar{D}_2)^T P(\rho) & 0 & 0 \end{bmatrix}.$$

Similarly to (4.16), the following condition is obtained from the Lipschitz condition (4.4)

$$\begin{aligned} &(\Phi(x) - \Phi(\hat{x}))^T (\Phi(x) - \Phi(\hat{x})) \leqslant e^T \Gamma^T \Gamma e, \\ \Leftrightarrow &\eta^T Q_g \eta \leqslant 0, \end{aligned} \tag{4.29}$$

where $Q_g = \begin{bmatrix} -\Gamma^T\Gamma & 0 & 0 \\ 0 & I & 0 \\ 0 & 0 & 0 \end{bmatrix}$.

Remark 4.3.3. *According to the same steps in Remark 4.3.2, the estimation error dynamics system (4.7) is robustly stable in the case of* $\omega = 0$ *if there exists a positive scalar* ϵ_{lg0} *such that*

$$\begin{bmatrix} (A - L_g(\rho)C)^T P(\rho) + P(\rho)(A - L_g(\rho)C) + \dot{\rho}\frac{\partial P}{\partial \rho} + \epsilon_{lg0}\Gamma^T\Gamma & P(\rho)B(\rho) \\ B(\rho)^T P(\rho) & -\epsilon_{lg0} I \end{bmatrix} < 0 \tag{4.30}$$

In order to satisfy the objective design w.r.t. the $\mathcal{L}_2$ gain disturbance attenuation, the $\mathcal{H}_\infty$ performance index is defined as:

$$\begin{aligned} J_g &= e_z^T e_z - \gamma_g^2 \omega^T \omega \\ &= \eta^T R_g \eta \end{aligned} \tag{4.31}$$

where $R_g = \begin{bmatrix} C_z^T C_z & 0 & 0 \\ 0 & 0 & 0 \\ 0 & 0 & -\gamma_g^2 I \end{bmatrix}$

By applying the $\mathcal{S}$-procedure ([Boyd et al. 1994]) to both contraints (4.29) and $J_g \geq 0$, then $\dot{V}_g < 0$ if there exists a scalar $\epsilon_{lg} > 0$ such that

$$\begin{aligned} &\dot{V}_g - \epsilon_{lg}(\eta^T Q_g \eta) + J_g < 0 \\ \Leftrightarrow &\eta^T (M_g - \epsilon_{lg} Q_g + R_g)\eta < 0 \end{aligned} \tag{4.32}$$

The condition (4.32) is equivalent to

$$\begin{aligned} &M_g - \epsilon_{lg} Q_g + R_g < 0 \\ \Leftrightarrow &\begin{bmatrix} \Omega_g(\rho) + \dot{\rho}\frac{\partial P}{\partial \rho} + \epsilon_{lg}\Gamma^T\Gamma + C_z^T C_z & P(\rho)B(\rho) & P(\rho)(\bar{D}_1 - L_g(\rho)\bar{D}_2) \\ B(\rho)^T P(\rho) & -\epsilon_{lg} I & 0 \\ (\bar{D}_1 - L_g(\rho)\bar{D}_2)^T P(\rho) & 0 & -\gamma_g^2 I \end{bmatrix} < 0 \end{aligned} \tag{4.33}$$

where $\Omega_g(\rho) = (A - L_g(\rho)C)^T P(\rho) + P(\rho)(A - L_g(\rho)C)$.

Note that the above inequality (4.33) holds if the following inequality holds

$$\begin{bmatrix} \Omega_g(\rho) \pm \nu\frac{\partial P}{\partial \rho} + \epsilon_{lg}\Gamma^T\Gamma + C_z^T C_z & P(\rho)B(\rho) & P(\rho)(\bar{D}_1 - L_g(\rho)\bar{D}_2) \\ B(\rho)^T P(\rho) & -\epsilon_{lg} I & 0 \\ (\bar{D}_1 - L_g(\rho)\bar{D}_2)^T P(\rho) & 0 & -\gamma_g^2 I \end{bmatrix} < 0 \tag{4.34}$$

Let define $Y(\rho) = -P(\rho)L_g(\rho)$ and substitute into (4.34), then the LMI (4.26) is obtained.

If (4.26) is satisfied, from (4.4), (4.32) implies that:

$$\dot{V}_g + J_g < 0 \tag{4.35}$$

Following the same steps, as presented in Chapter 3 (see Section 3.3.2), one obtains

$$\|e_z(t)\|_{\mathcal{L}_2}^2 < \gamma_g^2 \|\omega(t)\|_{\mathcal{L}_2}^2 \tag{4.36}$$

The proof of Theorem 4.3.2 is completed. □

It is worth noting that the solutions of $P(\rho)$ and $Y(\rho)$ are required to satisfy an infinite number of constraints overall the trajectories of ρ. To relax the problem, a gridding method is used to solve the LMI (4.26). It will be solved for a set of frozen values of the scheduling

parameter vector, assumed to belong to a gridded domain of ρ. Here, the polynomial form is chosen to express the functional dependence matrices $P(\rho)$, $L_g(\rho)$ and $Y(\rho)$ on ρ as follows:

$$P(\rho) = P_0 + \rho P_1 \tag{4.37}$$
$$L_g(\rho) = L_{g0} + \rho L_{g1} \tag{4.38}$$

From (4.37) and (4.38), the following form is obtained

$$\begin{aligned} Y(\rho) = -P(\rho)L_g(\rho) &= -P_0L_{g0} - \rho(P_1L_{g0} + P_0L_{g1}) - \rho^2 P_1L_{g1} \\ &= Y_0 + \rho Y_1 + \rho^2 Y_2 \end{aligned} \tag{4.39}$$

where

$$Y_0 = -P_0L_{g0} \tag{4.40}$$
$$Y_1 = -P_1L_{g0} - P_0L_{g1} \tag{4.41}$$
$$Y_2 = -P_1L_{g1} \tag{4.42}$$

From the solutions $P(\rho)$ and $Y(\rho)$ at gridded points, the matrices P_0, P_1, Y_0, Y_1, Y_3 are obtained.

From (4.40)-(4.42), the following equation is obtained

$$-\begin{bmatrix} P_0 & 0 \\ P_1 & P_0 \\ 0 & P_1 \end{bmatrix} \begin{bmatrix} L_{g0} \\ L_{g1} \end{bmatrix} = \begin{bmatrix} Y_0 \\ Y_1 \\ Y_2 \end{bmatrix} \tag{4.43}$$

which leads to the observer matrices L_0 and L_1 as follows:

$$\begin{bmatrix} L_{g0} \\ L_{g1} \end{bmatrix} = -\begin{bmatrix} P_0 & 0 \\ P_1 & P_0 \\ 0 & P_1 \end{bmatrix}^+ \begin{bmatrix} Y_0 \\ Y_1 \\ Y_2 \end{bmatrix} \tag{4.44}$$

where $(\cdot)^+$ is the generalized inverse of matrix $(\cdot)$.

4.4 Synthesis results and frequency domain analysis

In this section, the proposed approaches are applied to estimate the damper force in the vehicle suspension system. First let us recall the NLPV system model where the quarter car system is described by:

$$\begin{cases} \dot{x} &= Ax + B(\rho)\Phi(x) + \bar{D}_1\omega \\ y &= Cx + \bar{D}_2\omega \end{cases} \tag{4.45}$$

where the system matrices are as follows

$$A = \begin{bmatrix} 0 & 1 & 0 & -1 & 0 \\ -\frac{(k_s+k_0)}{m_s} & -\frac{c_0}{m_s} & 0 & \frac{c_0}{m_s} & -\frac{1}{m_s} \\ 0 & 0 & 0 & 1 & 0 \\ \frac{(k_s+k_0)}{m_{us}} & \frac{c_0}{m_{us}} & -\frac{k_t}{m_{us}} & -\frac{c_0}{m_{us}} & \frac{1}{m_{us}} \\ 0 & 0 & 0 & 0 & -\frac{1}{\tau} \end{bmatrix}, B(\rho) = \begin{bmatrix} 0 \\ 0 \\ 0 \\ 0 \\ \frac{f_c}{\tau}\rho \end{bmatrix}, \bar{D}_1 = \begin{bmatrix} 0 & 0 \\ 0 & 0 \\ -1 & 0 \\ 0 & 0 \\ 0 & 0 \end{bmatrix},$$

$$C = \begin{bmatrix} -\frac{(k_s+k_0)}{m_s} & -\frac{c_0}{m_s} & 0 & \frac{c_0}{m_s} & -\frac{1}{m_s} \\ \frac{(k_s+k_0)}{m_{us}} & \frac{c_0}{m_{us}} & -\frac{k_t}{m_{us}} & -\frac{c_0}{m_{us}} & \frac{1}{m_{us}} \end{bmatrix}, \bar{D}_2 = \begin{bmatrix} 0 & 0.01 \\ 0 & 0.01 \end{bmatrix},$$

the scheduling parameter ρ in the considered application is the control signal u. In practice, its derivative $\dot{\rho}$ is bouned $|\dot{\rho}| \leq \nu$ even if the controller change very fast (Skyhook controller) due to the limitation of the sampling time.

4.4.1 Synthesis results

As previously mentioned, the control signal u in the INOVE testbed (duty cycle of PWM signal) is limited in the range of $[0, 1]$. Therefore, the following values are obtained Therefore, the following values are obtained

- The lower bound of the scheduling parameter $\underline{\rho} = 0$.
- The upper bound of the scheduling parameter $\overline{\rho} = 1$.
- The rate-bounded value of the scheduling parameter $\nu = \frac{\overline{\rho}-\underline{\rho}}{T_s} = 200$ where $T_s = 0.005s$.

1) First case (constant Lyapunov function) (see subsection 4.3.2)

Solving Theorem 4.3.1 with the two vertices $\underline{\rho} = 0$ and $\overline{\rho} = 1$, leads to the minimum $\mathcal{L}_2$-induced gain $\gamma_p = 1.0001$, $\epsilon_{lp} l = 4$ and to the observer vertex matrices

$$L_{p1} = \begin{bmatrix} -3.4572 & -0.0015 \\ -3.7771 & -0.0022 \\ -5.1680 & -4.8398 \\ -0.4777 & 0.9998 \\ 107.9617 & -0.9147 \end{bmatrix}, L_{p2} = \begin{bmatrix} -3.4397 & -0.0015 \\ -3.7503 & -0.0022 \\ -5.1910 & -4.8392 \\ -0.4750 & 0.9998 \\ 42.2868 & 0.0204 \end{bmatrix}$$

Then, the varying observer gain $L_p(\rho)$ is as follows:

$$L_p(\rho) = \frac{|\rho - \overline{\rho}|}{\overline{\rho} - \underline{\rho}} L_{p1} + \frac{|\rho - \underline{\rho}|}{\overline{\rho} - \underline{\rho}} L_{p2}. \tag{4.46}$$

2) Second case (parameter dependent Lyapunov function) (see subsection 4.3.3)

Applying the Theorem 4.3.2 at the gridded points which are defined by ρ as follows

$$\rho = [0 \quad 0.1 \quad 0.2 \quad 0.3 \quad 0.4 \quad 0.5 \quad 0.6 \quad 0.7 \quad 0.8 \quad 0.9 \quad 1]\,. \tag{4.47}$$

leads to $\gamma_g = 1.4142$, $\epsilon_{lg} = 154.3930$ and to the observer matrices L_{g0} and L_{g1}

$$L_{g0} = \begin{bmatrix} -0.0164 & 0.0001 \\ 0.7678 & 0.0009 \\ -20.6704 & -0.0162 \\ -0.0233 & 1.0001 \\ 0.1226 & -4.1288e-05 \end{bmatrix}, L_{g1} = \begin{bmatrix} 0.0001 & 1.2217e-06 \\ 0.0023 & 4.5395e-06 \\ -0.1327 & -1.6305e-06 \\ 0.0002 & 4.7422e-07 \\ -0.0481 & 0.0001 \end{bmatrix}$$

Finally, the varying observer gain $L_g(\rho)$ is obtained by using the following polynomial function

$$L_g(\rho) = L_{g0} + \rho L_{g1}. \tag{4.48}$$

4.4.2 Frequency domain analysis

Before doing the frequency domain analysis, the estimation error dynamics system is recalled as follows:

$$\dot{e} = (A - L(\rho)C)e + B(\rho)(\Phi(x) - \Phi(\hat{x})) + (\bar{D}_1 - L(\rho)\bar{D}_2)\begin{pmatrix}\omega_r \\ \omega_n\end{pmatrix} \tag{4.49}$$

where the state estimation error $e = x - \hat{x}$ with $x = [z_s - z_{us}, \dot{z}_s, z_{us} - z_r, \dot{z}_{us}, F_{er}]^T$.

The above system (4.49) has the three inputs such as ω_r, ω_n and $\Phi(x) - \Phi(\hat{x})$, and the output being the state estimation error e. Therefore, in this section, the analysis of the effects of these inputs on e in the frequency domain will be done through the Bode diagrams of the transfer functions between these inputs and the output e.

The resulting attenuation of the road profile disturbance and of the sensor noises on the estimation errors is shown in Figures 4.1, 4.2, 4.3 and 4.4 respectively. The effect of the difference $(\Phi(x) - \Phi(\hat{x}))$ on the state estimation error e is shown in Figures 4.5 and 4.6. According these Figures, we have some comments as follows:

- Figures 4.1 and 4.2 show the Bode diagrams of the estimation error systems of the polytopic method at the frozen values of two vertices ($\rho = \underline{\rho} = 0$ (blue line) and $\rho = \overline{\rho} = 1$ (green dash-dot)) and of the gridding method at the frozen values of 11 grid points (red line) with input ω_r (road profile derivative) and outputs e_i with $i = 1 \div 5$ (the state estimation errors). These results emphasize the satisfactory attenuation level of the unknown road profile derivative effect on the 5 estimation errors e.
- In the case of the sensors noises attenuation, the transfer function between the state estimation errors and the input sensor noises ω_n of both methods are shown in the

Figures 4.3 and 4.4. We can see that the gridding method improves the ability of measurement noise rejection, which is indicated in the transfer function e_5/ω_r in Figure 4.4.

- Figures 4.5 and 4.6 show the the effect of the mismatch between estimated nonlinearity and real one $(\Phi(x) - \Phi(\hat{x}))$ on the state estimation error e in frequency domain. Figure 4.5 gives the Bode diagram of the transfer function $\|e/(\Phi(x) - \Phi(\hat{x}))\|$ of the polytopic method at the frozen values ($\rho = 0.01$ (blue line) and $\rho = 1$ (green dash-dot)) while Figure 4.6 shows the Bode diagram at frozen values of that transfer function at 11 grid point of the gridding method.

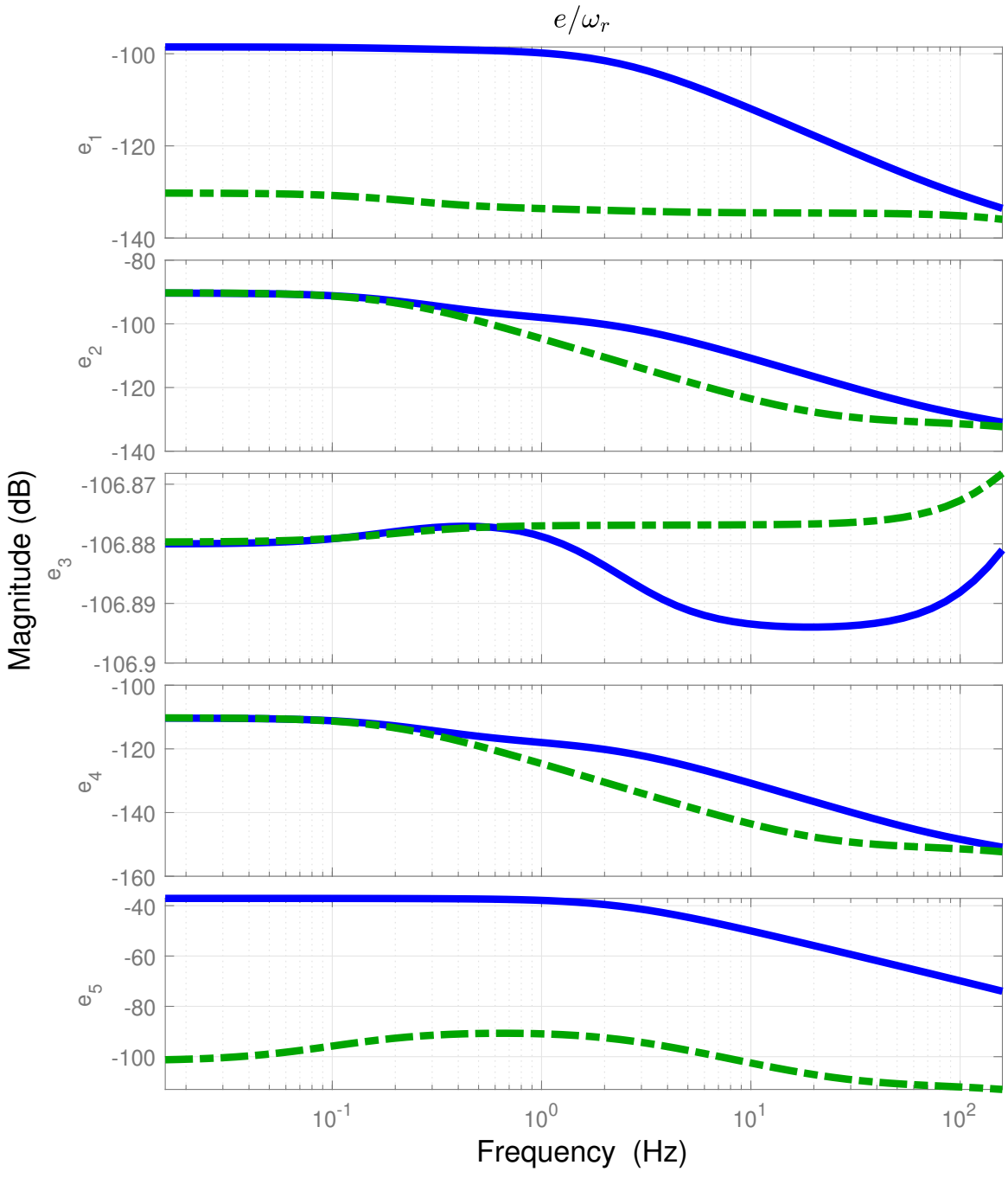

Figure 4.1: Transfer $\|e/\omega_r\|$- Bode diagrams of NLPV observer w.r.t. road profile derivative disturbance-polytopic method.

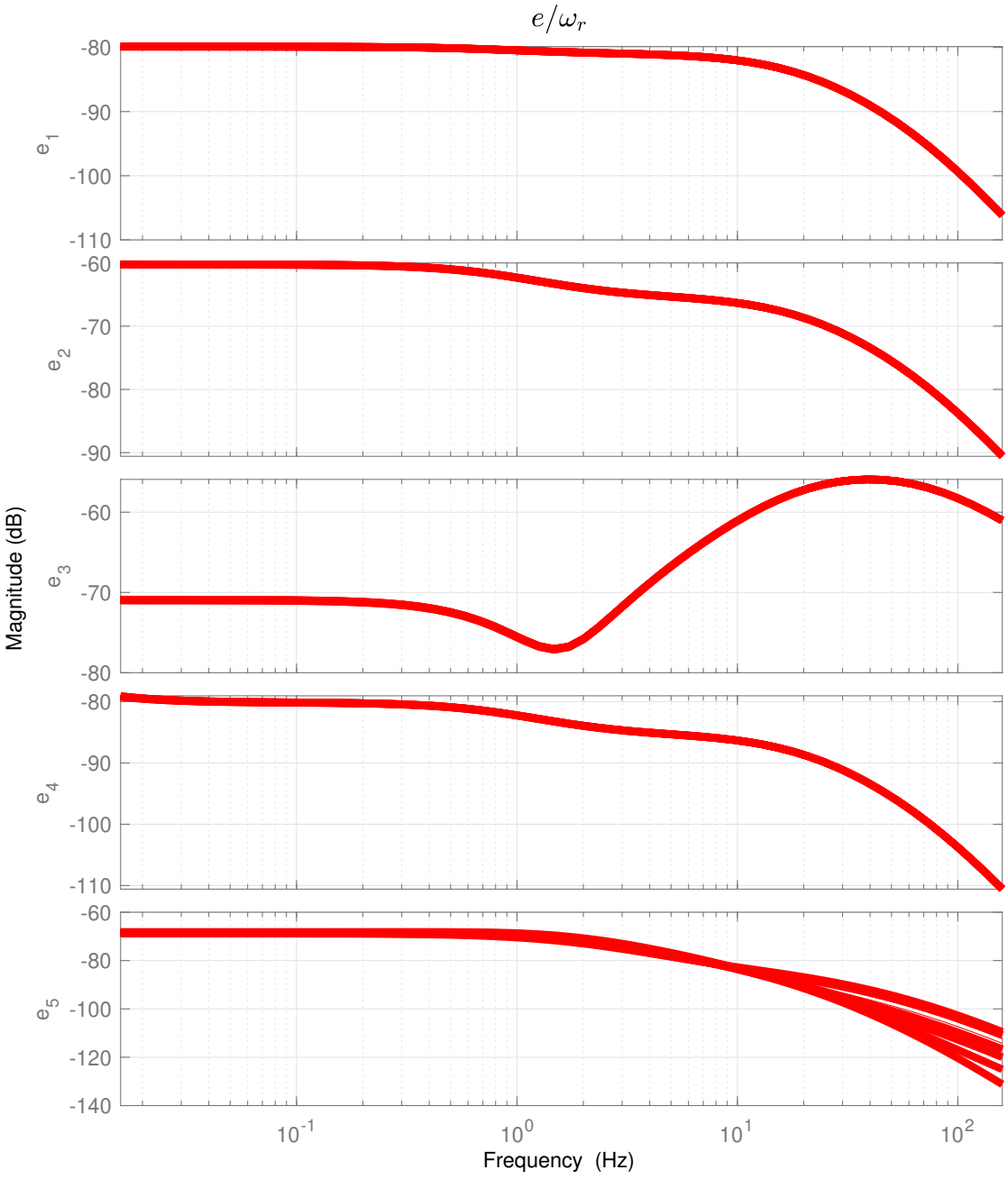

Figure 4.2: Transfer $\|e/\omega_r\|$- Bode diagrams of NLPV observer w.r.t. road profile derivative disturbance- gridding method.

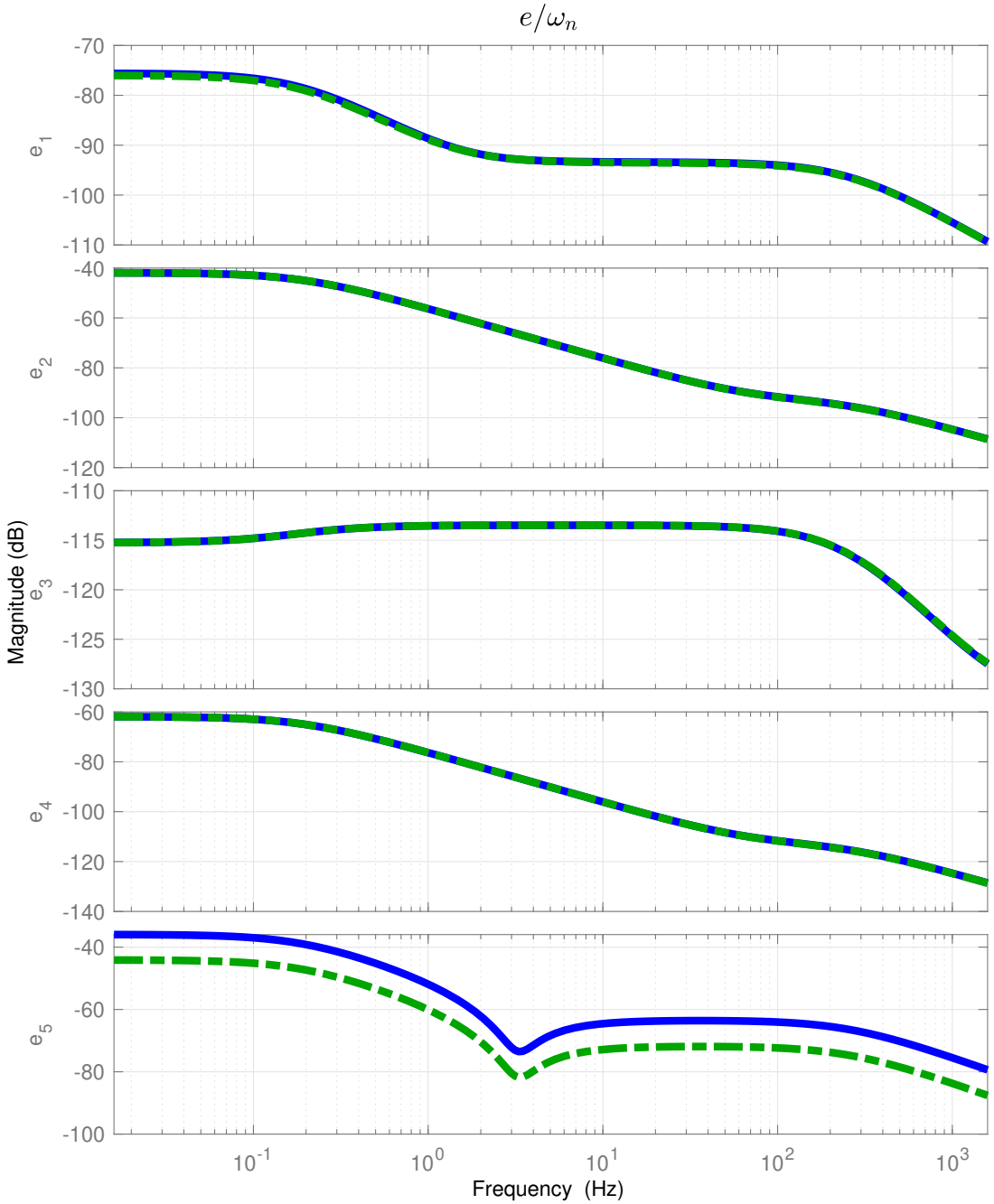

Figure 4.3: Transfer $\|e/\omega_n\|$- Bode diagrams of NLPV observer w.r.t. measurement noises-polytopic method .

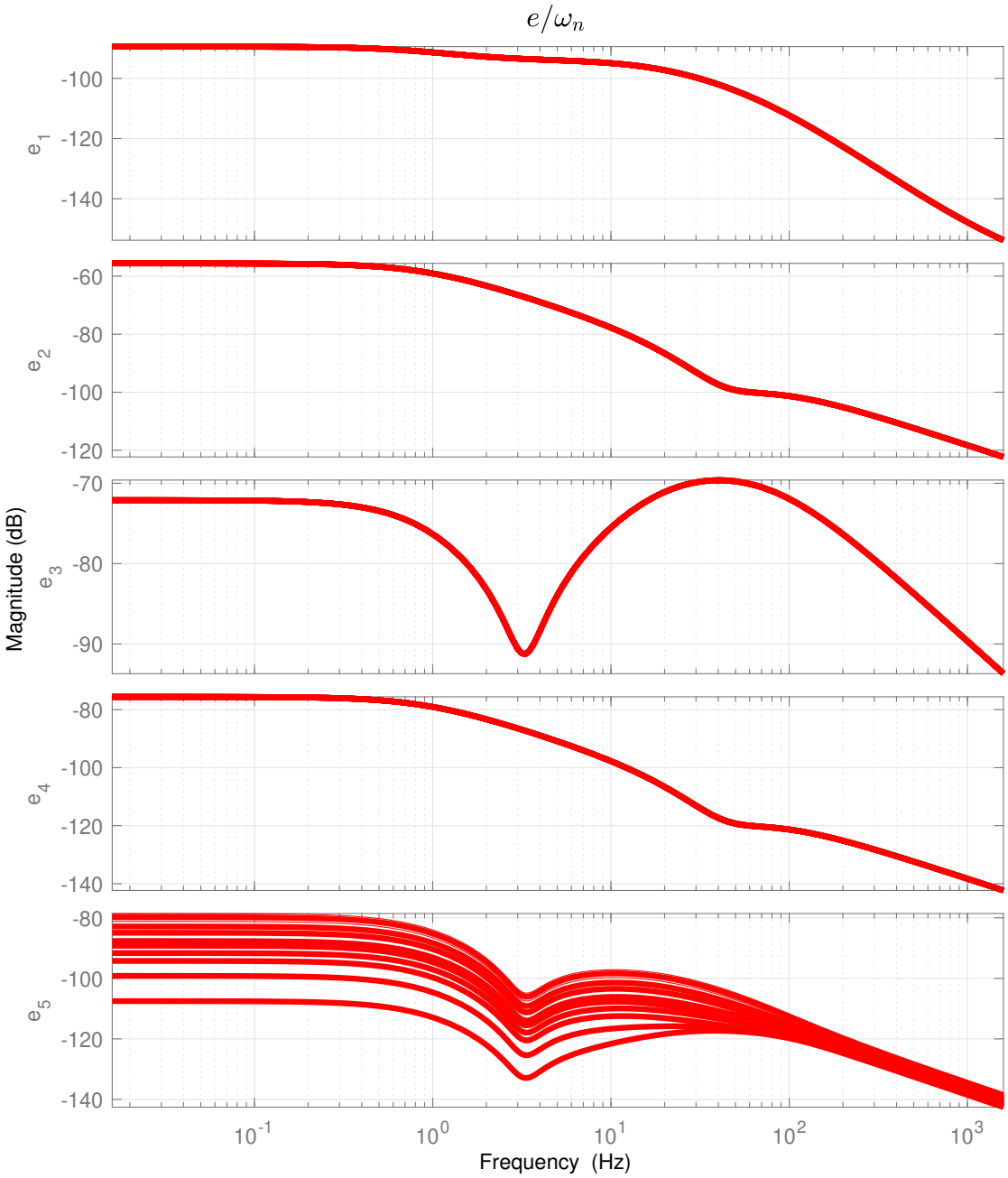

Figure 4.4: Transfer $\|e/\omega_n\|$- Bode diagrams of NLPV observer w.r.t. measurement noises-gridding method.

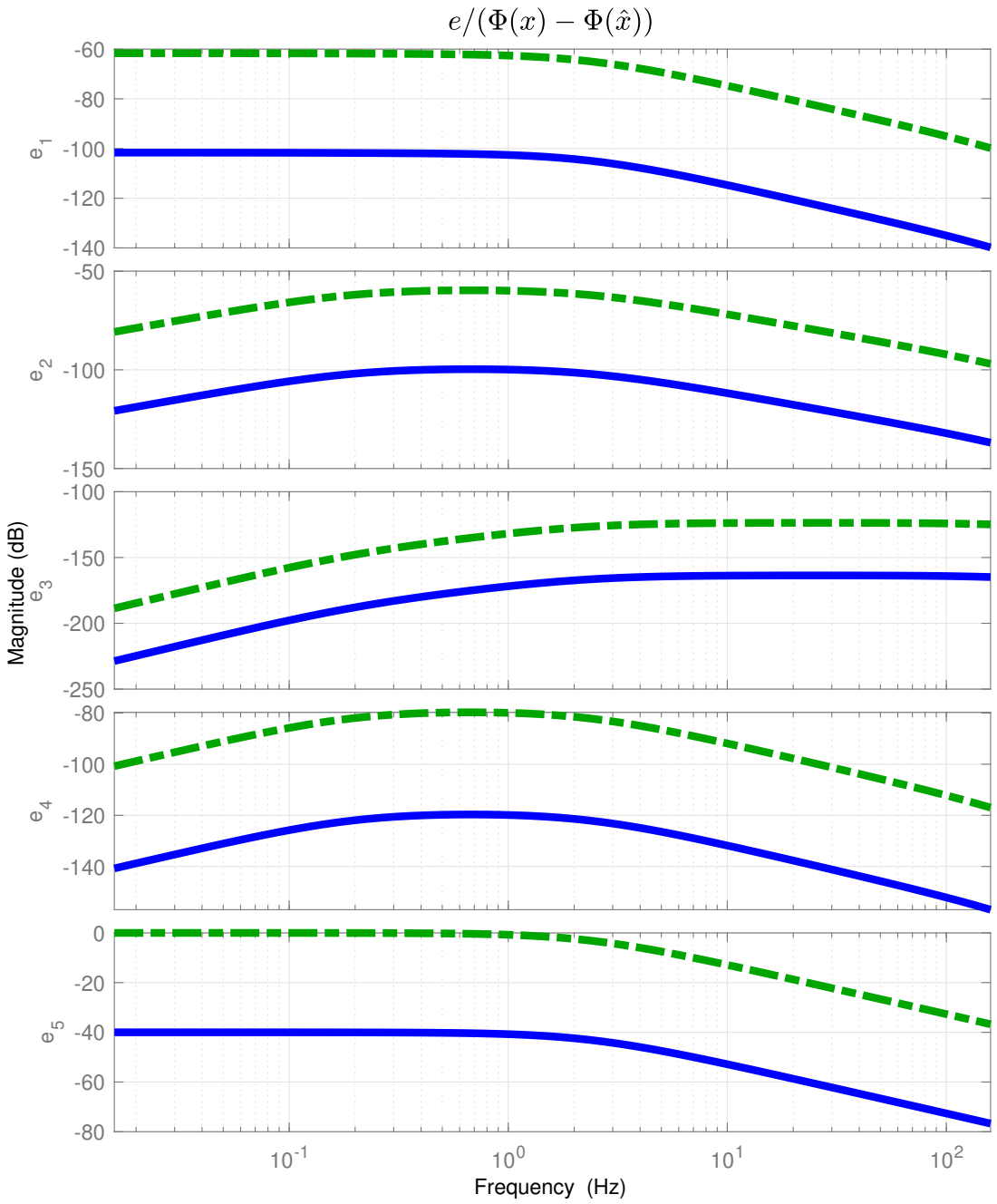

Figure 4.5: Transfer $\|e/(\Phi(x)-\Phi(\hat{x}))\|$- Bode diagrams of NLPV observer w.r.t. nonlinearity-polytopic method.

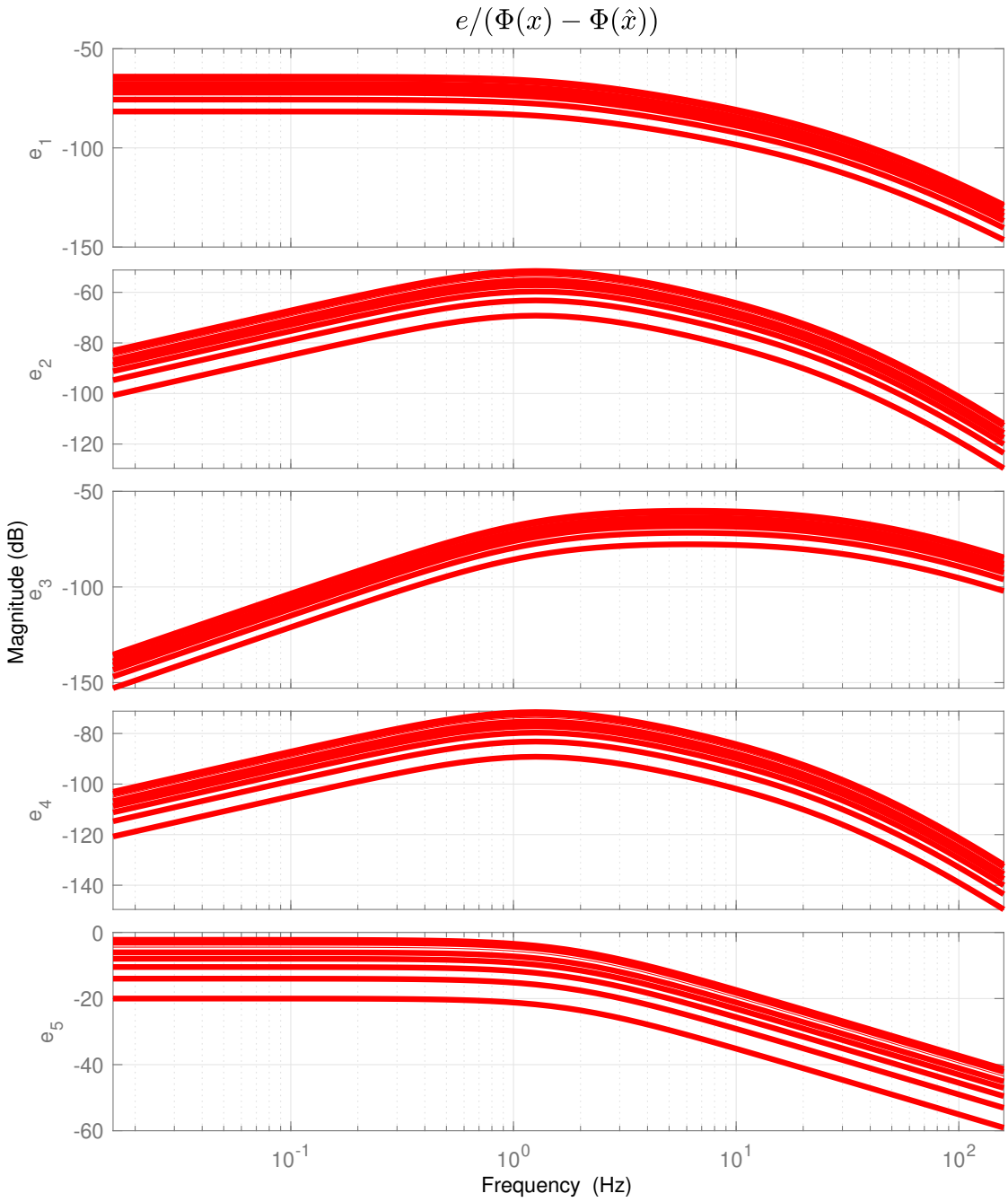

Figure 4.6: Transfer $\|e/(\Phi(x) - \Phi(\hat{x}))\|$- Bode diagrams of NLPV observer w.r.t. nonlinearity-gridding method.

Figures 4.7 and 4.8 show the upper bound on the singular values $\bar{\sigma}(e/\omega_r)$ and $\bar{\sigma}(e/\omega_n)$, respectively. Figure 4.7 shows the values $\bar{\sigma}(e/\omega_r)$ at fozen values of two vertices of the polytopic NLPV observer (blue line and green dash-dot) and the value $\bar{\sigma}(e/\omega_r)$ at fozen value of 11 gridded points of the gridding NLPV observer (red line). According to Figure 4.8, these results emphasize the effectiveness of the polytopic and gridding NLPV observers in terms of noise rejection, since the upper bound on the singular values decreases rapidly in the region of high-frequency noises [10Hz-1000Hz].

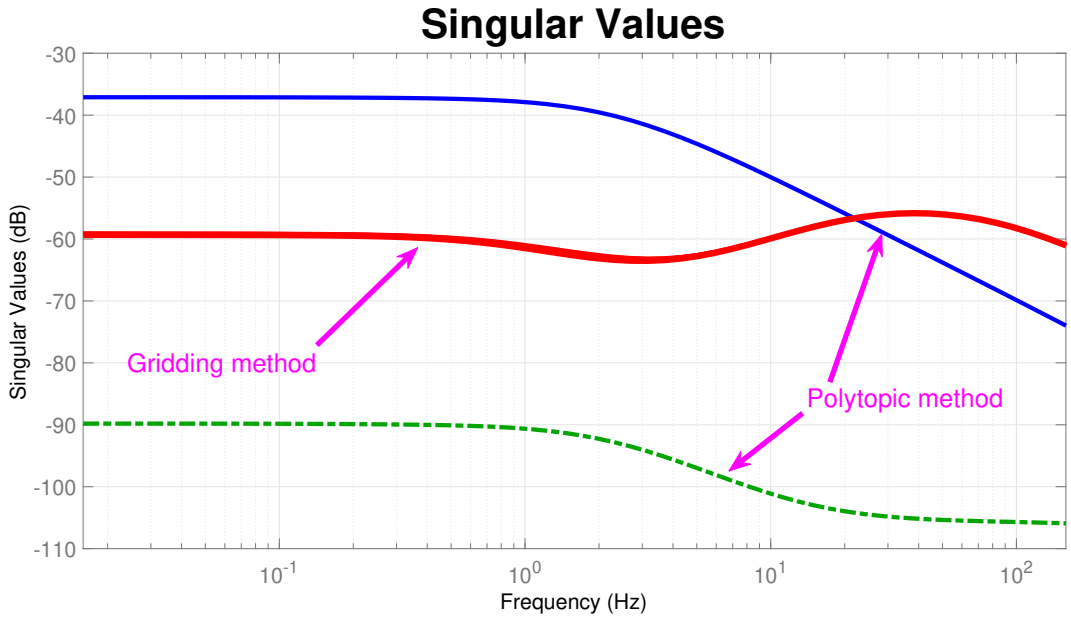

Figure 4.7: $\bar{\sigma}(e/\omega_r)$- (blue line and green dash-dot) Polytopic method and (red line) Gridding method.

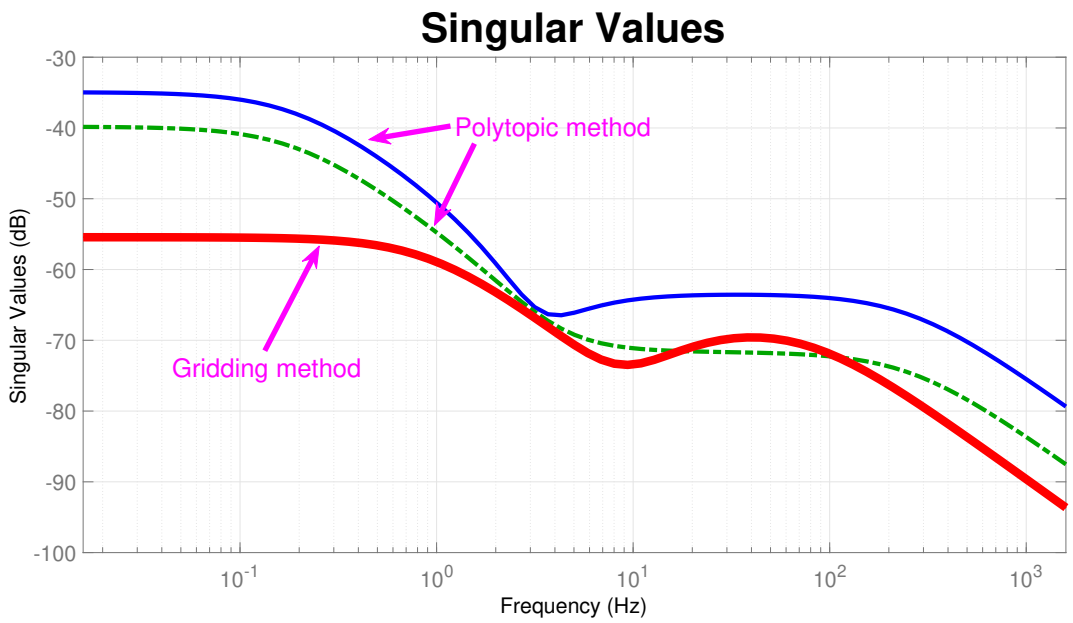

Figure 4.8: $\bar{\sigma}(e/\omega_n)$- (blue line and green dash-dot) Polytopic method and (red line) Gridding method.

4.5 Simulation Results

In this section, four simulations are performed with the nonlinear parameter varying system (4.2) and are analysed in the time-domain framework. The initial state conditions for the quarter car system (x_0), the polytopic NLPV observer ($\hat{x}_{p0}$) and the gridding NLPV observer ($\hat{x}_{g0}$) are chosen as follows:

$$x_0 = \begin{bmatrix} 0, & 0, & 0, & 0, & 0 \end{bmatrix}^T$$
$$\hat{x}_{p0} = \hat{x}_{g0} = \begin{bmatrix} 0.01, & -0.1, & 0.001, & -0.1, & 5 \end{bmatrix}^T$$

The estimated force F_d is then defined as: $F_d = k_0\hat{x}_1 + c_0(\hat{x}_2 - \hat{x}_4) + \hat{x}_5$.

The four simulation scenarios are designed to evaluate the performance of the proposed observers, detailed in the following subsections.

4.5.1 Simulation scenario 1

In the first scenario, a chirp signal as the road profile is used to evaluate the robustness of the observers for various road frequencies (from 0 Hz to 10 Hz). This simulation scenario is the following:

- The road profile input is a chirp signal with the amplitude at $4 \cdot 10^{-3}$ (m), shown in

Figure 4.9 (top).

- The control input u is constant ($u = 0.35$) as seen in Figure 4.9 (bottom).

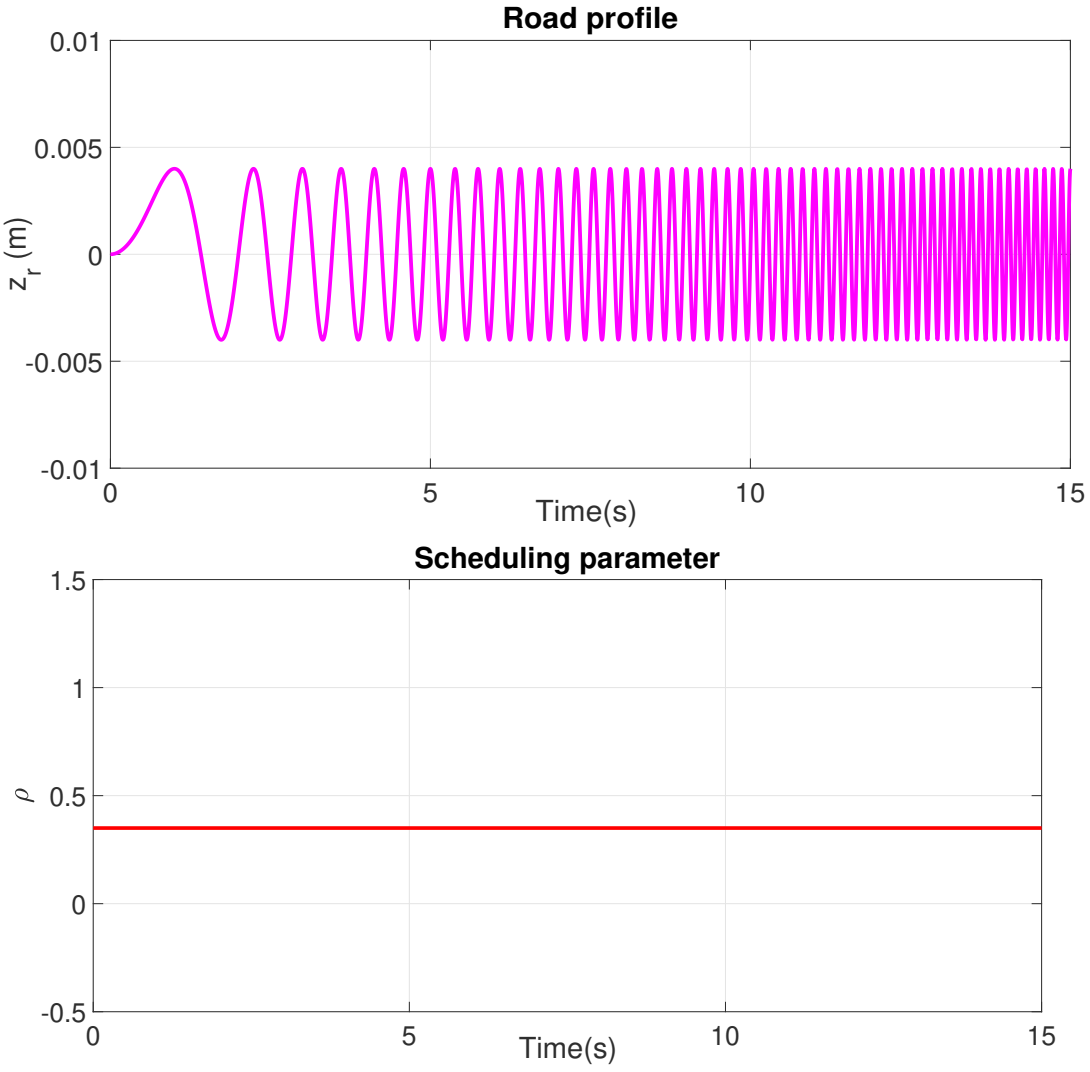

Figure 4.9: Simulation senario 1: (top) Road profile, (bottom) PWM signal

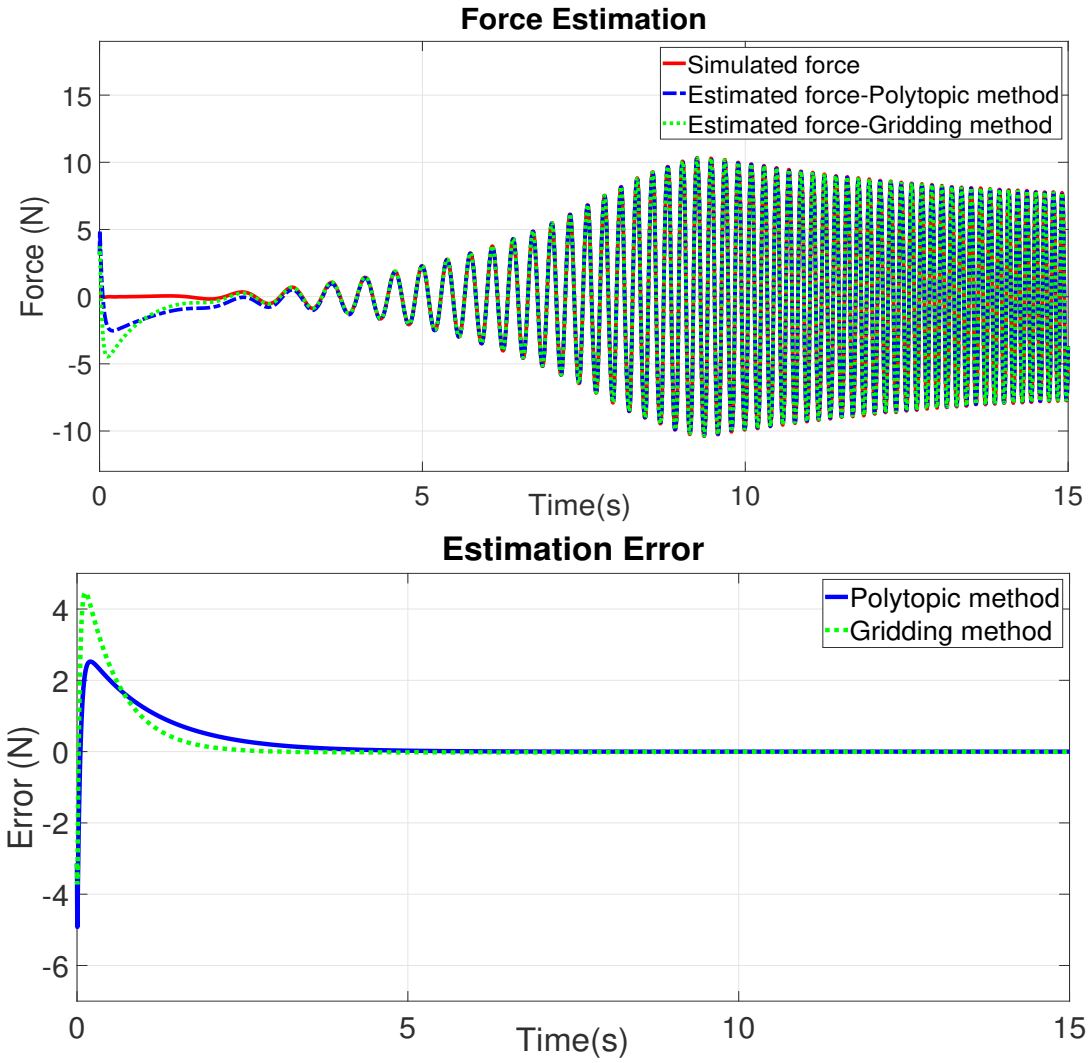

Figure 4.10: Simulation senario 1: (top) Damper force, (bottom) Estimation error

Figure 4.10 (top) shows the simulated force (solid red line), the estimated force of the polytopic NLPV observer (blue dash line), and the estimated force of the gridding NLPV observer (solid green dot line). The estimation error of the two proposed methods are shown in the right side of Figure 4.10. We can see that the estimation errors converges to 0 after 2 seconds for the gridding NLPV method (green dot line) and 3 seconds for the polytopic NLPV method (blue line); however the high overshoot occures for the gridding method. Therefore, the robustness of the proposed observers to the frequency content of the road profile disturbance is proved. Moreover, Figure 4.11 shows the estimated variable $\hat{z}_e$ and the variable z_e. These results prove the accuracy of the proposed observers not only in estimated damping force but also in estimated states.

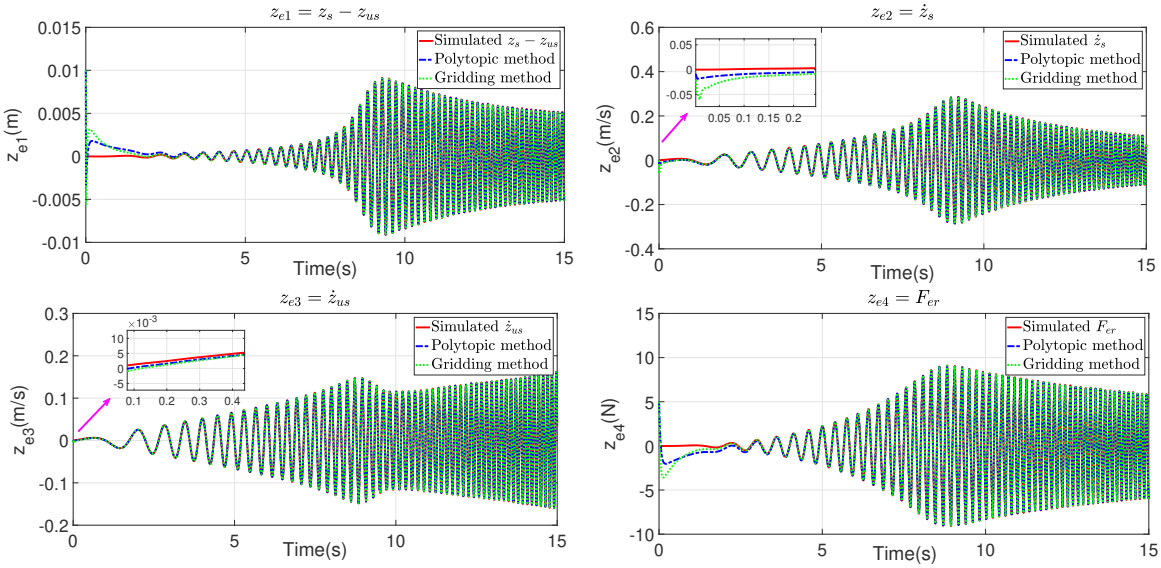

Figure 4.11: Simulation senario 1: (top-left) $z_{e1} = z_s - z_{us}$, (top-right) $z_{e2} = \dot{z}_s$, (bottom-left) $z_{e3} = \dot{z}_{us}$, (bottom-right) $z_{e4} = F_{er}$.

4.5.2 Simulation scenario 2

In the second simulation, the performance of the NLPV observers is assessed via the simulation scenario with a typical road disturbance and the low-frequency control input. This scenario is as follows:

- An ISO 8608 road profile signal (Type C) is used as seen in the top of Figure 4.12.

- The control input is a sine wave with the frequency at 0.1 Hz, shown in Figure 4.12 (bottom).

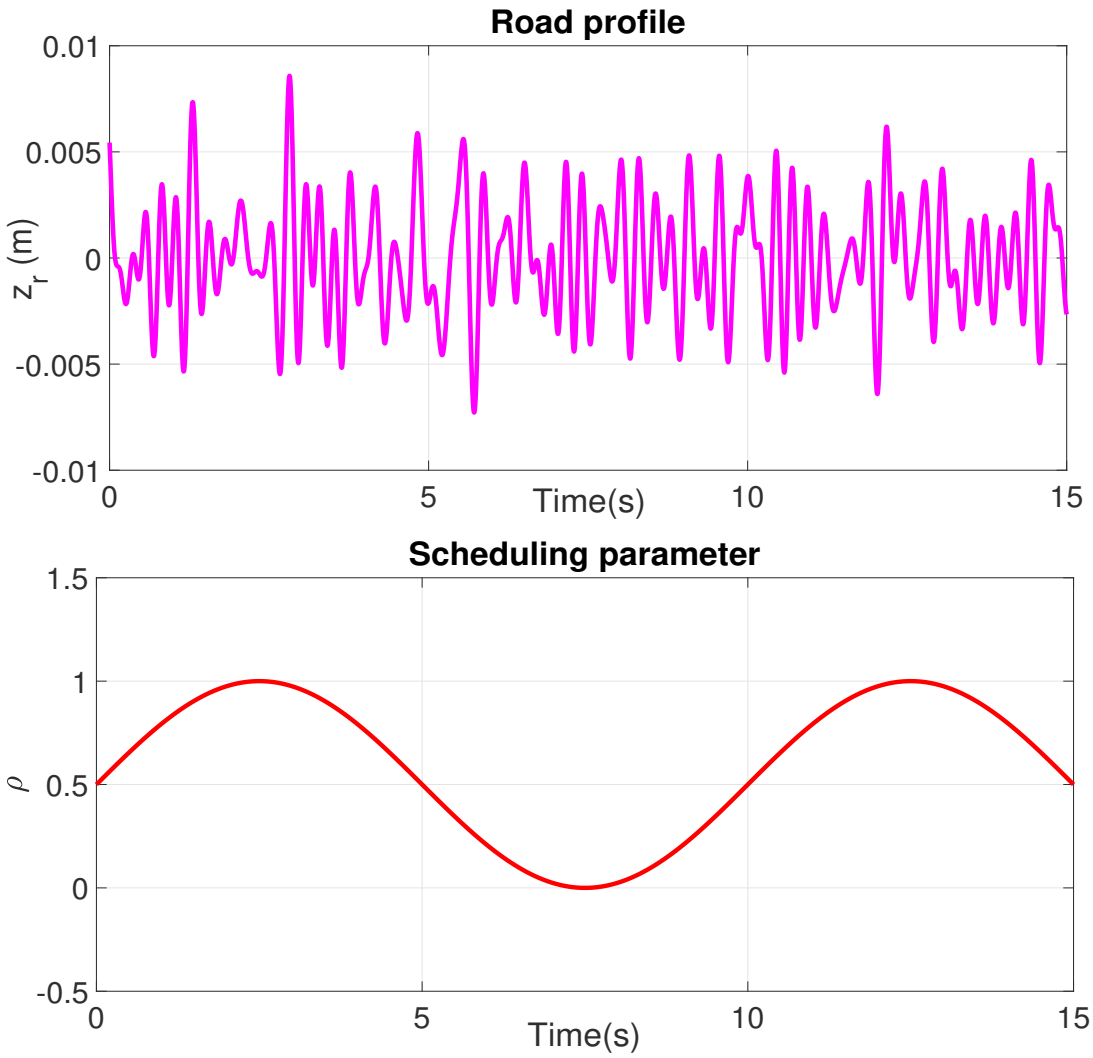

Figure 4.12: Simulation senario 2: (top) Road profile, (bottom) PWM signal

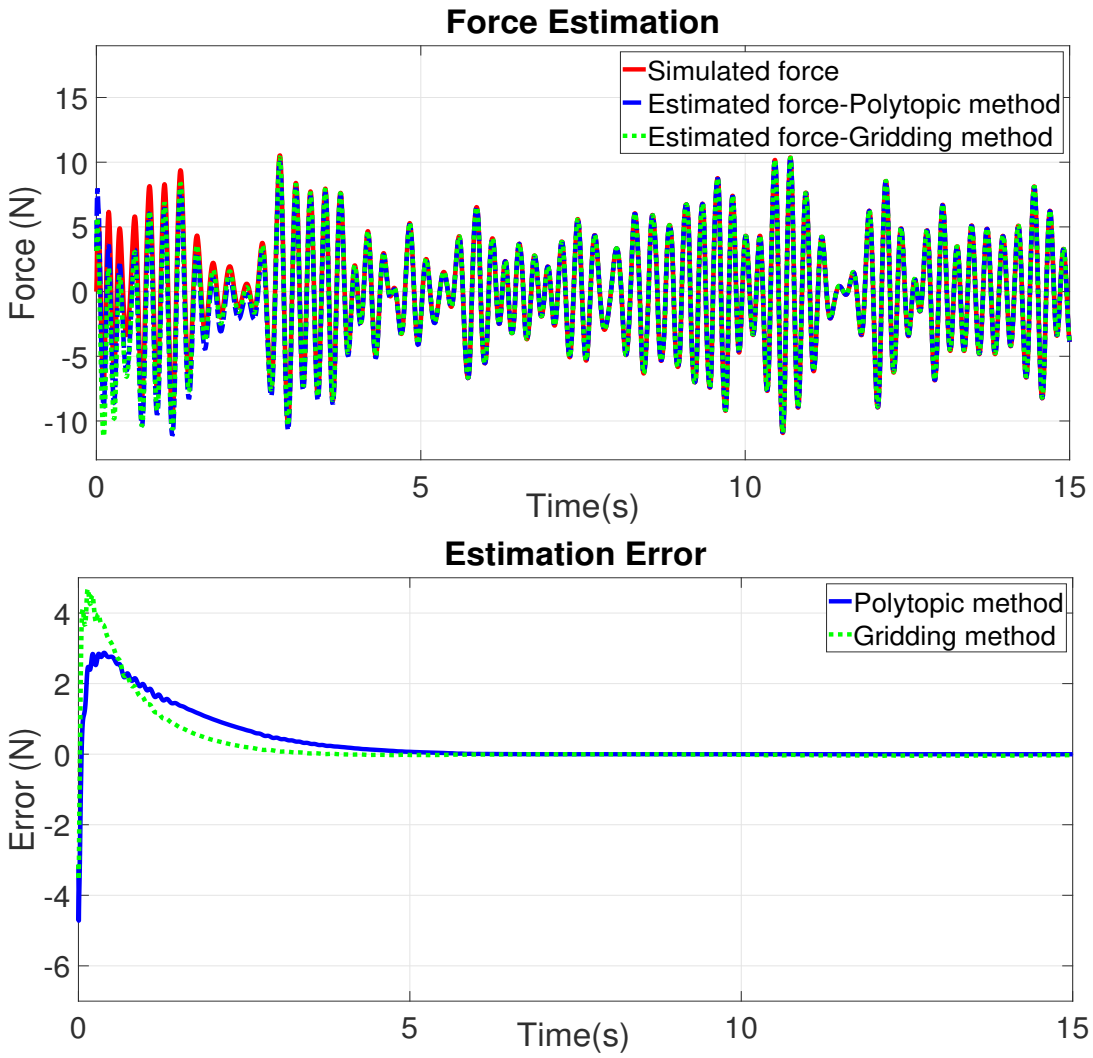

Figure 4.13: Simulation senario 2: (top) Damper force, (bottom) Estimation error

Figure 4.13 shows the damping force estimation on the left side and the estimation error on the right side. The simulation results in Figure 4.13 indicate that the proposed observers perform well in case of slow variations of scheduling parameter. Moreover, the convergence speed of the gridding method is better than that of the polytopic approach, highlighted on the bottom of Figure 4.13. To further describe the accuracy of the proposed observers, the estimated variable $\dot{z}_e$ and variable z_e are shown in Figure 4.14.

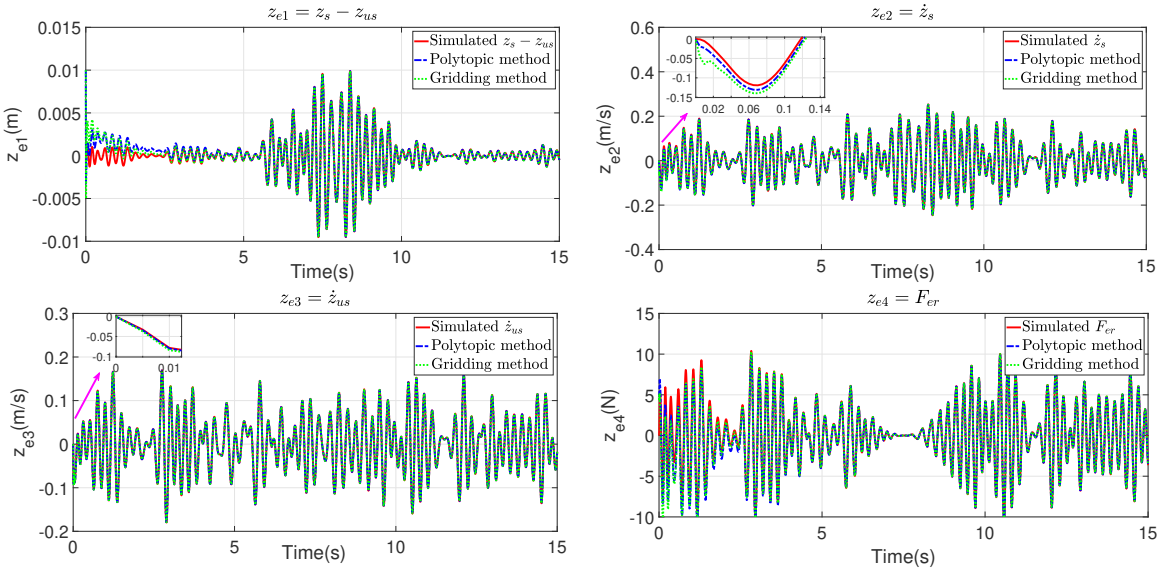

Figure 4.14: Simulation senario 1: (top-left) $z_{e1} = z_s - z_{us}$, (top-right) $z_{e2} = \dot{z}_s$, (bottom-left) $z_{e3} = \dot{z}_{us}$, (bottom-right) $z_{e4} = F_{er}$.

4.5.3 Simulation scenario 3

The third simulation scenario is used to test the stability of the NLPV observer in the following scenario:

- A step road profile is used.
- The control input u is obtained from a Skyhook controller

The ISO road profile and the control input in this test are shown in Figure 4.15.

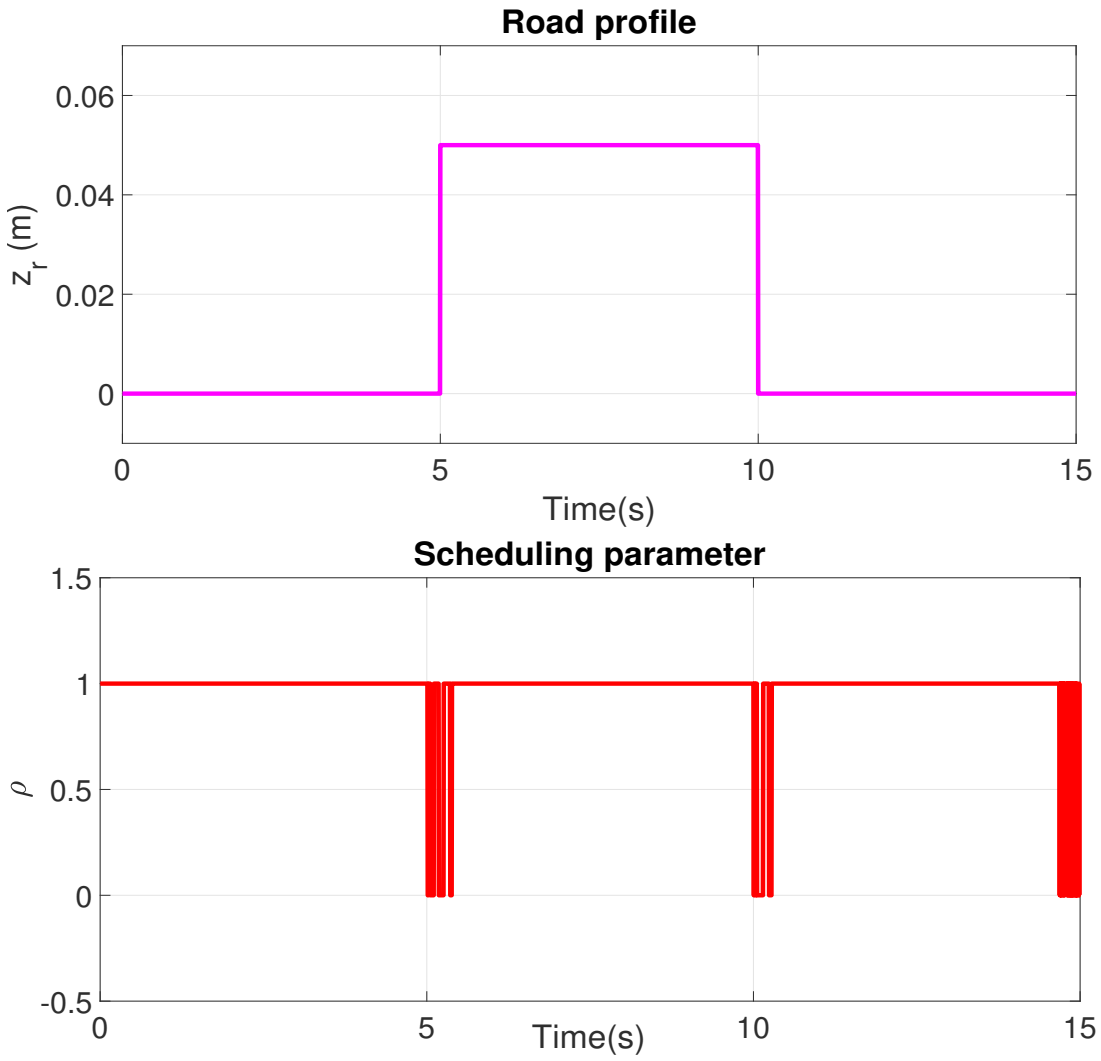

Figure 4.15: Simulation senario 4: (top) Road profile, (bottom) PWM signal

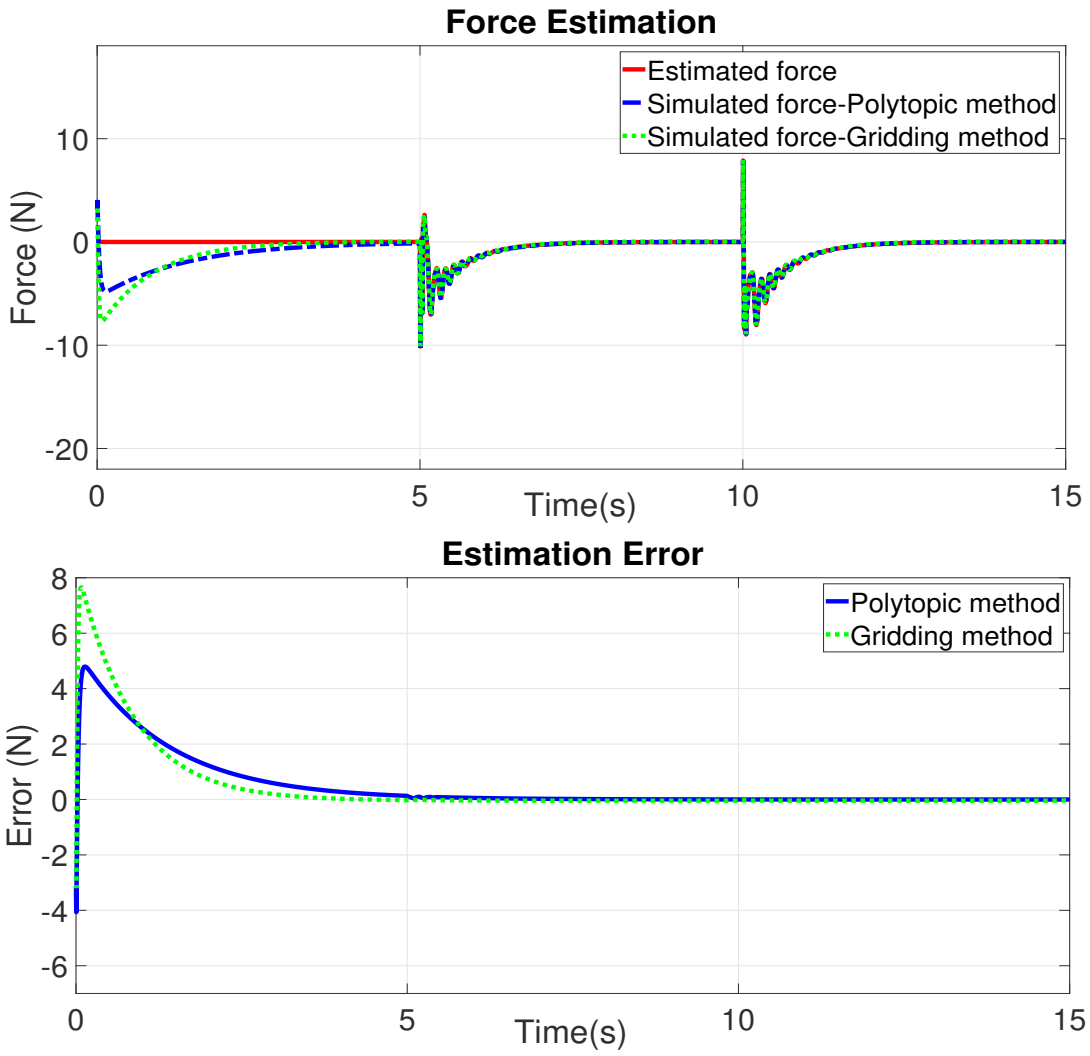

Figure 4.16: Simulation senario 4: (top) Damper force, (bottom) Estimation error

Figures 4.16 and 4.17 show the performance of the two proposed observers in the case of step bump road profile. The results indicate the stability of the proposed schemes $e \to 0$.

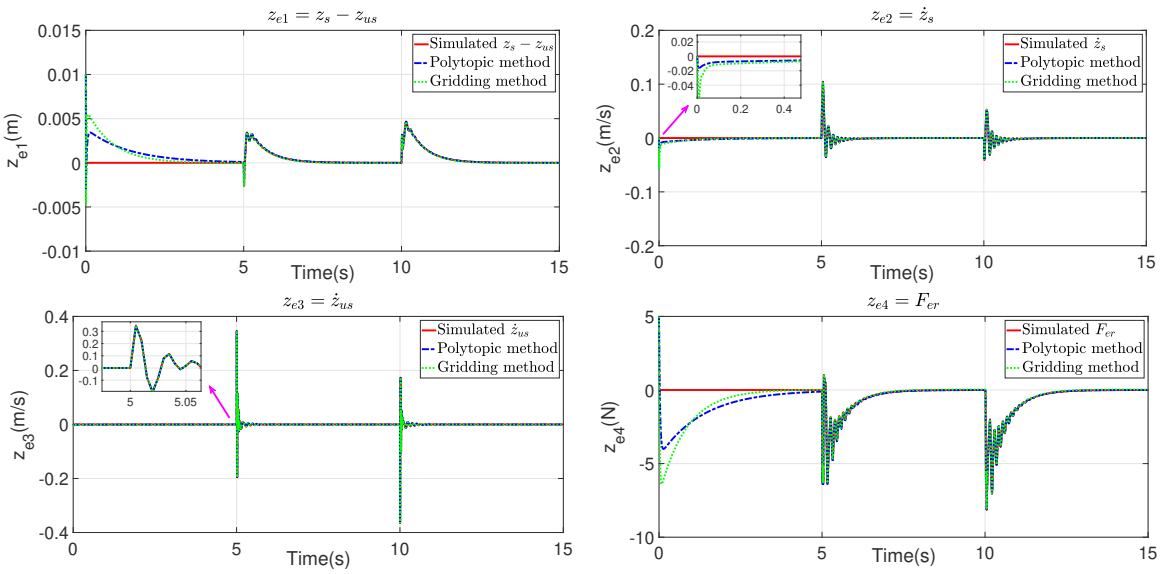

Figure 4.17: Simulation senario 1: (top-left) $z_{e1} = z_s - z_{us}$, (top-right) $z_{e2} = \dot{z}_s$, (bottom-left) $z_{e3} = \dot{z}_{us}$, (bottom-right) $z_{e4} = F_{er}$.

It is worth noting that the observer must work when the system is in closed-loop in the real application. Therefore, to assess the effectiveness of the observer in the closed-loop system, the realistic scenario are presented in the next section.

4.5.4 Simulation scenario 4

The final simulation scenario is designed to evaluate the performance of the proposed observers when operating in closed-loop system and when the scheduling parameter varies very quickly.

This scenario is detailed as follows (see Figure 4.18):

- An ISO 8608 road profile signal (Type C) is used.

- The control input u is obtained from a Skyhook controller

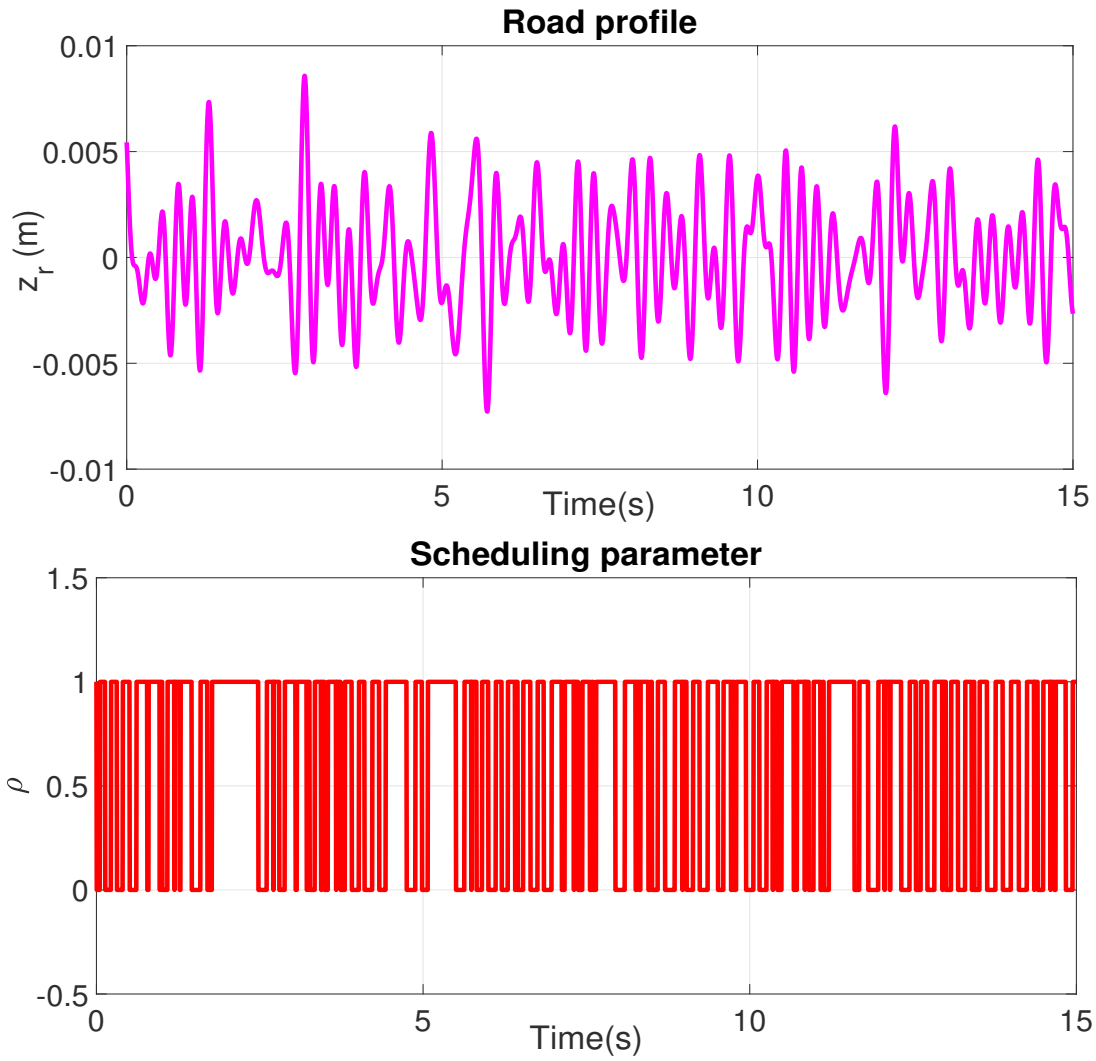

Figure 4.18: Simulation senario 4: (top) Road profile, (bottom) PWM signal

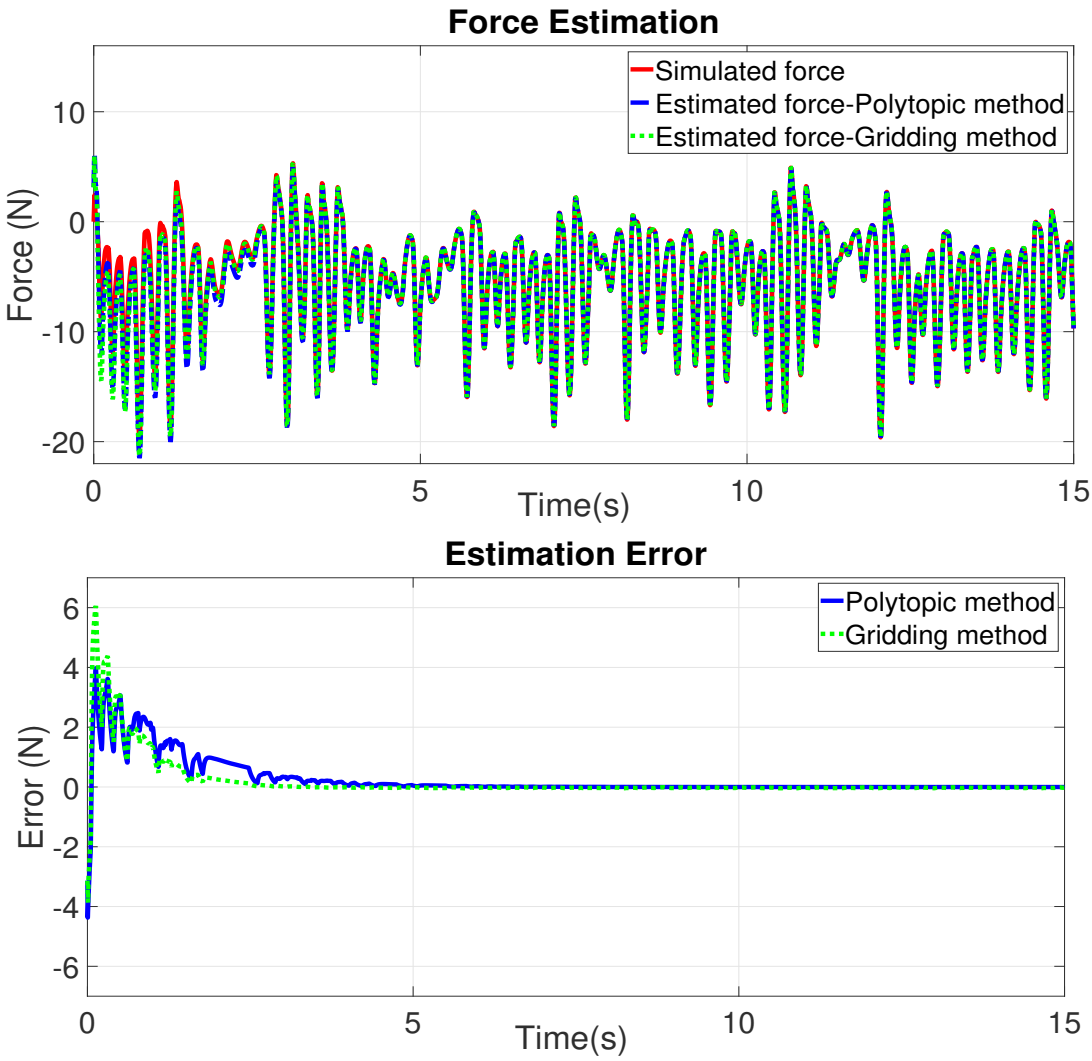

Figure 4.19: Simulation senario 4: (top) Damper force, (bottom) Estimation error

The simulation results of this test are shown in the Figures 4.19 and 4.20. The stability of the NLPV observers operating in closed-loop system is guaranteed when the scheduling parameter varies very fast. Hence, the efficiency of the proposed observer is proved in a realistic case.

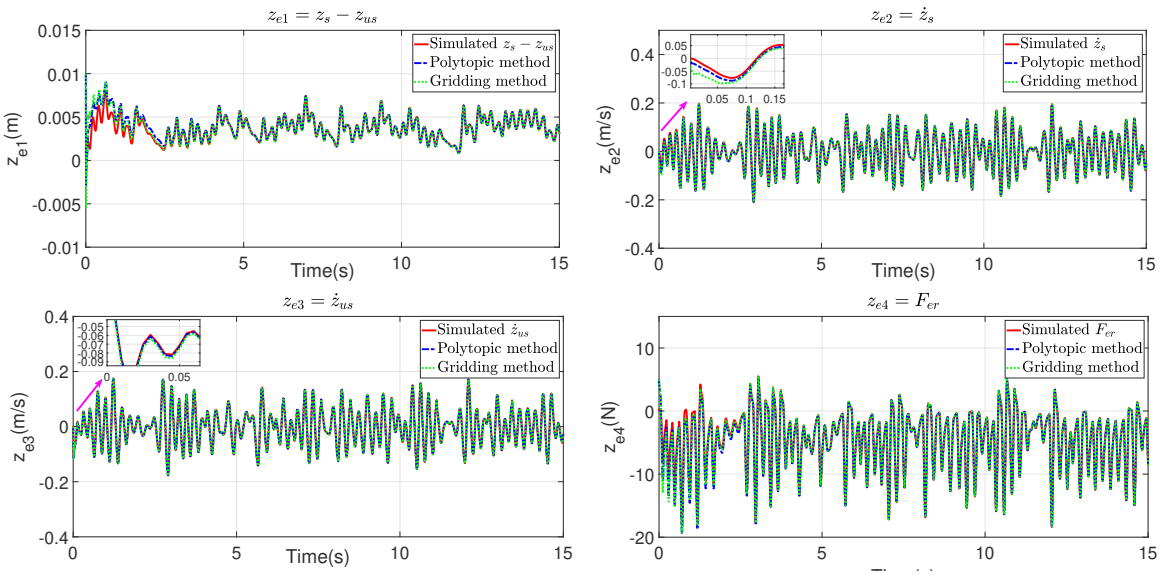

Figure 4.20: Simulation senario 1: (top-left) $z_{e1} = z_s - z_{us}$, (top-right) $z_{e2} = \dot{z}_s$, (bottom-left) $z_{e3} = \dot{z}_{us}$, (bottom-right) $z_{e4} = F_{er}$.

4.6 Experimental validation

For real-time performance assessment, the observer is implemented on the INOVE testbench of GIPSA-lab. The experimental procedure has already been detailed in Chapter 3 (see Section 3.6). It is important to note that the observers are implemented in real-time. Two experimental senarios are used to validate the performance of the proposed NLPV observers, as presented in following subsections:

4.6.1 Experiment 1

In the first experimental scenario, the proposed observers are performed with the system operating in closed-loop. The scenario is as follows:

- The road profile is a sequence of sinusoidal bumps (see on the top of Figure 4.21).
- The control input u is obtained from a Skyhook controller (shown on the bottom of Figure 4.21).

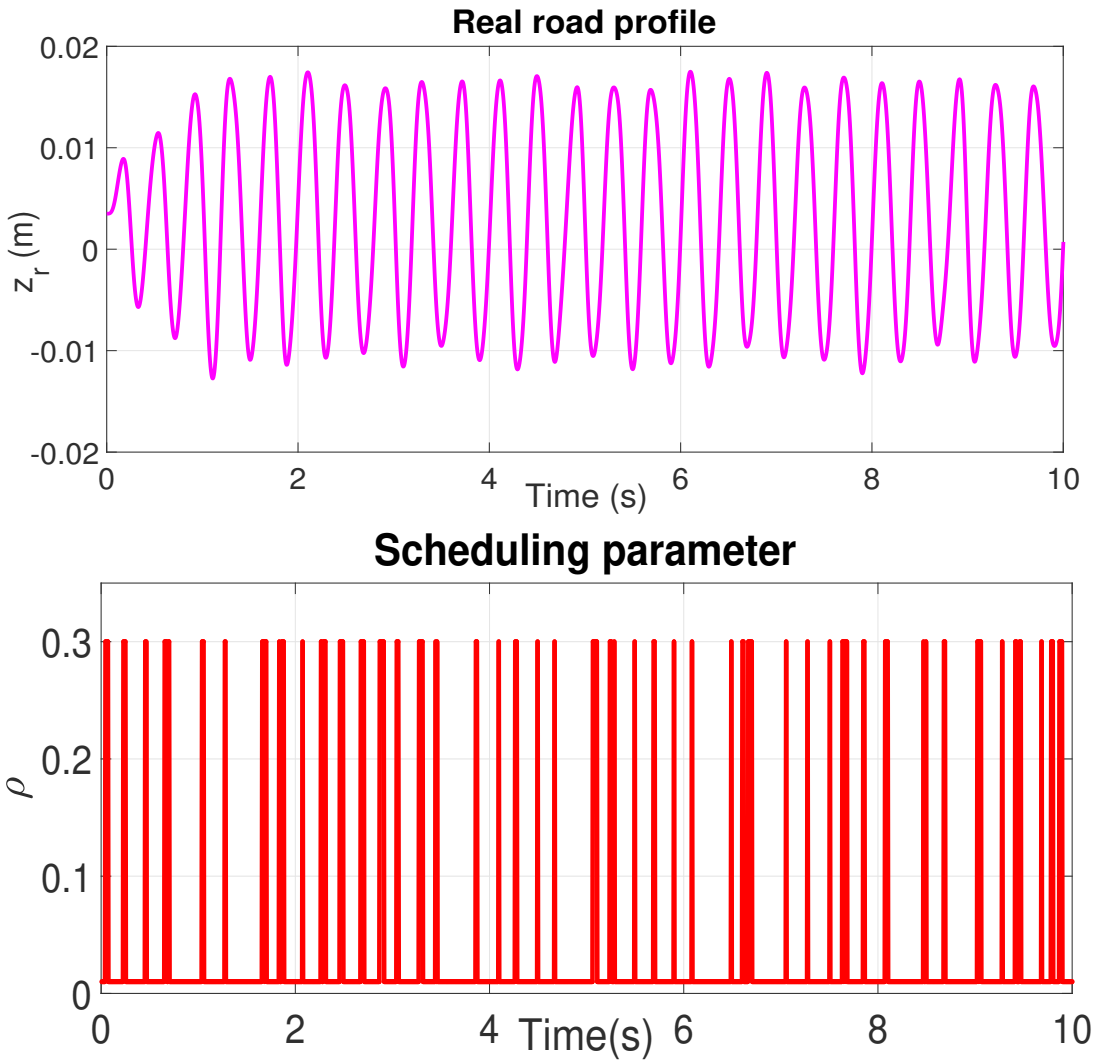

Figure 4.21: Experiment 1: (top) Road profile, (bottom) Scheduling parameter

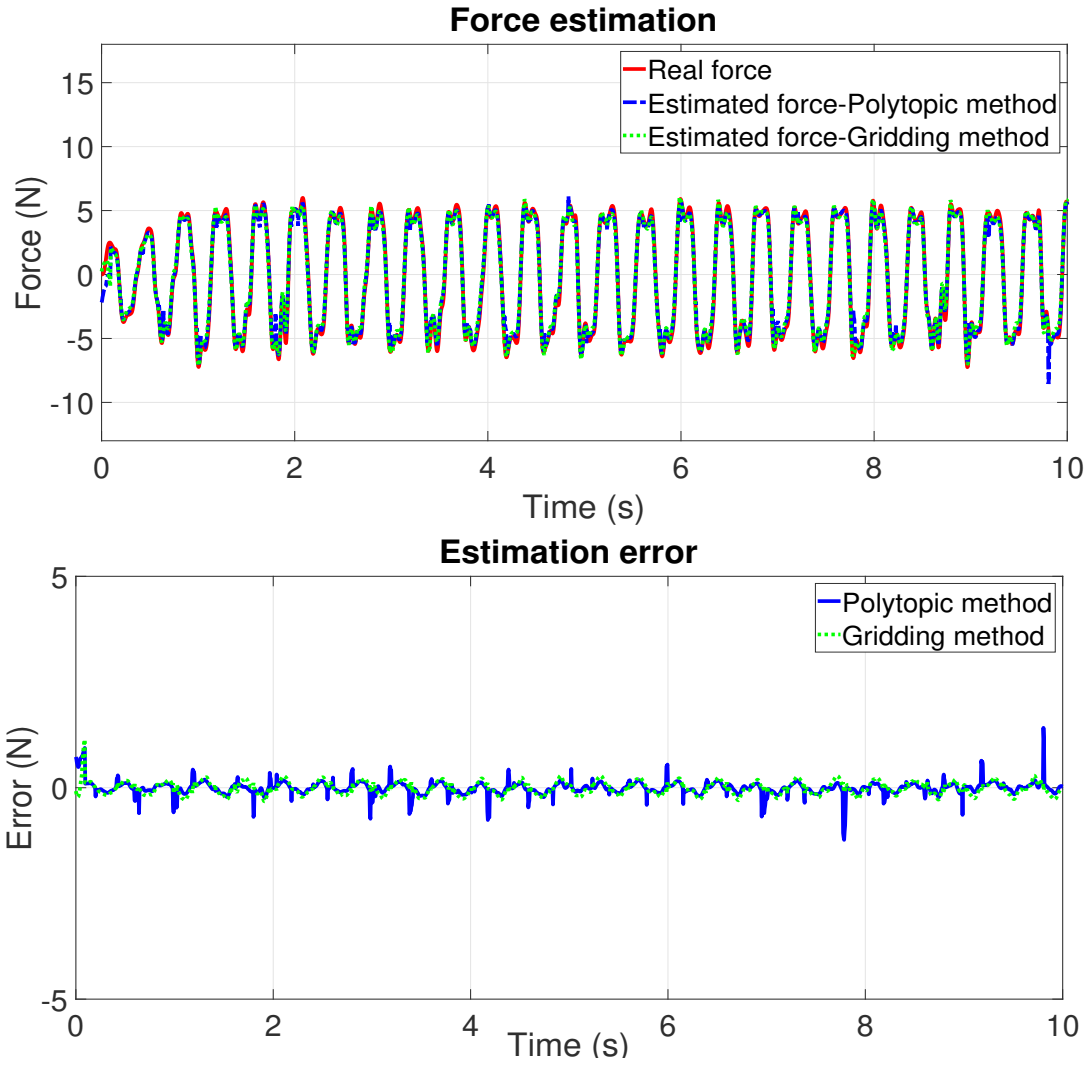

Figure 4.22: Experiment 1: (top) Damper force, (bottom) Estimation error

The experimental results of the damper force estimation in the first test are shown in Figure 4.22. The proposed observers present an accurate estimation in the case of the sinewave road profile. The normalized root-mean-square error for this test (shown in Table 4.1) is 4.81% for the polytopic method and 4.16% for the gridding method, which indicates the effectiveness of the proposed methods.

4.6.2 Experiment 2

In the second experimental scenario, the performances of the NLPV observers are evaluated in the case of a realistic road profile. The scenario detailed as follows:

- An ISO 8608 road profile signal (Type C) is used (see on the top of Figure 3.13).

- The control input u is obtained from a Skyhook controller (the bottom of Figure 3.13).

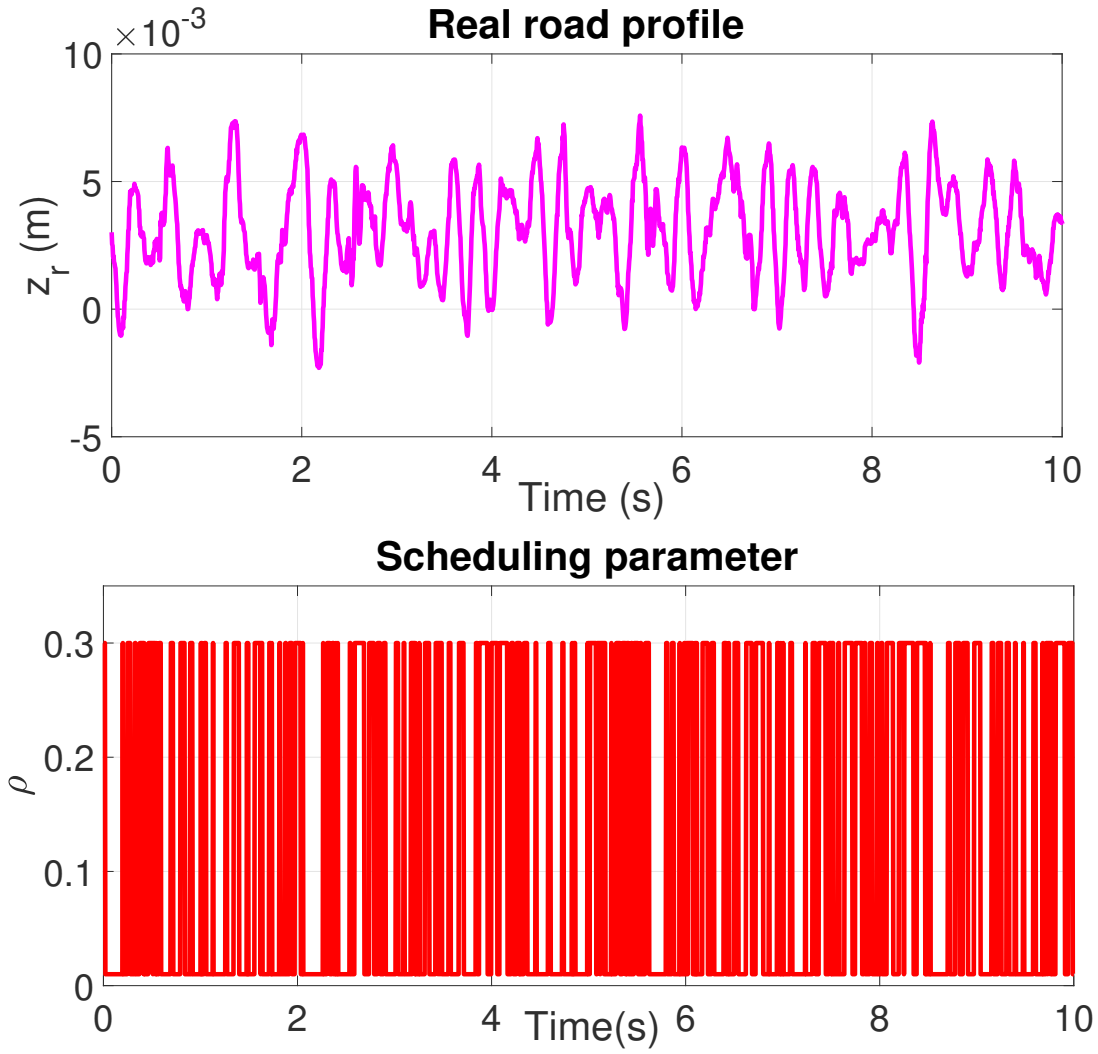

Figure 4.23: Experiment 2: (top) Road profile, (bottom) Scheduling parameter

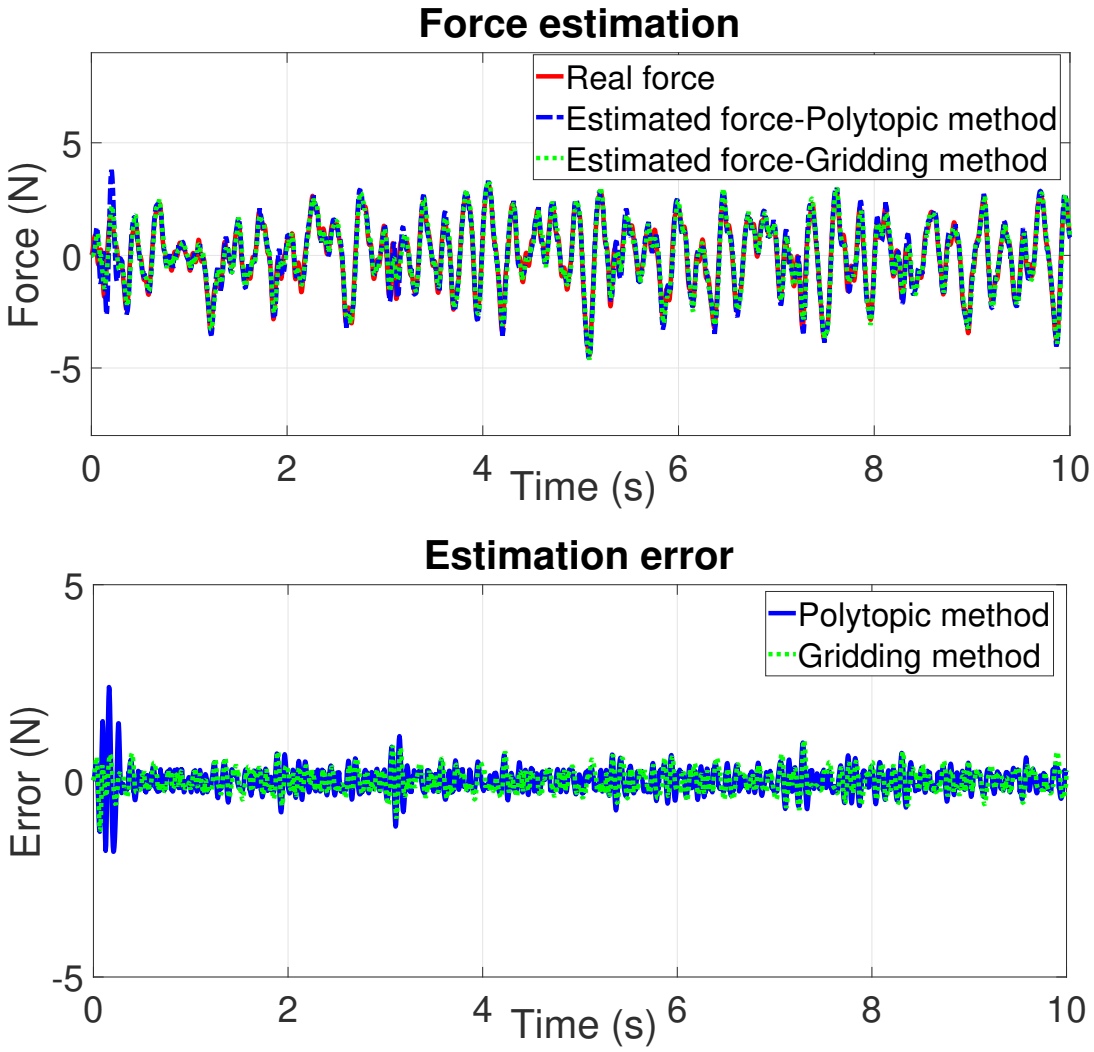

Figure 4.24: Experiment 2: (top) Damper force, (bottom) Estimation error

The experimental results of the force estimation are presented in Figure 4.24. They show the accuracy and efficiency of the proposed observers. To further quantify this accuracy, Table 4.1 gives the normalized root-mean-square errors ($NRMSE = 7.63\%$) and ($NRMSE = 7.08\%$) for the polytopic and gridding approaches, respectively, considering the difference between the estimated and measured forces for the experimental results presented in the right side of Figure 4.24.

Table 4.1: Normalized Root-Mean-Square Errors (NRMSE)

Road Profile	Polytopic method	Griding method
Sinusoidal bumps	0.0481	0.0416
ISO 8608 road	0.0763	0.0708

4.7 Conclusion

This chapter presented two $NLPV$ observers to estimate the damper force, using a dynamic nonlinear model of the ER damper. For this purpose, the quarter-car system is represented in a NLPV form by considering a phenomenological model of damper for which the nonlinearity term is bounded by a Lipschitz condition. Based on two accelerometers, two $NLPV$ observers are designed by using parameter-indepedent and parameter-dependent Lyapunov functions. They give good estimation results for the damping force. The force estimation error is minimized, accounting for the effect of unknown inputs (road profile derivative and measurement noises). Both simulation and experiment results assess the ability and the accuracy of the proposed models to estimate the damping force of the ER semi-active damper in real time.

Chapter 5

Comparison of three observer designs

Contents

This chapter aims at comparing three robust observers used to estimate the damping force of electrorheological (ER) damper in a vehicle suspension system. The first method, namely unified $\mathcal{H}_\infty$ observer, was presented in Chapter 3 while the latter two methods concerning NLPV observers have been introduced in Chapter 4. Three different comparison points are studied: behavior against unknown road profile, b) minimization of the sensor noise effect on the estimation errors, c) convergence time improvement.

5.1 Introduction

In this chapter, an insightful analysis is provided through the comparison of three proposed observers in Chapter 3 and Chapter 4. Let us first recall the considered nonlinear Lipschitz system (2.20) and the the nonlinear parameter varying system (2.21) of a quarter car model, as seen in Chapter 2:

- The nonlinear Lipschitz system is given as follows:

$$\begin{cases} \dot{x} &= Ax + B\Phi(x)u + D_1\omega_r \\ y &= Cx + D_2\omega_n \end{cases} \tag{5.1}$$

- The nonlinear parameter varying system describled by:

$$\begin{cases} \dot{x} &= Ax + B(\rho)\Phi(x) + \bar{D}_1\omega \\ y &= Cx + \bar{D}_2\omega \end{cases} \tag{5.2}$$

where $x = [z_s - z_{us}, \dot{z}_s, z_{us} - z_r, \dot{z}_{us}, F_{er}]^T \in \mathbb{R}^5$ represents the system states, $y = [\ddot{z}_s, \ddot{z}_{us}]^T \in \mathbb{R}^2$ represents the measured outputs, the scheduling variable $\rho = u \in \Delta_\rho \subset \mathbb{R}$ and $\omega = \begin{pmatrix} \omega_r \\ \omega_n \end{pmatrix}$, in which, ω_r is the road profile derivative and ω_n is the sensor noises.

Let us recall the proposed observer forms, as presented in Sections 3.2 and 4.2.

- The unified H_∞ observer is given by:

$$\begin{cases} \dot{z} = Nz + Jy + H\Phi(\hat{x})u + Mv \\ \dot{v} = Pz + Qy + Gv \\ \hat{x} = Rz + Sy \end{cases} \tag{5.3}$$

  where $z \in \mathbb{R}^5$, $v \in \mathbb{R}^5$

- The two NLPV observers have same form, is described as follows:

$$\begin{cases} \dot{\hat{x}} = A\hat{x} + L(\rho)(y - C\hat{x}) + B(\rho)\Phi(\hat{x}) \\ \hat{z}_e = C_z\hat{x} \end{cases} \tag{5.4}$$

  where $\hat{x} = \in \mathbb{R}^5$

From the formulations of the proposed observers, we have several qualitative comparisons as follows:

- Concerning the structure of the observers, the formulations of NLPV observers are Luenberger-like forms (consider as Proportional Observers); therefore, the design procedure is simple (only determine the observer gain $L(\rho)$). Meanwhile, the unified H_∞ observer used the new dynamic observer formulation, thereby increasing the complexity in the design procedure and increasing the implementation cost.

- The classical observer forms (5.4) only contain the proportional observer gains, while the unified H_∞ observer (5.3) contains the proportional, integral, and dynamic variable in the observer gain. Hence, it can improve the convergence time.

- The NLPV observers consider both road profile derivative (ω_r) and sensor noises (ω_n) as the unknown input disturbances (ω) and minimize the effect of ω on the state variable estimation errors by using an H_∞ criterion. On the other hand, the objectives of the unified observer are to decouple the effect of ω_r and to only minimize the effect of ω_n on the state estimation error e via an H_∞ framework. As a result, the unified observer is more efficiency in minimizing the effect of sensor noises than in the NLPV observers.

- The existence condition of the unified H_∞ observer concerns the decoupling condition, which is not always fulfilled in practice.

- Concerning the required sensors, all of three observers need only two measurements, which are sprung mass acceleration $\ddot{z}_s$, and unsprung mass acceleration $\ddot{z}_{us}$.

The comparison results between the NLPV observers and the unified H_∞ observer for damper force estimation are listed in detail in Table 5.1.

Table 5.1: The comparison between the NLPV and unified H_∞ observers

Evaluations	NLPV observers	Unified H_∞ observer
Decoupling the road profile	no	yes
Handling the variation of the nonlinearity amplitude	yes	no
Minimizing the measurement noises effect	yes	yes
Improving the convergence time	no	yes
Complexity level in the design steps	simple	complex
Implementation cost	low	high

The major contributions of this chapter are summarized as the following:

- Three damper force estimation approaches are compared in the time-domain simulation scenarios to evaluate the convergence time and the ability of minimizing the effect of measurement noises on the estimation errors.
- The three proposed observers have been implemented on a real scaled-vehicle test bench using the same scenarios, through the Matlab/Simulink Real-Time Workshop, to assess their behavior experimentally.

5.2 Comparison in the frequency domain

In this section, some results about the frequency analysis of the three proposed observers given in Sections 3.4 and 4.4 are recalled to compare the efficiency in minimizing the measurement noise effect. The Bode diagrams of the transfer functions between the measurements noises (ω_n) on the state estimation errors (e) of the three proposed observers (unified H_∞, NLPV polytopic method and NLPV gridding method observers) are given at Figures 5.1, 5.2 and 5.3, respectively. To easily compare between the unified observer and NLPV observers, these Bode diagrams are plotted in a single figure, shown in Figure 5.4. These results emphasize the satisfactory attenuation level of measurements noises on 5 state estimation errors e_i, $i = 1 \div 5$. In the region of high-frequency noises (10Hz-1000Hz), the unified H_∞ observer gives the best attenuation results of the effect of noises on 4 state estimation errors e_i, $i = 1 \div 4$, while the gridding method improves the ability of measurement noise rejection on the fifth state estimation error e_5 (see Figure 5.4). To explain this improvement, let us recall the damper force model (1.22) in chapter 1

$$\begin{cases} F_d = k_0(z_s - z_{us}) + c_0(\dot{z}_s - \dot{z}_{us}) + F_{er} \\ \tau \dot{F}_{er} + F_{er} = f_c.u.tanh(k_1(z_s - z_{us}) + c_1(\dot{z}_s - \dot{z}_{us})) \end{cases} \tag{5.5}$$

It can be seen that the fifth state in the three proposed observer is F_{er}, concerning the coupling of control input u and nonlinearity. This issue is solved by the NLPV gridding observer effectively.

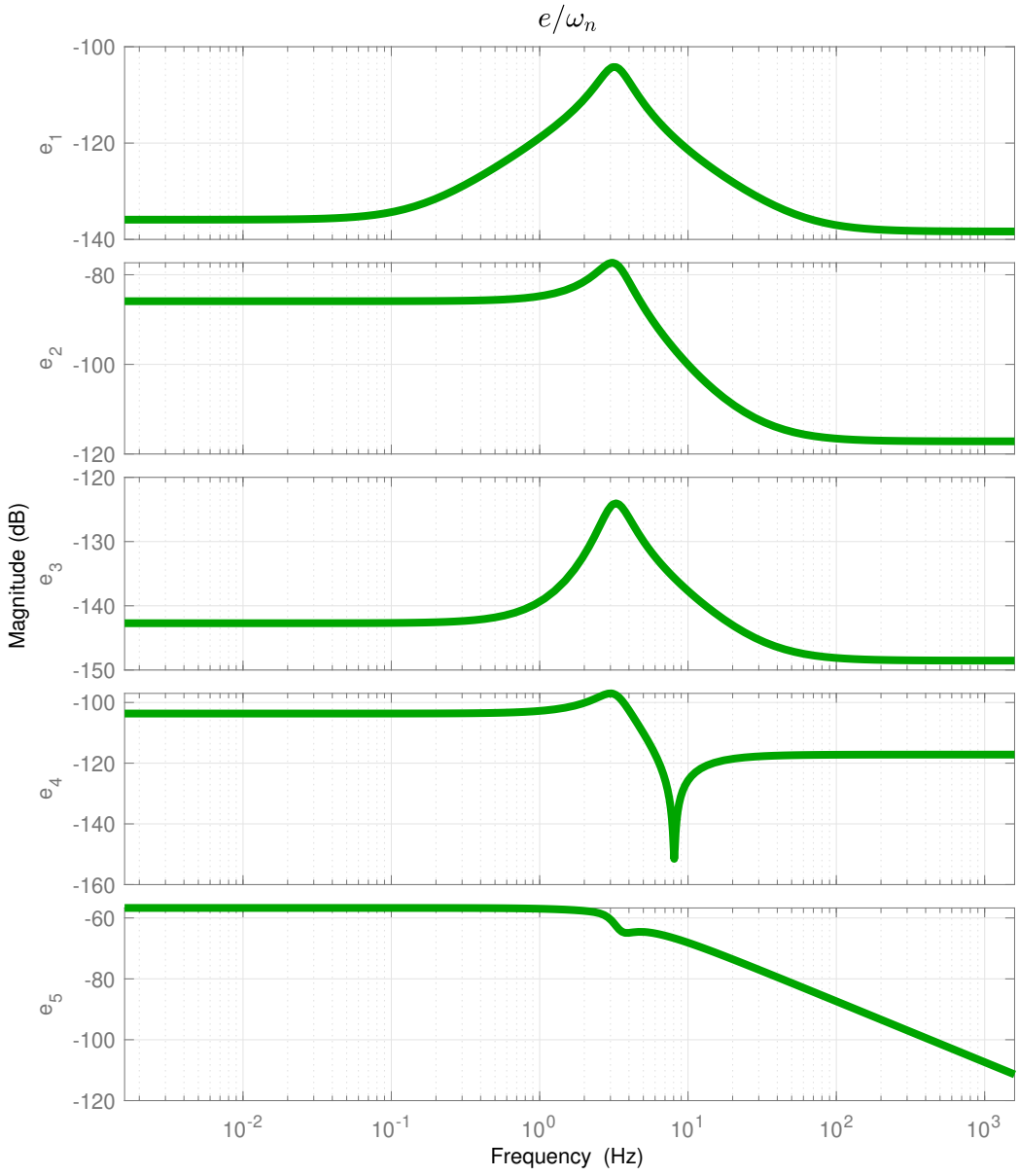

Figure 5.1: Transfer $\|e/\omega_n\|$- Bode diagrams of unified H_∞ observer w.r.t. measurement noises.

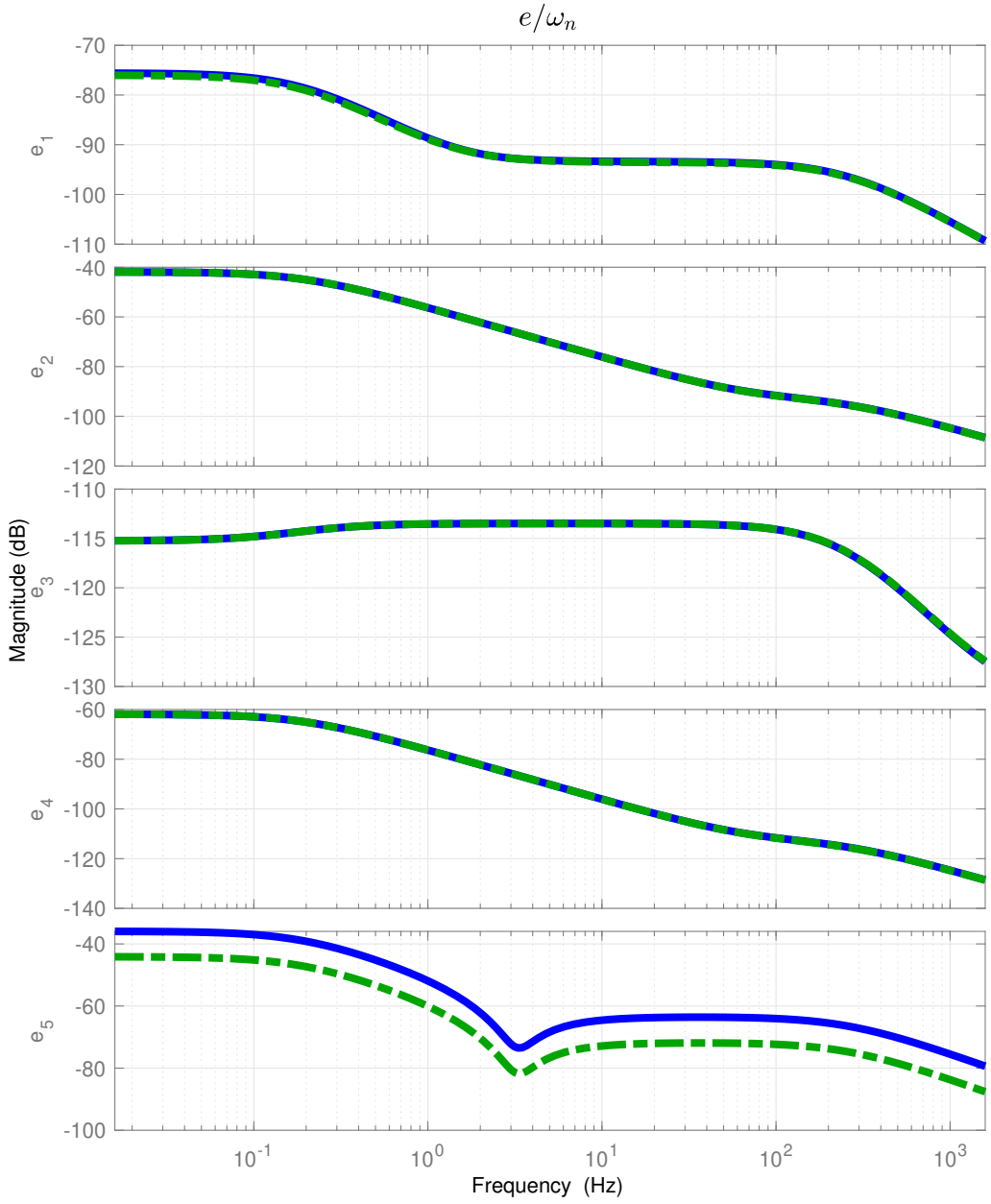

Figure 5.2: Transfer $\|e/\omega_n\|$- Bode diagrams of NLPV observer w.r.t. measurement noises- polytopic method .

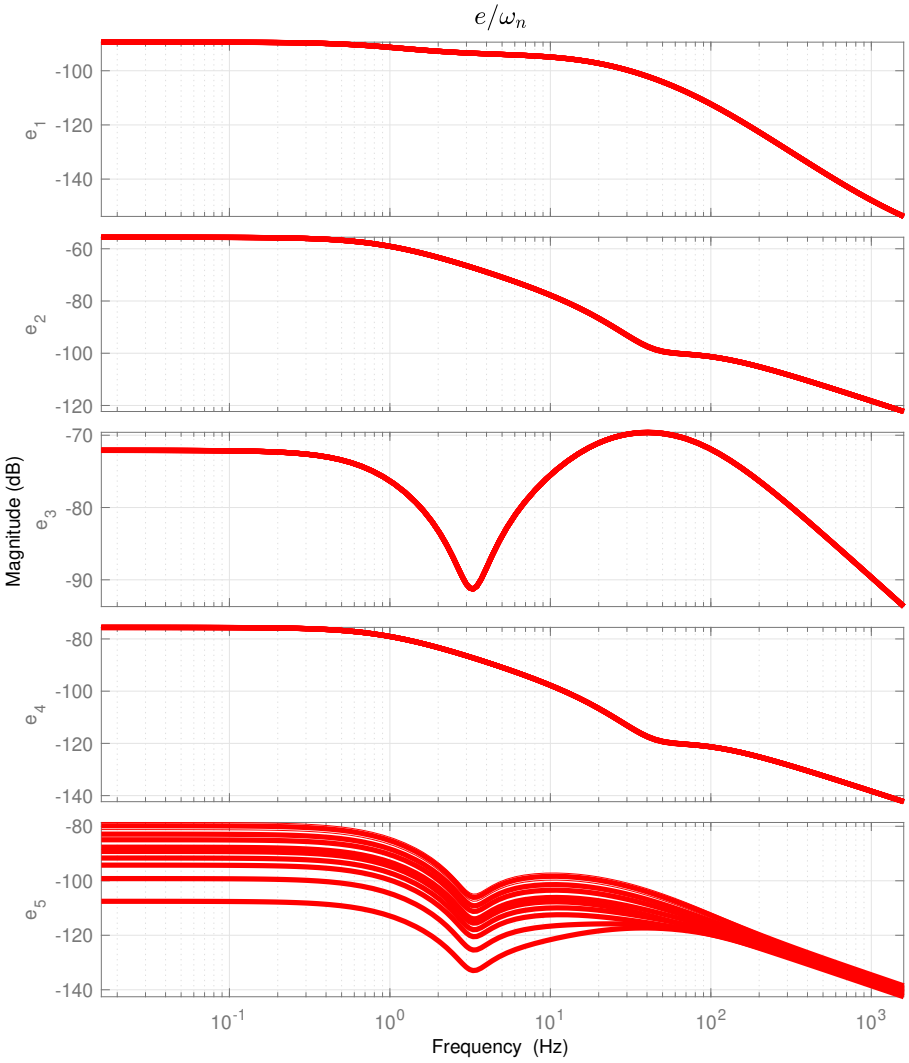

Figure 5.3: Transfer $\|e/\omega_n\|$- Bode diagrams of NLPV observer w.r.t. measurement noises-gridding method .

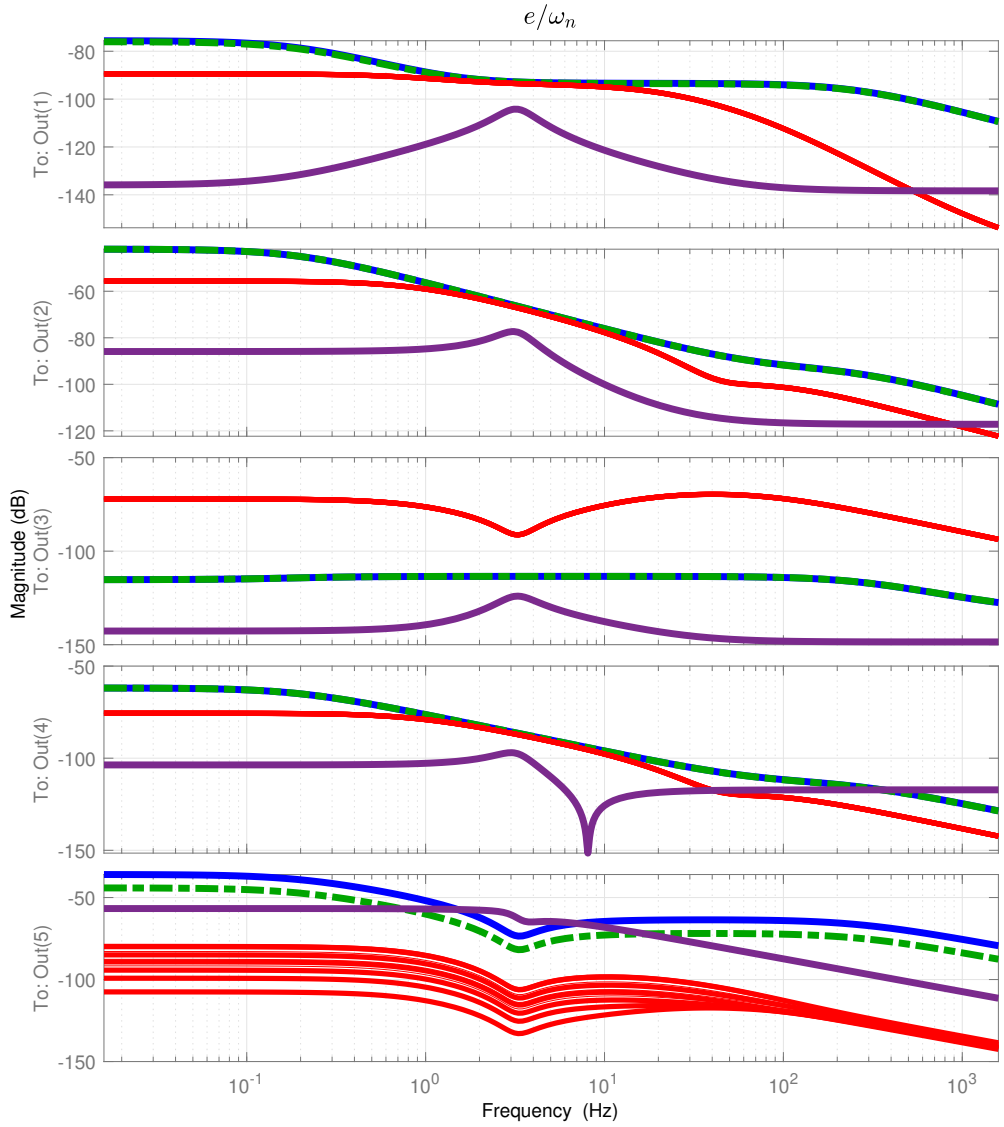

Figure 5.4: Transfer $\|e/\omega_n\|$- Bode diagrams of three observers w.r.t. measurement noises- Unified H_∞ observer (violet line), NLPV polytopic observer (green dash-dot and blue line) and NLPV gridding observer (red line)

5.3 Comparison in the time domain simulation

5.3.1 Simulation scenario 1: convergence time evaluation

To evaluate the convergence time of three proposed observers (see Figure 5.5), the simulations have been performed with the step road profile.

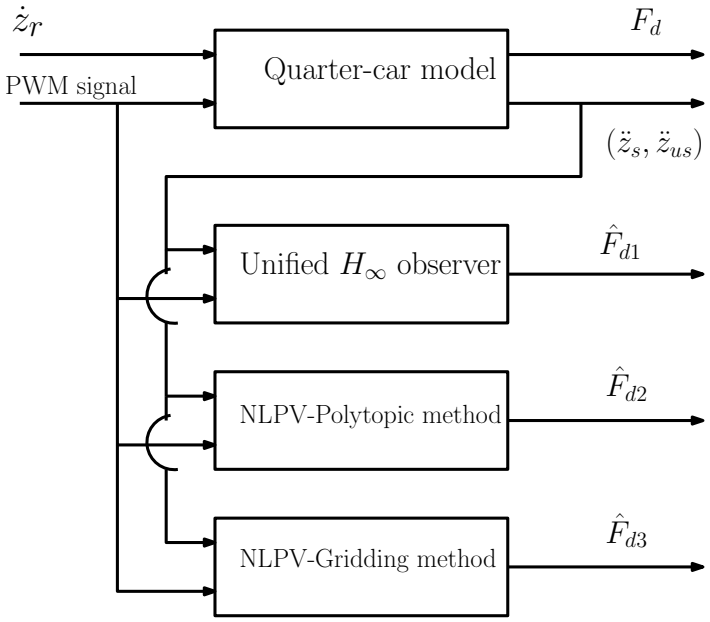

Figure 5.5: Block diagram for simulation of the three proposed observers in comparison scenario 1.

In the first scenario, three proposed observers are validated with the system operating in closed-loop and without measurement noise. it is detailed hereafter:

- A step road profile signal is used (top of Figure 5.6).

- The control input u is obtained from a Skyhook controller (bottom of Figure 5.6).

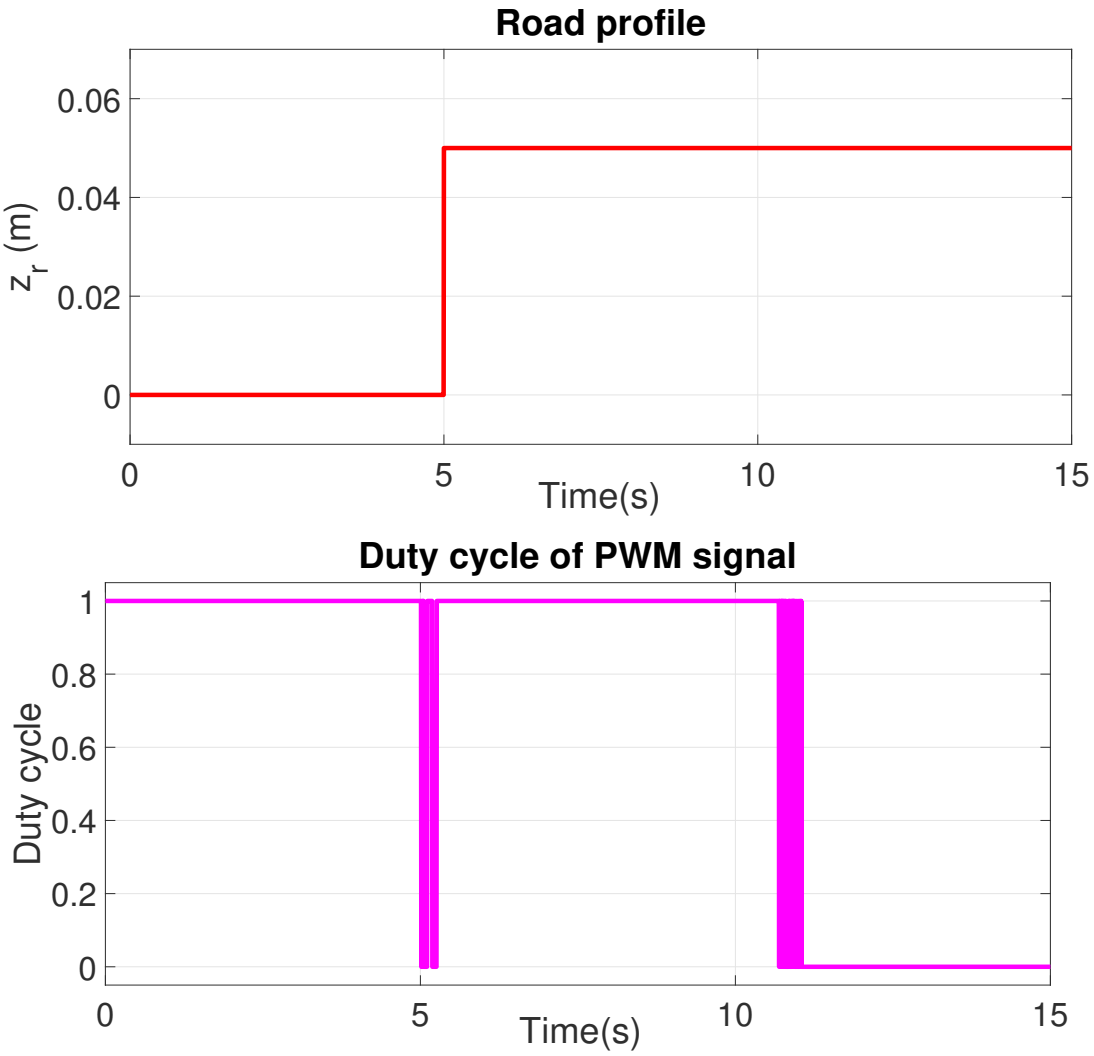

Figure 5.6: Comparison simulation senario 1: (top) Road profile, (bottom) Control input signal (PWM signal)

The simulation results are presented in Figure 5.7. The damper force estimation results are shown at the top of Figure 5.7. The solid red line represents the original simulated damper force of the system. The solid blue line, dot-dashed green line and dotted pink line represent the estimated force obtained by the NLPV observer with polytopic method, the gridding NLPV observer and the unified H_∞ observer, respectively. Moreover, the estimation errors are given at the bottom of Figure 5.7. The estimation errors obtained from NLPV observer with polytopic method, gridding NLPV observer and unified H_∞ observer are shown in the solid blue line, dot-dashed green line and dotted pink line, respectively. According to Figure 5.7, the unified H_∞ observer has a better convergence time (1 second) than the ones using the NLPV observers (2 seconds). To complete the comparison, Table 5.2 presents the normalized root-mean-square errors, considering the difference between the estimated and measured forces

given at the top of Figure 5.7. Notice that the NRMSE value of the NLPV gridding observer is higher due to the large overshoot in this scenario.

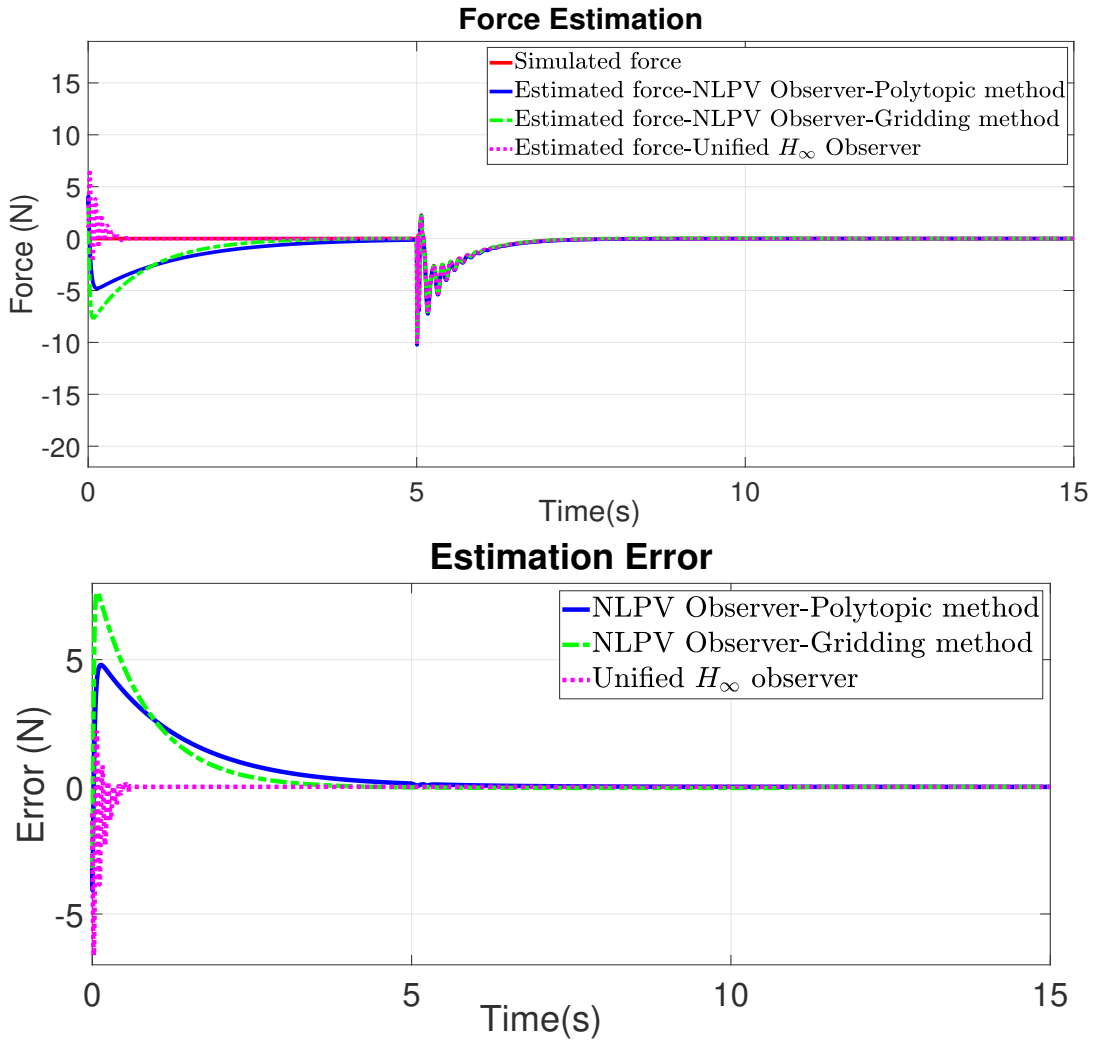

Figure 5.7: Comparison simulation senario 1: (top) Damper force, (bottom) Estimation error

Table 5.2: Normalized Root-Mean-Square Errors (NRMSE)

Observers	NRMSE
NLPV observer-polytopic method	0.0767
NLPV observer-gridding method	0.1023
Unified H_∞ observer	0.0212

5.3.2 Simulation scenario 2: measurement noise rejection evaluation

The second scenario (shown in Figure 5.8) is designed to compare the three observers subject to measurement noise.

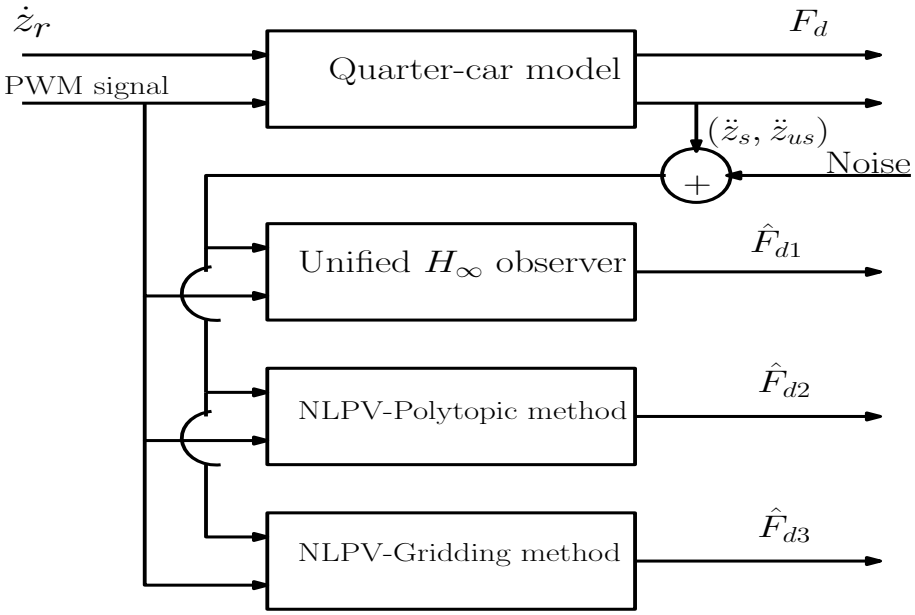

Figure 5.8: Block diagram for simulation of the three proposed observers in comparison scenario 2.

In this case, the observers are utilized with a realistic road profile (ISO standard) as the unknown input, and the measures are disturbed by white noise with a small amplitude. The details of this scenario are as follows

- An ISO standard road profile (type C) is used, top of Figure 5.9
- The control input u of the closed-loop system is obtained from a Skyhook controller (see bottom of Figure 5.9)
- The white noise added to $\ddot{z}_s$ and $\ddot{z}_{us}$ are shown in Figure 5.10.

The measurement noises in the two accelerometers are given in Figure 5.10. The red line and the blue line represent the noise of sprung mass ($\ddot{z}_s$) and unsprung mass ($\ddot{z}_s$) accelerometers, respectively. The amplitude of noise is around 0.025 (m/s^2). Figure 5.11 shows the sprung mass (red line) and unsprung mass (blue line) accelerations affecting by measurement noise.

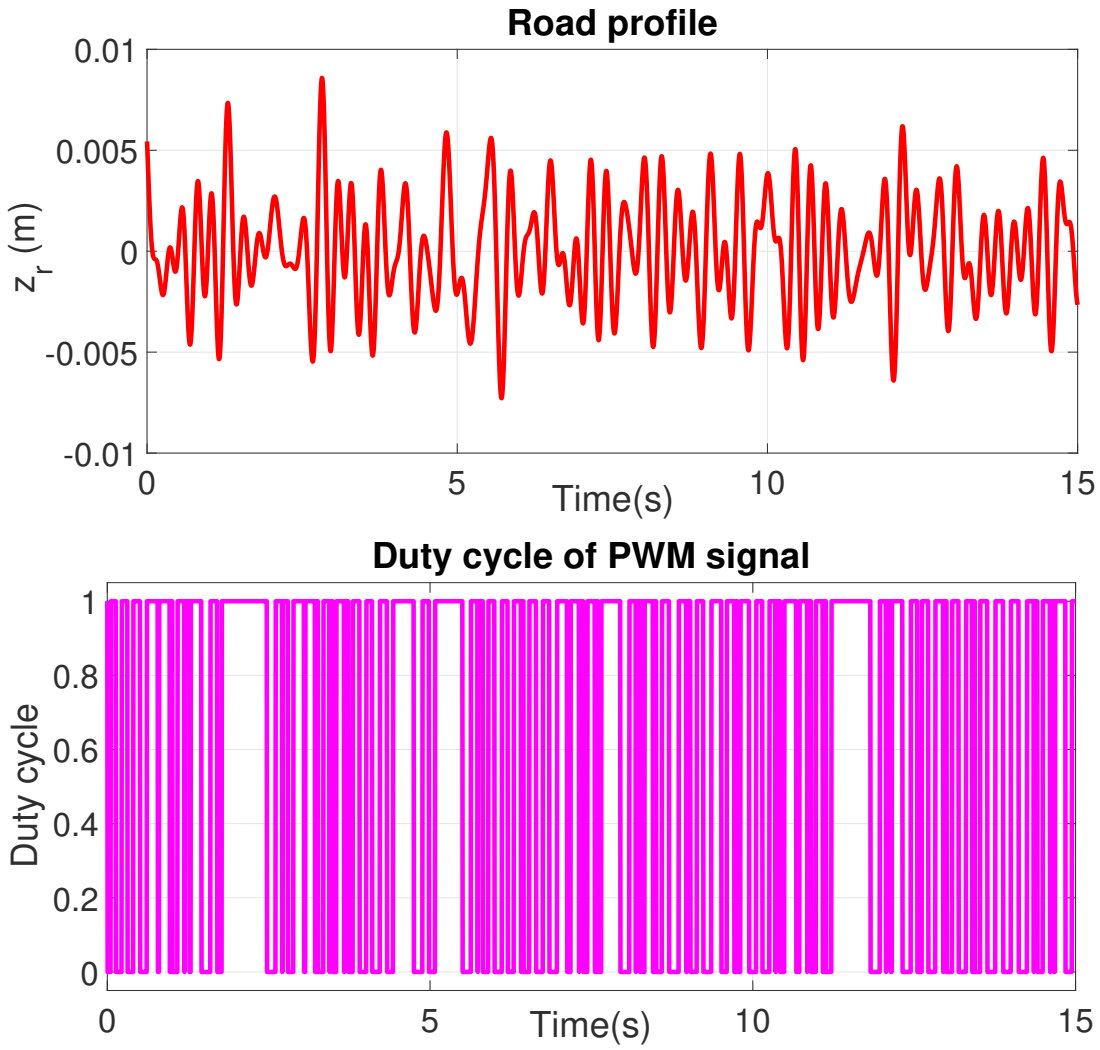

Figure 5.9: Simulation senario 2: (top) Road profile , (bottom) Control input signal (PWM signal)

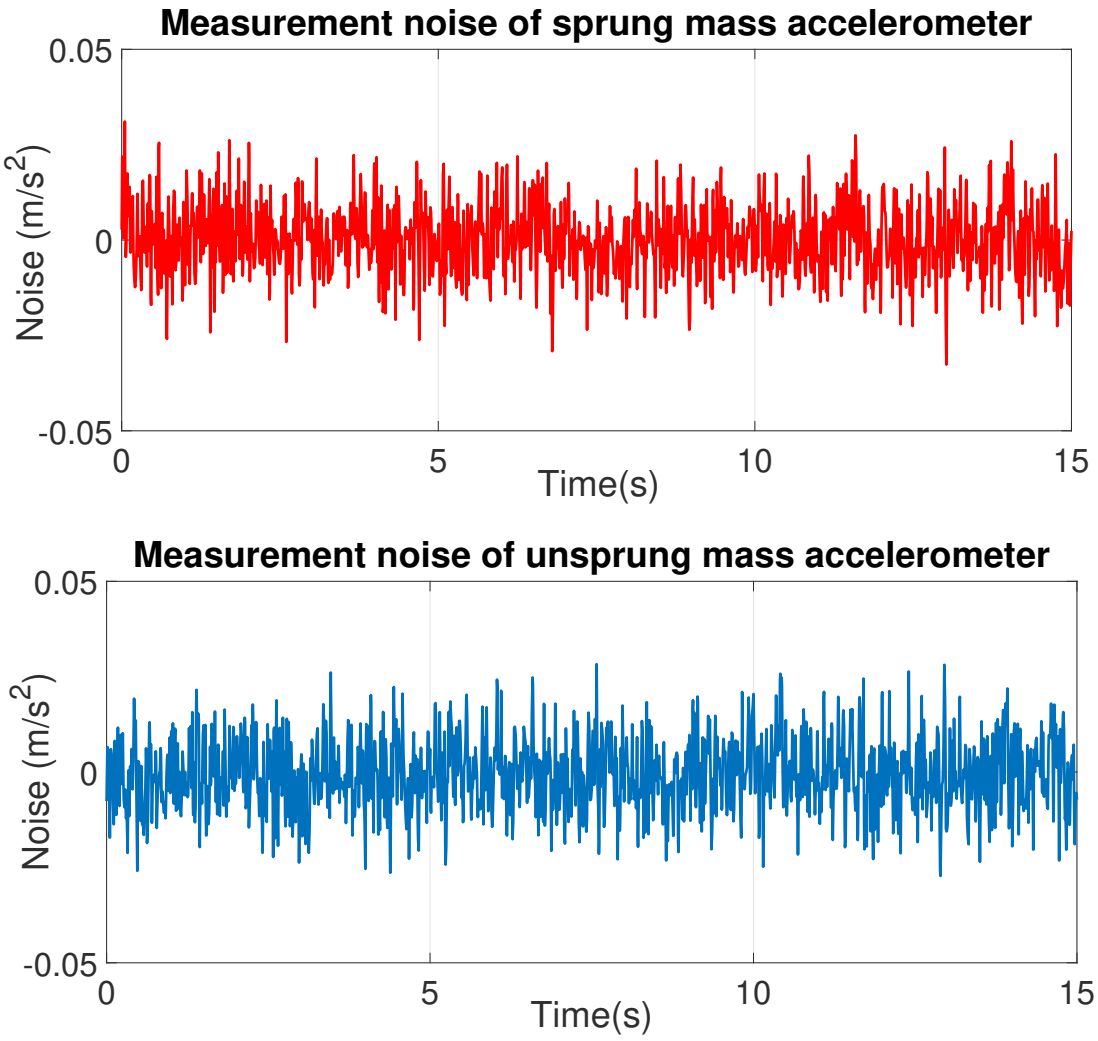

Figure 5.10: Simulation senario 2: Measurement noises

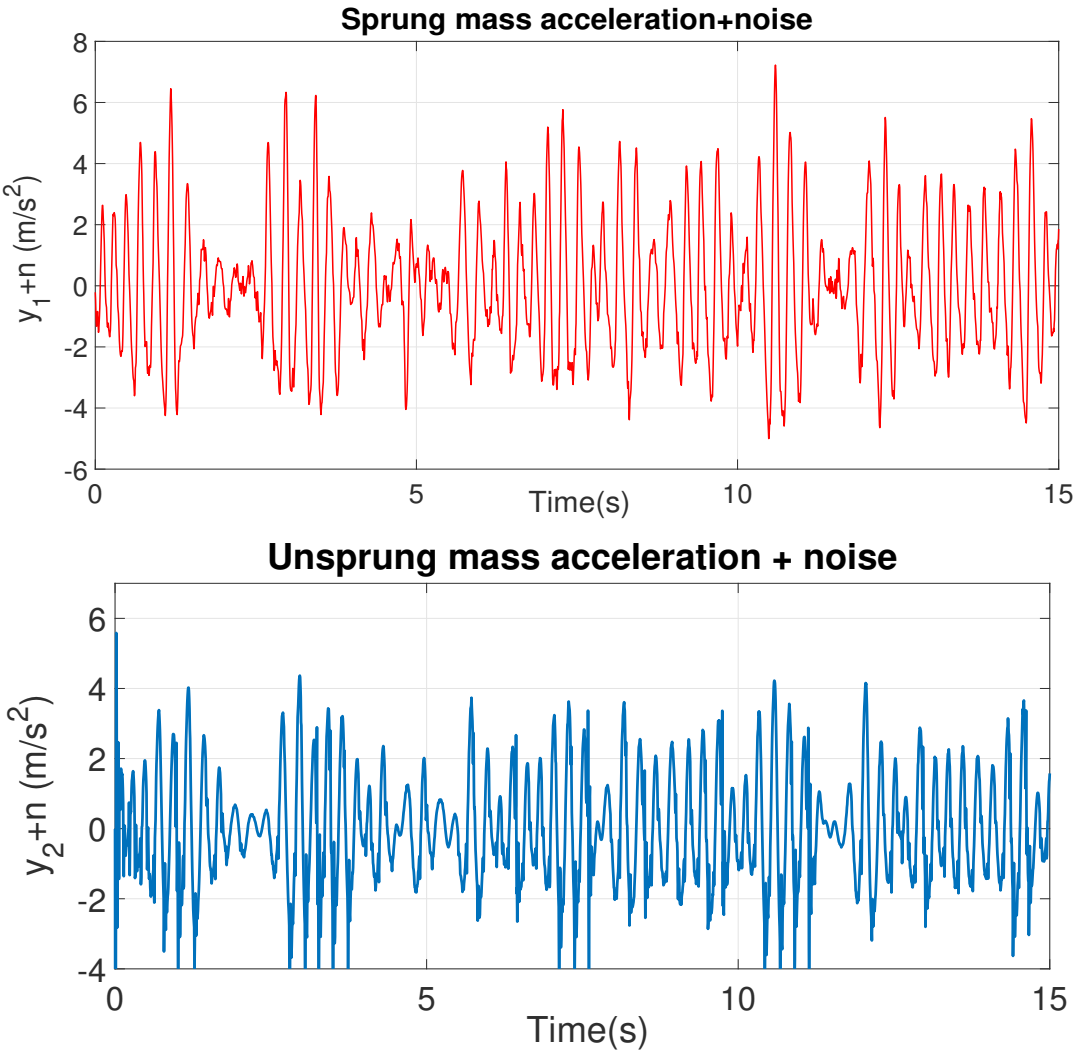

Figure 5.11: Simulation senario 2: (top) Sprung mass acceleration + noise , (bottom) Unsprung mass acceleration + noise)

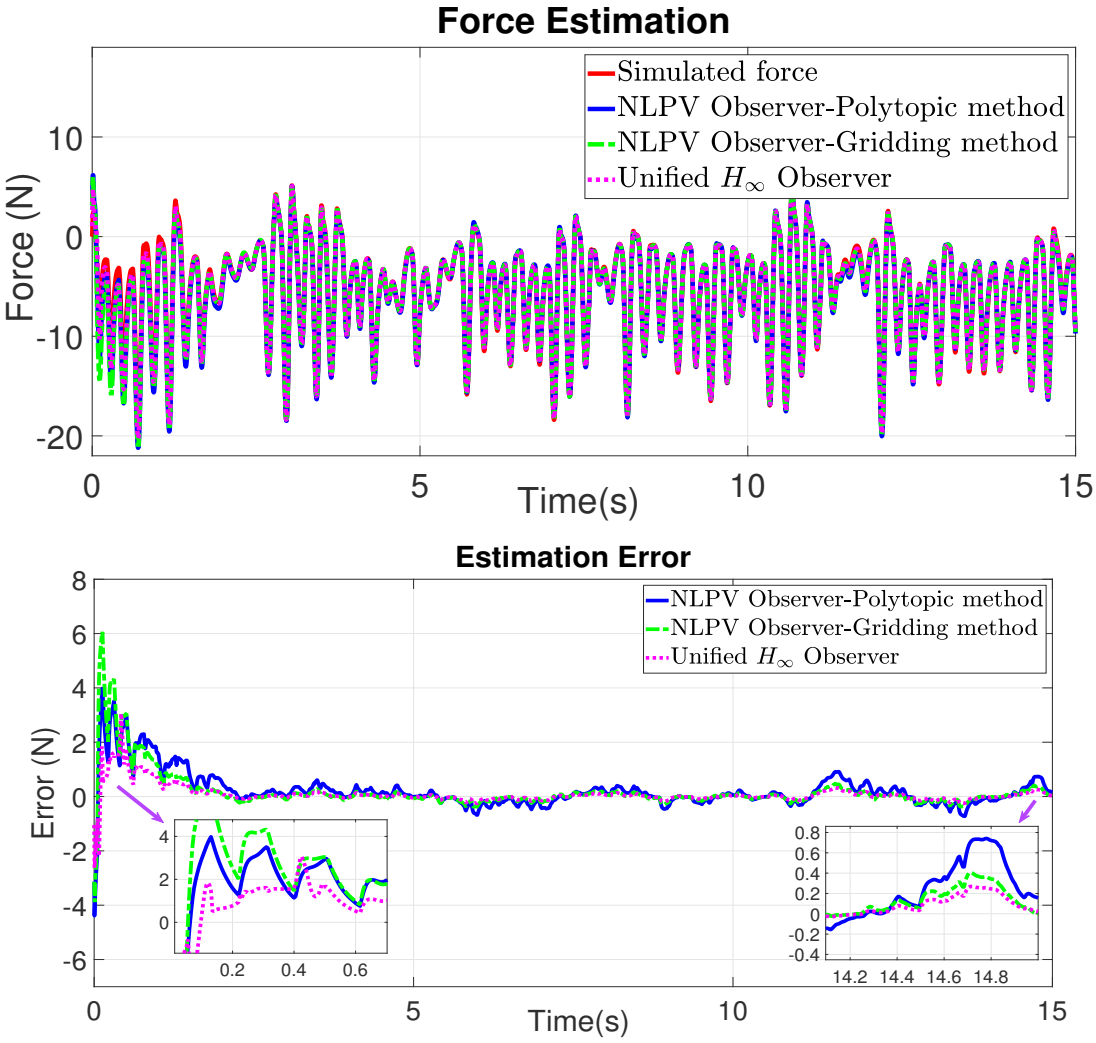

Figure 5.12: Simulation senario 2: (top) Damper force, (bottom) Estimation error

The simulation results are shown in Figure 5.12. The estimated damping force obtained from the three observers are at the top of Figure 5.12 while the bottom of Figure 5.12 shows the corresponding estimation errors. The simulated force is represented by the solid red line. The estimated force from the NLPV observers (polytopic and gridding approaches) and unified H_∞ observer are highlighted by blue solid, green dash-dotted and pink dotted lines, respectively. It can be seen clearly that the unified H_∞ observer performs better in the presence of measurement noise than the NLPV observers do. The Normalized Root-Mean-Square Errors (NRMSE) in Table 5.3 corresponding to the estimation errors in Figure 5.12 prove the better efficiency of the unified H_∞ observer subject to measurement noises. The Tables 5.4 and 5.5 show the NRMSE for the period $[0-2\text{s}]$ and $[13-15\text{s}]$, respectively. They show the faster convergence of the unified H_∞ observer for the period $[0-2\text{s}]$ and the better accuracy of the unified H_∞ observer for the period $[13-15\text{s}]$.

Table 5.3: Normalized Root-Mean-Square Errors (NRMSE) for the period $[0-15\text{s}]$

Observers	NRMSE
NLPV observer-polytopic method	0.0262
NLPV observer-gridding method	0.0277
Unified H_∞ observer	0.0142

Table 5.4: Normalized Root-Mean-Square Errors (NRMSE) for the period $[0-2\text{s}]$

Observers	NRMSE
NLPV observer-polytopic method	0.0712
NLPV observer-gridding method	0.0756
Unified H_∞ observer	0.0386

Table 5.5: Normalized Root-Mean-Square Errors (NRMSE) for the period $[13-15\text{s}]$

Observers	NRMSE
NLPV observer-polytopic method	0.0148
NLPV observer-gridding method	0.0081
Unified H_∞ observer	0.0057

5.4 Experimental comparison

To experimentally assess and compare the effectiveness of the proposed methodologies, the three proposed observers are implemented on the 1/5 car scaled car INOVE available at GIPSA-lab, shown in Chapter 1. The following block-scheme illustrates the experimental scenario of the observers (Figure 5.13).

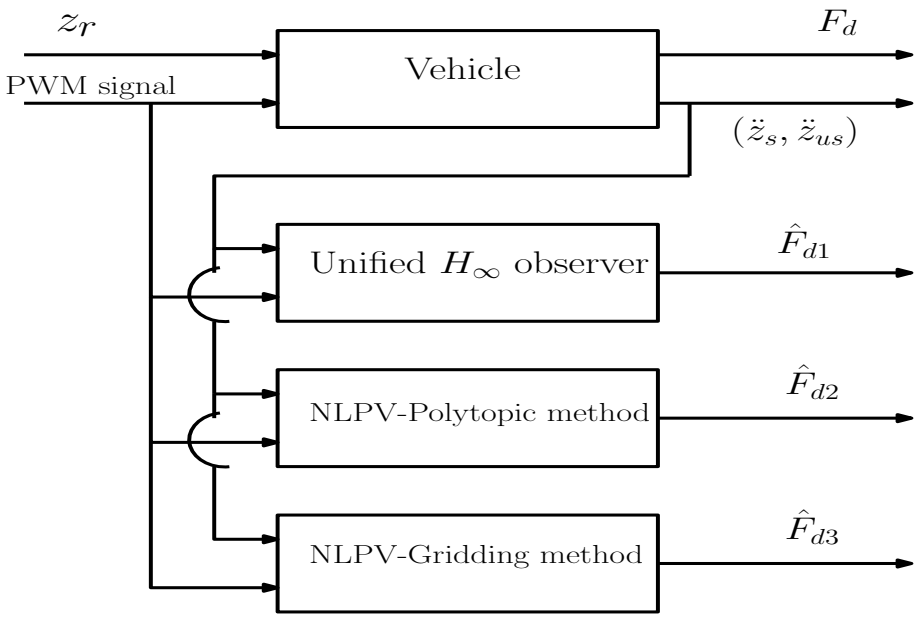

Figure 5.13: Block diagram for the implementation of the observers.

In this chapter, only one realistic scenario is shown for the experimental comparison of the three proposed observers. The experimental scenario is detailed as follows:

- The road profile shown at the top of Figure 5.9 is an ISO standard one.

- The control input u (duty cycle of PWM signal) is obtained from a Skyhook controller (see the bottom of Figure 5.14).

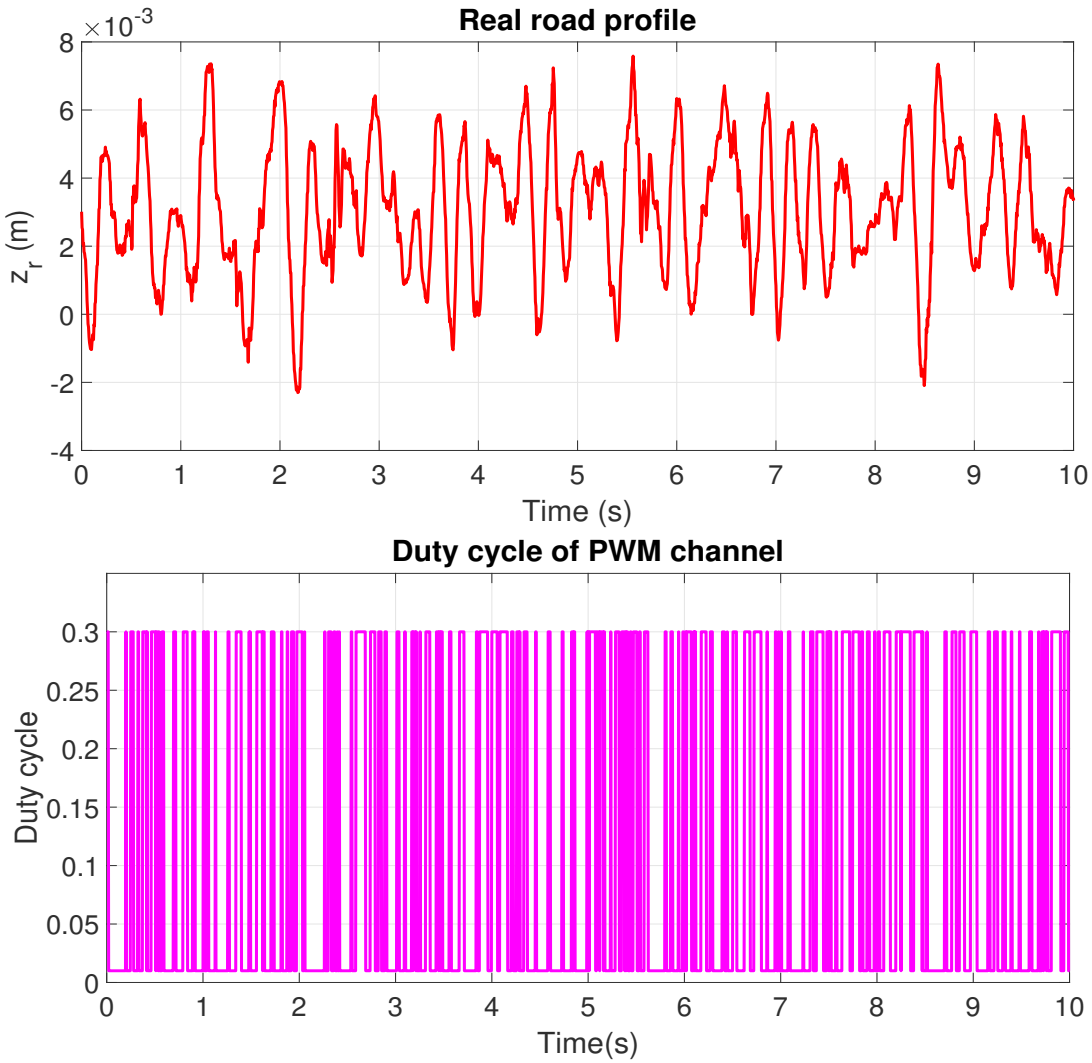

Figure 5.14: Experimental senario: (top) Road profile , (bottom) Control input signal (PWM signal)

The experimental results of the three observers are presented in Figure 5.15. The red line is the measurement force obtained from the force sensor inside the semi-active damper. The blue line and green dash-dotted line present the estimated forces from NLPV polytopic and gridding observers, respectively. The pink dotted line shows the estimated forces obtained from the unified H_∞ observer. Through these experimental results, the unified H_∞ observer exhibits a slightly better damper force estimation than do the NLPV observers. From Table 5.6, the unified H_∞ observer NRMSE is 5.63% whereas the NLPV observer with polytopic method NRMSE is 7.63% and gridding method NRMSE 7.45%, which confirm a little qualitative difference.

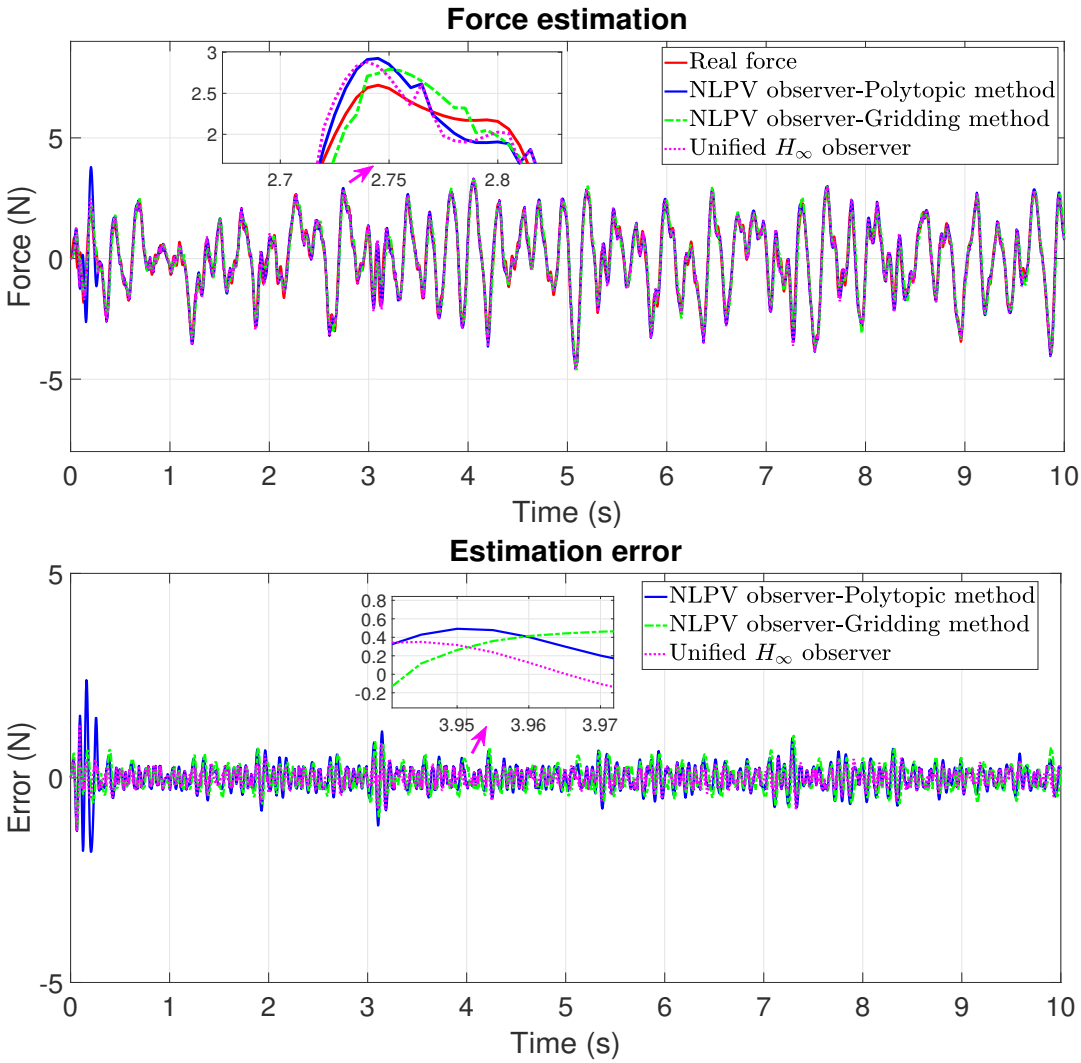

Figure 5.15: Experimental senario: (above) Damper force, (below) Estimation error

Table 5.6: Normalized Root-Mean-Square Errors (NRMSE)

Observers	NRMSE
NLPV observer-polytopic method	0.0763
NLPV observer-gridding method	0.0745
Unified H_∞ observer	0.0563

5.5 Conclusion

This chapter presented a comparison of the NLPV observers and the unified H_∞ observer to estimate the damper force. Both simulation and experiment results assess the ability and the accuracy of all the proposed models to estimate the damping force of the ER semi-active damper. To summarise the contributions of this chapter, the following table presents the advantages and drawbacks of each method:

Observers	Advantages	Drawbacks
Unified H_∞ observer	• Decoupling the road profile. • Minimizing the measurement noises effect. • Short convergence time .	• Need to fulfill the decoupling conditions. • Complex design procedure. • Higher implementation cost (9 matrices N; J;H;M; P; Q; G;R; S).
NLPV observers	• Handling the variation of the nonlinearity amplitude. • Minimizing the measurement noises effect. • Low implementation cost (2 gains L_0 and L_1). • Simple design procedure	• Long convergence time

Part III

Application to fault-tolerant control

Chapter 6

Fault Tolerant Control for the semi-active suspension system

Contents

This chapter presents the LPV Fault Tolerant Control method for the semi-active suspension system, in particular when some faults occur upon the damper. Synthetically, this study is two-fold: i) the first part analyses the possible faults on these dampers and incorporates their effect to the developed model, which is of paramount importance for diagnosis and reliability of suspension systems; ii) the second proposes Fault-Tolerant Control techniques based on the LPV method and the fault model. Throughout this study, simulation and experimental validation tests are performed on a real 1/5-scaled vehicle testbed. Results are shown to illustrate how the model can be used for *FTC* of semi-active suspension systems. The overall results assess the ability and efficiency of the proposed solution.

6.1 Introduction

In the automotive field, the effect of faults in Semi-Active suspension systems could be very detrimental to the vehicle driving performances [Hernández-Alcántara et al. 2016]. Faults that occur in the damper units can directly or indirectly generate a loss on the delivered force, which

should be taken into account in fault-tolerant control-oriented models. In the literature, *FTC* methods for *SA* can be found: in papers [Fleps-Dezasse and Brembeck 2016], [Fleps-Dezasse, Svaricek, and Brembeck 2017] and [Fleps-Dezasse, Svaricek, and Brembeck 2018], where the level of faults, in terms of saturation, schedules a controller tuned to enhance the vertical dynamics of the vehicle; in [Moradi and Fekih 2013], where a *PID*-sliding-mode approach is designed for the same goal; in [Nguyen, Sename, and Dugard 2015b], which addresses the issue via gain-scheduling and, recently, in [Morato, Sename, and Dugard 2019], where seven different state-feedback methods are developed. Concerning the control design problem of the semi-active suspension system, the key challenge is to take the dissipativity of the semi-active damper and the saturation into account. To this aim, the Fault Tolerant Control (FTC) is designed to preserve the vehicle performance in several fault cases.

The main contribution of this chapter is to present an application of FTC for the semi-active suspension system.

- To analytically include in the control-oriented model the effect of faults that might occur on these ER dampers and heavily degrade driving performances if not corrected. This opens doors to the design of FTC strategies.
- FTC techniques for SA suspensions are developed using the proposed ER damper model in order to adapt to the presence of the damper fault and to minimize the performance deterioration of the suspension system.

6.2 Control-oriented fault modelling: loss of effectiveness

This section aims to extend the obtained model (a parametric model) in chapter 1, to consider faulty conditions as well; this is the second main contribution of this paper. This is to be done on the basis assumption that the most common kinds of faults occurring in *ER* dampers, from a control point-of-view, lead to a loss on the delivered damping force.

Such loss of effectiveness terms (in the particular case of the *SA* system actuators, dampers) are usually represented in the literature as multiplicative faults (see [Hernández-Alcántara et al. 2016; Morato et al. 2019; Nguyen, Sename, and Dugard 2015a]). This simple representation is coherent with the methods developed in *FTC/FDD* works.

Henceforth, if a given kind of fault occurs, the interest is to find a multiplicative factor that describes its effect (loss) on the force delivered by the *ER* damper. By having an adequate model that comprises the force loss due to faults, one is able to directly synthesize *FDD* schemes as well as Fault Tolerant Control strategies. This work does not aim to deeply describe the underlying dynamics of faulty situations on *ER* dampers, but to grasp the direct consequence of faults in terms of the provided damper force.

One must recall that this work is based on the modelling of *ER* dampers via the use of an experimental platform. This platform has four semi-active *ER* dampers specifically man-

ufactured for the design, implementation and experimental testing of embedded suspension control strategies. Therefore, faulty experimentation on these dampers is not permitted to avoid their destruction, which is not suitable.

Therefore, for the following development, faults are experimentally emulated. This means that the duty-cycle signal $u(t)$ is modified in a such way that the delivered force is equivalent to that of a faulty condition. This kind of "fault mimicking" has been previously done by the authors in [Morato et al. 2019] and [Nguyen, Sename, and Dugard 2015a].

In this section, the static parametric damper model (1.6) is recalled as the following one:

$$\begin{cases} F_d = k_0 x_p + c_0 \dot{x}_p + F_{er} \\ F_{er} = \sigma u^{\beta} \text{sign}(\dot{x}_p) = F_{ER} \text{sign}(\dot{x}_p) \end{cases} \tag{6.1}$$

where $F_{ER} = \sigma u^{\beta}$, u is the duty cycle of PWM signal, parameters of model are shown in Table

6.2.1 Electrical issues

The feeding power circuit of the *ER* dampers must be considered as a first potential source of loss of effectiveness. The electric field only varies the yield stress term - i.e. the controllable part of the damping force $F_d(t)$. Therefore, the effect of faults in such circuits also occurs upon this controllable damping component of the delivered force. Suppose that the circuit sustaining the electric field completely fails, then the yield stress becomes null.
For this reason, the loss of effectiveness fault factor $f_1(t)$ is set only upon $F_{er}(t)$, as depicts Equation (6.2). This factor $f_1(t)$ can be computed as proportional to the losses on the generated electric field, derived from internal electronic failures on the circuit responsible for providing $E(t)$; note that the instrumentation details themselves will not be investigated herein.

$$F_d^{faulty} = k_0 x_p + c_0 \dot{x}_p + f_1 F_{ER} \text{sign}(\dot{x}_p) \tag{6.2}$$

Remark that f_1 is bounded inside the interval [0 , 1], where $f_1 = 0$ represents a complete electrical circuit crash.
To mimic the loss of effectiveness on the delivered force due to electrical issues, the duty cycle of *PWM* channel u_{f_1}, used to implement electrical fault case, is calculated, based on the measured data of faultless case with control input u, where the *PWM* signal u_{f_1} (used to simulate electrical faults) is obtained as

$$u_{f_1} = f_1^{\frac{1}{\beta}} u \tag{6.3}$$

In Figure 6.1 , a simulation of a sequence of electrical faults (6.3) is shown. The comparison of damper force from the sensor and the proposed fault-tolerant control-oriented electrical model is detailed in Figure 6.2. The effect of electrical fault on the Force vs. Velocity characteristic diagram (comparing healthy and faulty cases) is shown in Figure 6.3.

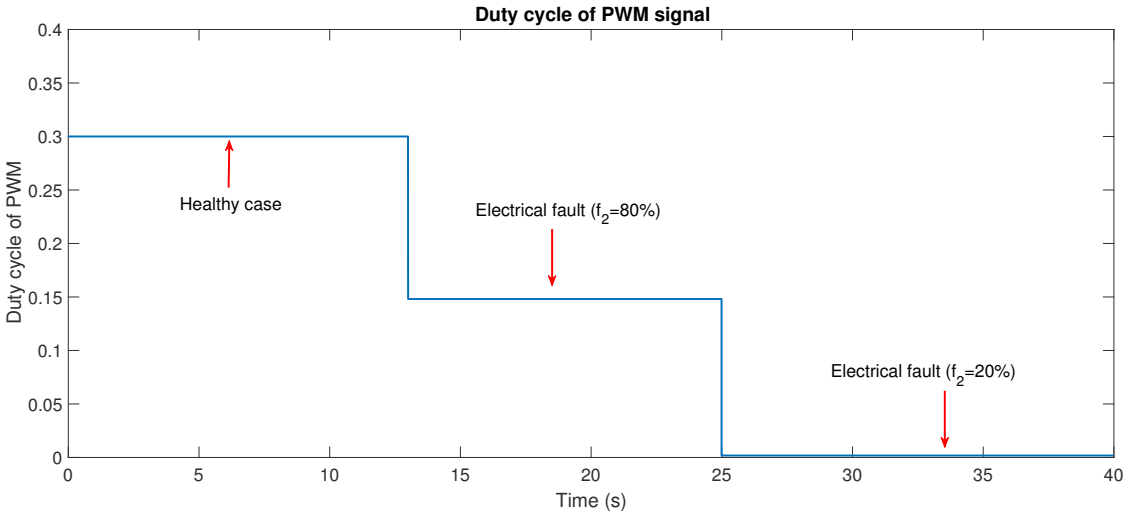

Figure 6.1: Electric Faults: Fault-mimic PWM signal

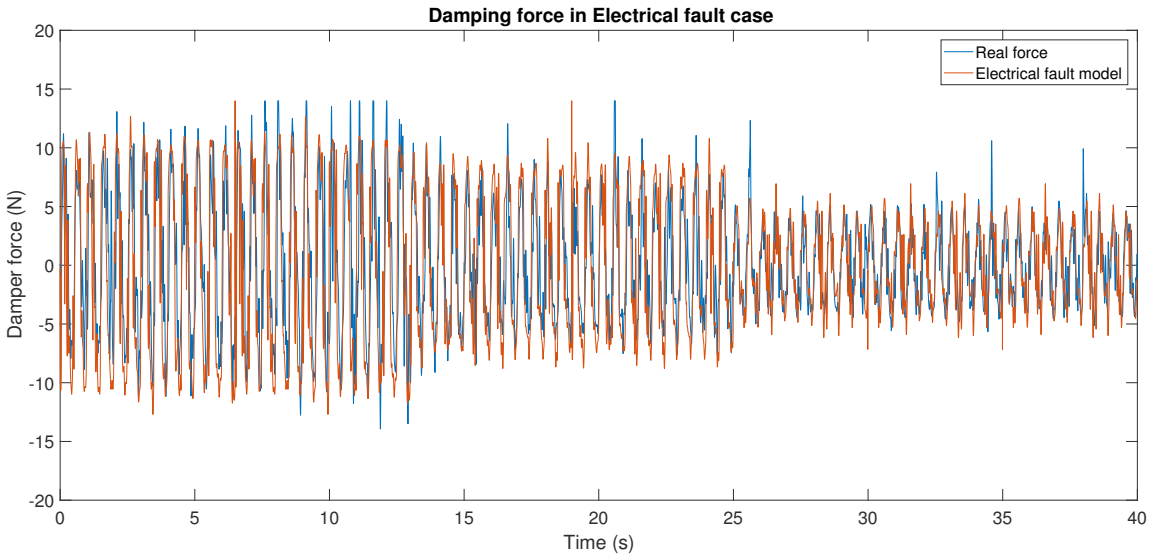

Figure 6.2: Electric Faults: ER Damper Force - measurement vs. model

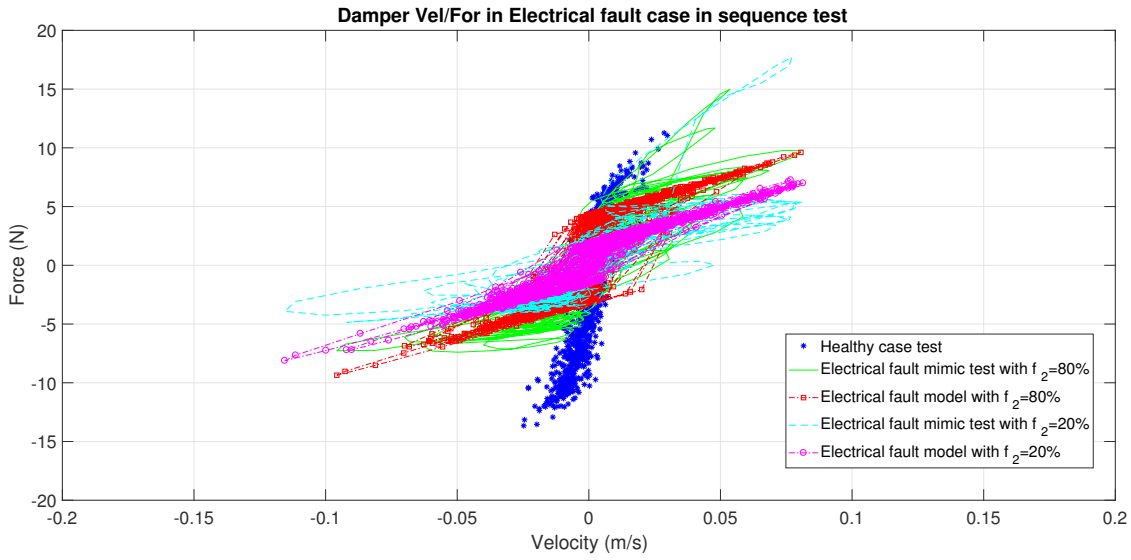

Figure 6.3: Electric Faults: Force vs. Velocity diagram - measurement vs. model

6.2.2 Oil leakage

As described repeatedly throughout this work, the *ER* damper can be defined as an advanced shock absorber. In the case of shock absorbers, the most common faults are oil leakages. Due to several reasons, such as the high pressures inside the system or simply an impact, the system may present a loss on the quantity of its damping fluid. This situation directly affects the global behaviour of the shock absorber.
This kind of oil leakage fault is of most interest to the scientific community for an accurate modelling of this phenomenon. If the amount of damping fluid decreases, the flow inside the damper chamber also decreases, which implies a loss of effectiveness of the damper's force.
Regarding the faulty Electro-Rheological damper situations, these faults can be considered as of multiplicative form upon the force produced by the damper. More specifically, one can represent such a fault with the use of a loss of effectiveness factor, as discussed in [Hernández-Alcántara et al. 2016], where some destructive tests have been done to model the oil leakage effect. These factors are assumed to be constant or slow-varying and can represent anything that leads to a loss in the delivered force (for instance, an oil leakage, physical deformation or even the presence of air inside the *ER* fluid duct).
The loss of effectiveness factor f_2 is (once again) bounded inside the set $[0\ ,\ 1]$, where $f_2 = 1$ means that the system is faultless and $f_2 = 0$ means that all the *ER* fluid has leaked from the damper chamber (which is a rather extreme case, not considered herein). To simulate such faults, this factor f_2 has to be incorporated into the proposed *ER* damper model (**??**), as follows:

$$F_d^{faulty} = f_2[k_0 x_p + c_0 \dot{x}_p + F_{ER}\text{sign}\{\dot{x}_p\}] \tag{6.4}$$

To mimic the loss of effectiveness of the delivered damper force due to oil leakage, it is necessary to find a duty cycle for PWM signal u_{f_2} to emulate such a case. The damper force that mimics the damper oil leakage is given by

$$F_d^{mimicf_2} = k_0 x_p + c_0 \dot{x}_p + F_{ER}^{f_2} \text{sign}(\dot{x}_p) \tag{6.5}$$

From Equations (6.4) and (6.5), $F_{ER}^{f_2}$ is obtained such that $F_d = F_d^{mimicf_2}$:

$$F_{ER}^{f_2} = (f_2 - 1)(k_0 x_p + c_0 \dot{x}_p)\text{sign}(\dot{x}_p) + f_2 F_{ER} \tag{6.6}$$

Therefore, the PWM signal u_{f_2} that mimics this kind of faults is computed as follows:

$$u_{f_2} = \left[\frac{(f_2 - 1)}{\sigma} (k_0 x_p + c_0 \dot{x}_p)\text{sign}(\dot{x}_p) + f_2 u^{\beta} \right]^{\frac{1}{\beta}} \tag{6.7}$$

In the following experimental tests, the oil leakage fault factor f_2 is chosen as 90% (which means 10 % of the fluid has leaked from the damper chamber). Based on measurement data (x_p, $\dot{x}_p$) and PWM signal of healthy case $u = 0.3$, the duty cycle of PWM signal (u_{f2}) is calculated using Equation (6.7), which gives the signal presented in Figure 6.4. Figure 6.5 compares the model-based faulty force with the actual measured force that is controlled to emulate a faulty condition, while Figure 6.6 gives the Force vs Velocity diagram comparing healthy and faulty cases (model and mimic).

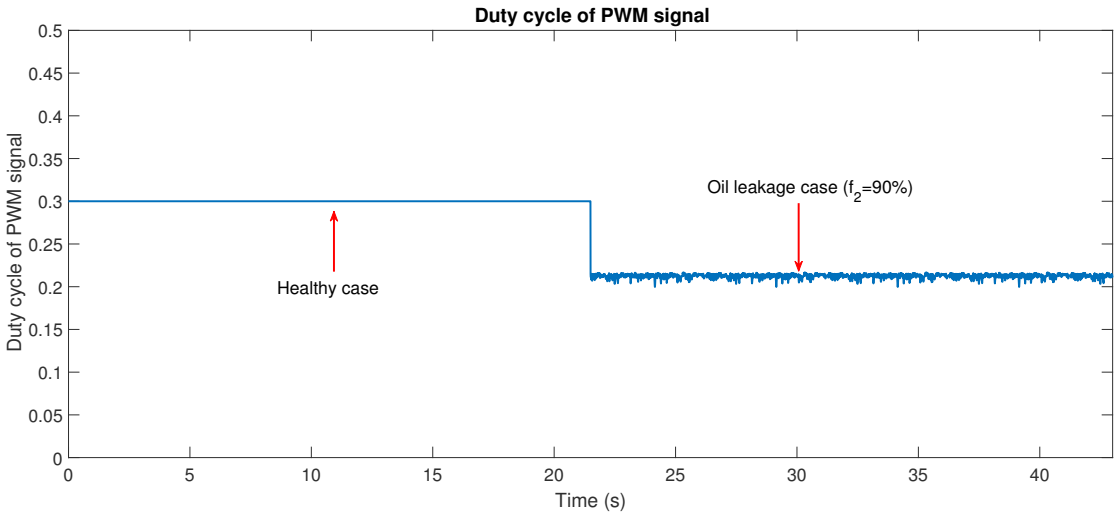

Figure 6.4: Oil leakage: Fault-mimic PWM signal

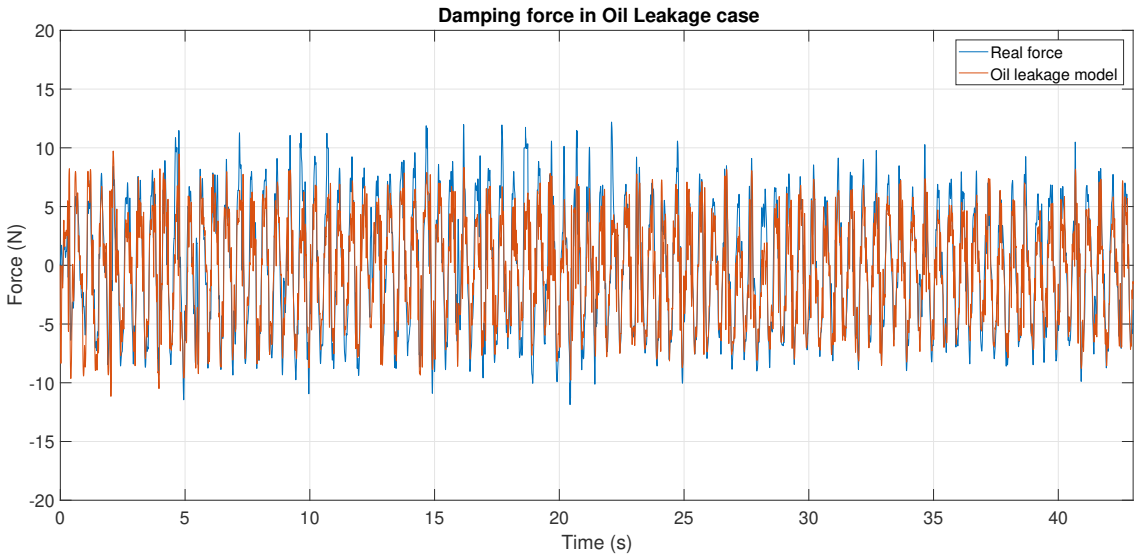

Figure 6.5: Oil leakage: *ER* Damper Force - measurement vs. model

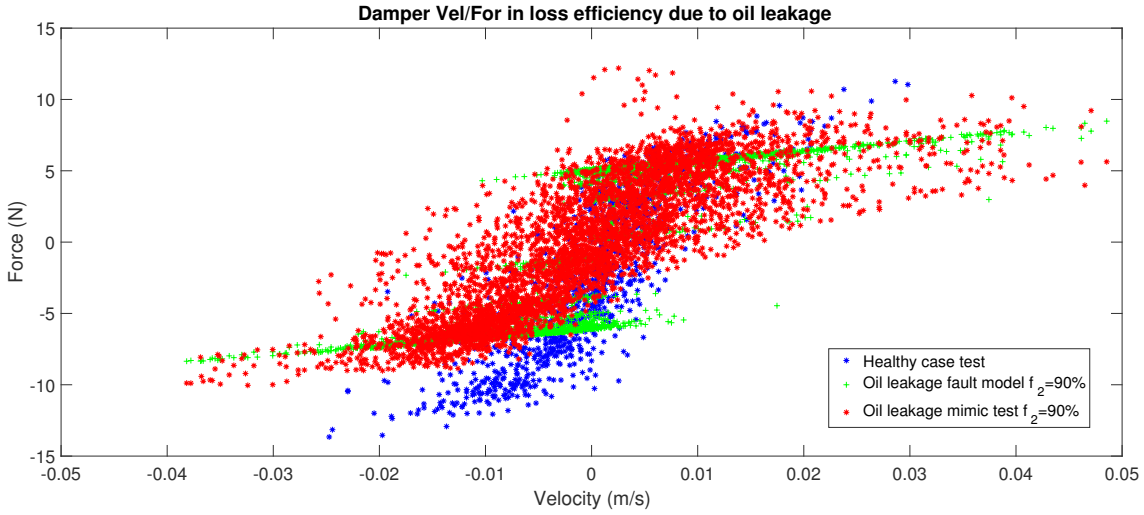

Figure 6.6: Oil leakage: Force vs. Velocity diagram - measurement vs. model

6.2.3 Physical deformation

In terms of physical faults, it is important to state that most industrial manufacturers of novel *ER* dampers add some spirals to the inner ducts of these dampers, in order to increase the path that the fluid must travel and thus to enlarge the damping effect. As the fluid has a longer path to travel, the force given by the damper increases, but the pressure inside the fluid chamber also increases. This higher pressure present in brand-new *ER* dampers has also to be considered as a third potential source of faults, since it might cause a physical deformation

of the inner path of the fluid.

When physical deformation happens, the length of the annular duct decreases. Note that this parameter is related both to the controllable force and the nominal viscosity; the gas compliance is not affected.

Therefore, this fault is expressed as in Eq. (6.8), where f_3 is the loss of force effectiveness factor for physical deformation faults. The fault term f_3 is bounded in $[0\,,\,1]$, with $f_3 = 0$ meaning that the physical deformation event completely destroyed the inner fluid path. Fault emulation results will not be presented for this fault category since they are similar to the previous ones.

$$\begin{aligned} F_d^{faulty} &= f_2(k_0 x_p + f_3[c_0 \dot{x}_p \\ &+ f_1 F_{ER}\text{sign}\{\dot{x}_p\}])\,. \end{aligned} \tag{6.8}$$

In order to experimentally emulate physical deformation faults in the real test-rig, the procedure is to find a PWM signal u_{f_3} that acts such that the delivered force corresponds to a faulty situation, similar to what has been done in the two previous subsections.
The damper force in the physical deformation fault case can be writen as:

$$F_d^{mimicf_3} = k_0 x_p + c_0 \dot{x}_p + F_{ER}^{f_3}\text{sign}(\dot{x}_p) \tag{6.9}$$

From Equations (6.8) and (6.9), $F_{ER}^{f_3}$ is calculated such that $F_d^{f_3} = F_d^{mimicf_3}$:

$$F_{ER}^{f_3} = (f_3 - 1)c_{vis}\dot{x}_p\text{sign}(\dot{x}_p) + f_3 F_{ER} \tag{6.10}$$

Thus, the PWM signal v_{f_3}, used to emulated physical deformation faults, is obtained as follows:

$$u_{f_3} = \left[\frac{(f_3 - 1)}{\sigma} c_{vis}|\dot{x}_p| + f_3 u^{\beta}\right]^{\frac{1}{\beta}} \tag{6.11}$$

The fault-mimic PWM signal (u_{f_3}) which is computed by Equation (6.11) with $f_3 = 90\%$ (which stands, for instance, for fluid duct which is $10\,\%$ deformed) and $u = 0.3$, is shown in Figure 6.7. Figure 6.8 presents both the model-based force (with physical deformation condition) and the measured ER damper force emulating such faulty case. Finally, Figure 6.9 shows the Force vs Velocity diagram comparing healthy and faulty conditions (model and emulated by testbed).

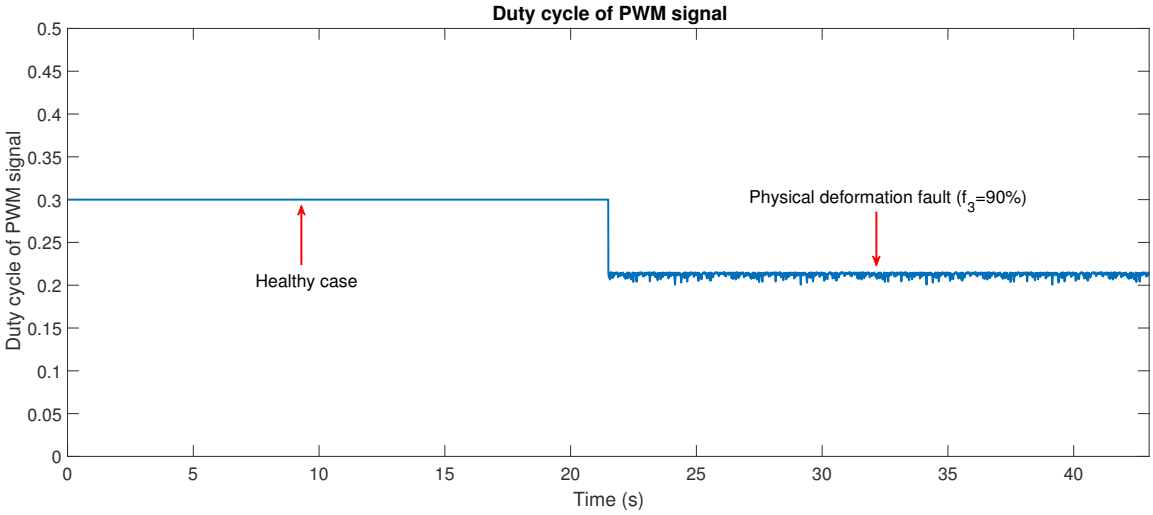

Figure 6.7: Physical deformation: Fault-mimic PWM signal

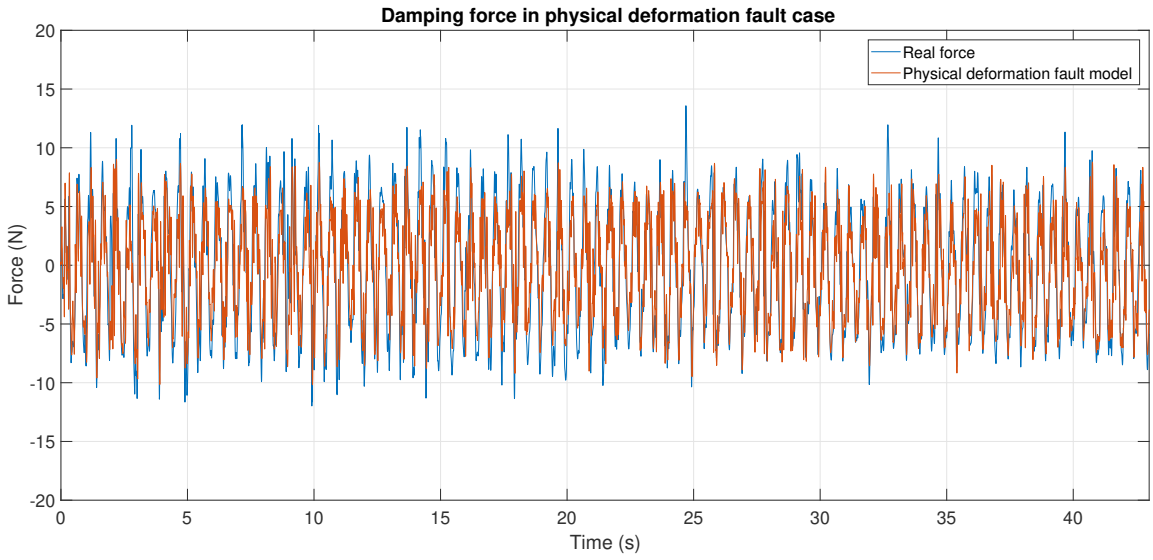

Figure 6.8: Physical deformation: ER Damper Force - measurement vs. model

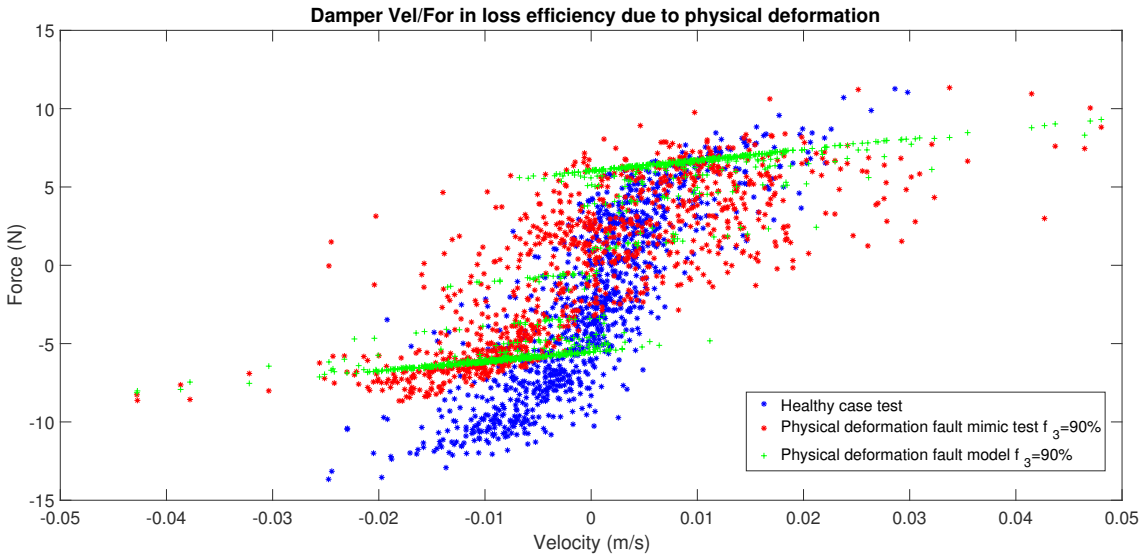

Figure 6.9: Physical deformation: Force vs. Velocity diagram - measurement vs. model

6.3 Fault tolerant LPV semi-active suspension control

Concerning the semi-active suspension control problem, the key challenge is to take both the dissipativity of the damper and the saturation into account. In ([Poussot-Vassal et al. 2008]), a kind of LPV anti-windup controller has been presented to deal with such a constraint. Indeed, the considered semi-active damper is simply modeled as a static map of lower and upper bounds of the achievable forces, denoted as the dissipative domain $\mathcal{D}(\dot{z}_{def})$. The scheduling parameter is then chosen as a function of the difference "ε" between the computed damper force F_d (obtain from the controller) and the achievable one $F_d^{\perp}$. As a result, the scheduling parameter depends on $\mathcal{D}(\dot{z}_{def})$. Therefore, this method gives very good results in nominal condition i.e without faults. However, if faults (oil leakages, electric shortages or physical defiances) occur upon the controlled ER damper of these SA suspensions, the force domain is reduced (as illustrated in Figure 6.10), and, thus, FTC mechanisms must be put in practice to make sure graceful performance degradation can be obtained..

Literature shows several different *FTC* strategies for *SA* suspensions with faulty dampers, as in [Tudon-Martinez et al. 2013], [Fleps-Dezasse, Svaricek, and Brembeck 2017], [Morato, Sename, and Dugard 2019]. All these works rely on the essential idea of adapting the control law so that the dissipativity domain is always respected, as gives:

$$F_d(t) \quad \in \quad \mathcal{D}(\dot{x}_p, x_p, f)\,. \tag{6.12}$$

This means, in practice, that the controlled damping force $F_d(t)$ must always belong to the feasibility set $\mathcal{D}$ despite time-varying faults $f(t)$. The available damping force is related to the level of faults upon the damper: faults lead to smaller forces and increased damping

motion $\dot{z}_{def_{ij}}$, which means that $\mathcal{D}$ shrinks and shifts[1] according to f, as suggested in [Morato, Sename, and Dugard 2019] and [Nguyen, Sename, and Dugard 2015b]. Figure **??** illustrates which are the dissipativity constraints and how they become stricter when some oil leakage faults occur.

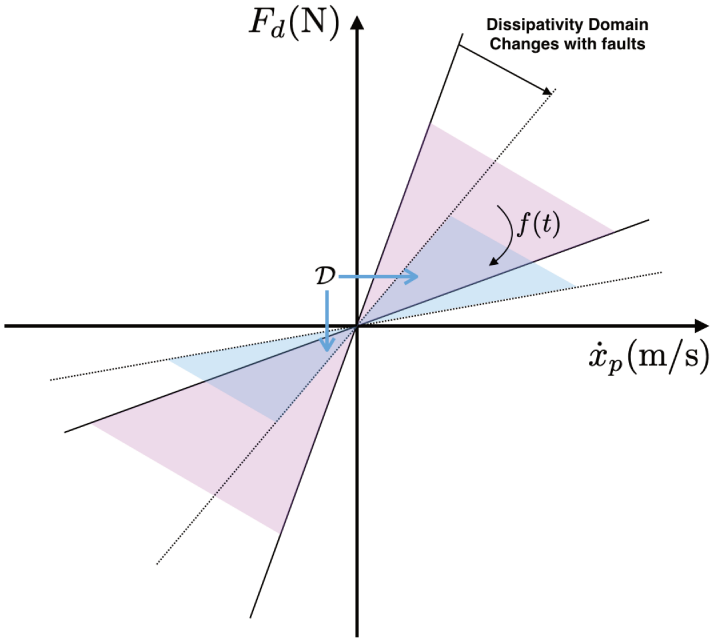

Figure 6.10: The ideal dissipative force domain $\mathcal{D}_f$ in presence of fault

As a consequence, if this saturation constraint is not adapted online, then the dissipativity condition of the *ER* damper is not guaranteed any more. Indeed, as discussed in [Nguyen, Sename, and Dugard 2015b], the required force could be outside the range of feasible "faulty" forces if no fault information ($\hat{f}$) is included in the control design, leading to very poor performances. Thus, due to the described limitations, an LPV-FTC strategy is presented to achieve good performance in case of faults upon the semi-active ER damper.

6.3.1 FTC/LPV semi-active suspension control design

In this section, an LPV fault scheduling state feedback control is designed to ensure the damper dissipativity and to keep good dynamic performances of the faulty semi-active suspension system. Let us recall the LTI system of the quarter car model (2.8) and complete it by the measurement and controlled output equations as follows:

$$\Sigma_1 : \begin{cases} \dot{x}_s = A_s x_s + B_s u_{er} + D_{s\omega}\omega_s \end{cases} \tag{6.13}$$

[1] By design, the min. / max. force constraints decrease with faults, shrinking the available set in size, but also shifts it sideways, as illustrates the Figure.

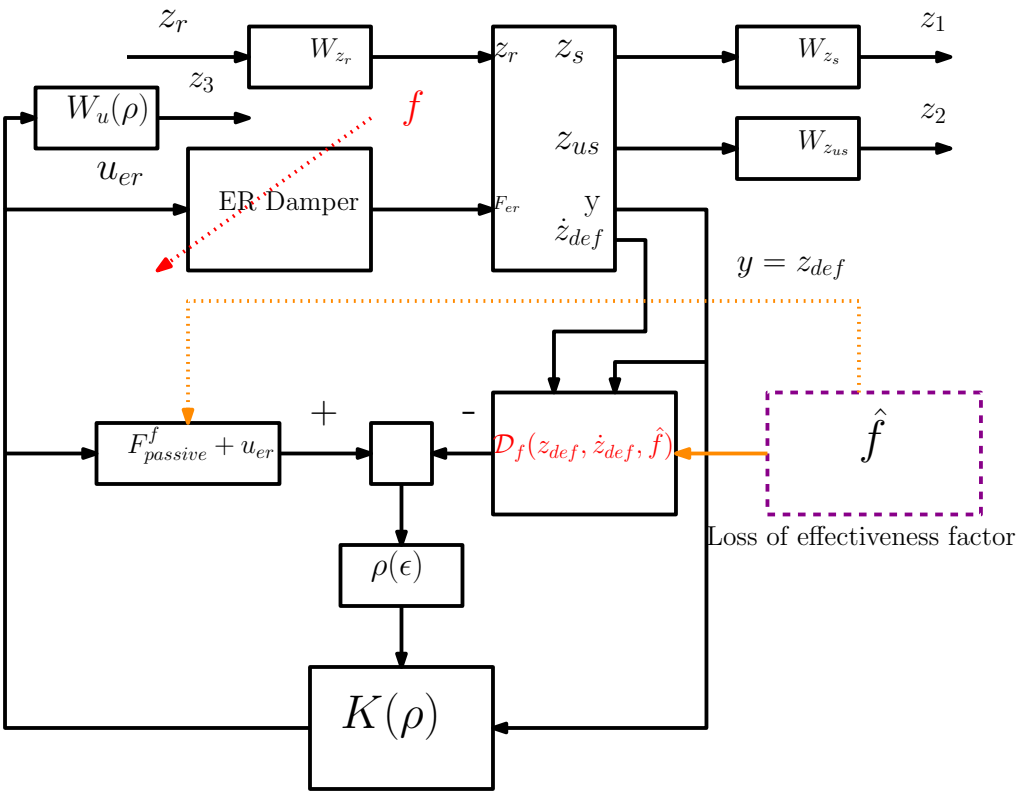

Figure 6.11: General FTC/LPV control design scheme

The overall control structure is presented in Fig.(6.11). The LPV output feedback controller $K(\rho)$ receives the measurement vector y ($y = z_{def}$) as an input and computes the controlled forces u_{er}. The controlled part will be added to the passive forces ($F_{passive} = k_0 z_{def} + c_0 \dot{z}_{def}$) in order to improve the vehicle performances. This LPV controller is scheduled by the parameter ρ that constraints the control signal or not, in such a way that the required forces F_d remain semi-active and adapted to fault situations. The estimated loss of effectiveness factor is used to modify the dissipativity domain $D_{\hat{f}}(z_{def}, \dot{z}_{def}, \hat{f})$ of the semi-active suspension allowing to schedule the parameter ρ. The domain $D_{\hat{f}}(z_{def}, \dot{z}_{def}, \hat{f})$ in case of the ER damper loss of effectiveness due to oil leakage. The $D_{\hat{f}}(z_{def}, \dot{z}_{def}, \hat{f})$ is defined the domain between F^f_{dmax} and F^f_{dmin} as follows

$$D_{\hat{f}}(z_{def}, \dot{z}_{def}, \hat{f}) : \begin{cases} F^f_{dmax} = \hat{f}_2(k_0 z_{def} + c_0 \dot{z}_{def} + \sigma \cdot u^{\beta}_{max} \cdot sign(\dot{z}_{def})) \\ F^f_{dmin} = \hat{f}_2(k_0 z_{def} + c_0 \dot{z}_{def} + \sigma \cdot u^{\beta}_{min} \cdot sign(\dot{z}_{def})) \end{cases} \tag{6.14}$$

where $\hat{f}_2$ is the estimated loss of effectiveness factor due to oil leakage, u_{max} is the maximum value of the duty cycle of the PWM signal ($u_{max} = 1$), u_{min} is the minimum value of the duty cycle of the PWM signal ($u_{min} = 0$).

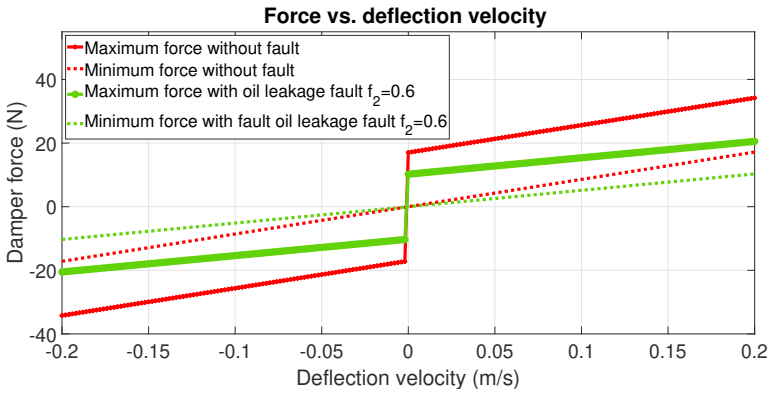

Figure 6.12: The real dissipative force domain $\mathcal{D}_f$ in presence of oil leakage fault with $f_2 = 60\%$

The real dissipative force domain of ER damper in the INOVE testbed is shown in Figure 6.12. The red line and red-dot are the maximum and minimum force of the heathy damper, respectively. The maximum and minimum force of the faulty damper ($f_2 = 60\%$) are represented by the green line and green-dot, respectively.

Remark 6.3.1. *In case of healthy damper ($f_2 = 1$), the domain $D_{\hat{f}}(z_{def}, \dot{z}_{def}, \hat{f})$ becomes*

$$D_{\hat{f}}(z_{def}, \dot{z}_{def}, \hat{f}) : \begin{cases} F_{dmax} = k_0 z_{def} + c_0 \dot{z}_{def} + \sigma \cdot u_{max}^{\beta} \cdot sign(\dot{z}_{def}) \\ F_{dmin} = k_0 z_{def} + c_0 \dot{z}_{def} + \sigma \cdot u_{min}^{\beta} \cdot sign(\dot{z}_{def}) \end{cases} \tag{6.15}$$

Remark 6.3.2. *In this chapter, we assume that the loss of effectiveness factor is known by using fault observer. This observer, to estimate the loss of efficiency factor on the ER damper of INOVE testbed, has been done in the work of [Morato et al. 2019], a Ph.D. student of the SLR team.*

6.3.1.1 Weighting functions

Some weighting functions are designed to improve the performances of the vehicle as follows

- $W_{z_r} = 7 \cdot 10^{-2}$ is used to shape the road disturbance effects z_r
- $W_{z_s} = 2\frac{2\pi f_1}{s+2\pi f_1}$relates to the comfort performances
- $W_{z_{us}} = \frac{2\pi f_2}{s+2\pi f_2}$ relates to the road-holding performances
- $W_u(\rho) = \rho\frac{2\pi 50}{s+2\pi 50}$ is used to penalize (more or less) the control input signal amplification according to the ρ signal. The scheduling parameter ρ will presented in next sections

In order choose the frequencies f_1 and f_2, Bode diagram of the tranfer z_s/z_r, z_{us}/z_r and z_{def}/z_r of the quarter-car model with passive damper force ($u_{er} = 0$) are shown in Figures 6.13, 6.14, 6.15.

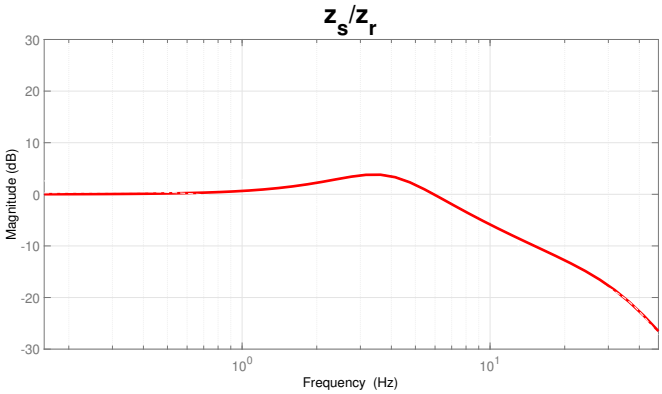

Figure 6.13: Transfer $\|z_s/z_r\|$-Passive damper

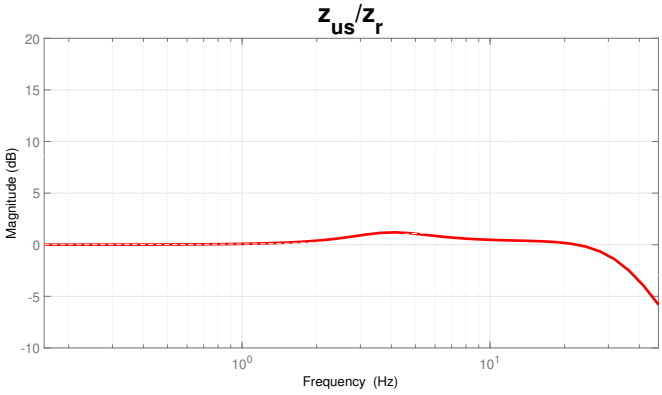

Figure 6.14: Transfer $\|z_{us}/z_r\|$-Passive damper

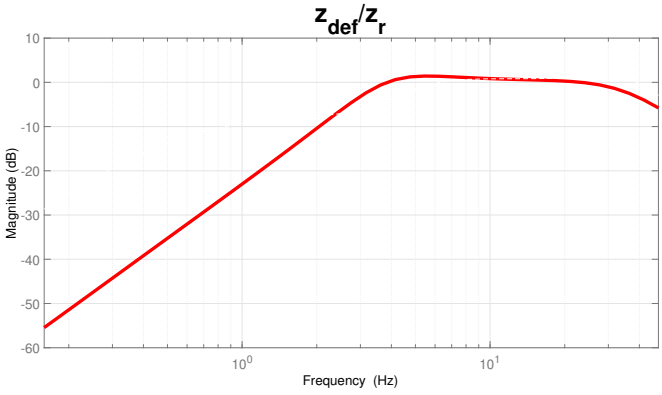

Figure 6.15: Transfer $\|z_{def}/z_r\|$-Passive damper

According to these figures, we can see that the first peak of the bode diagrams at 4 Hz and the second peak around 20 Hz. Therefore, we choose the frequencies $f_1 = 4$Hz and $f_2 = 20$ Hz.

6.3.1.2 Scheduling parameter

The method proposed in the previous work of [Poussot-Vassal et al. 2008] and [Nguyen, Sename, and Dugard 2015b] for a quarter car model in order to fulfill the dissipativity constraint, aims at increasing or decreasing the gain of the weighting filter W_u on the damper control signals, according to a given scheduling strategy. Indeed, if the required force computed by the controller is active, a scheduling parameter allows the controller to enhance or not the performance specifications, so that the required force remains dissipative. This method is extended here in the case of a faulty damper.

More precisely, the ρ parameter is tuned as following:

- when ρ is low, $W_u(\rho)$ is small and it does not penalize the control signal u.
- when ρ is high, $W_u(\rho)$ is large and it attenuates the control signal u to remain in the semi-active domain.

For that purpose, the following scheduling strategy $\rho(\varepsilon)$ is introduced:

$$\rho(\varepsilon) := \begin{cases} \underline{\rho} & \text{if } \varepsilon < \mu \\ \underline{\rho} + \frac{\overline{\rho}-\underline{\rho}}{\mu}(\varepsilon - \mu) & \text{if } \mu \leq \varepsilon \leq 2\mu \\ \overline{\rho} & \text{if } \varepsilon > 2\mu \end{cases} \tag{6.16}$$

$$\varepsilon = F_d^f - F_d^{\perp} \tag{6.17}$$

where $F_d^f = f_2(k_0 z_{def} + c_0 z_{def}) + u_{er}$, $F_d^{\perp}$ is the orthogonal projection of F_d^f on domain $D_{\hat{f}}(z_{def}, \dot{z}_{def}, \hat{f})$, μ is a design parameter that modifies the dead-zone of the $\rho(\varepsilon)$ function (μ is chosen sufficiently low, e.g $\mu = 0.1$).

Remark 1.
- *As defined previously, $\rho(\varepsilon)$ belongs to $[\underline{\rho}, \overline{\rho}]$ which is essential in the LPV framework ($\underline{\rho} = 0.01$, $\overline{\rho} = 1$).*
- *$\varepsilon \neq 0$ means that the required force is outside the domain $D_{\hat{f}}(z_{def}, \dot{z}_{def}, \hat{f})$. Conversely, $\varepsilon = 0$ means that the force required by the controller is inside the domain $D_{\hat{f}}(z_{def}, \dot{z}_{def}, \hat{f})$.*

Notice that the varying parameter can be obtained online and is used to schedule the designed output feedback controller.

6.3.1.3 H_∞/LPV control design for FTC

It is worth noting that, while the model car is a LTI system, the generalized plant (which consists of the quarter car model (6.13) and the weighting functions ()) is LPV because of parameter dependant weighting function $W_u(\rho)$. Then, the following parameter dependent

suspension generalized plant ($\Sigma_s(\rho)$)is expressed by:

$$\Sigma_s(\rho): \begin{cases} \dot{x_g} = A(\rho)x_g + B_1(\rho)w_s + B_2 u_{er} \\ z = C_1(\rho)x_g + D_{11}(\rho)w_s + D_{12}u_{er} \\ y \ = C_2 x_g \end{cases} \tag{6.18}$$

where x_g includes the state vectors of the quarter car model and of the weighting function respectively.
$z = [z_1 \ \ z_2 \ \ z_3]^T$ are the controlled outputs,
$w_s = [z_r]$: the disturbance input signal,
$y = [z_{def}]$: measured output.
$u =_{er}$: the suspension control signal derived from the H_∞/LPV framework,
ρ : the varying parameter, $\rho \in [0.01\ 1]$.

According to [Apkarian, Gahinet, and Becker 1995], since the system matrices ($A(\rho)$, $B_1(\rho)$, $C_1(\rho)$, $D_{11}(\rho)$ are affine in ρ and since the scheduling parameter ρ varies in a polytope $\mathcal{Y}_\rfloor$ of 2 vertices $\rho \in [\underline{\rho}$, the generalized plant (6.18) can be expressed as a polytopic system composed by $N = 2$ vertices:

$$\Sigma_s(\rho) = \sum_{i=1}^{2} \alpha_i(\rho)\Sigma_{s_i}, \qquad \alpha_i(\rho) \geqslant 0, \qquad \sum_{i=1}^{2} \alpha_i(\rho) = 1. \tag{6.19}$$

where $\Sigma_{s_1} = \Sigma_s(\underline{\rho})$ and $\Sigma_{s_2} = \Sigma_s(\overline{\rho})$

The LPV controller $K(\rho)$ with the scheme as shown in Figure 6.11 is defined as:

$$K(\rho): \begin{bmatrix} \dot{x}_c \\ u_{er} \end{bmatrix} = \begin{bmatrix} A_c(\rho) & B_c(\rho) \\ C_c(\rho) & D_c(\rho) \end{bmatrix} \begin{bmatrix} x_c \\ y \end{bmatrix} \tag{6.20}$$

The controller $K(\rho)$ it can be transformed into a convex interpolation as follows:

$$K(\rho) = \sum_{i=1}^{2} \alpha_i(\rho) \begin{bmatrix} A_{c_i} & B_{c_i} \\ C_{c_i} & D_{c_i} \end{bmatrix} \tag{6.21}$$

The closed-loop system ($CL(\rho)$) can be derived from the generalized plant ($\Sigma_s(\rho)$) and the LPV controller ($K(\rho)$) as follows:

$$CL(\rho): \begin{bmatrix} \dot{\eta} \\ z \end{bmatrix} = \begin{bmatrix} \mathcal{A}(\rho) & \mathcal{B}(\rho) \\ \mathcal{C}(\rho) & \mathcal{D}(\rho) \end{bmatrix} \begin{bmatrix} \eta \\ w \end{bmatrix} \tag{6.22}$$

where $\eta = [x_g, x_c]^T$.

Similarly, the closed system (6.22) can be transformed in to a polytopic system with 2 vertices $\rho \in [\underline{\rho}, \overline{\rho}]$

$$CL(\rho) = \sum_{i=1}^{2} \alpha_i(\rho) CL_i \tag{6.23}$$

The control goal is to find an LPV controller $K(\rho)$ expressed in equation (6.20) such that:

- The system (6.22) is internally stable
- Minimize γ_∞ such that $\|z\|_{\mathcal{L}_2} < \gamma_\infty \|\omega\|_{\mathcal{L}_2}$

Then, thanks to the Bounded Real Lemma (BRL), the above requirement is solved if and only if there exist a symmetric positive definite matrix $\mathcal{P}$ such that (see [Scherer, Gahinet, and Chilali 1997]):

$$\begin{bmatrix} \mathcal{A}_i^T\mathcal{P} + \mathcal{P}\mathcal{A}_i & \mathcal{P}\mathcal{B}_i & \mathcal{C}_i^T \\ \mathcal{B}_i^T\mathcal{P} & -\gamma_\infty^2 I & \mathcal{D}_i^T \\ \mathcal{C}_i & \mathcal{D}_i & -I \end{bmatrix} < 0, \quad i = 1, 2 \tag{6.24}$$

Notice that (6.24) is a Bilinear Matrix Inequality (BMI). Via a change of basis expressed in [Scherer, Gahinet, and Chilali 1997], BMI (6.24) can be founded (with decision matrices X, Y, $\widetilde{A_i}$, $\widetilde{B_i}$, $\widetilde{C_i}$ and $\widetilde{D}$).

$$\begin{bmatrix} A_iX + XA_i^T + B_2\widetilde{C_i} + \widetilde{C_i}^T B_2^T & * & * & * \\ \widetilde{A_i} + A_i^T + C_2^T\widetilde{D_i}^T B_2^T & YA_i + A_i^TY + \widetilde{B_i}C_2 + C_2^T\widetilde{B_i}^T & * & * \\ B_{1_i}^T & B_{1_i}^TY & -\gamma_\infty I_{n_u} & * \\ C_{1_i}X + D_{12}\widetilde{C_i} & C_{1i} + D_{12}\widetilde{D_i}C_2 & D_{11_i} & -\gamma_\infty I_{n_y} \end{bmatrix} < 0$$
$$\begin{bmatrix} X & I_n \\ I_n & Y \end{bmatrix} > 0 \tag{6.25}$$

Solving (6.25) leads to the $\mathcal{H}_\infty$ optimal solution. Then, choosing M and N such that $MN^T = I_n - XY$, the controller is obtained by solving:

$$\begin{cases} \widetilde{D_i} &= D_{c_i} \\ \widetilde{C_i} &= D_{c_i}C_2X + C_{c_i}M^T \\ \widetilde{B_i} &= YB_2D_{c_i} + NB_{c_i} \\ \widetilde{A_i} &= YA_iX + YB_2D_{c_i}C_2X + NB_{c_i}C_2X \\ &+ YB_2C_{c_i}M^T + NA_{c_i}M^T \end{cases} \tag{6.26}$$

6.3.2 Synthesis results and frequency domain analysis

Solving LMIs 6.25 with the two vertices $\underline{\rho} = 0.01$ and $\overline{\rho} = 1$, leads to the minimum $\mathcal{L}_2$-induced gain $\gamma_\infty = 0.1903$ and to the controller vertex matrices. Then the LPV-FTC controller is a convex combination of the controllers computed at each vertex, so the control input can be expressed as:

$$u_{er} = \left(\frac{|\rho - \overline{\rho}|}{(\overline{\rho} - \underline{\rho})} K(\underline{\rho}) + \frac{|\rho - \underline{\rho}|}{(\overline{\rho} - \underline{\rho})} K(\overline{\rho}) \right) y \tag{6.27}$$

The resulting attenuation of the road profile disturbance on the sprung mass displacement () and unsprung mass displacement are shown in Figures , 6.16 and 6.17 respectively. Figure 6.16 gives the Bode diagram of the transfer function z_s/z_r of the closed-loop system with LPV controller at the frozen values ($\rho = 0.01$ (red dash line) and $\rho = 1$ (green dash line)),

while the blue line represents the Bode diagram of the transfer between the sprung mass displacement (z_s) and road profile (z_r) of the quarter car system with a passive damper. The Bode diagram of the transfer function z_{us}/z_r of the closed-loop system and the the passive system are presented in Figure 6.17, where the green dash and red dash lines represent for the closed-loop system at the frozen values $\rho = 0.01$ and $\rho = 1$, respectively. Note that these closed-loop transfers provide a good frequency behavior (good performances), improving comfort in the range $1 - 10$Hz (see Figure 6.16) and road holding in the range $1 - 5$Hz. Therefore, these results emphasize the satisfactory attenuation level of the unknown road profile effect on the z_s and z_{us}.

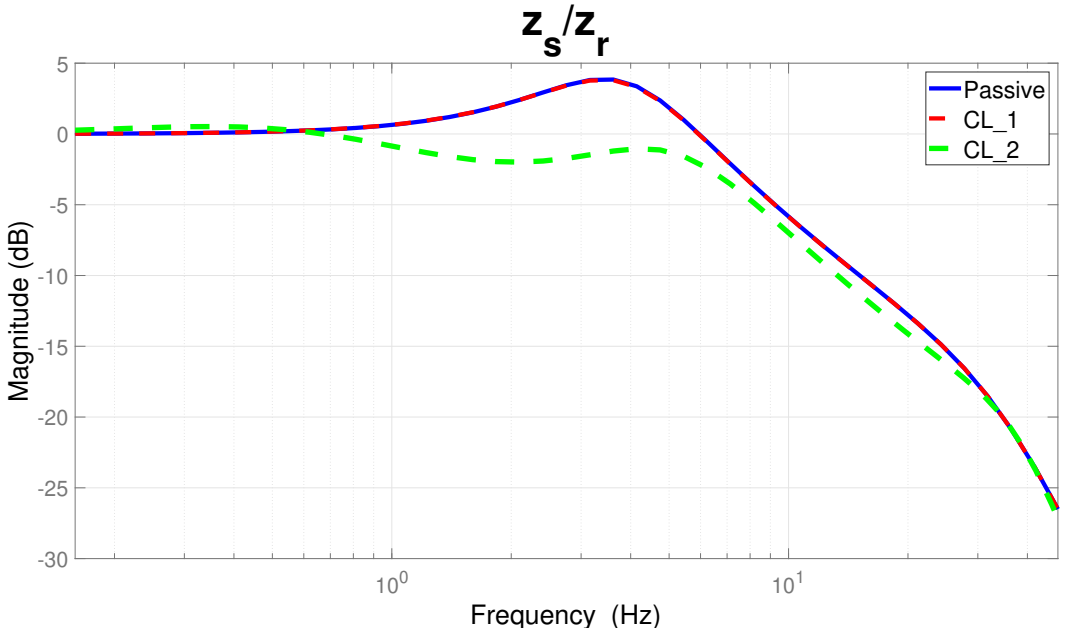

Figure 6.16: Transfer $\|z_s/z_r\|$-Bode diagram

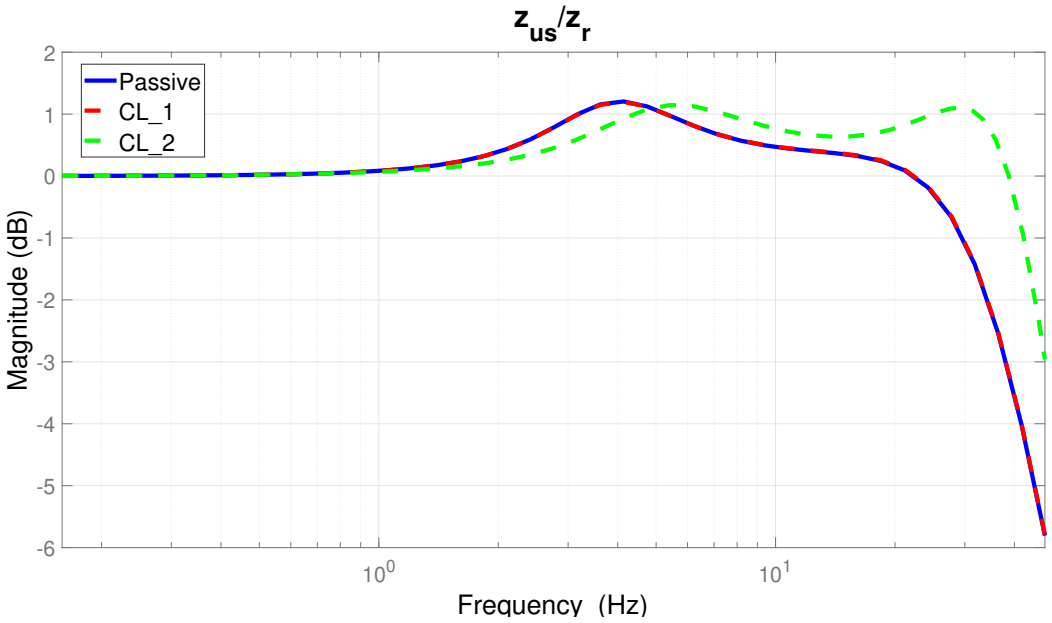

Figure 6.17: Transfer $\|z_{us}/z_r\|$-Bode diagram

6.4 Some simulation in time domain

In this Section, some simulations are performed on the quarter car model when an oil leakage fault occurs upon the semi-active ER damper. To emphasize the interest of the proposed method, the proposed LPV/FTC controller is compared with the nominal controller. It is LPV controller without changing the domain $\mathcal{D}$ according to the loss of effectiveness factor.

6.4.1 Scenario 1

The first simulation scenario is given as follows:

- A step the road profile is used, shown in Figure 6.18 .
- The damper undergoes an oil leakage fault with $f_2 = 60\%$.

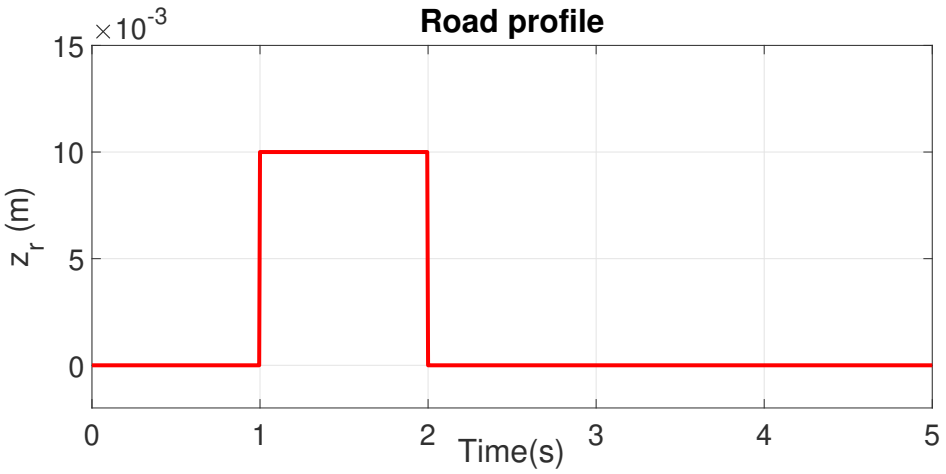

Figure 6.18: Road profile

The results are presented in Figures 6.19 and 6.20, which indicate that the fault tolerant controller designed according to the previous discussion indeed obtains a better performance than in the nominal one. According to Figure 6.19, the deflection of the suspension becomes smaller with the FTC technique.

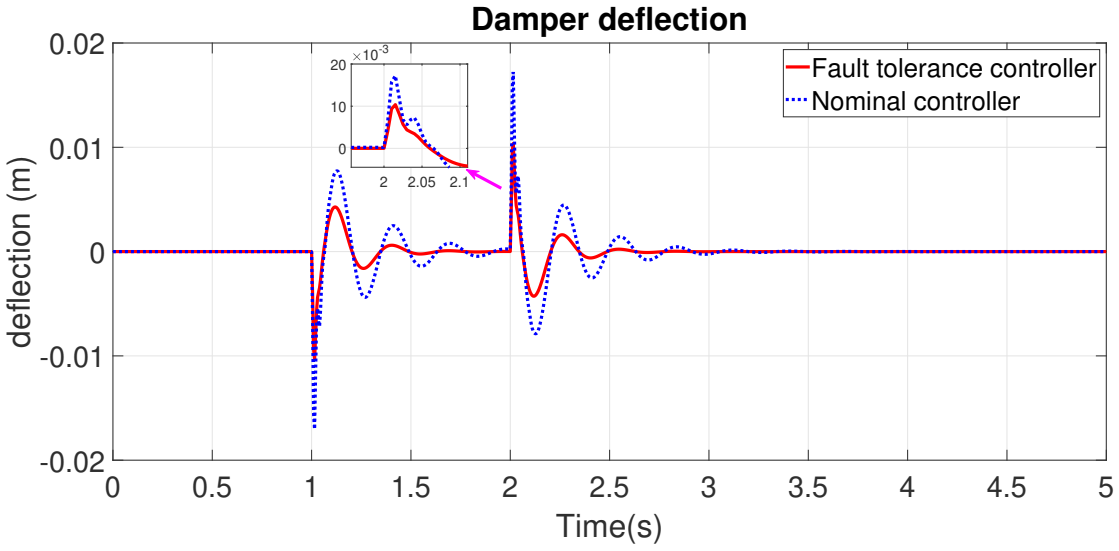

Figure 6.19: Suspension deflection

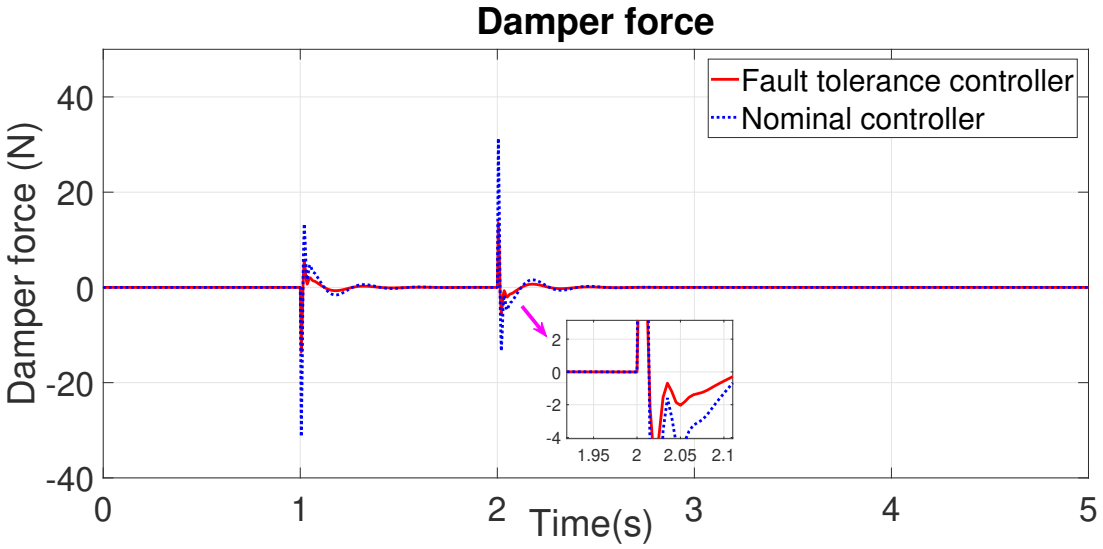

Figure 6.20: Damper force

6.4.2 Scenario 2

The second simulation scenario is as the following:

- An ISO road profile is used, shown in Figure 6.21 .
- The oil leakage is the same in the first scenario ($f_2 = 60\%$).

Figure 6.21: Road profile

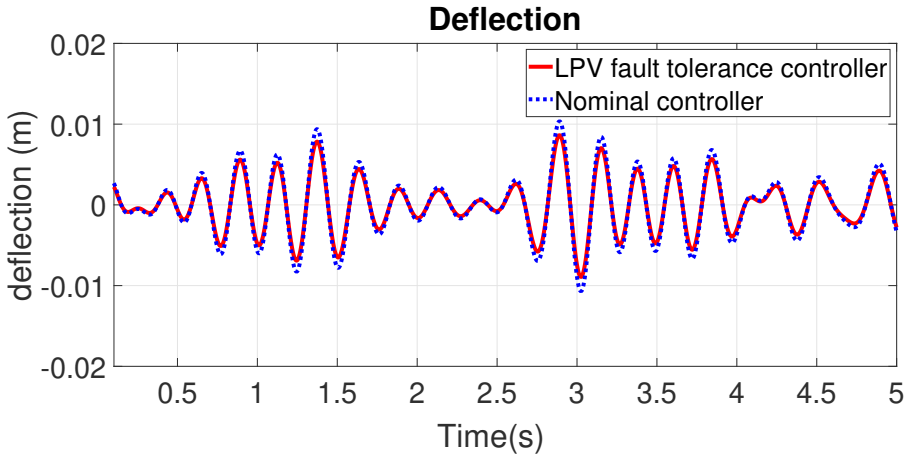

Figure 6.22: Suspension deflection

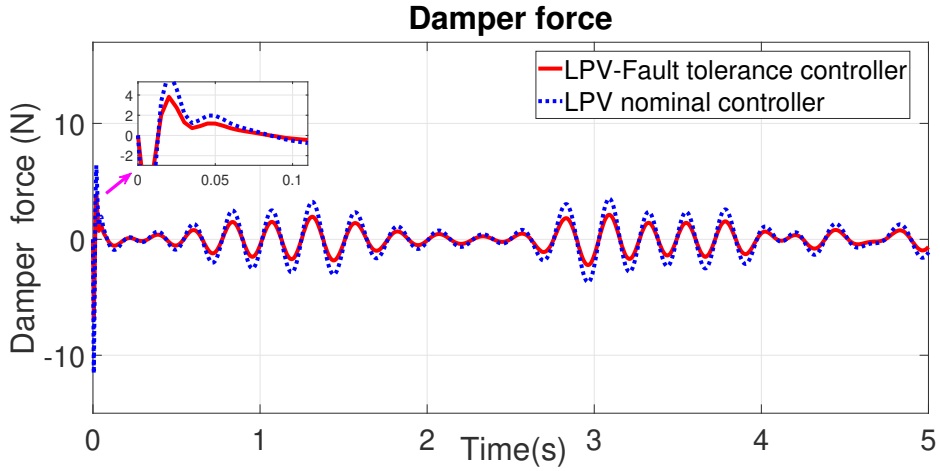

Figure 6.23: Damper force

Figures 6.22 and 6.23 show the simulation results of the scenario 2. The deflection (shown in Figure 6.22) and the damper force (see Figure 6.23)of the suspension are lower with the FTC controller. Therefore, the efficiency of the proposed solution is proven.

6.5 Conclusion

This chapter presented a $LPV/\mathcal{H}_\infty$ fault-tolerant control for the semi-active suspension system when a fault, such as oil leakages, occurs in the damper. Firstly, the effect of faults that might occur on these ER dampers is analyzed. The LPV FTC is designed to ensure the damper dissipativity constraint based on the fault model. This FTC method allows reconfiguring online the provided suspension force according to the fault situation, to reach a better performance

than obtained with the nominal controller.

Notice that the obtained controller in this chapter is $u_{er} = F_{er}$. In order to implement this controller on the INOVE testbed, the inner force controller is needed to compute the PWM signal u. On the other have, the inverse model can be used as follows:

$$u = \left(\frac{u_{er}}{\sigma} sign(z_{def})\right)^{\frac{1}{\beta}}$$

Conclusion and Perspectives

General Conclusions

This thesis has been concerned with observation and control studies of a semi-active suspension system equipped with Electro-Rheological dampers. The results of this thesis have been presented in 3 parts and 6 chapters. In summary, the main contributions of the thesis are as follows:

In terms of modelling and identification:

- Two nonlinear control-oriented models for ER dampers are proposed by using two approaches (parametric and hysteresis based) (Chapter 1);
- A unified identification procedure is presented to identify the model parameters. Then the control-oriented models are validated with various tests on the INOVE testbed. (Chapter 1).
- The extended quarter car models augmented with the dynamical nonlinear damper model are presented, which captures the main behaviors of the ER dampers (dynamic and nonlinear). The extended models are represented in the nonlinear Lipschitz and nonlinear parameter varying systems, respectively (Chapter 2).

In terms of damper force estimation methodologies:

- An extension of the synthesis of a unified $\mathcal{H}_\infty$ observer for a class of nonlinear Lipschitz systems is presented. Then the observer is applied to estimate the damper force in the semi-active suspension system and it is implemented on the INOVE testbench from GIPSA-lab (1/5-scaled real vehicle) for real-time performance assessment (Chapter 3).
- Two NonLinear Parameter Varying observers are proposed to estimate, in real-time, the damper force in the road vehicle suspension system via a constant Lyapunov function (polytopic method) and a parameter-dependent Lyapunov function (gridding method). The proposed observers have been implemented on a real scaled-vehicle test bench to assess with experimental tests (Chapter 4).
- An insightful analysis is provided through the comparison of three proposed observers (unified $\mathcal{H}_\infty$ and NLPV observers). Then the advantages and drawbacks of each method are presented (Chapter 5).

In terms of Fault-Tolerant Control methodology:

- The possible faults on the ER dampers are analyzed and the effects of these faults are incorporated into the damper model. Then a Fault Tolerance Control technique was proposed using the LPV method and fault model (Chapter 6).

Perspectives

During the thesis, several developements were initated and some results have been obtained. According to the author, the following perspectives also seem to be of great interest could be continued and developed further:

Short-term perspectives:

- **Implementation**: The real-time implementation of the Fault-Tolerant Control approach are to be conducted on the INOVE testbench to validate the performance of the proposed method experimentally.
- **NLPV observer design**: In the thesis, the nonlinearity in the semi-active damper model is bounded by a Lipschitz condition. Alternatively, this nonlinear function can also be kept inside the parameter-varying block using a Linear Fractional Transformation (LFT). The comparison between the two approaches would give a deeper analysis and provide the interest of each method.
- **Unified $\mathcal{H}_\infty$ observer** :As can be seen in Chapter 3, the full order unified $\mathcal{H}_\infty$ observer was developed, thereby increasing implementation cost. Therefore, a reduced-order observer should be designed and the comparison between the reduced-order and full order unified $\mathcal{H}_\infty$ observer will be of great interest in the future.
- **Fault detection** As discussed in Chapter 6, the loss of effectiveness of the damper should be considered to guarantee the performance of the vehicle. Therefore, the fault observer used to estimate the loss of effectiveness factor plays an important role in diagnosis and fault-tolerant control. Concerning the fault observer design problem, the system dynamics can be written in the Nonlinear Lipschitz Descriptor system. This model will be used to design the fault observer in future work.

Long-term perspectives:

- **Full car suspension system:** All of the works in this thesis focus on the quarter car model. For the future line of work, the methods are intended to be augmented to the full car suspension system.
- **Robust stability:** In chapter 4, the robust stability of the NLPV observer is developed using the maximum and minimum values of $\dot{\rho}$, i.e. $|\dot{\rho}| \leq \nu$. Let us recall the LMI (4.33)

$$\begin{bmatrix} \Omega_g(\rho) + \dot{\rho}\frac{\partial P}{\partial \rho} + \epsilon_{lg}\Gamma^T\Gamma + C_z^T C_z & P(\rho)B(\rho) & P(\rho)(\bar{D}_1 - L_g(\rho)\bar{D}_2) \\ B(\rho)^T P(\rho) & -\epsilon_{lg} I & 0 \\ (\bar{D}_1 - L_g(\rho)\bar{D}_2)^T P(\rho) & 0 & -\gamma_g^2 I \end{bmatrix} < 0 \qquad (6.28)$$

  where $\dot{\rho} \in \Delta_{\dot{\rho}}$. The assumption may be relaxed by solving above LMI with the set of value of $\dot{\rho}$, leading to an infinite number of constraints overall the trajectories of $\dot{\rho}$. Hence, the scenario approach [Calafiore and Campi 2006] may be applied to relax the limitation with a finite number of samples of $\dot{\rho}$.

- **Fault-tolerant control:** As mentioned in Chapter 6, three reasons (electrical issues, oil leakage, and Physical deformation) concern about the loss of effectiveness of the damper. Each reason has a different effect on the performance of the system. Therefore, the FTC strategies should adapt to the difference of each fault.

Bibliography

Acerbi, Emilio and Giuseppe Mingione (2002). "Regularity results for stationary electro-rheological fluids." In: *Archive for Rational Mechanics and Analysis* 164.3, pp. 213–259 (cit. on p. 14).

Ahmadian, Mehdi, Xubin Song, and Steve C Southward (2004). "No-jerk skyhook control methods for semiactive suspensions." In: *Transactions of the ASME-L-Journal of Vibration and Acoustics* 126.4, p. 580 (cit. on p. 15).

Apkarian, Pierre, Pascal Gahinet, and Greg Becker (1995). "Self-scheduled H_∞ control of linear parameter-varying systems: a design example." In: *Automatica* 31.9, pp. 1251–1261 (cit. on pp. 93, 164).

Ashfak, A, KK Abdul Rasheed, and J Abdul Jaleel (2013). "Modeling, simulation and experimental validation of Magneto-Rheological damper." In: *International Conference on Advanced Nanomaterials and Emerging Engineering Technologies*. IEEE, pp. 267–274 (cit. on p. 13).

Aubouet, Sébastien (2010). "Semi-active SOBEN suspensions modeling and control." PhD thesis. Institut National Polytechnique de Grenoble-INPG (cit. on pp. 2, 13, 55).

Bingham, Eugene C (1929). "Rheology. I. The nature of fluid flow." In: *Journal of Chemical Education* 6.6, p. 1113 (cit. on p. 18).

Bird, R Byron, GC Dai, and Barbara J Yarusso (1983). "The rheology and flow of viscoplastic materials." In: *Reviews in Chemical Engineering* 1.1, pp. 1–70 (cit. on p. 17).

Boyd, Stephen et al. (1994). *Linear matrix inequalities in system and control theory*. Vol. 15. SIAM (cit. on pp. 68, 94, 95, 97).

Bremner, Ronald Dean (2005). *Active seat suspension control system*. US Patent 6,886,650 (cit. on p. 12).

Calafiore, Giuseppe C and Marco C Campi (2006). "The scenario approach to robust control design." In: *IEEE Transactions on automatic control* 51.5, pp. 742–753 (cit. on p. 174).

Canale, Massimo, Mario Milanese, and Carlo Novara (2006). "Semi-active suspension control using "fast" model-predictive techniques." In: *IEEE Transactions on control systems technology* 14.6, pp. 1034–1046 (cit. on p. 45).

Carlson, J David, DM Catanzarite, and KA St. Clair (1996). "Commercial magneto-rheological fluid devices." In: *International Journal of Modern Physics B* 10.23n24, pp. 2857–2865 (cit. on p. 14).

Chang, Chih-Chen and Paul Roschke (1998). "Neural network modeling of a magnetorheological damper." In: *Journal of intelligent material systems and structures* 9.9, pp. 755–764 (cit. on p. 15).

Chang, Chih-Chen and Li Zhou (2002). "Neural network emulation of inverse dynamics for a magnetorheological damper." In: *Journal of Structural Engineering* 128.2, pp. 231–239 (cit. on p. 15).

Choi, S-B, S-K Lee, and Y-P Park (2001). "A hysteresis model for the field-dependent damping force of a magnetorheological damper." In: *Journal of sound and vibration* 245.2, pp. 375–383 (cit. on pp. 13, 14).

Choi, SB, HK Lee, and EG Chang (2001). "Field test results of a semi-active ER suspension system associated with skyhook controller." In: *Mechatronics* 11.3, pp. 345–353 (cit. on p. 14).

Choi, SB et al. (1998). "Control characteristics of a continuously variable ER damper." In: *Mechatronics* 8.2, pp. 143–161 (cit. on p. 19).

Choi, Seung-Bok and Sang-Soo Han (2003). "H_∞ control of electrorheological suspension system subjected to parameter uncertainties." In: *Mechatronics* 13.7, pp. 639–657 (cit. on pp. 18, 19).

Choi, Seung-Bok, Hwan-Soo Lee, and Young-Pil Park (2002). "H8 control performance of a full-vehicle suspension featuring magnetorheological dampers." In: *Vehicle System Dynamics* 38.5, pp. 341–360 (cit. on p. 44).

Darouach, Mohamed, Latifa Boutat-Baddas, and Mohamed Zerrougui (2011). "H_∞ observers design for a class of nonlinear singular systems." In: *Automatica* 47.11, pp. 2517–2525 (cit. on pp. 60, 63).

Do, Anh Lam (2011). "Approche LPV pour la commande robuste de la dynamique des véhicules: amélioration conjointe du confort et de la sécurité." PhD thesis (cit. on pp. 2, 44).

Do, Anh-Lam, Olivier Sename, and Luc Dugard (2012). "LPV modeling and control of semi-active dampers in automotive systems." In: *Control of linear parameter varying systems with applications*. Springer, pp. 381–411 (cit. on p. 12).

Do, Manh-Hung, Damien Koenig, and Didier Theilliol (2018). "Robust H_∞ Proportional-Integral Observer for Fault Diagnosis: Application to Vehicle Suspension." In: *IFAC-PapersOnLine* 51.24, pp. 536–543 (cit. on p. 45).

Du, Haiping, Kam Yim Sze, and James Lam (2005). "Semi-active H_∞ control of vehicle suspension with magneto-rheological dampers." In: *Journal of Sound and Vibration* 283.3, pp. 981–996 (cit. on p. 15).

Dugard, Luc et al. (2012). "Full vertical car observer design methodology for suspension control applications." In: *Control Engineering Practice* 20.9, pp. 832–845 (cit. on p. 13).

Dyke, SJ et al. (1996). "Modeling and control of magnetorheological dampers for seismic response reduction." In: *Smart materials and structures* 5.5, p. 565 (cit. on p. 14).

Estrada-Vela, Alfonso et al. (2018). "Hinf Observer for Damper Force in a Semi-Active Suspension." In: *IFAC-PapersOnLine* 51.11, pp. 764–769 (cit. on p. 56).

Fergani, S (2015). "Commande Robuste LPV/H_∞ Multivariable pour la dynamique véhicule." PhD thesis. Université Grenoble Alpes (cit. on p. 44).

Fergani, Soheib (2014). "Robust multivariable control for vehicle dynamics." PhD thesis (cit. on p. 2).

Fleps-Dezasse, Michael and Jonathan Brembeck (2016). "LPV control of full-vehicle vertical dynamics using semi-active dampers." In: *IFAC-PapersOnLine* 49.11, pp. 432–439 (cit. on p. 150).

Fleps-Dezasse, Michael, Ferdinand Svaricek, and Jonathan Brembeck (2017). "Damper fault-tolerant linear parameter-varying semi-active suspension control." In: *IFAC-PapersOnLine* 50.1, pp. 8592–8599 (cit. on pp. 150, 158).

— (2018). "Design and Experimental Assessment of an Active Fault-Tolerant LPV Vertical Dynamics Controller." In: *IEEE Transactions on Control Systems Technology* 99, pp. 1–8 (cit. on pp. 44, 45, 55, 150).

Gamota, DR and FE Filisko (1991). "Dynamic mechanical studies of electrorheological materials: moderate frequencies." In: *Journal of rheology* 35.3, pp. 399–425 (cit. on p. 14).

Gao, Nan, Mohamed Darouach, and Marouane Alma (2018). "Dynamic observer design for a class of nonlinear systems." In: *2018 IEEE 3rd Advanced Information Technology, Electronic and Automation Control Conference (IAEAC)*. IEEE, pp. 373–376 (cit. on p. 60).

Gao, Nan et al. (2016). "New unified H_∞ dynamic observer design for linear systems with unknown inputs." In: *Automatica* 65, pp. 43–52 (cit. on pp. 59, 60, 63, 69).

Gillespie, Thomas D (1992). *Fundamentals of vehicle dynamics*. Tech. rep. SAE Technical Paper (cit. on pp. 12, 44).

Guo, Shuqi, Shaopu Yang, and Cunzhi Pan (2006). "Dynamic modeling of magnetorheological damper behaviors." In: *Journal of Intelligent material systems and structures* 17.1, pp. 3–14 (cit. on pp. 14, 20).

Hernández-Alcántara, Diana et al. (2016). "Modeling, diagnosis and estimation of actuator faults in vehicle suspensions." In: *Control Engineering Practice* 49, pp. 173–186 (cit. on pp. 14, 45, 149, 150, 153).

Ismail, Mohammed, Fayçal Ikhouane, and José Rodellar (2009). "The hysteresis Bouc-Wen model, a survey." In: *Archives of Computational Methods in Engineering* 16.2, pp. 161–188 (cit. on p. 21).

J Lozoya-Santos, Jorge de et al. (2012). "Magnetorheological damper—an experimental study." In: *Journal of Intelligent Material Systems and Structures* 23.11, pp. 1213–1232 (cit. on pp. 13, 14, 21).

Jordan, Therese C and Montgomery T Shaw (1989). "Electrorheology." In: *IEEE Transactions on Electrical Insulation* 24.5, pp. 849–878 (cit. on p. 19).

Kamath, Gopalakrishna M and Norman M Wereley (1997). "A nonlinear viscoelastic-plastic model for electrorheological fluids." In: *Smart Materials and Structures* 6.3, p. 351 (cit. on p. 14).

Kamelreiter, Michael, Wolfgang Kemmetmüller, and Andreas Kugi (2012). "Digitally controlled electrorheological valves and their application in vehicle dampers." In: *Mechatronics* 22.5, pp. 629–638 (cit. on p. 14).

Kiencke, Uwe and Lars Nielsen (2005). *Automotive control systems: for engine, driveline, and vehicle*. Springer Science & Business Media (cit. on p. 44).

Kim, Yeesock, Reza Langari, and Stefan Hurlebaus (2009). "Semiactive nonlinear control of a building with a magnetorheological damper system." In: *Mechanical Systems and Signal Processing* 23.2, pp. 300–315 (cit. on p. 14).

Kloiber, T., G. Koch, and B. Lohmann (2010). "Modified optimal control of a nonlinear active suspension system." In: *49th IEEE Conference on Decision and Control (CDC)*, pp. 5572–5577 (cit. on p. 44).

Koch, Guido, Tobias Kloiber, and Boris Lohmann (2010). "Nonlinear and filter based estimation for vehicle suspension control." In: *Decision and Control (CDC), 2010 49th IEEE Conference on*, pp. 5592–5597 (cit. on p. 55).

Koenig, Damien (2006). "Observers design for unknown input nonlinear descriptor systems via convex optimization." In: *IEEE Transactions on Automatic control* 06, pp. 1047–1052 (cit. on p. 60).

Koo, Jeong-Hoi, Fernando D Goncalves, and Mehdi Ahmadian (2006). "A comprehensive analysis of the response time of MR dampers." In: *Smart materials and structures* 15.2, p. 351 (cit. on p. 20).

Ljung, Lennart (1999). "System identification." In: *Wiley Encyclopedia of Electrical and Electronics Engineering*, pp. 1–19 (cit. on p. 25).

Makris, Nicos, Scott A Burton, and Douglas P Taylor (1996). "Electrorheological damper with annular ducts for seismic protection applications." In: *Smart Materials and Structures* 5.5, p. 551 (cit. on p. 14).

Marquardt, Donald W (1963). "An algorithm for least-squares estimation of nonlinear parameters." In: *Journal of the society for Industrial and Applied Mathematics* 11.2, pp. 431–441 (cit. on p. 31).

Martins, Samir Angelo Milani and Luis Antonio Aguirre (2016). "Sufficient conditions for rate-independent hysteresis in autoregressive identified models." In: *Mechanical Systems and Signal Processing* 75, pp. 607–617 (cit. on p. 21).

Metered, H, P Bonello, and SO Oyadiji (2010). "The experimental identification of magnetorheological dampers and evaluation of their controllers." In: *Mechanical systems and signal processing* 24.4, pp. 976–994 (cit. on p. 13).

Milliken, William F and Douglas L Milliken (1995). *Race car vehicle dynamics*. Vol. 400. Society of Automotive Engineers Warrendale (cit. on p. 44).

Moradi, Morteza and Afef Fekih (2013). "Adaptive PID-sliding-mode fault-tolerant control approach for vehicle suspension systems subject to actuator faults." In: *IEEE Transactions on Vehicular Technology* 63.3, pp. 1041–1054 (cit. on p. 150).

Morato, Marcelo M et al. (2019). "Fault estimation for automotive Electro-Rheological dampers: LPV-based observer approach." In: *Control Engineering Practice* 85, pp. 11–22 (cit. on pp. 45, 150, 151, 161).

Morato, Marcelo Menezes, Olivier Sename, and Luc Dugard (2019). "Design and Analysis of Several State-Feedback Fault-Tolerant Control Strategies for Semi-Active Suspensions." In: *IFAC-PapersOnLine* 52.17, pp. 48–53 (cit. on pp. 150, 158, 159).

Nguyen, M. Q., O. Sename, and L. Dugard (2016). "Comparison of observer approaches for actuator fault estimation in semi-active suspension systems." In: *2016 3rd Conference on Control and Fault-Tolerant Systems (SysTol)*, pp. 227–232 (cit. on p. 45).

Nguyen, Manh Quan (2016). "LPV approaches for modelling and control of vehicle dynamics: application toa small car pilot plant with ER dampers." PhD thesis (cit. on pp. 2, 44, 45).

Nguyen, Manh Quan, Olivier Sename, and Luc Dugard (2015a). "A switched LPV observer for actuator fault estimation." In: *IFAC-PapersOnLine* 48.26, pp. 194–199 (cit. on pp. 45, 150, 151).

— (2015b). "An lpv fault tolerant control for semi-active suspension-scheduled by fault estimation." In: *IFAC-PapersOnLine* 48.21, pp. 42–47 (cit. on pp. 150, 159, 163).

Nguyen, Manh-Quan et al. (2015). "Semi-active suspension control problem: Some new results using an LPV/Hinf state feedback input constrained control." In: *Decision and Control (CDC), 2015 IEEE 54th Annual Conference on*, pp. 863–868 (cit. on p. 55).

Osorio-Gordillo, Gloria-L et al. (2019). "Generalised dynamic observer design for Lipschitz non-linear descriptor systems." In: *IET Control Theory & Applications* 13.14, pp. 2270–2280 (cit. on p. 60).

Pérez-Estrada, A-J et al. (2018a). "Generalized dynamic observers for quasi-LPV systems with unmeasurable scheduling functions." In: *International Journal of Robust and Nonlinear Control* 28.17, pp. 5262–5278 (cit. on p. 90).

Pérez-Estrada, Abraham-Jashiel et al. (2018b). "Hinf generalized dynamic unknown inputs observer design for discrete LPV systems. Application to wind turbine." In: *European Journal of Control* 44, pp. 40–49 (cit. on p. 60).

Pertew, Amr M, Horacio J Marquez, and Qing Zhao (2006). "Hinf observer design for lipschitz nonlinear systems." In: *IEEE Transactions on Automatic Control* 51.7, pp. 1211–1216 (cit. on p. 60).

Pham, Thanh-Phong, Olivier Sename, and Luc Dugard (2019a). "Comparative study of three robust observers for automotive damper force estimation." In: *IOP Conference Series: Materials Science and Engineering*. Vol. 707. 1. IOP Publishing, p. 012014 (cit. on p. 56).

— (2019b). "Design and Experimental Validation of an H_∞ Observer for Vehicle Damper Force Estimation." In: *IFAC-PapersOnLine* 52.5, pp. 673–678 (cit. on p. 56).

— (2019c). "Real-time Damper Force Estimation of Vehicle Electrorheological Suspension: A NonLinear Parameter Varying Approach." In: *IFAC-PapersOnLine* 52.28, pp. 94–99 (cit. on pp. 56, 90).

— (2019d). "Unified Hinf Observer for a Class of Nonlinear Lipschitz Systems: application to a real ER Automotive Suspension." In: *IEEE Control Systems Letters* (cit. on pp. 56, 60).

Pham, Thanh-Phong et al. (2018). "Real-time estimation of the damping force of vehicle electrorheological suspension." In: *VSDIA 2018 - The 16th Mini Conference on Vehicle System Dynamics, Identification and Anomalies*. Budapest, Hungary (cit. on p. 56).

Phanomchoeng, G and R Rajamani (2010). "Observer design for Lipschitz nonlinear systems using Riccati equations." In: *American Control Conference (ACC), 2010*. IEEE, pp. 6060–6065 (cit. on p. 61).

Poussot-Vassal, Charles (2008a). "Commande robuste LPV multivariable de chassis automobile." PhD thesis. Grenoble INPG (cit. on pp. 2, 44).

— (2008b). "Robust LPV multivariable Automotive Global Chassis Control." PhD thesis. Institut National Polytechnique de Grenoble-INPG (cit. on p. 44).

Poussot-Vassal, Charles et al. (2008). "A new semi-active suspension control strategy through LPV technique." In: *Control Engineering Practice* 16.12, pp. 1519–1534 (cit. on pp. 55, 158, 163).

Poussot-Vassal, Charles et al. (2012). "Survey and performance evaluation on some automotive semi-active suspension control methods: A comparative study on a single-corner model." In: *Annual Reviews in Control* 36.1, pp. 148–160 (cit. on pp. 13, 55).

Priyandoko, Gigih, Musa Mailah, and Hishamuddin Jamaluddin (2009). "Vehicle active suspension system using skyhook adaptive neuro active force control." In: *Mechanical systems and signal processing* 23.3, pp. 855–868 (cit. on pp. 12, 55).

Rajamani, Rajesh (1998). "Observers for Lipschitz nonlinear systems." In: *IEEE transactions on Automatic Control* 43.3, pp. 397–401 (cit. on p. 60).

Ramirez Mendoza, Ricardo Ambrocio (1997). "Sur la modélisation et la commande des véhicules automobiles." PhD thesis. Grenoble INPG (cit. on p. 1).

Rathai, Karthik Murali Madhavan, Olivier Sename, and Mazen Alamir (2019). "GPU-Based Parameterized NMPC Scheme for Control of Half Car Vehicle With Semi-Active Suspension System." In: *IEEE Control Systems Letters* 3.3, pp. 631–636 (cit. on p. 45).

Reineh, Maryam Sadeghi and Matteo Pelosi (2013). "Physical modeling and simulation analysis of an advanced automotive racing shock absorber using the 1D simulation tool AMESim." In: *SAE International Journal of Passenger Cars-Mechanical Systems* 6.2013-01-0168, pp. 7–17 (cit. on p. 19).

Sammier, Damien (2001). "Sur la modélisation et la commande de suspension de véhicules automobiles." PhD thesis (cit. on p. 1).

Sato, Masayuki (2012). "Gain-scheduled observers using inexact scheduling parameters." In: *IFAC Proceedings Volumes* 45.13, pp. 369–374 (cit. on p. 90).

Savaresi, D et al. (2019). "On-line Damping Estimation in Road Vehicle Semi-active Suspension Systems." In: *IFAC-PapersOnLine* 52.5, pp. 679–684 (cit. on p. 56).

Savaresi, Sergio M, Sergio Bittanti, and Mauro Montiglio (2005). "Identification of semi-physical and black-box non-linear models: the case of MR-dampers for vehicles control." In: *Automatica* 41.1, pp. 113–127 (cit. on pp. 14, 15).

Savaresi, Sergio M and Cristiano Spelta (2008). "A single-sensor control strategy for semi-active suspensions." In: *IEEE Transactions on control systems Technology* 17.1, pp. 143–152 (cit. on p. 55).

Savaresi, Sergio M et al. (2010). *Semi-active suspension control design for vehicles*. Elsevier (cit. on pp. xi, 12, 13).

Scherer, Carsten, Pascal Gahinet, and Mahmoud Chilali (1997). "Multiobjective output-feedback control via LMI optimization." In: *IEEE Transactions on automatic control* 42.7, pp. 896–911 (cit. on p. 165).

Schurter, Kyle C and Paul N Roschke (2000). "Fuzzy modeling of a magnetorheological damper using ANFIS." In: *Fuzzy Systems, 2000. The Ninth IEEE International Conference on*. Vol. 1. IEEE, pp. 122–127 (cit. on p. 15).

Skelton, Robert E, Tetsuya Iwasaki, and Dimitri E Grigoriadis (1997). *A unified algebraic approach to control design*. CRC Press (cit. on p. 69).

Spencer Jr, BF et al. (1997). "Phenomenological model for magnetorheological dampers." In: *Journal of engineering mechanics* 123.3, pp. 230–238 (cit. on p. 15).

Stanway, RSJL, JL Sproston, and NG Stevens (1987). "Non-linear modelling of an electro-rheological vibration damper." In: *Journal of Electrostatics* 20.2, pp. 167–184 (cit. on p. 14).

Tanelli, Mara, Matteo Corno, and Sergio Saveresi (2014). *Modelling, simulation and control of two-wheeled vehicles*. John Wiley & Sons (cit. on pp. 12, 44).

Tudon-Martinez, Juan C et al. (2013). "Fault tolerant strategy for semi-active suspensions with LPV accommodation?" In: *Control and Fault-Tolerant Systems (SysTol), 2013 Conference on*. IEEE, pp. 631–636 (cit. on p. 158).

Tudón-Martínez, Juan C et al. (2015). "Adaptive road profile estimation in semiactive car suspensions." In: *IEEE Transactions on Control Systems Technology* 23.6, pp. 2293–2305 (cit. on pp. xiii, 15).

Tudon-Martinez, Juan C et al. (2017). "Full vehicle combinatory efficient damping controller: Experimental implementation." In: *IEEE/ASME Transactions on Mechatronics* 23.1, pp. 377–388 (cit. on p. 55).

Tudon-Martinez, Juan C et al. (2018). "Parameter-Dependent Hinf Filter for LPV Semi-Active Suspension Systems." In: *IFAC-PapersOnLine* 51.26, pp. 19–24 (cit. on pp. 56, 90).

Unger, Andreas et al. (2013). "Application of LQ-based semi-active suspension control in a vehicle." In: *Control Engineering Practice* 21.12, pp. 1841–1850 (cit. on p. 44).

Wen, Yi-Kwei (1976). "Method for random vibration of hysteretic systems." In: *Journal of the engineering mechanics division* 102.2, pp. 249–263 (cit. on p. 15).

Witters, Maarten and Jan Swevers (2010). "Black-box model identification for a continuously variable, electro-hydraulic semi-active damper." In: *Mechanical Systems and Signal Processing* 24.1, pp. 4–18 (cit. on pp. 13, 14).

Yakoh, Takahiro and Tojiro Aoyama (2000). "Application of electro-rheological fluids to flexible mount and damper devices." In: *26th Annual Confjerence of the IEEE Industrial Electronics Society*. Vol. 3. IEEE, pp. 1815–1820 (cit. on p. 18).

Yamamoto, Kazusa (2017). "Control of electromechanical systems, application on electric power steering systems." PhD thesis. Grenoble Alpes (cit. on p. 12).

Yoshimura, T et al. (2001). "Construction of an active suspension system of a quarter car model using the concept of sliding mode control." In: *Journal of Sound and Vibration* 239.2, pp. 187–199 (cit. on p. 12).

Zemouche, Ali and Mohamed Boutayeb (2013). "On LMI conditions to design observers for Lipschitz nonlinear systems." In: *Automatica* 49.2, pp. 585–591 (cit. on pp. 60, 61).

Zin, Alessandro (2005). "Sur la commande robuste de suspensions automobiles en vue du contrôle global de châssis." PhD thesis (cit. on pp. 1, 45).

Résumé — De nos jours, les suspensions semi-actives ont reçu beaucoup de considération de l'industrie et du monde universitaire en raison de leurs avantages par rapport aux suspensions actives et passives en réduisant les effets des perturbations routières sur les passagers à bord (confort) et en maintenant le contact pneu/chaussée (sécurité). Les études de cette thèse se concentrent sur la modélisation, l'observation et la commande d'un système de suspension automobile équipé d'amortisseurs Electro-Réologiques semi-actifs,. Le travail est divisé en trois parties principales. La première partie présente l'étude de modélisation et l'identification de deux modèles non linéaires simplifiés pour les amortisseurs ER. Dans la deuxième partie, trois observateurs sont proposés (dans le cadre de l'approche Hinfini pour les systèmes à Paramètres Variants) afin d'estimer la force d'amortissement de l'amortisseur ER, ceci étant crucial pour le diagnostic et la commande de la dynamique véhicule. La dernière partie est dédiée au contrôle tolérant aux fautes du système de suspension semi-active en utilisant l'approche LPV. Les méthodes proposées sont mises en œuvre sur le banc d'essai INOVE de GIPSA-lab (véhicule réel à l'échelle 1/5) pour l'évaluation des performances en temps réel. La simulation et les résultats expérimentaux démontrent l'efficacité des approches proposées.

Mots clés : Suspension semi-active, observateur NLPV, observateur unifié H_∞, contrôle LPV, Nonlinéarité de type Lipschitz, amortisseur Electro-Rhéologique, stabilité quadratique, stabilité robuste.

Abstract — Nowadays, the semi-active suspensions have received a lot of consideration from industry and academia due to their advantages compared to active and passive suspensions in reducing the effects of the road disturbances on the on-board passengers (comfort) and in maintaining tire-road contact (safety). The research studies of this thesis focus on the modeling, observer and control design of the semi-active automotive suspension system equipped with Electro-Rheological dampers. The research work is divided into three main parts. The first part presents the modeling study and identification of two nonlinear control-oriented models for ER dampers. In the second part, three observers (in the Hinfinity context for Parameter Varying systems) are proposed to estimate the damping force of ER damper in the suspension system, which is of great importance for vehicle dynamic diagnosis and control. The final part is dedicated to the fault-tolerant control of the semi-active suspension system using the LPV approach. The proposed methods are implemented on the INOVE testbench of GIPSA-lab (1/5-scaled real vehicle) for real-time performance assessment. Both simulation and experimental results demonstrate the effectiveness of the proposed approaches.

Keywords: Semi-active suspension system, NLPV observer, unified H_∞ observer, LPV control, Lipschitz nonlinearity, Electro-Rheological damper, quadratic stability, robust stability.